University of Canterbury

Department of Electrical and
Computer Engineering

Growth and Characterisation of Au Colloid Catalysed Zinc Oxide Nanowires

---

A thesis submitted in partial fulfilment

of the requirements for the Degree of

Doctor of Philosophy

in Electrical and Electronic Engineering

at the

University of Canterbury

By

Max F. Lynam

August 2016

Final Revision May 2017

Abstract

This thesis concerns new and in-depth research into the use of eclipse pulsed laser deposition (EPLD) to grow ZnO and ZnMgO nanowires and the use of chemically synthesised gold colloids and atomic clusters with precisely controlled dimensions as catalysts to control the dimensions of the resulting nanowires. The nanowires grown by these methods were characterised using a range of electrical and optical techniques. ZnO nanowires grown by collaborators using different growth methods were also characterised and compared to those produced by EPLD.

A new method was developed for applying the nanoscale quantities of catalyst metal required for vapour-liquid-solid (VLS) nanowire growth. Chemically synthesised gold colloids were tethered to the surface of the sapphire substrate without aggregation using a silanising ligand, 3-aminopropyl trimethoxysilane (APTMS). ZnO and ZnMgO nanowires were grown on these gold colloid tethered substrates using EPLD. The operating parameters of the EPLD system were optimised to produce well-ordered arrays of nanowires. These nanowires had a tapered morphology and their tip diameters could be reproducibly controlled across a range of 5-40 nm by selecting the diameters of the gold catalyst colloid nanoparticles.

Atomically precise, non-metallic gold clusters were used to investigate whether a lower limit exists on the size of Au nanoparticle catalysts for VLS ZnO nanowire growth. Chemically synthesised clusters of 101 and 9 Au atoms were separately applied to sapphire substrates using the APTMS ligand tethering method and used to catalyse ZnO nanowire growth by EPLD. These nanowires had tip diameters of less than 1.5 nm (the measurement limit of the scanning electron microscope used), indicating that non-metallic Au clusters are able to catalyse VLS nanowire growth in ZnO.

A method was developed for fabricating permanent ohmic and Schottky contacts onto individual nanowires using electron beam lithography (EBL). The nanowires were found to be very resistive, but highly sensitive to UV illumination, with more than three orders of magnitude increase in current measured after 30 s of 365 nm UV illumination while being held at a constant voltage of 1V. This photocurrent was highly persistent and decayed to pre-illumination levels over approximately 5000 s in atmosphere. By illuminating contacted nanowires in vacuum and in atmosphere, it was shown that the photocurrent in ZnO nanowires is generated by two parallel mechanisms: the formation of electron-hole pairs across the bandgap and the hole-induced desorption of oxygen adsorbed on the crystal surface. Photogenerated electron hole pairs decayed exponentially with time both in atmosphere and in vacuum, but the desorbed surface oxygen

could not be recovered in vacuum, leading to a permanent increase in conductivity while the nanowire remained under vacuum conditions.

Photoluminescence (PL) and x-ray diffraction spectroscopy (XRD) were used to assess the crystallinity, the dominant donor impurities and preferential growth direction of the ZnO nanowires grown by EPLD. The dominant excitonic PL peak was found to be I_9, indicating that indium was the most significant impurity present. PL line widths were very narrow, indicating excellent crystal quality. No detectable PL emission in the visible defect band region was observed, with at least five orders of magnitude increase in emission intensity between the excitonic UV emission and any defect band emission. The complete absence of defect band emission is unusual even in ZnO nanowires and is a further indicator of high crystal quality. The preferred growth direction of the nanowires was confirmed by XRD to be in line with the ZnO <002> plane.

An ultra-thin sputtered film of palladium was used for the first time as a catalyst to grow ZnO nanowires. Despite having a significantly higher melting point than the EPLD ZnO growth temperature, a size dependent melting point reduction effect is proposed that enables the palladium film to dewet into liquid droplets that catalyse the VLS nanowire growth.

Acknowledgements

I would like to start by thanking my supervisor Associate Professor Martin Allen. Martin has been a great help at every step of my postgraduate work, finding opportunities for me to travel abroad and attend conferences and other research facilities. A hardworking leader with a contagious enthusiasm for his research, he gave me the positivity I needed to push on when the going was tough, but the grounding to keep going in a logical and methodical manner when the going was good. Postgraduate students are often assigned strange tasks by their supervisors, but helping Martin demonstrate electric fields to his 100-level electronics class, dressed as Darth Vader and armed with a fluorescent tube "lightsabre" was a task I wouldn't have expected from anyone other than Martin.

Thanks also to Dr. Nei-Jin Ke and her supervisor Dr. Vladimir Golovko, who collaborated with me throughout this project, providing the chemistry expertise to manufacture and apply the gold colloids which were crucial to my work. I must admit, at such a significant milestone as finishing one's postgraduate study it's heartening to know that Dr. Ke has been employed in an exciting job working on super-capacitors.

To Gary Turner and Helen Devereaux, the magical pair who oversee the operation of the cleanroom, I am also very grateful. From them, I learned most of the skills that I developed over the course of my study and none of it would have been possible without their uncanny knowledge of how things, both mechanical and human, work in the laboratory. Likewise, thank you to Mike Flaws from Mechanical Engineering for tuition and supervision of the JEOL-7000 SEM.

A big thank you to Dr Farrel and Professor Reeves from Physics for tolerating a grubby engineer like myself in the Physics laser lab and for helping me with the deposition end of my experiments. Dr Farrel truly appeared to know every nut and every bolt in the entire laser lab and was a great source of information on the operation and principles of the equipment, no matter how in depth my questioning on it got.

Thanks to Alex Neimann and Dr. Robert Heinhold for their tireless dedication to the fine art of photoluminescence. The PL data presented in this work is of world-class quality, due entirely to their skill and their knowledge of the equipment.

Thanks also to Adam Hyndman for his help with MBE and XRD and also for the off-topic chatter waiting in the laser lab together for various vacuum systems to pump up or down or heat up or cool down.

My gratitude to Conor Burke-Govey from Victoria University, who travelled down to learn my technique of nanowire contacting. Nanowires are a difficult and uniquely frustrating thing to work with and it was great to be able to have a frank discussion with someone who knew this as well as I did.

A special thanks to my fellow metal-oxides Ph.D. researcher Alana Hyland, who helped me with the sputtering and contacting parts of my work. Thank you for the encouragement, commiseration and emotional support through the most frustrating moments of my postgraduate study.

Last but not least, a great thank you to my parents, Graeme and Jenny Lynam. You've been an inspiration to succeed and a solid foundation of willpower and support throughout my study. I'm proud to be your son.

Table of Contents

Conference Contributions

[1] Max Lynam, Sabrina Ke, Martin Allen, Vladimir Golovko, Alison Downard. *Gold nanoparticle catalyzed growth of ZnO nanowires by pulsed laser deposition.* The Sixth International Conference on Advanced Materials and Nanotechnology (AMN-6), Auckland, NZ (2013), Talk.

[2] Max Lynam, Martin Allen, Adam Hyndman. *Effects of growth conditions on the optical and electrical properties of ZnO nanowires.* The 8th International Workshop on Zinc Oxide and Related Materials Niagara Falls, Canada (2014), Talk.

[3] Max Lynam, Martin Allen, Adam Hyndman, Nei-Jin Ke, Vladimir Golovko. *Persistent photocurrent in ZnO nanowires.* The Sixth Annual Conference on Advanced Materials and Nanotechnology (AMN-6), Nelson, NZ (2015), Poster.

[4] Max Lynam, Martin Allen, Sabrina Ke, Alex Neimann, Vladimir Golovko, *Au Colloid and Nanocluster Catalysed Growth of Ultrafine ZnO Nanowires by Eclipse PLD*. Cluster Symposium 2016, Christchurch, NZ (2017), Keynote Talk.

List of Figures

Chapter 1

Chapter 2

Chapter 3

Chapter 4

Chapter 5

Chapter 6

Chapter 7

Chapter 8

List of Tables

Chapter 2

Chapter 3

Chapter 6

Chapter 8

Contributions

Chapter 3

13 nm Au colloids synthesised by Dr Jin Ke and her supervisor Dr Golovko. Colloid deposition for initial experiments conducted by Dr Ke, later colloid and APTMS depositions conducted collaboratively by both Dr Ke and I.

Initial ZnO nanowire PLD growth (Growth #1, see Appendix 1) conducted with active supervision by laboratory supervisor Dr Farrell. All subsequent growths were carried out independently.

The thesis of Reuben Mendelsberg provided technical instruction specific to the operation of the UC PLD equipment relevant to the growth of ZnO nanowires. Dr Mendelsberg was not involved with the work conducted in this thesis and the scope of Dr Mendelsberg's work is only tangential to my own. Special attention to his work is only paid because it was conducted using the same apparatus, specifically the eclipse plates, for which there is relatively little independent literature regarding.

Chapter 4

Au101 and Au9 clusters were synthesised by Dr Golovko from the Department of Chemistry. Calculations of the weight of clusters required and deposition of the clusters onto the growth substrates was a collaborative effort by Dr Golovko and I.

Chapter 5

Dr Lord from the University of Swansea and Prof. Watkins from Simon Fraser University contributed samples of nanowires grown by different methods at their respective laboratories. No further input was taken from these groups as to the direction of experiments, although results were relayed back to these collaborators.

Chapter 6

Operation of the photoluminescence apparatus was conducted by Alex Neimann from the Department of Physics and Astronomy under the direction of Assoc. Prof. Allen and I.

Operation of the XRD apparatus was conducted by Adam Hyndman from the Department of Physics and Astronomy under the direction of Assoc. Prof. Allen and I.

Chapter 7

Operation of the photoluminescence apparatus was conducted by Alex Neimann from the Department of Physics and Astronomy under the direction of Assoc. Prof. Allen and I.

Chapter 8

Molecular Beam Epitaxy growth was conducted collaboratively by Adam Hyndman from the Department of Physics and I.

Chapter 1: Introduction and Background

1.1 Nanotechnology

"Nanotechnology" has long been a buzzword in the Western consciousness. Used in the context of science fiction, it provides a general purpose justification for any technology that the author wishes the audience to suspend their disbelief for. Nanotechnology is a type of magic that is somehow more plausible than the supernatural. In the popular conception, it can be swarms of tiny, self-replicating robots, a chemical that can spontaneously generate power or a material harder than diamond but lighter than foam. Of course these things do exist in reality: Nanobots are being trialled to deliver medical payloads into the cores of tumours [1], organic and dye sensitised solar cells can create power seemingly out of thin air [2] and carbon nanotubes have demonstrated some astounding mechanical properties [3].

As always, science is viewed by the media and entertainment industries with a certain sense of wonder, embellishment and romanticisation. In many regards, this could be considered a great and fortunate thing. So called "Pop Science" pages, posting quips and statistics about recent discoveries have large and devoted followings on social media. While neither science fiction nor pop science present an especially realistic or academically sound view of the field, they spread a conviction among the public that scientific research is a powerful tool of good to be encouraged and supported.

However science and in particular nanotechnology, is not all spaceships and nano-drones. People are often surprised to hear that nanotechnology is in a large part, an extension of materials science. Nanotechnology concerns the interaction of materials with one another at a nanometre scale, where tiny forces such as the Hall Effect, lattice strain and the attraction between electrons and holes dominate. It is this type of intimate understanding of materials science that allows the nanobots and the billion-transistor CPUs to function and to advance. So nanotechnology is built from a bottom-up approach, starting at the movement of electrons and working up to spaceships from there.

I began my forays into nanotechnology in my final project for my undergraduate year of electrical engineering. I elected to take on a project making transparent, thin-film transistors for then Senior Lecturer Dr. Martin Allen. Dr. Allen's group focused on metal oxides and wide bandgap semiconductors, primarily zinc oxide, but also touching on magnesium oxide, tin oxide and with a rising interest in the latest headline-making material gallium-indium-zinc oxide. Over the course of this project, I worked in a cleanroom and by the time it came to hand in my report, I had created the world's first metal-semiconductor field effect transistors (MESFETs) on cathodic-arc ZnO as shown in Figure 1. My devices were the basis of two academic papers by Dr. Allen's postgraduate students [4, 5]. Inspired, I decided to continue my studies in "The Science of Small" on metal oxides.

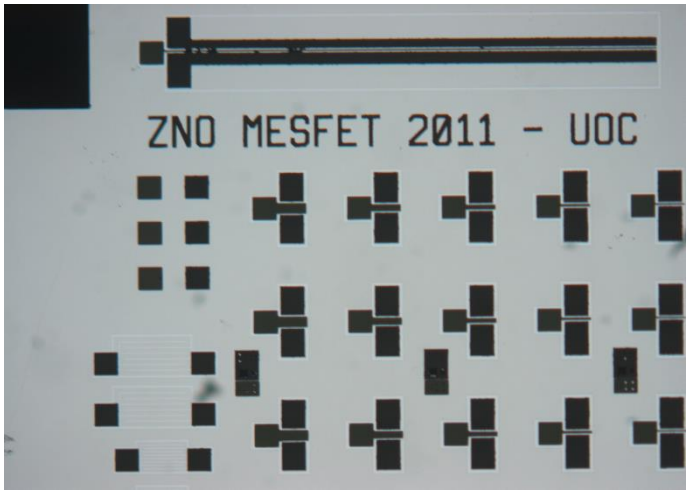

Figure 1: The world's first cathodic arc ZnO based MESFETs, fabricated in my final year of undergraduate study.

1.2 Zinc Oxide, a Transparent, UV semiconductor

ZnO is a II-VI semiconductor with a number of useful properties that allow it to compete with the dominant incumbent silicon in various areas of the semiconductor industry. It has a wide, direct bandgap of 3.3 eV at room-temperature. This means that it absorbs and emits strongly in the UVA region but has very high transmittance to the less energetic wavelengths in the visible spectrum. This property has found uses for ZnO in medical studies of solar radiation [6] and in solar cells and UV detectors [7]. Combined with a low toxicity and an erythemal response similar to human skin, it has also become a staple ingredient in commercial sunscreen lotion.

ZnO also features a high exciton binding energy of 60 meV [8]. An exciton is a quasi-particle formed when an electron in a high purity semiconductor becomes excited and jumps from the valence band into the conduction band, leaving a positively charged hole behind, illustrated in Figure 2. In the absence of defects, the electron and the hole orbit each other, their movements governed by Coulomb interaction [9]. The exciton only exists for a short amount of time until the two constituent parts recombine and the electron returns to the valence band. The lifetime of the exciton system and by extension, the distance it can travel, are governed by the exciton binding energy: the energy required to separate the pair. While an exciton has a hydrogenic waveform (ie. Similar to a hydrogen atom with one negative electron orbiting a positive

proton), the exciton has a much lower binding energy than a hydrogen atom. This is due partly to the much lower mass of the exciton's positively charged hole than the hydrogen atom's proton and also to Coulomb screening from other electrons in the semiconductor's conduction band.

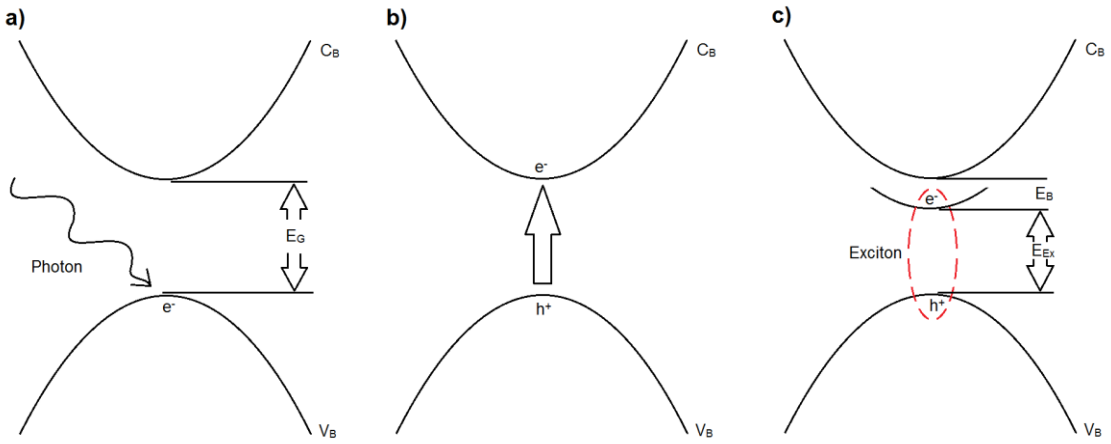

Figure 2: Formation of an exciton. a) An incident photon is absorbed by an electron in the valence band V_B. b) The electron is energised to jump the bandgap. c) The electron becomes attracted to the positive hole left behind in the valence band and the two orbit one another. The exciton has energy E_{Ex} and binding energy E_B.

The formation and recombination of excitons is a desirable property in optical devices as exciton formation enhances absorption and recombination enhances emission. ZnO's exciton binding energy of 60 meV compares very favourably to silicon's 17.4 meV and even GaAs's 24 meV. Combined with the UV bandgap of ZnO, this led many in the early to mid 2000's to believe that ZnO based blue/violet LED's and laser diodes would soon revolutionise the field of optoelectronics [10]. Unfortunately, despite early promising signs [11], these predictions have not yet come true as research has run aground on the problem of creating reliable, stable p-type ZnO for the required PN junctions.

Despite efforts to force it to behave otherwise, ZnO is intrinsically an n-type semiconductor and remains resolutely so, even at extremely high purity levels and in the absence of n-type dopants. Zinc interstitials and oxygen vacancies in the crystal lattice are believed to be responsible and even heavy handed doping has been unable to counteract this tendency. This problem has hobbled the commercial adoption of ZnO for the ubiquitous complimentary metal-oxide-semiconductor (CMOS) architecture, but proponents of MESFET architecture point out that ZnO readily forms high quality Schottky contacts with various metals. Assoc. Prof. Allen discovered in his own PhD research that Schottky contacts on ZnO are even more effective when made with metal oxides such as silver oxide (AgO_x) [12, 13]. Schottky contacts and their associated MESFET devices actually have a lower forward voltage drop than the more ubiquitous MOSFET (Metal Oxide Semiconductor Field Effect Transistor) architecture, resulting in faster switching speeds and greater power efficiency.

An incremental improvement in speed and efficiency alone would not be enough to entice the deeply entrenched silicon microelectronics industry to take note, as such gains are offset by the financial hysteresis of building new infrastructure and funding R&D in a new field. However, ZnO and its derivatives have another important selling point, touched on earlier: transparency in the visible range. The visible spectrum of light ranges from approximately 1.65-3.26 eV, lower than the bandgap energy of ZnO (3.3 eV) but higher than the bandgap of silicon (1.1 eV [14]). Even a violet (3.26 eV) photon still does not have enough energy required to excite an electron across ZnO's wide bandgap, so visible wavelength photons just pass straight through the ZnO lattice.

ZnO is not the only transparent semiconductor on the market, in fact many metal oxides are transparent to visible light and able to function as semiconductors. Indium-doped tin oxide (ITO) is an especially prominent example, but GaO and MgO are also transparent semiconductors. However the strong intrinsic doping which keeps ZnO n-type gives it a higher mobility and consequently lower resistance than other metal oxides. Undoped bulk crystal ZnO's intrinsic n-type mobility of approximately 205 $cm^2V^{-1}s^{-1}$ [15] is lower than monocrystalline silicon's typical 1400 $cm^2V^{-1}s^{-1}$, but commercial requirements for scalability often preclude the use of expensive single crystals in favour of polycrystalline or amorphous materials. ZnO can be combined with indium and gallium to form amorphous indium-gallium-zinc-oxide (IGZO). IGZO has an incredibly high mobility for an amorphous material of up to 60 $cm^2V^{-1}s^{-1}$ [16] due to the large, overlapping electron orbitals of the indium atoms. For large area applications such as electronic displays, where monocrystalline silicon is prohibitively expensive, IGZO's mobility is considerably higher than the current industry standard of amorphous silicon, where a mobility of just 1 $cm^2V^{-1}s^{-1}$ is considered very high [17].

This has attracted interest from LCD panel giants such as LG and Sharp. Flat panel LCD screens require a positive and a negative electrode on either side of a liquid crystal cell, with a transistor to switch the cell on and off. As pixel resolution increases, space comes at an increasing premium. A transparent, oxide-based transistor can be laid in front of the cell, taking up no additional lateral room and allowing a designer to place more pixels closer together. Some of the highest resolution displays on the market today are already starting to incorporate IGZO to great success. Japanese company Sharp shocked commentators at the 2013 IFA consumer electronics show in Berlin by unveiling their prototype IGZO display, a tiny 5.5" panel with a pixel resolution of 3840 x 2160 that blew competing products out of the water by almost a factor of two in resolution. It seems certain that whatever the future of consumer electronics contains, ZnO and other metal oxides are likely to be a part of it.

1.3 Strange Phenomena in ZnO

There is still much that is not well understood about the most basic fundamentals of metal oxide semiconductors. ZnO exhibits a range of strange surface effects. ZnO forms a wurtzite crystal structure at room temperature and pressure. Due to the high ionicity of the Zn-O bond, the ZnO crystal lattice can be considered to be formed from alternating sheets of positive Zn^{2+} ions and negative O^{2-} ions. This makes sense through the bulk of the material, but what about the surfaces where this regular crystal lattice is truncated? One face of the crystal is covered with exposed positive Zn^{2+} ions and the other is comprised of negative O^{2-} ions. This sort of surface is called a Tasker-III ionic material and should make these faces of the crystal electrostatically unfavourable and energetically unstable [18]. This effect is so pronounced as to allow for spontaneous and piezoelectric polarisations of the ZnO crystal along the (0001) axis. Despite all this, the Zn and O faces of the crystal are actually stable!

One theory to explain this involves the adsorption of oxygen and hydrogen onto the surfaces. The Zn face is capped with a layer of OH groups and the O face is capped with a layer of adsorbed H groups. It has been shown by research from our department that these groups can be driven off by high temperature annealing in a vacuum but that they reattach very quickly the moment the crystal is exposed to even moderately low vacuum, let alone atmosphere [18]. Previous work by researchers in my department showed that these hydroxyl groups could be measured by using in-situ X-ray photoelectron spectroscopy (XPS) to monitor a commercial ZnO substrate that was exposed to cycles of heating, followed by dosing with water vapour [19]. A further curiosity is triangular shaped structures observed on the surface of the crystal by Scanning Electron Microscopy (SEM) and Atomic Force Microscopy (AFM). These have been argued to be a self-assembled, geometric method of balancing the polar surfaces' charge during crystal growth [20]. ZnO is also one of a small group of n-type semiconductors whose conduction and valence bands bend downwards at their polar surfaces, indicating the presence of a surface electron accumulation layer and a high concentration of donorlike states. So ZnO crystals are neutral in charge when they shouldn't be, they adsorb gases from the air onto their surface, exhibit band bending the opposite direction to what would be expected, create electron accumulation layers where they don't seem needed and are capable of arranging their surface geometry to enable this. A lot of strange and interesting things happen on the surface of the ZnO crystal!

No material or wondrous electrical device is any good if it cannot be connected to a circuit. Any circuit requires connections and wherever a connection occurs, the behaviour of that connection will be determined by the interface of the materials being connected. The world's highest mobility transistor channel would be worthless if no material could make a good ohmic contact onto it. A sound understanding of the surface of a material is therefore critical to any applications that material might have.

Studying the surface of a material can be done in various ways, many of which are used in this thesis. SEM offers a clear picture of the surface of a sample at magnifications of up to 100,000x. Analytical techniques with relatively low penetration such as X-Ray Diffraction (XRD) and Reflective High Energy Electron Diffraction (RHEED) graze the surface of the sample and reveal information about the first few atomic layers. Transmission Electron Microscopy (TEM) allows a researcher to observe the atoms in the lattice as they approach the surface of the material. A more practical, applications driven approach is being taken by my fellow postgraduate student Alana Hyland in manufacturing and testing electrical contacts on ZnO with many diverse kinds of materials. All of these techniques are useful for studying surface effects, but a different avenue of materials science offers us an opportunity to concentrate and enhance these effects for easier study: Nanostructures.

1.4 ZnO Nanostructures

Nanostructures are any structure with dimensions measured in nanometres- the range of sizes that bridges the microscale with the molecular scale. “Nanostructures” is a blanket term that covers a vast range of different shaped objects, ranging from nanotubes, rods, bridges and wires to nanodots, clusters and even nanoflowers [21, 22]. Literature is filled with new phrases being coined for novel types of nanostructures, often self-assembled by various means. In a lot of cases, the complexity of creating nanostructures and the difficulty in handling or manipulating them has relegated them to the position of academic curiosities, but a few examples do stand out as commercial success stories. Materials enhanced with bulk carbon nanotubes have already started to appear in commercial and industrial markets. Finnish company Amroy Europe Oy manufactures a resin called Hybtonite that uses chemically activated carbon nanotubes and epoxy to create a bond it claims is 20-30% stronger than competing products. In 2010 Zyvex Technologies released a prototype unmanned surface vessel called the Piranha built from a carbon nanotube enhanced composite called Arovex. Zyvex claims this enables the 54’ craft to weigh “significantly less” than similar boats and that Arovex material is 20-50% stronger than other construction matierals.

ZnO nanostructures have been grown and fabricated in many forms in the last two decades. In fact, ZnO nanostructures take so many diverse forms that Wang [22] makes the bold claim that “ZnO probably has the richest family of nanostructures among all materials, both in structures and in properties.”. In his review paper, Wang covers the synthesis of all manner of novel nanostructures, but the simplest and perhaps most practical nanostructure of ZnO is the one with the fewest dimensions: the nanorod or nanowire. Nanorods are lengths of material with diameters in the nanometer scale and lengths ranging from hundreds of nanometers up to several microns. Nanowires are nanorods with high length to width ratios and are often

thought of as being 1-dimensional due to their narrow diameters. An object of such extreme dimensions brings with it a few very useful properties. Most notably for research into the surface of the ZnO crystal, nanowires have extremely high surface area. If the surface effects discussed earlier concern the first five atomic layers and the lattice constant of the crystal is 0.5 nm, then the area of interest for studying those effects is the first 2.5 nm. Using even a thin film of 100 nm thickness, the effects being studied would be present in only 2.5% of the volume of the sample and could potentially be drowned out by bulk effects from the other 97.5%. However, in an array of circular nanowires 10 nm in diameter, these surface effects would be present in 50% of the sample's diameter and 75% of its volume!

1.5 Nanowire Growth

Nanowires are self-assembled: they form naturally when conditions are satisfied [23-27]. This is possible because the materials that they are made of have a preferred crystallographic growth direction and the strength of this preference can be enhanced by controlling the growth conditions. The preferential growth direction depends on the lattice structure of the crystal being grown. In wurtzite ZnO, growth is preferred along the (0001) C-axis. Wen-Jun Li *et al*. [28] propose that the reason for this is to do with the orientation of the coordination tetrahedrons at each face of the ZnO crystal. The coordination number for both Zn an O atoms in the ZnO crystal is four; each O^{2-} shares electrons with four Zn^{2+} ions in a tetrahedral shape. The corners of these tetrahedrons share electrons with neighbouring units. An incoming atom joining the crystal can arrive at one of three locations: at a face, at a point or at an edge. An atom that arrives at a corner makes one bond and can then bond to three more atoms, as shown in Figure 3. An atom arriving at an edge makes two bonds and can make two more. An atom arriving at a face

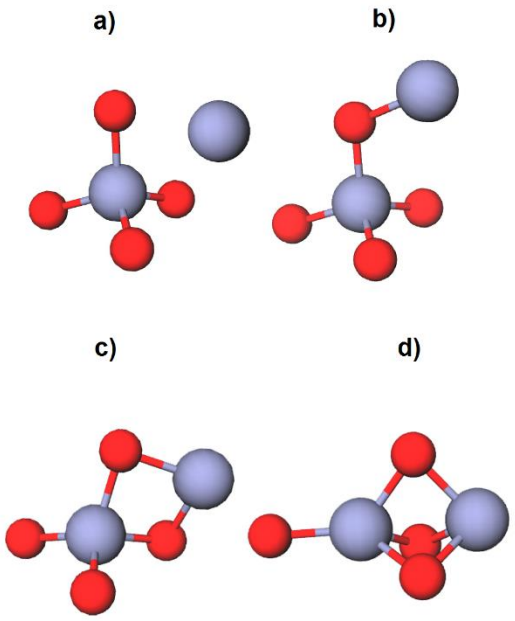

Figure 3: Zinc coordination tetrahedron showing Zn (grey) and O (red). a) An additional Zn atom approaches the ZnO lattice. It can bond to the lattice in three ways: b) The Zn atom makes one bond to a single O atom. c) The Zn atom makes two bonds to two O atoms. d) The Zn atom makes three bonds to three O atoms.

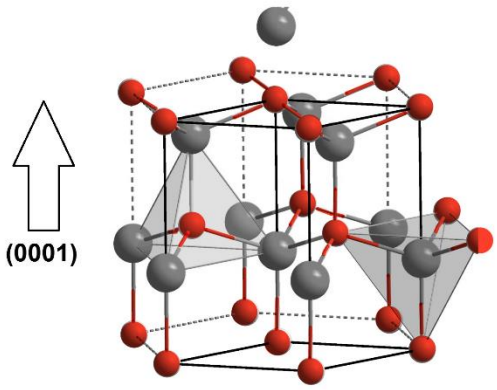

Figure 4: Extended ZnO lattice, showing an incoming Zn atom. At the (0001) plane, all the bond sites are coordination tetrahedron corners. Image: Creative Commons.

makes three bonds and can only make one more. Making one bond is easier than making two or three, so the bonding force at a corner of a tetrahedron is strongest, followed by the edges and lastly by the faces. How fast each plane of a crystal grows can therefore be predicted by determining whether the coordination tetrahedrons at that plane are presenting faces, edges or corners. In the (0001) plane, the coordination tetrahedrons are presenting corners, but in the $(000\bar{1})$ direction, they present only faces as shown in Figure 4. The $(01\bar{1}0)$ faces each have half and half coordination faces and corners presented at the interface and the $(01\bar{1}1)$ faces have half and half coordination edges and corners. Therefore, it can be predicted that the (0001) plane will grow the fastest, followed by the $(01\bar{1}0)$ plane, then the $(01\bar{1}1)$ plane and lastly the $(000\bar{1})$ plane [29].

In a solution based nanowire growth technique this is shown most strongly, where the nanowires are free to grow in any direction, the result is a pencil shape [28, 29]. The length is caused by strong growth in the (0001) direction, the width is caused by the moderate growth in the $(01\bar{1}0)$ direction. The sharp, tapering point is due to relatively fast growth in the $(01\bar{1}1)$ direction, but the flat bottom is in the slowest growing $(000\bar{1})$ direction.

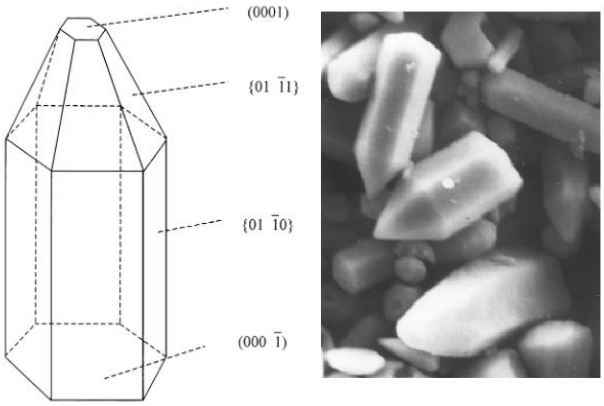

Figure 5: Images published by Wen-Jun *et al.* [23], comparing an ideal ZnO crystal, free to grow unconstrained in all directions with each plane growing at a rate prescribed by its coordination tetrahedrons (left) and real ZnO nanocrystals grown in solution (right).

1.6 Epitaxy

In order to grow a self-assembled nanostructure, this tendency to grow in a preferential direction must be promoted, but in many growth mechanisms, the nanocrystals don't have as many degrees of freedom to form in. Often a crystalline substrate is used and the incoming ZnO precursors will have to form their crystals in contact with and in interaction with that substrate. The process of depositing or growing a crystal on an existing crystal substrate is known as epitaxy. Just as atoms that arrive at a growing crystal arrange

themselves preferentially in certain positions over others, the same is true for atoms arriving at a bare substrate. Epitaxy is important for the growth of nanostructures because while the dominant growth directions will determine the morphology of the nanostructure, the interface with the substrate will determine what direction the growth planes of the nanostructure will be oriented in with relation to the substrate surface [30, 31]. There are several different types of epitaxy that relate to the crystal structure of both the substrate and the overlayer film [32].

In commensurate (POP- Point on Point) epitaxy, the lattice constants of the overlayer are integer multiples of those of the substrate. This means that every point on the overlayer lattice is overlaid on a point on the substrate lattice and that lattice lines in each crystal are parallel. Commensurate epitaxy is the optimal type of epitaxy for growing high quality crystals because the substrate and the overlayer match perfectly.

Coincidence epitaxy has several subcategories, IA, IB and II but in each of them, the lattice lines are parallel without perfect overlay of lattice points. Coincidence IA (POL- Point on Line) requires that each point on the overlayer lattice lies over at least one lattice line of the substrate and that the scale factor between the lattice vectors of the overlayer and the substrate be an integer in one dimension. In the other dimension, they can be non-integer but must remain rational. Because of the rationality clause, a supercell can be constructed of several adjacent primitive overlayer cells, such that the corners of the supercell are commensurate. Coincidence IB (POL) also places all points of the overlayer lattice on at least one primitive lattice line of the substrate but does not require that the scale factor be rational. Therefore, no supercell can be constructed that would allow commensurism. Note that a situation where the physical confines of a sample would preclude a supercell large enough from forming is functionally the same as there being no available supercell. Coincidence II has rational, non-integer scale factors in both dimensions, so only some points on the overlayer lie on the primitive lattice lines of the substrate. However, since a commensurate supercell can be constructed, it can still be considered a coincident relationship. Coincidence epitaxy is not as effective at growing high quality crystals as commensurate epitaxy, but there is a good enough relationship between the substrate and the crystal that the crystal will grow with a good amount of order.

All remaining interactions are considered incommensurate, that is to say that scale factors in both directions between the substrate and overlayer lattice contain irrational numbers. There is no meaningful pattern to where points on one lattice fall with regard to points on the other. Incommensurate epitaxy is bad for crystal growth as atoms arriving at the interface will simply form islands and start to grow in all directions. As these islands expand into one another grain boundaries and discontinuities will appear.

Atoms arriving at an overlayer on top of a substrate preferentially bind where the interface energy is the lowest. In an ideal case, the substrate and the overlayer will be commensurate and this interface energy will

be minimal. Coincidence also has a low interface energy, but because not all points are commensurate, the atoms between overlaid points on the lattice are less preferred and have higher energy required to bond. The total interface energy of coincidence will be ultimately determined by the ratio of coincident points to non-coincident points and we can deduce that Coincidence IA will therefore be preferred over IB. Coincidence II is a rare exception and here the alternating energies of coincident and non-coincident points actually creates a plane wave across the surface [32].

In practise, with the exception of homoepitaxy (where the overlayer is the same material as the substrate), the overlayer is almost never going to be perfectly commensurate or even coincident with the substrate. Each crystal, even involving similar elements will have different bond lengths and a slightly different sized unit cell. However often, if the overlayer is close to being commensurate or coincident it can distort slightly at the interface to become one of these favourable conditions and minimise its interface energy. This distortion is called strain. How much this happens, if at all, is determined by the balance between the energy loss of incommensurism and the energy required by atoms in the overlayer to distort their lattice. The latter is determined by the elastic constants of the crystal. If the interaction between the substrate and the overlayer is very strong, the lattice of the overlayer will distort to accommodate a commensurate alignment. If the overlayer crystal is very internally stable and significant energy has to be expended to move atoms away from their thermodynamic minimums, an incommensurate film is likely to form.

So what does this mean for nanowire growth? It means that choice of substrate is very important, especially for very thin films and nanostructures where the surface and substrate interface make up a large proportion of the material [33]. A poor match between substrate and overlayer can result in “mosaicking” where rather than forming a continuous crystal, the overlayer splinters into misaligned sub-grains [34]. This is very undesirable in nanostructures as we want to study the surface effects without interference in our measurements from the boundaries of these grains and associated defects, which are detectable in common surface measurement systems such as XRD and Photoluminescence [35].

Ideally, we want to study the crystal free of these effects, or failing that, with the defects caused by strain minimised. Ohtomo *et al*. [36] have grown extremely high quality ZnO films by molecular beam epitaxy (MBE) on an unusual substrate, $ScAlMgO_4$, which they claim has a lattice mismatch as small as 0.09%. Their best films had atomically flat terraces and a step height of 0.26 nm, the size of a charge-neutral unit cell of ZnO. Unfortunately, bulk crystal substrates are often prohibitively expensive for carrying out a large series of tests. More common substrates are often used for ZnO growth, even though their lattice mismatch is a lot higher [37]. These include Si (40.1% mismatch), GaAs (42.4% mismatch), GaN (1.8% mismatch), SiC (3.5% mismatch) and α-Al_2O_3 (c-plane sapphire, 18.4% mismatch). Despite the lattice mismatch, c-

plane sapphire remains a popular and relatively inexpensive substrate choice for ZnO. Quality single-crystal films have been grown on it both abroad [38] and by researchers at the University of Canterbury [39]. Being aware of the lattice mismatch and taking steps such as using a buffer layer has been shown to be a practicable and sensible solution [40].

A further option for completely eliminating lattice mismatch in crystal growth is to employ homoepitaxy, which is to simply grow the overlayer film on top of a bulk crystal of the same material. However, researchers attempting homoepitaxial thin film growth have struggled with uneven 3D growth patterns for films [41], perhaps due to the tendency for ZnO crystals to grow preferentially in one direction described above, rather than in an even, flat film.

1.7 ZnO Nanostructure Growth Methods

With a substrate chosen, a growth method can then be selected. Growth of ZnO nanostructures can be divided into two broad categories, catalytic and non-catalytic. Non-catalytic growth does not rely on a foreign catalyst to drive the self-assembly and often functions by direct adsorption of Zn and O onto a solid surface. In order to create the nucleation sites for the nanostructures, nanoparticles of ZnO or other material can be applied to the substrate, but these do not take part in the reaction [42, 43]. ZnO has a high melting point (1975 °C), typical of its nature as an ionic crystal. With no present in the reaction, that non-catalytic growth occurs by the vapour-solid (VS) method where incoming vapour condenses directly into solid form without forming a liquid first. Non catalytic growth of ZnO is anisotropic and is responsible for some of the more complex nanostructures reported [22].

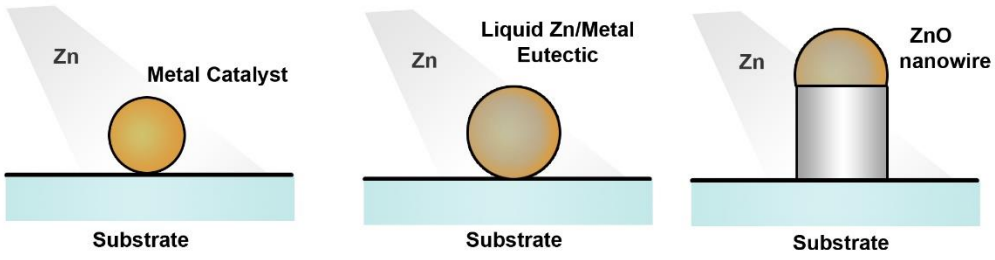

Figure 6: Graphical explanation of the VLS nanowire growth mechanism. From left, the metal catalyst is exposed to a flux of Zn vapour. The Zn is incorporated into the nanoparticle, forming a liquid eutectic. As more Zn is added, the droplet becomes supersaturated and precipitates out beneath the droplet, forming a nanowire.

The growth of ZnO nanostructures can be enhanced with a metal catalyst via the method known as the vapour-liquid-solid (VLS) method, a method that favours the simple and one-dimensional nanowire over other structures. VLS nanowire growth was first reported in the 1960's in the growth of silicon nanowires [44], but it is a process applicable to other materials including ZnO. The catalytic process involves the

production of metal nanoparticles on the surface of the substrate. At appropriate temperature and pressure conditions, these nanoparticles take in incident zinc vapour, forming a eutectic alloy: an alloy with a lower melting point than either of its components. These become nanodroplets of molten metal and absorb more zinc until they become super-saturated with Zn and begin to precipitate out ZnO. The nanowire is then built up layer by layer. Being that it functions as a catalyst, the metal in the droplet is not consumed by this process, in fact many sources report finding solidified metal alloy drops still mounted on the tips of nanowires grown by this process [22, 23, 45]!

Various metals have been reported in literature to have this catalytic effect, including copper [46], tin [30], silver [23], platinum [47] and germanium [48] but by far the most common catalyst is gold. Gold is non-reactive to oxygen, which is often present at high temperatures in film or nanostructure growth. Because the VLS method requires the formation of a liquid metal eutectic, the formation of an oxide such as AgO_x, can be undesirable. For ZnO nanowire growth, at least one group has concluded that gold is superior to other noble metals such as platinum for long, thin nanowires at the temperatures favourable for nanowire growth [47].

Understanding the methods behind the two primary modes of nanowire growth, we can look into the various methods used to implement those modes. ZnO nanowires have been grown by a diverse range of techniques, both with and without a catalyst. These range from traditional methods of film growth such as chemical vapour deposition (CVD) [24, 26], hydrothermal [25, 49, 50] and pulsed laser deposition (PLD) [51, 52] to creative and novel methods such as catalytic growth using bamboo charcoal in solution [53] and controlled oxidation of brass [54].

The most commonly employed methods in both catalytic and non-catalytic ZnO nanowire growth are the family of chemical vapour deposition (CVD) techniques. The specifics of these methods vary a great deal, but the basic operation is fairly consistent. A zinc rich precursor, which can be a powder of ZnO mixed with a catalyst like graphite [24] or a liquid like diethyl-zinc [55], is heated until it sublimates or boils into the vapour phase. In most situations, the precursor is not pure ZnO as ZnO has an impractically high decomposition point of 1975 °C. Graphite powder is added to ZnO powder as it catalyses the decomposition, allowing it to take place at a more easily attainable temperature. The vapour is then carried by a gas flow through a furnace tube to the substrate where it condenses and recrystallizes into a film or into nanostructures. The substrate can be bare or it may have been treated with a catalyst. Growth conditions to be controlled include the temperature and temperature gradient, the composition of the precursor, the species and flow rate of the background gas and the placement of the boat containing the precursor relative to the substrates.

Perhaps the second most commonly used family of methods for ZnO nanowire synthesis are the hydrothermal methods. Hydrothermal growth takes place in solution phase and as such is a liquid-solid nanowire growth. This brings a few significant advantages, most notably that it can be performed at much lower temperature than vapour phase methods [25, 49]. Solution based methods are often preferred for industrial application of nanoscale techniques as they can usually be scaled very favourably. However as a research tool where throughput is less important than quality and reproducibility, hydrothermally grown nanowires exhibit poorer surface quality than nanowires grown in vapour phase growth [49].

Much of the work detailed in this thesis has to do with another method of nanowire growth: physical vapour deposition (PVD). Physical vapour deposition is similar to chemical vapour deposition in terms of the processes occurring at the substrate, but the mechanism by which the zinc carrying vapour is produced is quite different. The primary method employed in this work is pulsed laser deposition (PLD), described in depth in Chapter 2, Section 2 and in Chapters 3 and 4, but the physical vapour deposition family of techniques includes more than just PLD. Sputter coating (described in Section 6, Chapter 2) and cathodic arc deposition are also methods found under the umbrella of the term physical vapour deposition. Physical vapour deposition techniques offer the distinct advantage over other deposition techniques of using stoichiometric precursors or targets [56]. Because high energy ablation techniques like lasers and plasma are used to deliver energy to a pure ZnO precursor, there is lower chance of contamination from foreign species. PVD techniques are often carried out under high to ultra-high vacuum and produce extremely pure crystals [56].

1.8 Testing and Applications of Nanowires

What remains to consider is what tests and experiments can be performed on metal oxide nanowires to generate useful data on the materials' surfaces. Nanowires can be measured as grown in their arrays or as single wires to obtain different types of data. As a transparent semiconductor with applications in optoelectronics, optical measurements that probe the surface with various types of radiation and examine the responses are of interest. Photoluminescence and XRD direct UV laser light and x-rays respectively onto the surface and measure the emitted photons to examine the composition and crystal structure of the array and compare them against bulk single crystals and thin films.

Electrical measurements are somewhat harder to make on nanowires as they rely on having a physical interface between the nanowires and the testing apparatus. However, it is not impossible. Various groups have succeeded in applying electrical contacts to nanowires in a variety of ways. Nanowires can be left standing in their array with a conducting substrate connected to one terminal. A second contact can then be

carefully deposited on top of the array, contacting many wires at the opposite end from the substrate [57]. A vertical transistor can be fabricated bottom-up in a similar fashion, using a wrap-around gate between the top and bottom contacts [58].

If a single nanowire can be removed from its array and replaced on a flat surface, then contacts can be deposited onto it. Conventional photolithography, in all but the most advanced industrial laboratories is too poor in resolution and in spatial precision to fill this role, but other techniques such as electron beam lithography can be employed for resolutions as low as 20 nm. A challenge of this method is the difficulty of each lithography step. A common approach for fabricating devices such as MOSFETs is the back gate approach wherein the substrate has a conducting layer underneath an insulating layer and serves as both the gate and the gate insulation, reducing the number of lithography steps by two [59].

Some scanning electron microscopes such as the Omicron UHV Nanoprobe operated by UC collaborators Lord *et al.* [60] from Swansea University in the UK are equipped with nanoscale probes, which are capable of making direct contact to nanowires, allowing measurements to be easily taken. Other SEM systems comprise a built-in metallisation function for direct writing of contacts onto a sample being examined. These capacities significantly expedite the process of creating and testing individual nanowires' electrical properties.

1.9 Scope of this work

Zinc oxide and its nanostructures have been studied with keen interest since the early-mid 2000's when researchers really began to notice the benefits it could offer. Assoc. Prof. Allen's silver oxide gated ZnO MESFETs broke world records and researchers at the University of Canterbury have published papers using both our own and our collaborators' formidable testing equipment to expand our understanding of the surfaces of the ZnO crystal. When Dr. Vladimir Golovko and his PhD student Jin Ke from the Department of Chemistry approached us with their work on production, size control and tethering of gold nanoparticles, a collaboration was formed with the intent to combine our expertise to learn more about the growth mechanisms, surface properties and potential applications of catalytically grown ZnO nanowires.

The objectives of this work are as follows: To devise and optimize a method of growing well aligned, high aspect ratio ZnO nanowires using discrete nanoparticles as VLS catalysts and to determine if the morphology of the nanowires can be controlled by selecting the size of these catalysts. These nanowires should then be characterized thoroughly using electrical, optical and diffractive techniques. The results of the characterization should be compared against nanowires grown by more conventional methods. If

successful, the methods developed herein should be tested for adaptability to further experimentation using other materials and different growth methods.

In Chapters 3 and 4, the growth of ZnO nanowires by pulsed-laser deposition is optimised, using gold colloids and atomically precise nanoclusters as catalysts. Several methods of preparing substrates for growth are investigated and an optimal method is determined using a citrate ligand to bind gold colloids in place on the surface of the substrate. The effects of changing various parameters of the PLD system and the challenges and benefits of PLD as a means of crystal growth are discussed. ZnO nanowires are contacted using electron beam lithography in Chapter 5 and ohmic and rectifying contacts are fabricated onto individual nanowires. Nanowire samples grown by the methods described in Chapter 3 and 4 are investigated with a range of optical techniques in Chapter 6 and compared to literature and in-house results on nanowires, films and bulk crystal. In Chapter 7, the growth principles developed in Chapters 1 and 2 are applied to the ZnMgO alloy and the resulting nanowires and films are characterised with the optical methods described in Chapter 6. Finally in Chapter 8, a few miscellaneous experiments are compiled. Molecular beam epitaxy is used to grow films using the substrate preparation methods from Chapter 3 and 4 and a novel series of PLD ZnO nanowire growths catalysed by platinum group methods is conducted.

1.10 References

[1] T. Jacob, K. Hemavathy, J. Jacob, A. Hingorani, N. Marks, and E. Ascher, "A nanotechnology-based delivery system: Nanobots. Novel vehicles for molecular medicine," *Journal of Cardiovascular Surgery,* vol. 52, pp. 159-167, 2011.

[2] S. Günes, H. Neugebauer, and N. S. Sariciftci, "Conjugated polymer-based organic solar cells," *Chemical Reviews,* vol. 107, pp. 1324-1338, 2007.

[3] A. K. T. Lau and D. Hui, "The revolutionary creation of new advanced materials - Carbon nanotube composites," *Composites Part B:Engineering,* vol. 33, pp. 263-277, 2002.

[4] S. Elzwawi, H. S. Kim, R. Heinhold, M. Lynam, G. Turner, J. G. Partridge, *et al.*, "Device quality ZnO grown using a Filtered Cathodic Vacuum Arc," *Physica B: Condensed Matter*, vol. 407, pp. 2903-2906, 2012.

[5] S. Elzwawi, H. S. Kim, M. Lynam, E. L. H. Mayes, D. G. McCulloch, M. W. Allen, *et al.*, "Stable n-channel metal-semiconductor field effect transistors on ZnO films deposited using a filtered cathodic vacuum arc," *Applied Physics Letters,* vol. 101, 2012.

[6] R. McKenzie, B. Liley, P. Johnston, R. Scragg, A. Stewart, A. I. Reeder, *et al.*, "Small doses from artificial UV sources elucidate the photo-production of vitamin D," *Photochemical and Photobiological Sciences,* vol. 12, pp. 1726-1737, 2013.

[7] M. Allen and R. McKenzie, "Enhanced UV exposure on a ski-field compared with exposures at sea level," *Photochemical and Photobiological Sciences,* vol. 4, pp. 429-437, 2005.

[8] D. G. Thomas, "The exciton spectrum of zinc oxide," *Journal of Physics and Chemistry of Solids,* vol. 15, pp. 86-96, 1960.

[9] G. D. Scholes and G. Rumbles, "Excitons in nanoscale systems," *Nature Materials,* vol. 5, pp. 683-696, 2006.

[10] D. C. Look and B. Claflin, "P-type doping and devices based on ZnO," *Physica Status Solidi (B) Basic Research,* vol. 241, pp. 624-630, 2004.

[11] J. H. Lim, C. K. Kong, K. K. Kim, I. K. Park, D. K. Hwang, and S. J. Park, "UV electroluminescence emission from ZnO light-emitting diodes grown by high-temperature radiofrequency sputtering," *Advanced Materials,* vol. 18, pp. 2720-2724, 2006.

[12] M. W. Allen, S. M. Durbin, and J. B. Metson, "Silver oxide Schottky contacts on n-type ZnO," *Applied Physics Letters,* vol. 91, 2007.

[13] M. W. Allen, R. J. Mendelsberg, R. J. Reeves, and S. M. Durbin, "Oxidized noble metal Schottky contacts to n -type ZnO," *Applied Physics Letters,* vol. 94, 2009.

[14] R. Hull and INSPEC, *Properties of Crystalline Silicon*: INSPEC, the Institution of Electrical Engineers, 1999.

[15] A. Janotti and C. G. Van De Walle, "Fundamentals of zinc oxide as a semiconductor," *Reports on Progress in Physics,* vol. 72, 2009.

[16] C. J. Chiu, S. P. Chang, and S. J. Chang, "High-performance a-igzo thin-film transistor using Ta2O 5 gate dielectric," *IEEE Electron Device Letters,* vol. 31, pp. 1245-1247, 2010.

[17] H. Gleskova, P. I. Hsu, Z. Xi, J. C. Sturm, Z. Suo, and S. Wagner, "Field-effect mobility of amorphous silicon thin-film transistors under strain," *Journal of Non-Crystalline Solids,* vol. 338-340, pp. 732-735, 2004.

[18] R. Heinhold, "Hydrogen-related effects in the optical and surface electronic properties of ZnO," Doctor of Philosophy PhD, Department of Electrical and Computer Engineering, University of Canterbury, 2014.

[19] R. Heinhold, G. T. Williams, S. P. Cooil, D. A. Evans, and M. W. Allen, "Influence of polarity and hydroxyl termination on the band bending at ZnO surfaces," *Physical Review B - Condensed Matter and Materials Physics,* vol. 88, 2013.

[20] H. Meskine and P. A. Mulheran, "Simulation of reconstructions of the polar ZnO(0001) surfaces," *Physical Review B - Condensed Matter and Materials Physics,* vol. 84, 2011.

[21] R. Wahab, S. G. Ansari, Y. S. Kim, H. K. Seo, G. S. Kim, G. Khang, *et al.*, "Low temperature solution synthesis and characterization of ZnO nano-flowers," *Materials Research Bulletin,* vol. 42, pp. 1640-1648, 2007.

[22] Z. L. Wang, "Zinc oxide nanostructures: Growth, properties and applications," *Journal of Physics Condensed Matter,* vol. 16, pp. R829-R858, 2004.

[23] Y. W. Heo, D. P. Norton, L. C. Tien, Y. Kwon, B. S. Kang, F. Ren, *et al.*, "ZnO nanowire growth and devices," *Materials Science and Engineering R: Reports,* vol. 47, pp. 1-47, // 2004.

[24] M. H. Huang, Y. Wu, H. Feick, N. Tran, E. Weber, and P. Yang, "Catalytic growth of zinc oxide nanowires by vapor transport," *Advanced Materials,* vol. 13, pp. 113-116, 2001.

[25] J. Wang and L. Gao, "Hydrothermal synthesis and photoluminescence properties of zno nanowires," *Solid State Communications,* vol. 132, pp. 269-271, 2004.

[26] Y. W. Wang, L. D. Zhang, G. Z. Wang, X. S. Peng, Z. Q. Chu, and C. H. Liang, "Catalytic growth of semiconducting zinc oxide nanowires and their photoluminescence properties," *Journal of Crystal Growth,* vol. 234, pp. 171-175, 2002.

[27] M. Wei, D. Zhi, and J. L. MacManus-Driscoll, "Self-catalysed growth of zinc oxide nanowires," *Nanotechnology,* vol. 16, pp. 1364-1368, 2005.

[28] W. J. Li, E. W. Shi, W. Z. Zhong, and Z. W. Yin, "Growth mechanism and growth habit of oxide crystals," *Journal of Crystal Growth,* vol. 203, pp. 186-196, 1999.

[29] Q. Ahsanulhaq, A. Umar, and Y. B. Hahn, "Growth of aligned ZnO nanorods and nanopencils on ZnO/Si in aqueous solution: Growth mechanism and structural and optical properties," *Nanotechnology,* vol. 18, 2007.

[30] Y. Ding, P. X. Gao, and Z. L. Wang, "Catalyst-Nanostructure Interfacial Lattice Mismatch in Determining the Shape of VLS Grown Nanowires and Nanobelts: A Case of Sn/ZnO," *Journal of the American Chemical Society,* vol. 126, pp. 2066-2072, 2004.

[31] J. B. Baxter and E. S. Aydil, "Epitaxial growth of ZnO nanowires on a- and c-plane sapphire," *Journal of Crystal Growth,* vol. 274, pp. 407-411, // 2005.

[32] D. E. Hooks, T. Fritz, and M. D. Ward, "Epitaxy and molecular organization on solid substrates," *Advanced Materials,* vol. 13, pp. 227-241, 2001.

[33] X. Liu, X. Wu, H. Cao, and R. P. H. Chang, "Growth mechanism and properties of ZnO nanorods synthesized by plasma-enhanced chemical vapor deposition," *Journal of Applied Physics,* vol. 95, pp. 3141-3147, 2004.

[34] V. Srikant, J. S. Speck, and D. R. Clarke, "Mosaic structure in epitaxial thin films having large lattice mismatch," *Journal of Applied Physics,* vol. 82, pp. 4286-4295, 1997.

[35] R. Ghosh, D. Basak, and S. Fujihara, "Effect of substrate-induced strain on the structural, electrical, and optical properties of polycrystalline ZnO thin films," *Journal of Applied Physics,* vol. 96, pp. 2689-2692, 2004.

[36] A. Ohtomo, K. Tamura, K. Saikusa, K. Takahashi, T. Makino, Y. Segawa, *et al.*, "Single crystalline ZnO films grown on lattice-matched ScAIMgO4(0001) substrates," *Applied Physics Letters,* vol. 75, pp. 2635-2637, 1999.

[37] Ü. Özgür, Y. I. Alivov, C. Liu, A. Teke, M. A. Reshchikov, S. Doğan, *et al.*, "A comprehensive review of ZnO materials and devices," *Journal of Applied Physics,* vol. 98, pp. 1-103, 2005.

[38] Y. Chen, D. M. Bagnall, Z. Zhu, T. Sekiuchi, K. T. Park, K. Hiraga, *et al.*, "Growth of ZnO single crystal thin films on c-plane (0 0 0 1) sapphire by plasma enhanced molecular beam epitaxy," *Journal of Crystal Growth,* vol. 181, pp. 165-169, 1997.

[39] A. R. Hyndman, M. W. Allen, and R. J. Reeves, "Growth of epitaxial ZnO films on sapphire substrates by plasma assisted molecular beam epitaxy," in *Proceedings of SPIE - The International Society for Optical Engineering*, 2015.

[40] T. Nakamura, Y. Yamada, T. Kusumori, H. Minoura, and H. Muto, "Improvement in the crystallinity of ZnO thin films by introduction of a buffer layer," *Thin Solid Films,* vol. 411, pp. 60-64, 2002.

[41] M. W. Cho, C. Harada, H. Suzuki, T. Minegishi, T. Yao, H. Ko, *et al.*, "Issues in ZnO homoepitaxy," *Superlattices and Microstructures,* vol. 38, pp. 349-363, 2005.

[42] A. O. Dikovska, N. N. Nedyalkov, and P. A. Atanasov, "Fabrication of ZnO nanorods using metal nanoparticles as growth nuclei," *Materials Science and Engineering B: Solid-State Materials for Advanced Technology,* vol. 176, pp. 1548-1551, // 2011.

[43] T. Okada, B. H. Agung, and Y. Nakata, "ZnO nano-rods synthesized by nano-particle-assisted pulsed-laser deposition," *Applied Physics A: Materials Science and Processing,* vol. 79, pp. 1417-1419, 2004.

[44] R. S. Wager and W. C. Ellis, *Appl. Phys. Lett.*, vol. 4, 1964.

[45] P. Yang, H. Yan, S. Mao, R. Russo, J. Johnson, R. Saykally, *et al.*, "Controlled growth of ZnO nanowires and their optical properties," *Advanced Functional Materials,* vol. 12, pp. 323-331, // 2002.

[46] S. Y. Li, C. Y. Lee, and T. Y. Tseng, "Copper-catalyzed ZnO nanowires on silicon (1 0 0) grown by vapor-liquid-solid process," *Journal of Crystal Growth,* vol. 247, pp. 357-362, 2003.

[47] Z. Zhang, S. J. Wang, T. Yu, and T. Wu, "Controlling the growth mechanism of ZnO nanowires by selecting catalysts," *Journal of Physical Chemistry C,* vol. 111, pp. 17500-17505, 2007.

[48] Z. W. Pan, S. Dai, C. M. Rouleau, and D. H. Lowndes, "Germanium-catalyzed growth of zinc oxide nanowires: A semiconductor catalyst for nanowire synthesis," *Angewandte Chemie - International Edition,* vol. 44, pp. 274-278, 2005.

[49] L. E. Greene, M. Law, J. Goldberger, F. Kim, J. C. Johnson, Y. Zhang, *et al.*, "Low-temperature wafer-scale production of ZnO nanowire arrays," *Angewandte Chemie - International Edition,* vol. 42, pp. 3031-3034, 2003.

[50] Y. H. Ni, X. W. Wei, J. M. Hong, and Y. Ye, "Hydrothermal preparation and optical properties of ZnO nanorods," *Materials Science and Engineering B: Solid-State Materials for Advanced Technology,* vol. 121, pp. 42-47, 2005.

[51] Z. W. Liu and C. K. Ong, "Synthesis and size control of ZnO nanorods by conventional pulsed-laser deposition without catalyst," *Materials Letters,* vol. 61, pp. 3329-3333, // 2007.

[52] I. A. Palani, D. Nakamura, K. Okazaki, T. Shimogaki, M. Higashihata, and T. Okada, "Influence of ZnO buffer layer on growth of Sb doped ZnO nano wires using nano particle assisted pulsed laser deposition (NAPLD) using Sb as catalyst," *Advanced Materials Letters,* vol. 3, pp. 66-70, 2012.

[53] L. Gong, H. Jiang, and F. Zhu, "A facile and green approach for the fabrication of ZnO nanorods using bamboo charcoal as the template," *Materials Letters,* vol. 64, pp. 2582-2584, // 2010.

[54] B. Behera and S. Chandra, "Synthesis and Characterization of ZnO Nanowires and ZnO-CuO Nanoflakes from Sputter-Deposited Brass (Cu0.65-Zn0.35) Film and Their Application in Gas Sensing," *Journal of Materials Science and Technology,* vol. 31, pp. 1069-1078, 2015.

[55] G. W. Cong, H. Y. Wei, P. F. Zhang, W. Q. Peng, J. J. Wu, X. L. Liu, *et al.*, "One-step growth of ZnO from film to vertically well-aligned nanorods and the morphology-dependent Raman scattering," *Applied Physics Letters,* vol. 87, pp. 1-3, 2005.

[56] D. H. Lowndes, D. B. Geohegan, A. A. Puretzky, D. P. Norton, and C. M. Rouleau, "Synthesis of novel thin-film materials by pulsed laser deposition," *Science,* vol. 273, pp. 898-903, 1996.

[57] B. O. Jung, D. C. Kim, B. H. Kong, J. H. Lee, J. Y. Lee, and H. K. Cho, "Direct formation of transparent ITO top electrodes on high-density ZnO nanowires by magnetron sputtering," *Electrochemical and Solid-State Letters*, vol. 14, pp. H446-H449, 2011.

[58] H. T. Ng, J. Han, T. Yamada, P. Nguyen, Y. P. Chen, and M. Meyyappan, "Single crystal nanowire vertical surround-gate field-effect transistor," *Nano Letters*, vol. 4, pp. 1247-1252, 2004.

[59] Y. K. Park, A. Umar, S. H. Kim, J. H. Kim, E. W. Lee, M. Vaseem, *et al.*, "Comparison between the electrical properties of ZnO nanowires based field effect transistors fabricated by back- and top-gate approaches," *Journal of Nanoscience and Nanotechnology*, vol. 8, pp. 6010-6016, 2008.

[60] A. M. Lord, T. G. Maffeis, A. S. Walton, D. M. Kepaptsoglou, Q. M. Ramasse, M. B. Ward, *et al.*, "Factors that determine and limit the resistivity of high-quality individual ZnO nanowires," *Nanotechnology*, vol. 24, 2013.

Chapter 2: Experimental Methods

2.1 Synthesis and Deposition of Au Catalyst Nanoparticles

2.1.1 Colloidal Au Nanoparticles

The preparation of substrates using colloidal gold as catalyst was key to the novelty of my research into metal oxide nanowires. This was a multi-step process with many points of optimisation. Substrates were cleaned thoroughly, treated with a citrate ligand and then coated with chemically synthesised, colloidal gold nanoparticles, ready for nanowire growth. All glassware used in each step of this method was cleaned thoroughly before use with nitric acid. Metal tools were first ultrasonicated in toluene, acetone then methanol.

The gold colloids themselves were prepared at the Department of Chemistry according to a method published by Grabar *et al.* [1]. Colloid preparation was carried out by collaborator Ms. Ke from the Department of Chemistry for much of the work detailed in Chapter 3. After training and familiarisation, I began to assist Ms. Ke's preparation and eventually prepared a few batches alone. The colloids were formed in solution by precipitation from a mixture of gold chloride and sodium citrate. Both reagents were received as powders and needed to be carefully weighed and dissolved in deionised water. 250 mL of 1 mmol/L was made from $HAuCl_4{:}3H_2O$ weighing 98.46 mg. Sufficient sodium citrate powder to make 250 mL of 38.8 mmol/L sodium citrate solution weighed 285.23 mg.

The yellow-tinged gold chloride solution was stirred on a hotplate using a magnetic stirrer and brought to the boil. Aluminium foil was used to wrap the flask as the solution is known to degrade with exposure to UV light. Once the gold chloride solution had reached boiling point, the citrate was added as suddenly as possible. This reaction is very fast and proceeds through several colour changes in a few seconds: from yellow, to clear, to very dark purple-red and finally to a dark, crimson red. The solution was left stirring for a further 10-15 minutes to ensure that all reagents had been consumed.

The resulting solution contained a dispersion of colloids with a uniform size distribution of approximately 13 nm. The success of the preparation could be measured directly by applying to a silicon sample and viewing under SEM or TEM and more easily by UV-Vis spectroscopy (Section 2.3 and 2.10 respectively). The concentration of the gold colloids in this solution was 17 mmol/l. If lower concentrations were required by an experiment, these were made up by dilution with deionised water.

Substrates were prepared for colloid deposition by ultrasonication in trichloroethylene, acetone and methanol followed by blow drying with clean nitrogen. In order to promote adhesion of gold nanoparticles to the substrates, the substrates could be treated with a citrate, 3-Aminopropyltrimethoxysilane (APTMS). APTMS is a chain molecule that binds to OH groups on the surface of the substrate at one end and to a single gold colloid at the other end, tethering the colloid to the surface of the substrate. This bond is strong enough that the substrate can then be rinsed in deionised water without removing the gold colloids. APTMS was supplied as a 97% pure liquid and was therefore diluted in methanol to a concentration of 1%.

APTMS coating of several samples was performed simultaneously using a specially made carousel that fit inside a 250 mL beaker. The design of this sample holder enabled many samples to be lowered into the beaker and removed, while keeping all of them standing on their edges. This allowed the APTMS access to both surfaces of the square substrates. Allowing both sides to be coated with the citrate improves tolerance for accidentally inverting the samples during any later handling, as each side of a double side polished sapphire substrate appears identical. Using this holder, the samples were immersed for 10 minutes in the 1% APTMS solution. The beaker was filled with more than enough solution to cover the samples to make sure that there was no drop in concentration from APTMS molecules binding to the surface of the samples and/or holder.

After 10 minutes, the samples and holder were withdrawn from the beaker and placed into a beaker of clean methanol. Gentle agitation was manually applied to the sample holder to assist in the removal of any APTMS molecules not chemically bound to the substrate surface. In approximately two minute intervals, the sample holder was transferred first to a new beaker with a fresh change of methanol, followed by two beakers containing deionised water.

Application of the gold colloids to the APTMS coated samples was performed individually so that variations in the deposition conditions could be implemented. Deposition of colloid was performed by several methods. In each case, the deposition was performed in a dark or UV controlled room, to minimise exposure of the colloid solution to UV light. Colloid deposition was initially performed by Ms. Ke (early Chapter 3), but subsequent depositions were carried out by myself at the Electrical Engineering Nanolab.

The drop coating method was the first method investigated. The samples were placed on a fresh cleanroom wipe. A 3 mL disposable transfer pipette was used to apply single drops of gold colloid solution to different regions of each sample. The substrates were then covered with a clean beaker or petri dish lid and left to evaporate in air until no liquid remained. This method was intended to guarantee that all the gold from the droplets would be deposited on the surface of the sample, while minimising the total amount of valuable gold used in each experiment.

The second method investigated was dip coating. This allowed for more homogenous coverage of the samples with gold nanoparticles. For each sample to be coated, a small, single use jar or vial was filled with enough colloid solution to cover the sample. A specially made Teflon holder was placed at the bottom of each jar, again such that the sample inserted into it could stand on its end. The samples were quickly lowered into position in the holders using clean tweezers and allowed to sit for a designated time, very carefully measured using a stopwatch. After the allocated time had elapsed, the samples were removed and rinsed off in two changes of deionised water then blown dry with nitrogen.

The final method used was an extension of the drop coating method, intended as a compromise between the benefits of drop coating and dip coating. In this method, the substrate was placed on a fresh cleanroom wipe. A 3 mL disposable transfer pipette was again used to apply colloid solution, but instead of single droplets, colloid solution was applied to the whole of the sample. The process created a large drop of colloid on the surface, held in place on the sample by surface tension at the edges. Colloid was added gently and gradually until any more would overwhelm surface tension and spill over the edges of the substrate. The substrates were then covered with a clean beaker or petri dish lid and allowed to sit for an allocated time. The substrates were then rinsed in two changes of deionised water and blown dry with nitrogen.

2.1.2 Atomically Precise Au Clusters

Atomically precise Au clusters were prepared by collaborator Dr. Golovko at the Department of Chemistry, for use as ZnO nanowire catalysts by methods compiled in Anderson *et al.* [2, 3]'s comparison of Au clusters. The synthesis of these clusters was more complicated than that of the colloidal Au and differed between the Au101 and the Au9 clusters.

Au101 clusters were chemically synthesised by a method published by Weare *et al.* [4]. Tetraoctylammonium bromide (1.40 g) was added to 120 mL of tetrachloroauric acid (1 g) in 50/50 toluene and deionised water. This mixture was stirred vigorously for 5 minutes to form a golden coloured, biphasic solution. 2.3 g of triphenylphosphine was then added and the solution was stirred for an additional 10 minutes, causing the organic phase to turn white and cloudy. A solution of 2g of sodium borohydride in deionised water was then added to the mixture, immediately turning the organic phase dark purple and causing vigorous bubbling. The reaction mixture was left to stir for a further three hours. The organic, Au-containing layer which forms was then be separated out, filtered, washed in solvent to remove impurities, byproducts and leftover reactants and then dried in a rotary evaporator to form approximately 200-250 mg of black powder. This powder could be redissolved in chloroform for application onto substrates with or without APTMS treatment, using the hybrid drop coating method described above.

Au9 clusters were chemically synthesised by a method first reported by Wen *et al.* [5]. 0.072 g of sodium borohydride dissolved in 92 mL of ethanol was added to 4.0 g of $AuPPh_3(NO_3)$ in 160 mL of ethanol. After stirring for 2 hours, the solution became a deep red. This solution was filtered for insoluble impurities and the solvent removed, to yield a black powder. After further washing and drying with various solvents, a green crystalline precipitate was produced which could be redissolved in chloroform for application, much like the Au101 powder.

2.2 Eclipse Pulsed Laser Deposition

Pulsed Laser Deposition (PLD) is a physical vapour deposition method that was central to the production of nanowires throughout this work. PLD uses pulses from a very high energy laser, such as a KrF excimer 248 nm laser to ablate a target of known stoichiometry inside a vacuum. A plume of vapour and plasma is produced by the explosive heating of the target at the focal spot of the beam and this material is allowed to drift across a small separation to be deposited on the substrate mounted opposite on a heated element. Eclipse PLD is a refinement of the technique that places a physical shield, referred to as an eclipse plate, between the substrate and the target in order to block a direct path between the two as shown in Figure 1. This has been shown to lower the deposition rate of the system, but is conducive to higher film purity as it enables only molecules small enough to diffuse around the plate to reach the substrate [6, 7]. During this work, growths were conducted growth with and without the eclipse plate.

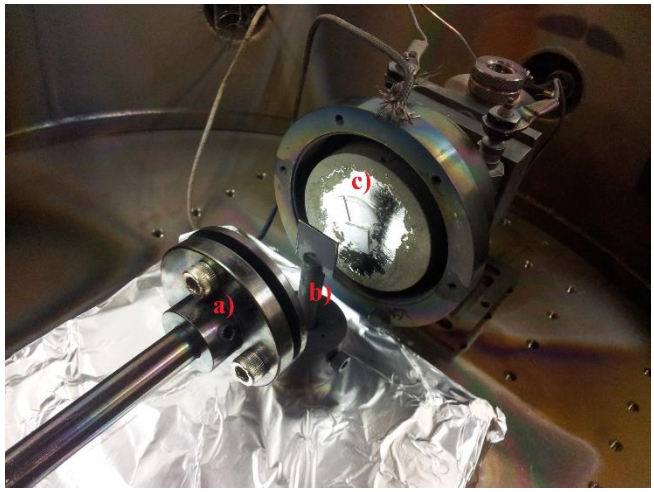

Figure 1: The inside of the UC PLD system showing a) Target holder b) Eclipse plate and c) The substrates mounted on the substrate heater.

The growth of either film or nanostructures by PLD requires calibration of several key parameters. The first is laser fluence, which is the energy density of the laser at the surface of the target. Fluence is affected by two parameters: the pulse energy of the laser, and the spot size of the beam when it reaches the target. The energy of the laser is able to be directly and discretely programmed on the control panel of the machine so it is the most logical and systematic way to vary the fluence. The spot size is determined by the geometry of the chamber and throughout this work, measures were taken to keep this constant. The beam travels through air between the laser and the chamber and is focused by a 750 mm lens on a sliding track. The size

of the beam exiting the laser aperture is fixed at 28 mm x 12.5 mm (350 mm^2, 3.5 cm^2). Fluence is measured in Jcm^{-2}, so using a standard 100 mJ/pulse setting on the KrF laser and no lens, the fluence would be ~0.029 Jcm^{-2}. For nanowire growth, the required order of magnitude is 1-10 J cm^{-2} so the aforementioned lens is used to focus the spot onto a smaller area. This does not increase total energy of the pulses, but it does increase the energy density, greatly enhancing the local effect.

To increase the fluence at 100 mJ of laser energy to 4J cm^{-2}, for example, the simple formula is used:

$$\rho = \frac{E}{A} \quad \textbf{[1]}$$

Where ρ is fluence, E is laser energy and A is area. Therefore, rearranging for A:

$$A = \frac{E}{\rho} \quad \textbf{[2]}$$

This gives a required spot size of 0.025 cm^2 or 2.5 mm^2. The ratio of height (H_1) to width (W_1) of the unfocused beam is 28/12.5 = 2.24 and is preserved through the lens so the shape of the spot can be described as:

$$A = H_2 W_2 \quad \textbf{[3]}$$

$$A = 2.24 {W_2}^2$$

Substituting the value of 2.5 mm^2 for A, it follows that the width of the spot must be 1.056 mm. A 750 mm lens will focus the 28 mm x 12.5 mm beam down to a point if placed at 750 mm. Some simple trigonometry, illustrated in Figure 2, can then be used to determine the distance after passing through the lens, d, that the beam will be reduced in size to a width of 1.056 mm.

The ratio of this triangle shown in Figure 2's height to base width is 750/12.5 = 60. The system can be solved to find the distance to the focal point from the point where the width of the triangle is 1.056 mm. Therefore the lens must be place 750 mm – 63.39 mm = 686.6 mm from the target in order to produce a 2.5 mm^2 spot size and hence a fluence of 4 Jcm^{-2}.

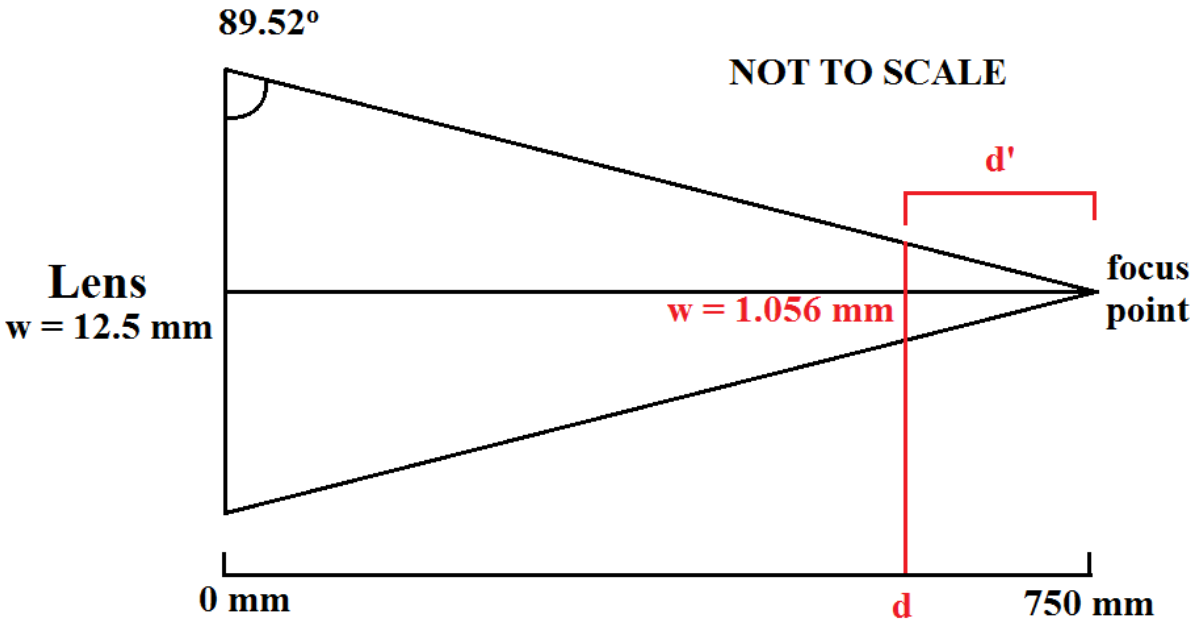

Figure 2: Diagram showing the calculation of the PLD lens placement. The lens is moved such that the PLD target is at position d, where the spot width is 1.056 mm. The length of d' can be calculated by trigonometry to be tan(89.52) x 0.528 mm, which is 63.39 mm. Hence, d = 686.6 mm.

Other PLD parameters are easier to control directly. The substrate is mounted on a ceramic heater, which is controlled by a simple heater driver and is electrically grounded. Heat out is directly proportional to power in and is adjusted in percentage points. Unfortunately there is no feedback in the system and the temperature has to be measured using a thermocouple and the power adjusted manually. Small issues involving the seating of the thermocouple's sensor notwithstanding, once the heater was calibrated, it could be assumed that a given percentage value correlated reliably to a resultant temperature output. Throughout many of my growths for example, I used the value of 58% to generate a temperature of 750 °C. The chamber has a safe operating limit of approximately 800 °C.

Chamber pressure is controlled in our setup through a series of valves. The chamber has two pumps connected to it in series, a roughing pump and a high-vacuum turbo pump. Both pumps extract gas through a large valve in the bottom of the chamber. The roughing pump is capable of bringing the pressure in the chamber down to approximately 1.5 Torr after several minutes of pumping, or to 1.0 Torr after an extended period. Once the chamber is below 2 Torr, it is safe to start the turbo pump, which is water cooled and can reach a high vacuum of as low as $1x10^{-5}$ Torr over the course of 1-2 hours or $5x10^{-6}$ Torr overnight. The base pressure of the system is affected by many factors that would be impractically difficult to control for:

tiny leaks, water adsorption, sample and holder outgassing etc. In order to provide a stable and repeatable baseline for my experiments, the main valve on the chamber was partially closed after reaching a stable base pressure. This deliberately decreases the efficiency of the pump and allows the operator to increase the pressure in the chamber by an arbitrary amount. In my growths, I used the value of $1x10^{-4}$ Torr. Because this effect is much larger than the small effects causing pressure discrepancies at low pressure, it allows the chamber base pressure to be set to the same number each time, usually with only fluctuations of less than $\pm 1x10^{-5}$ Torr.

During the growth, oxygen is added to the chamber via a pin valve connected to a cylinder. The oxygen pressure is manually controlled by opening and closing this valve. Throughout my experiments, this valve was found to drift a little and it was important to adjust it as appropriate to retain the correct pressure. A problem with the gas system is the pressure gauges the chamber is equipped with. Pressure is measured by a standard pressure gauge at high pressures and by an ion gauge at low pressure. Unfortunately, these two gauges have a blind spot between $1.27x10^{-2}$ Torr at the pressure gauge's minimum value and approximately 10^{-3} Torr where the ion gauge reaches overpressure. As it is generally unwise to operate measuring equipment near their limits of accuracy, growths have had to have been conducted at high enough oxygen pressure to utilise the pressure gauge.

Because of the sensitivity of the chamber and the nanowires to contaminants, a very strict standard of cleanliness was required for any object brought into contact with the chamber. All samples used in the PLD system were first cleaned using ten minutes of ultrasonication in trichloroethylene, then acetone, then methanol. Tools used in the chamber were also to be cleaned as above using toluene, acetone and methanol. Any glassware used in the cleaning of samples or tools was also first cleaned using a concentrated HCl acid etch.

The laser itself is a Lambda Physik 248 nm KrF excimer laser. Excimer lasers function by using a high voltage (in the order of kV) to form an excited pseudo-molecule called an excimer that decays rapidly, emitting laser radiation. The laser is controlled digitally and has several modes of operation. The most appropriate mode for oxide film and nanowire growth is constant energy mode, wherein the user specifies an output pulse energy and the laser produces the appropriate voltage to output that energy. Laser energy has a lower limit of 76 mJ and an upper limit of over 300 mJ, which is dependent on the pressure of the KrF gas in the reservoir. Frequency of pulses can also be controlled digitally from 1 Hz to over 30 Hz. Each pulse lasts on the order of nanoseconds so pulses do not overlap, even at high frequency.

The PLD target is a 1" x 0.25" sintered ZnO disc. Targets were provided by Kurt J Lesker, PA, USA and by Testbourne, Hampshire, UK, and were of at least 99.99% purity. The target is mounted on the end of an electrically grounded rotating arm, which moves at a controllable speed. The speed of the target is relatively unimportant, but some rotation is necessary to prolong the life of the target by ensuring that the laser spot is moved around the surface of the target evenly, rather than boring a hole in a single spot. Non-integer frequencies close to 1 Hz were used for the rotation speed, as a rotation of 1 Hz paired with a 10 Hz laser frequency would simply result in 10 spots evenly spaced on the target being ablated. Rotation frequencies such as 1.03 Hz resulted in a smooth "track" of ablated area. The clamping system that held the target was somewhat fragile and had a tendency to come loose during the growth, which was a leading cause of growth failure. Care was taken to tighten the screws without putting too much pressure on the target to minimise this issue. The target holder is shown in Figure 3.

Figure 3: A ZnO target mounted in the PLD target holder. The screws enter from behind. Note the dark track worn by laser ablation.

A significant weakness in the University of Canterbury PLD setup is the window of the PLD chamber that the laser passes on through its path to the target. The window is made from high purity quartz and has a stated UV transmission at 248 nm of approximately 85-90%. However, ablated material from the target can diffuse around the chamber and settle in other locations other than the sample and the heater. Necessarily, there is a direct, unobstructed path from the target to the laser window and ablated material can settle on the window. To make matters worse, ZnO absorbs strongly in the UV region, even though 248 nm is higher energy than ZnO's bandgap. Ablated material from successive growths accumulating on the window was found to have a profoundly negative impact on the transmission of the window, lowering it on occasion to as low as 40%. To compound matters, the laboratory supervisor, Dr. Ian Farrell concluded that oxidation made the problem worse if the chamber was regularly exposed to air. The window's transmission could be measured using a special device which required disassembly and reassembly of the lens and chamber setup. A lens found to have especially low transmission could be removed, along with its associated gaskets and cleaned with an HCl acid etch to remove contaminants. As I shared the equipment with other people, the rate of accumulation on the window was not only dependent on my growths. Measuring the transmission of the window before and after each deposition was too impractical, so to address the issue, a custom plate was fabricated to cover the chamber end of the tube attached to the laser

window. This plate featured a small hole in the centre for the laser to pass through, but covered the rest of the tube. This was found to result in a significant increase in the lifetime of a laser window, but the problem could only be minimised and not removed entirely.

2.3 Molecular Beam Epitaxy

Molecular Beam Epitaxy (MBE) is a deposition technique highly valued for its ability to grow single crystals and also for its capacity for epitaxial growth. Nanowires are often reported as being very close to if not completely monocrystalline so it was of interest to investigate whether ZnO nanowires could be grown using this technique. Working with Physics PhD student Adam Hyndman, the possibility of growing nanorods on our normal substrates using this technique instead of EPLD was investigated.

MBE is a thermal evaporation technique conducted in ultra-high vacuum (In the order of 10^{-9} Torr). Crucibles containing material to be deposited are heated until the material gently sublimates inside what is referred to as a Knudsen effusion cell. The stream of vapour can be considered a "beam" due to the very small mean free path and as a result, atoms reach the substrate from different sources without interacting until they arrive at the surface. Crystals are grown one crystal monolayer at a time by single atoms condensing and joining the lattice of the crystal substrate; the lack of clusters or molecules allowing the atoms to arrange themselves epitaxially to the surface of the substrate.

For growth of a simple oxide crystal such as ZnO, the zinc is supplied from a zinc cell but the oxygen is produced by an oxygen plasma source. The nature of the MBE system however, does not preclude the use of multiple cells in parallel or in rapid series. The thinness of the beams of vapour allows for several cells to be connected to the same chamber in order to grow advanced spintronic materials such as InGaGdN [8] and rare earth nitrides [9]. In addition, the monolayer at a time growth rate makes it a favoured method for the formation of layered structures such as quantum wells, where a thin and precisely dimensioned layer of one material might need to be grown between two layers of another material [10].

An advantage of MBE is the ability to grow epitaxial films. Epitaxy is described by John Arthur [11] as "a film which has crystalline order with respect to the underlying substrate". It can refer to homoepitaxy, which is where the film is grown on a substrate of the same material, or heteroepitaxy where the substrate is of a different material to the film. Epitaxy allows for the growth of crystals free from strain imposed by a lattice mismatch at the interface of the film and substrate, resulting in fewer defects and higher quality crystal structure.

A critical concern for MBE growth is the cleanliness of the crystal surface and accordingly, the purity of the vacuum chamber. The deposited species arrive slowly, on the order of one molecular layer per second, so any contamination can severely affect the quality of the crystal. It can be shown that in a vacuum as high as 10^{-6} Torr, the number of atoms of reactive residual (background) gas arriving at the substrate surface is comparable to the deposition rate of the desired species. Even at a good UHV of 10^{-10} Torr, the substrate surface could become fouled in just a few hours [11]. The relative inertness of common substrates such as sapphire and quartz goes some way to ameliorate this fouling, but great care is still taken to prevent reactive species entering the chamber. Modern UHV systems such as ours feature a loadlock system, where the substrate can be mounted to its holder externally and loaded into a small, separately sealed chamber adjacent to the growth chamber. The loading chamber can then be independently pumped down and the sample transferred under UHV into the larger main chamber once the loadlock has reached an appropriate pressure. This reduces the volume that needs to be pumped down to UHV pressures for each growth, which increases throughput and after a long period of time, all surfaces and instruments inside the main deposition chamber will have thoroughly outgassed and will not contribute to recontamination. With our UHV chamber, the general procedure was that samples were to be loaded the previous day from a planned growth so that they could pump down and outgas overnight.

Whilst MBE offers many options for growing precise layers of complex crystal structures, when the material to be deposited is as simple as ZnO, there are essentially three variables to be modified: substrate temperature, deposition time and the flux of the constituent Zn an O cells.

Control of deposition time is trivial: Shutters over each cell can be opened and closed nearly instantly to control the start and finish time. The ultra-high vacuum and the tightness of the beams means that one the source is shuttered, very little residual material remains in the chamber to accumulate on the substrate. Control of the substrate temperature is maintained in a similar manner to the temperature in the PLD system, with the sample attached to a heated plate using the surface tension of melted Indium-Tin. The overnight pump down ensures that any outgassing from this material should have concluded well before the growth begins. Flux in each cell can be controlled independently by varying the current going through the heating coils.

In situ measurement of film thickness is not feasible with our current setup, but we do have in situ Reflection High-Energy Electron Diffraction (RHEED), which can run throughout the growth. RHEED is a surface analysis technique that strikes the sample at a low angle with a beam of electrons. These electrons interact with the crystal structure of the sample and diffract due to their wavelike behaviour. The diffracted electrons constructively interfere at various angles and are collected on a detector. By knowing the wavelength of the incident electrons, we can use Ewald spheres to make inferences about the atomic spacing and crystal structure of the surface layers of the sample. The output data from the RHEED is a pattern of lines and dots, which takes a certain amount of understanding to read and is interpreted into useful data by the human observer. A RHEED pattern recorded during an attempted ZnO nanowire growth is shown in Figure 8.

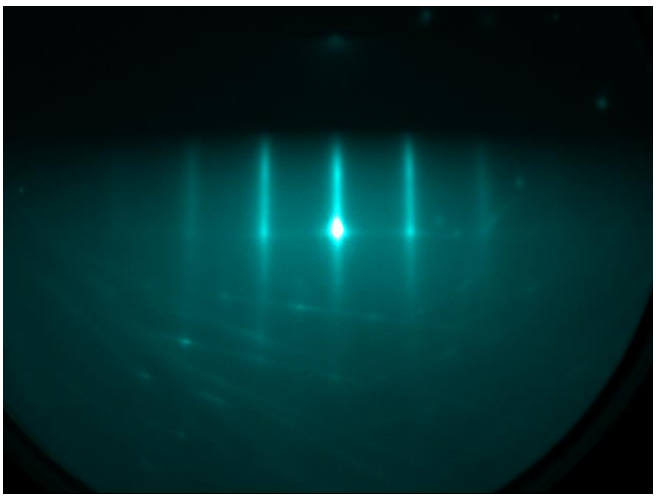

Figure 4: RHEED pattern during a ZnO growth. Note the bright 0^{th} order spot in the centre.

The Ewald sphere is a geometric device useful for visualising the reciprocal lattice of a crystal, which is the Fourier transform of the physical, or real lattice of the crystal. In wave diffraction experiments such as RHEED, the reciprocal lattice is manifested as the lattice formed from points of constructive interference. If an incoming wave vector k_0 of length $2\pi/\lambda$ and wavelength λ, experiences a completely elastic collision at the sample surface and diffracts, any resultant diffracted vector k_i, having lost no energy in the collision must have the same length as k_0. The difference between k_0 and k_i is the scattering vector, Δk. Because k_0 and k_i are of the same length, Δk must lie on the surface of a sphere of radius $2\pi/\lambda$. This sphere is the Ewald sphere. For diffraction to occur, the scattering vector must be equal to a vector in the reciprocal lattice (as diffraction has integer orders), so if the origin of reciprocal space is place at the tip of k_0, then diffraction will only occur at reciprocal lattice points on the surface of the Ewald sphere.

The diffraction pattern on the screen of the RHEED relates to the Ewald sphere's geometry, so by knowing the position of the detector and the wavelength of the incident electrons, the reciprocal lattice can be calculated (and therefore the real lattice easily inferred). Compared to bulk crystal analysis, the RHEED system conditions impose certain boundary conditions on the data. The low incidence angle and subsequent lack of representation of more than the first few atomic layers means that the lattice being examined is essentially 2D rather than 3D and there is not the integer-order diffraction conditions in the dimension perpendicular to the sample. Therefore, the reciprocal lattice to a plane surface is, rather than a lattice of

points, instead a series of infinitely long columns extending out normal to the sample surface from the conventional 2D reciprocal lattice points in that plane. Diffraction conditions are satisfied wherever one of these columns intersects with the Ewald sphere (of radius $2\pi/\lambda$). Due to the high energy and consequent small wavelength of the incident electrons, the Ewald sphere is actually very large in comparison to the spacing between the reciprocal lattice columns. A row of such columns can be considered to approximately model a plane. The planes intersect the Ewald sphere in concentric circles, known as Laue circles.

The brightest spot on the RHEED display is the 0^{th} order beam, or specular beam. This is the 0^{th} order diffracted beam on the 0^{th} order Laue circle (the Laue circle with the smallest diameter). It is typically labelled (00) on the RHEED diagrams. Other points are similarly labelled by the order of diffraction they represent and the order of the Laue circle that they fall on. Using a certain scaling factor, the spacing between the points can reveal information about the spacing of atoms in the lattice. During the first few minutes of an MBE growth, RHEED images are saved approximately every ten seconds when the greatest change is occurring as the surface of the sample shifts from being dominated by the substrate to being dominated by the deposited material.

In practice, the rods do not intersect the Ewald sphere at discrete points. Electrons in the beam have a distribution of energies, meaning the Ewald sphere has a non-zero thickness and contains points where the diffraction conditions are satisfied for each electron's energy. This manifests on the RHEED screen as streaks, even on a perfectly smooth film. Broadening of the streaks or patchiness indicates strain or other imperfection in the lattice, so an ideal single crystal will present clean vertical streaks.

If the system is ideally calibrated, an effect that has been reported [11] is that an observer can see an oscillation in the intensity of the streaks on the RHEED screen while the MBE growth is running. These oscillations have a frequency corresponding to the time required to deposit a complete monolayer. This is due to dynamic scattering of the beam off atomic ledges on the surface. If the sample surface is a complete monolayer, atoms arriving at the sample form islands. Additional atoms preferentially attach themselves to the lattice at the edges of these islands until they join up, forming a new, complete atomic layer. Hence, the mean surface roughness varies sinusoidally between 0 and 0.5 atomic layers. When the surface roughness and related dynamic scattering is maximum at half coverage of the atomic layer, the intensity will be minimum, but when the monolayer is complete again, the roughness and scattering will be minimum and hence the intensity will reach a maximum. Observing these oscillations is a way to measure the deposition rate and to demonstrate that one layer is being deposited at a time. Unfortunately this phenomenon has not been observed by any researchers at the University of Canterbury using our system. Speculated reasons for this include vibrations from the turbo pump creating noise in the signal and various models for the growth

of ZnO in particular, which suggest that it does not generally grow in monolayers but rather in triangular terraced structures [12].

Not all reflected electrons are from elastic collisions. Electrons that undergo a single, elastic scattering event at the surface are called kinematically scattered electrons. Electrons that undergo more than one scattering event and lose some of their energy due to interactions with the crystal are termed dynamically scattered electrons. Analysis of dynamical scattering is extremely complicated and is often to do with the brightness of spots on the display. A feature of dynamic scattering that I did observe from my nanowire samples is the presence of what are known as Kikuchi lines, which appear as diagonal bands linking points on the display. Kikuchi lines cross the diffraction patterns of single crystal samples in a semi-regular manner and can be used in the identification of unknown materials or structures. However, for our purposes detecting them with the RHEED is taken as an indication of a very high level of crystal quality as the lines are drowned out by other features if the crystal is not highly monocrystalline.

A final parameter of interest for the RHEED is the azimuthal angle, which is the angle relative to the crystal lattice that the incident electron beam strikes the sample. The sample stage is able to be freely rotated, so the beam can strike the sample from any angle. This is useful as it allows the user to examine different crystal planes of the sample and measure the angle between them.

2.4 Scanning Electron Microscopy

Critical to any work involving structures on the nanoscale is a method to resolve and observe objects far too small to see, even with a conventional optical microscope. The University of Canterbury has at least three Scanning Electron Microscopes on site, of which I used two in the characterisation of my nanowires and devices: The Raith 150 housed in the Electrical Engineering nanolab and the JEOL-7000 housed in the Mechanical Engineering department. While the operating principles of both were the same, the two each had advantages. The Raith 150 was situated close to the rest of the Electrical Engineering nanofabrication facilities, had casual availability and was easy to focus for good quality images up to 30,000x magnification, increasing to 100,000x magnification after the machine was moved to its new location in the warehouse. The JEOL-7000 had the ability to tilt the stage by an arbitrary amount and produced generally higher quality images between 20,000x - 50,000x but it was also subject to heavy booking from multiple departments with limited afterhours access.

The first true Scanning Electron Microscope was built by German physicist Manfred von Ardenne in 1938 and based on a machine that had been constructed by electrical engineer Max Knoll to study secondary electrons. While von Ardenne's machine was unsuccessful due to its unfavourable performance compared to contemporary Transmission Electron Microscopes (TEMs), the same principles of operation remain in use today, made viable by modern technology [13].

An SEM operates by using a high voltage to accelerate a beam of electrons through a series of magnetic lenses and onto a sample in a vacuum chamber, illustrated in Figure 4. The emitted and back-scattered electrons are collected and used to form an image of the sample surface. The electrons are emitted from a current carrying filament contained within an ultra-high vacuum and accelerated towards the sample by an anode ring. Magnetic lenses, (which are electromagnets rather than optical lenses), collimate and then focus the beam to a small spot size on the sample. Coils charged with a sawtooth wave placed between the collimating and objective lenses scan the beam in two dimensions across the sample.

When the beam strikes the sample, two types of electron emission are measured. Secondary electrons are emitted when an atom near the surface of the sample absorbs an electron and then emits an electron with a different energy level. Backscattered electrons are electrons which collide with and are reflected from the sample without being absorbed. Because incident electrons have different velocities, the backscattered electrons can be reflected from the surface or from deeper in the sample. Some electrons are also transmitted through the sample and do not contribute to forming an image. X-rays can also be emitted by absorption of electrons and these can also be detected by a suitably equipped machine. This is conducted under a high vacuum as gas molecules in the sample chamber would interfere with the beam.

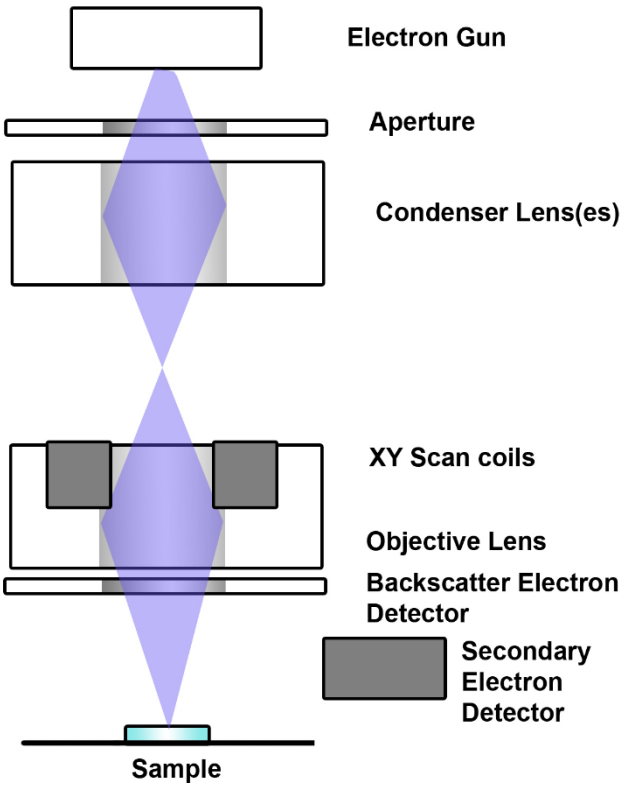

Figure 5: Simplified schematic of SEM operation. Control electronics and user interface have been omitted.

Backscattered and secondary electrons collected by their respective detectors are then mapped into an image, using the same sawtooth wave as used to scan the beam to decode where the received electrons originated. Historically, this was done with a cathode ray tube or on von Ardenne's 1938 design, a rotating barrel of photographic film, but more current designs favour digital signal processing [13].

The actual operation of a modern SEM is fairly streamlined. The sample is first loaded into a load lock, the load lock is pumped down to the chamber pressure and then the sample is transferred into the main chamber. An accelerating voltage and a beam aperture size is chosen: generally for normal use, 10 kV and 30 µm respectively are used with the Raith 150. Once the beam has been turned on, focus is achieved by adjusting the distance between the stage and the objective lens, known as the working distance.

In addition to focus, the user has to correct for astigmatism. Astigmatism is an error present in the output of an SEM caused by the fact that the magnetic fields produced by the lenses are never quite perfectly circular, due to contamination, defects in the lens material or shape or other factors. When astigmatism is present, electrons arriving from a point source will not come to a single point focus. It is a reasonable assumption that the stigmated magnetic field has elliptical symmetry (Higher order asymmetry can occur, but is rarely of great enough magnitude to cause severe problems) and this results in the electrons converging on two separate line foci. To correct for this problem, a stigmator is added to the device. The stigmator produces a weak, corrective field which also has elliptical symmetry but is continuously variable along both axes. Adjusting for astigmatism on the operator's end is a matter of selecting the correct values in x and y for the stigmator's magnetic field to cancel the effect of the built in astigmatism [13].

A limitation of the SEM is its relative inability to image insulating samples. In a conductive sample, electrons that are absorbed or transmitted can easily reach the positively charged stage, completing the circuit back to the electron gun. If the sample is non-conductive however, electrons are still absorbed by the sample. With no path to ground, they build up around where the beam is focussed, creating a net negative charge on the surface. This charge deflects and scatters incoming electrons, creating artefacts and distortion of the image with increasing magnitude the longer the sample is allowed to charge. This was not normally a problem when viewing conductive ZnO films and nanowires but it became a problem when viewing non-conductive quartz diode substrates and samples coated with poorly conductive photoresist.

Workarounds exist for viewing non-conductive samples. A simple method for larger scale samples is to sputter coat the surface of the sample with a few nanometres of gold or aluminium. Some larger SEM units include an in-situ gold coating function within the SEM chamber for this purpose. Unfortunately, this is not suitable for samples that are still being processed or where the insulating property is required. A compromise I found for samples that required an insulating substrate was to use a moderately thin (300 nm)

layer of insulating SiO_2 on top of a conducting layer of doped silicon rather than a quartz or sapphire substrate. In this way, charge only had to travel at most 300 nm to reach a path to the stage, rather than 0.5 mm, the thickness of a quartz chip. Some charging was observed when photoresist was applied to these samples, but it was kept to a manageable level.

2.5 Photolithography

Optical photolithography is a standard method for patterning substrates which is effective from the macro to the nano scale and can accomplish good results at the micro scale using relatively low cost equipment and materials. The University of Canterbury nanofabrication laboratory has a Karl Süss MA6 mask aligner and a Heidelberg Instruments µPG 101 mask writer, which are commonly used with MicroChemicals GmbH AZ1518 photoresist. This setup can produce patterning with micron precision.

The procedure of photolithography can be inferred from the name. Photo, referring to the use of light and lithography, which is a method of rapid printing, using a mask of hydrophobic grease to allow ink to be applied only to desired areas of a print. Photolithography can therefore be thought of as being similar to traditional lithography, but using light instead of ink. A mask is created that selectively blocks the exposure of a photosensitive material to a UV light source, thus imprinting the features on the mask into the material. A developer is then used to remove the photosensitive material from either the exposed or unexposed areas, allowing processing to be done on the substrate underneath only in those areas.

The first step in the photolithography process is to design a mask. This can be done in one of many CAD programs, but the standard tool at The University of Canterbury was Tanner Tools' L-Edit plugin. L-Edit produces a .dxf file that can be read by the mask writer. It is important to determine at this point whether the mask is to be light-field or dark-field. A light-field mask is a mask where the features to be patterned are solid and the background is transparent, where a dark-field mask is the opposite. This choice is determined by whether the photoresist to be used is positive or negative and the shape of the features needed. When exposed to UV light, what happens to a photoresist is the opposite between positive and negative resists. A positive resist will change with UV exposure, becoming more soluble in the developer and allowing exposed areas of photoresist to be washed away. Negative resist polymerises when exposed to UV light, becoming less soluble in the developer, leaving photoresist remaining only in those exposed areas after development.

Once the .dxf file is complete, it can be written onto a Nanofilm, (CA, USA) Soda Lime pre-coated glass mask using the mask writer. Photomasks are transparent, coated on one side with a layer of electron-beam

sensitive photoresist underneath a layer of chrome, which is reflective on one side. The pattern written by the mask writer is then developed by much the same method as I am about to describe for the sample, using MicroChemicals GmbH, (Ulm, Germany) AZ326 MIF developer. This removes the photoresist from the exposed areas and the pattern can be etched through the chrome using a solution of ceric-ammonium nitrate and perchloric acid. Once this is complete, the pattern from the .dxf file will be patterned in chrome on the mask.

Photoresist is typically applied by spin coating. When a droplet of photoresist is applied to a substrate and then spun at high speed, it spreads out into a thin film of several microns in thickness. The thickness of a given resist can be controlled within a certain margin by varying the spin speed and duration of the spinning. Thickness is an important parameter because it determines how effective the photoresist will be as at masking areas from processing. If that processing is etching, or lifting off a layer of metal, the thickness needs to be sufficient to not be completely eroded before the etch is finished, or thick enough to be removed later even after the metal layer has been added. For all of the work requiring photolithography in this thesis, AZ1518 resist spun at 3000 rpm to give a thickness of 3 µm was sufficient.

After spinning, the photoresist is baked in order to harden the surface and improve discrimination between features. Care must be taken not to bake for too long or at too high a temperature, otherwise the resist will become “hard baked” and will dry out and become almost completely insoluble, even in acetone. In the use of AZ1518, the prescribed baking time and temperature is either 100 °C for 2 minutes on a hotplate, or 90 °C for 30 minutes in an oven. The discrepancy being due to better heat conduction on the hotplate.

Once this has been completed, the sample and the mask are loaded into the mask aligner. For a simple exposure such as the contact pad arrays for my nanowire devices, no real alignment was necessary to position a 3 mm pattern approximately centrally on a 10 mm x 10 mm substrate. For a more complicated pattern, such as my earlier prototype contact arrays, which had an etched channel to collect the nanowires, alignment was necessary. In these situations, each layer to be patterned included alignment markers as well as the active structures. These are basic geometric shapes that tessellate together only when the position of the two layers is aligned both in x, y, and θ. If alignment markers placed in four corners of the

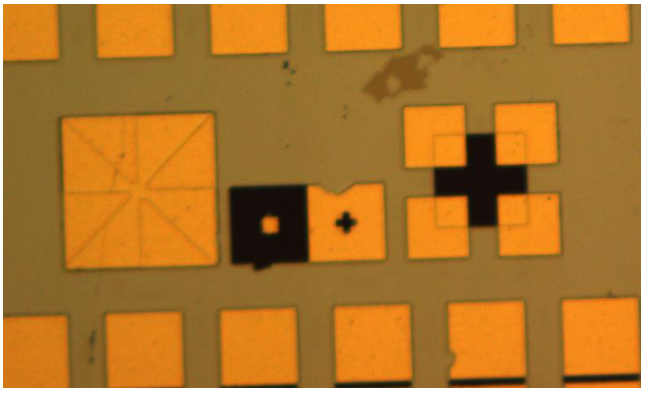

Figure 6: Optical microscope image of my preferred alignment markers. The light gold is gold metal, the dark black is RIE-etched channels in the green-grey SiO_2.

sample all show correct alignment, it can be inferred that the patterns on the layers are also aligned correctly. My experience conversing with other researchers indicates that there is no agreed upon optimal alignment marker structure as an individual researcher will chose a shape that they feel they are best able to perceive a slight imperfection in. In my research, I found a pattern of squares and a spiral shaped cross to be effective, as shown in Figure 5, as any rotation would cause significant enough disruption as to be easy to see.

The UC Nanolab's Karl Süss MA6 is capable of performing multiple exposures on many different settings. The functions required for creating the patterns used in this thesis were fairly simple. The mask is pressed up to the surface of the substrate, with a clearance defined by user settings. The substrate is then illuminated through the mask with UV light, exposing the photoresist for a number of seconds prescribed by the thickness and type of resist. An incorrect setting on the exposure time will result in loss of detail in the pattern. Underexposure will leave areas that are supposed to be clear still coated with photoresist present after development and overexposure will result in exposed areas creeping outwards as UV light refracts around the edges of the mask. A small error in exposure time leads to a poor edge profile (where the walls of the exposed areas are not 90° to the substrate), a large error will result in total loss of the pattern. When using AZ1518, a sufficient exposure time was 10 seconds.

After exposure, the sample is developed. Developers are paired to their respective photoresists as the developer needs to be able to dissolve only the defined areas. Generally speaking, developers are not able to perfectly discriminate between exposed and un-exposed areas, so care must be taken not to overdevelop the sample. Overdevelopment will result in rough, poorly defined edges and loss of features. For AZ1518, 35 seconds in MIF326 developer proved effective at removing all exposed resist, while retaining good feature integrity. Samples are then rinsed in two changes of deionised water to wash off any remaining developer and dissolved photoresist.

At the conclusion of the photlithography process, the sample will carry the pattern from the mask in photoresist on the surface. It can then be etched or metal can be deposited by any method desired. If metal is deposited, lift off is fairly easy using AZ1518 resist. The high thickness of the AZ1518 resist means that most metals lift off very fast in acetone, usually within a few seconds. Any resistance can usually be overcome simply by gently agitating the sample grasped with tweezers in the solvent.

2.6 Electron Beam Lithography

Electron Beam Lithography (EBL) is an advanced, digital technique for patterning extremely finely detailed features. It is labour and resource intensive and has poor scalability but is able to produce features as fine

as 10-20 nm and does not require a physical mask, allowing it to be used to create freeform shapes and features, rather than being constrained to a pre-made design. The operating principle of EBL is similar to that of standard photolithography, with extreme control of the exposing beam used as a substitute for the need of a mask. Commercial EBL machines are extremely expensive dedicated devices, but in research, they are usually modified scanning electron microscopes, which can be operated with only marginally compromised performance. The University of Canterbury microelectronics laboratory possesses the only EBL system in New Zealand, the Raith 150 SEM/EBL. Priced at over $2 million, it is the most expensive machine in the laboratory.

A sample to be patterned is spin-coated with an EBL photoresist which is sensitive to an electron beam rather than to UV light as in conventional photolithography. As with photolithography, many such competing chemicals are available from different suppliers offering various advantages, but the chemical most commonly used at the Univeristy of Canterbury is Poly Methyl Methacrylate, or PMMA, provided by Sigma Aldrich, MO, USA. PMMA is a polymer that undergoes de-cross-linking when exposed to an electron beam or to deep-UV light (higher energy than normally used in photolithography). This weakens the exposed areas allowing them to be dissolved, using the common solvent Methyl Isobutyl Ketone (MIBK) mixed 1:3 with methanol as a developer. PMMA is therefore a positive resist.

PMMA spins on a great deal thinner than AZ1518, a common UV photoresist, which contributes to its high resolution, however this comes at a cost of greater constraints on the type and thickness of materials that can be easily lifted off. In normal photolithography, a rule of thumb is that the resist should be at least an order of magnitude thicker than the material to be lifted off; a 100 nm layer of Ti/Au might be deposited onto 2-3 µm of AZ1518 and expected to lift off easily. PMMA does not afford such luxury. At 3000 rpm for 60 s, a spin-coated layer of PMMA is approximately only 70-80 nm thick. A second layer can be added after the first has been baked to double the thickness but even this requires making do with a layer of photoresist only 2-3 times the thickness of a 50 nm thick layer of metal. A trick to aid in the lift off procedure is to use different molecular weights of PMMA for each layer. As a polymer, PMMA can be purchased with different average chain lengths. A longer chain has more cross-linking sites and exposes less readily than a short chain. If the top layer of resist has a long chain and the bottom layer a comparatively short chain, the result is that the bottom layer is more affected by the beam and a small amount of undercutting occurs. Undercutting is often considered undesirable in photolithography as too much can degrade the integrity of the pattern but it also allows the solvent used in lift off to get under the edges of the metal and assists in removing the resist. The small amount of undercut afforded by the PMMA bilayer is considered helpful in the lift off process and has not shown to significantly degrade the pattern quality. After spinning, each layer is baked at 185 °C for 30 minutes.

The sample is loaded into the Raith 150 the same way as it would for SEM. Aperture size is more important to set appropriately for EBL than for SEM, as the width of the aperture controls the beam current. SEM is used to align a sample for EBL and it requires balancing two mutually opposed variables. The user wants to observe the sample closely in order to align the pattern accurately, however any scanning of the electron beam for SEM also exposes the resist in that area. Too many scans over an area of interest and the resist will be completely exposed unintentionally, resulting in metal being deposited in the wrong place after development.

The EBL can be used in a similar manner to the mask-writing step of photolithography. A premade mask file is loaded into the computer, a starting point is defined and the Raith writes the mask into the photoresist autonomously. In this case, the area to be written is usually large and the entire pattern can be written without observing the individual areas of the pattern. The EBL delivers a specified dose of electrons per unit area to expose the resist, so setting a large beam current allows it to deliver that dose faster. Because SEM is only used to start the process, no unnecessary exposure occurs even with high beam current.

The second technique I used with the EBL was much more involved and in my case was used to write custom contact pads onto individual nanowires- an extremely precise application of very fine features. Nanowires were scattered at random on the substrate. Each wire would need to be individually found and then a miniature mask made just for one area. In this mode, I found that even a quick, single scan with high beam current was enough to prematurely expose the entire area viewed, but each exposure only took a few seconds. As a result, it was much more practical to reduce the beam current at a penalty of slightly longer exposure time.

After loading the samples and setting the aperture size and accelerating voltage, the beam current is measured using a Faraday cup. The Faraday cup is simply a pit in the metal stage, designed so that few electrons can escape from inside it. The current passing through the stage when the beam is aimed into the Faraday cup is a good measure of the current in the beam. Knowing the beam current is important to calculate the specified dose mentioned above.

The beam then needs to be carefully focussed in order to prevent distortion in the pattern being written. This can usually be accomplished by searching the edges of the sample for a small piece of dirt. Even with rigorous cleaning, there are usually one or two small flecks at the micron scale. In cases where patterns are being written onto existing features, alignment markers and other non-essential marks can be used to focus the beam.

The EBL uses an absolute XY coordinate system measured across the entire stage to map the sample. A proxy coordinate system, UV, is incorporated into the software for ease of use. UV maps onto XY by setting

a UV zero point and a rotation. In this way, a convenient position on the sample (often the bottom left corner of a square substrate) can be defined as zero and the U = 0 and V= 0 lines set parallel to the edges of the sample. It is helpful to set these up once the beam has been focused.

An important variable in the EBL is the writefield size. The writefield size can be thought of as the magnification at which the EBL performs an exposure. If the pattern is larger than the writefield, more than one writefield will need to be stitched together to form the whole pattern. In order to do this, the writefields must be aligned. This is correction for error in the electromagnetic lenses that the Raith uses to focus the beam on the correct spot. The stage is very precisely controlled in XY (UV) and is assumed to be accurate. The correction is thusly made in the lenses. To make the correction, the user focuses on a feature, often a piece of dirt. Using a special interface, a point is marked on an easily recognisable landmark- an extrusion or pit on the speck. Care must be taken with samples prone to charging that the landmark is real and not an illusion caused by charging. Once the point has been marked, the stage is driven to what it thinks are three points in the same writefield as the marked point. At each one, the marked point is highlighted again by the user and the EBL records the correction. After all three movements, the machine proposes its list of corrections in XY (UV) and angle θ. If the correction involves a shift of more than a prescribed tolerance, the process is repeated using a smaller writefield and a different marked point until the resultant correction is small enough as to be considered insignificant. The beam can then be considered to be in line with the stage. With this setup completed, the exposure is almost ready to begin. The Raith software takes in beam current, area dose and writefield size and calculates the area dwell time and beam speed necessary to satisfy the input parameters. Although these variables are not specified directly by the user, it is worth checking that they conform to expectations as a means of error-checking user inputs.

If the exposure is a pre-programmed mask file, the stage can then simply be driven to the start location and the exposure run. The EBL is very much a high resolution, low throughput technique and a pattern as small as 10 mm^2 can require up to an entire day to write if the level of detail is high. To accommodate this with other users' requirements with the Raith, I tended to run such exposures starting at about 3pm in the afternoon and going through the night. If custom exposures of small areas are being performed, the process is usually quicker, but much more involved. Some method must be devised in order to move the sample such that the desired feature to be written falls within the writefield without using the microscope or turning on the beam. My method was using an array of pre-deposited contact pads around which, my EBL features would be written. With a known distance between them in X and Y, I could skip between the areas of interest on the substrate by moving the stage in increments of the pad separation. Without a grid or other co-ordinate system available on the sample, finding an area as small as a single writefield would be extremely difficult. Once the area to be written has been found, a single SEM scan is performed (rather than

the continuous scans of the SEM operation). At an aperture size of 10 µm, it is possible to perform more than one single scan on the same area without exposing the resist completely, but as each scan does erode the resist, it is highly advisable to take only the minimum number of scans needed. The scan is shown in a special window and alongside it, an editor window can be opened for a new GDSII file.

The toolbox of the GDSII editor is rudimentary at best, but can be used to draw basic shapes and lines. The pattern in the editor can be set to overlay onto the scanned image, showing where the patterned shapes will go, but this does not refresh automatically when changes are made. The process of creating a pattern and laying it onto the scan is one of guess and check. This can be made easier by lining the two windows up together and making sure the visible area in the editor is the same as in the scan, but there is no way that I found to draw directly onto the scanned image. If the pattern to be written is larger than a single writefield, the Raith can handle the stitching so long as the writefield alignment was performed, but in my work, I wrote one at a time for simplicity. If a sample needs multiple exposures for one reason or another, these can all be loaded into a position list and set to automatically expose, even if they are spaced across a large sample.

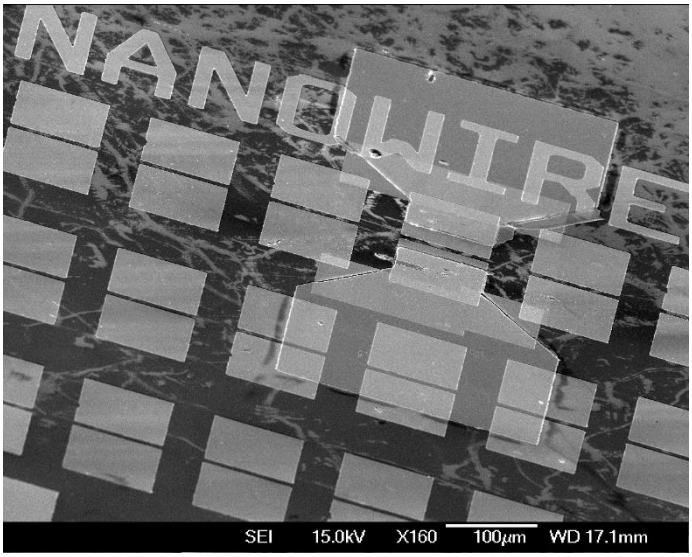

Figure 7: An SEM image showing an example of each type of EBL pattern. The text and contact pads are written using a premade mask, the tiny nanowire contacts are written manually.

The exposure settings are the same for custom exposures as for pre-made masks. The exposure times for such exposures are generally much shorter as the patterns are usually just one or two writefields, but overall machine time can often be very long as multiple areas are likely to need writing. Figure 6 shows an example of both types of EBL exposure on a single sample. Large, regular patterns such as the text and the pairs of pads can easily be exposed automatically, but the small, distinct nanowire contacts must be written individually.

2.7 Metal Deposition

Essential to any device-focused semiconductor research is the ability to fabricate metal contacts to connect a device to the rest of an arbitrary circuit. Deposition of the material used for these generic contacts needs to be uncomplicated and capable of a high throughput. During my research, I employed three methods of depositing metals: sputtering (both by DC and RF), electron beam evaporation and thermal evaporation. The former two methods are each carried out using the same vacuum chamber, a BOC Edwards Auto 500.

Sputtering is a physical vapour deposition technique that uses atoms ejected from a target by atom or ion bombardment to coat a sample. There are many methods of creating the sputtering effect, including chemical reactions and focused ion beams, but in my research I employed two subtypes of magnetron sputtering: DC and RF magnetron sputtering. Magnetron sputtering uses very high electric and magnetic fields to generate and contain a plasma on the surface of the target. The polarity of the fields can be constant as in DC sputtering, or alternating as in RF sputtering. In general DC is simple for use with conducting or metallic targets, while RF is preferred for insulating targets where charging of the target might otherwise occur. In both cases the chamber is pumped to a high vacuum (of the order of 10^{-5} mbar) before processing. An inert gas (Argon is commonly used) is then injected into the chamber to a process pressure of the order of 10^{-3} mbar. This gas serves to provide a medium for the plasma and also to reduce the energy of the atoms and ions reaching the sample through atomic collisions. Reactive gasses such as oxygen can also be added in order to deposit oxides or other compounds.

Power for the DC sputtering system is directly adjustable. Different materials require more or less power to sputter and materials that require a high power sometimes also employ ramping in order to reduce strain and thermal shock on the targets. RF sputtering is more nuanced, requiring a matching circuit in order to maximise delivered power and minimise reflected power, but much of this complexity is performed automatically by the control unit. Typically, a high reflected power was usually indicative of either a problem in the system or a loss of plasma.

While sputtering can be used on diverse materials including oxides and even organics, electron beam evaporation is reserved for the deposition of metals and is carried out in vacuum and without the presence of plasma. In this technique, the metal to be deposited is held in an insulated crucible and heated by direct application of a high energy electron beam. The voltage and current of the beam are variable and used to control the rate of evaporation, although the voltage is normally held constant at 5 kV. Current is varied between values as low as 50 mA and as high as 250 mA, and is chosen based on the properties of the material to be heated. The optimal current for a given metal is chosen based on a compromise between a convenient high deposition rate and the spattering of molten material caused by rapid thermal expansion in

the crucible. When the current is set correctly, evaporated metal rises up to coalesce on the sample mounted over the crucibles.

Both sputter guns are controlled by the same unit. A crystal monitor is placed in the chamber to measure the thickness of the deposited material and calculate the deposition rate. By knowing the resonant frequency of the crystal and the acoustic impedance of the material being deposited, the thickness of material arriving at the crystal can be determined from the shift in resonant frequency. For each material then, it is essential to know this parameter so that the thickness can be accurately measured. The thickness of material arriving at the chamber-mounted crystal is not a perfect representation of the material arriving at a sample positioned over each of the three deposition guns, especially if rotation is used on the sample holder. To accommodate for this discrepancy, an empirically determined "tooling factor" is derived for each material. The tooling factor is a linear scale factor that is applied to the amount of material measured by the crystal to predict the amount of material arriving at the sample. It is dependent on the mean free path of the material, but more so on the geometry of the chamber. Samples mounted far from the crystal monitor will require a larger tooling factor than samples mounted next to it. With the relevant power (or current) set and the tooling factor entered, the electronic control unit makes deposition fairly straight forward. An operator simply enters a desired thickness, checks the the tooling factor and acoustic impedance and sets the machine to run. Deposition is controlled by a shutter over each source.

Aside from the Edwards unit, the other primary means of metal deposition at my disposal was thermal evaporation using the Balzer thermal evaporator shown in Figure 6. Although very similar in principle to electron beam evaporation, it was found that titanium deposited by this method was more effective at lifting off with PMMA EBL resist than titanium deposited by e-beam evaporation. The thermal evaporator also induces evaporation in vacuum, but it uses a conductive metal boat, heated by a high current in order to generate the required temperatures to cause the contents of the boat to sublimate.

Figure 8: The Balzer thermal evaporator with the vacuum bell raised, showing the sample holders and shutters.

Thickness control is carried out in the same way as the sputterer and e-beam evaporator, by using tooling factors and acoustic impedance to translate data measured by a

crystal monitor placed close to the sample holder. Shutters over the evaporation boats open and close when deposition starts and when the desired thickness has been reached.

A drawback to the thermal evaporator is the unavoidably limited lifetime of the boats. Even when care is taken to mount them correctly and to heat and cool using ramped current in order to avoid thermal shock, the boats inevitably fail and snap after a few growths. In anticipation of this, boats were readily available, but the prospect of a deposition failing midway through, almost at random, meant that the thermal evaporator was far less user-friendly than the sputterer and the electron beam evaporator.

2.8 Oxide Growth

One of the major factors in the establishment of silicon as the dominant force in semiconductors has been the multi-faceted convenience of its oxide, silicon dioxide (SiO_2). SiO_2 is strongly insulating, mechanically strong and resistant to damage or corrosion from commonly encountered concentrations of chemicals present in the environment. To further recommend it, it only forms at appreciable speed at high temperatures and the growth curves are well documented. Etches that are used on SiO_2 such as HF do not strongly affect bare silicon, allowing an oxide layer to be etched down to the bare silicon without damaging it. Lastly, SiO_2 requires only heat and oxygen to grow and the process is very simple, although as with anything, controls must be observed in order to produce oxide of research quality.

The University of Canterbury has several facilities available for the deposition of SiO_2, some of which are covered elsewhere in this chapter: sputtering and pulsed laser deposition are both equipped to deposit SiO_2 and are especially useful in situations where for some reason, a silicon substrate cannot tolerate high temperatures, or where the substrate is not silicon. For most applications however, SiO_2 can be grown on silicon using a furnace. The UC nanolab runs a Brute furnace system with three tubes which can be operated independently of each other. As well as setting the temperature from 400 °C to 1200 °C, the tubes can also maintain a temperature gradient if needed, with three points per tube of temperature control. The tubes can optionally be supplied with several different gases and the option is also available for the gas to be piped in through a vessel of deionised water so that it is “wet” when it enters the tube. This feature is convenient for the growth of SiO_2, which grows faster in the presence of water.

The growth rate curves for SiO_2 are well documented for both wet and dry methods. At the same temperature, the oxide grows faster in the presence of water vapour. However, the wet grown oxide has been found empirically to be of marginally lower quality and consistency. This drop in quality is generally only considered important for the interface layers of oxide. When highest quality is not needed throughout,

standard operating procedure is to begin with a thin layer of dry grown oxide, followed by the bulk thickness grown by wet oxidation and then a final capping layer of dry oxide. This enables the thickness to be grown in bulk by the faster method while preserving the quality of the interfaces. Disconnecting the water supply from the tube is a simple rerouting of a gas line, so it does not cause any significant delay.

2.9 Reactive Ion Etching

Reactive Ion Etching (RIE) is a powerful, plasma-assisted dry etching process. It is useful for etching tough materials such as quartz or silicon without the need to expose the user to extremely powerful and hazardous chemicals such as HF which would otherwise be required to etch them. RIE uses chemically reactive plasma to etch the surface of a sample, using the reactivity of the plasma to bind to and carry off material. The University of Canterbury operates an Oxford Plasmalab 80 Plus RIE machine (shown in Figure 7), supplied with multiple gases and a mixing board to combine them in various combinations.

RIE is performed under high vacuum (approximately 10^{-6} Torr). During the etching process, a plasma is created by an RF electric field that ionises the gas species that are introduced to the chamber. The sample to be etched is placed on a DC isolated chuck but the walls and ceiling of the chamber are grounded. As the field alternates, electrons in the gas are accelerated up and down over the sample. Electrons that strike the ceiling of the chamber are grounded and removed from the system, but electrons that are absorbed by the chuck remain isolated and begin to build up a negative charge. This negative charge creates a large DC voltage that attracts the much heavier positive ions to the surface of the sample, enhancing the number of reactions occurring.

Figure 9: The Plasmalab 80 Plus reactive ion etcher.

Different species of gas are used depending on the material to be etched. Usually there is a reactive gas such as SF_6 or CHF_3 and an inert buffer gas such as Ar or N_2. The RIE at the University of Canterbury is equipped with the following gases: Nitrogen, Argon, CHF_3, SF_6, Oxygen, Helium.

Reactive Ion Etching presents two major advantages over wet chemical etching: First, the electric field and vertical movement of the reactive ions can create a very anisotropic (vertical) etching profile, where wet etching often has an isotropic (slanted) etch profile. Secondly, the process is contained within a vacuum

chamber and requires much less personal protective gear to operate than acid etches. Silicon is easily etched by RIE using CHF_3 gas, but requires an extended etch in HF to do on a benchtop with wet etching.

Operation of the Plasmalab 80 Plus machine is fairly simple. Samples are loaded onto one of several chucks made from different materials including Si, NiCr and SiO_2. The chuck material has an effect on the charge build-up and the behaviour of the plasma, but in general this choice can be compensated for by input parameters. After the chamber is evacuated and a base pressure and desired temperature have been reached, the wattage of the plasma and the etch time are set via the console. The desired gases are turned on and allowed to enter the process chamber and the plasma is struck. After the programmed time has elapsed, the plasma is switched off automatically and the chamber is evacuated, ready for unloading.

2.10 Photoluminescence

Photoluminescence (PL) was used to examine the composition of the metal oxide nanowires and films grown. PL is a non-destructive analytical technique, which enables a researcher to learn about the composition of a film or crystal in great detail. A beam of laser light is shone directly onto the sample and the spectrum of emitted photons is captured and examined. The University of Canterbury operates a Photoluminescence facility at the Department of Physics and Astronomy, which has produced results of world-leading fidelity in recent years [7, 12, 14-16]. I collaborated with Physics PhD student Alex Neiman and his supervisor Professor Roger Reeves as well as former PhD student Robert Heinhold in order to obtain a variety of PL scans of the most promising and interesting samples I produced.

The emission of light from semiconductors is a powerful phenomenon responsible with many applications in research and in industry. Photons of light of various wavelengths can be emitted under many different circumstances whenever an electron drops to a lower energy state. Photoluminescence stimulates this emission by irradiating the sample with a UV laser. The laser commonly used in our PL setup to characterise ZnO is a Kimmon He-Cd 325 nm laser; higher in energy than the bandgap of ZnO. The photons from the laser are absorbed by electrons in the valence band of the crystal, which are excited into the conduction band. This leaves a hole in the valence band. Because the photon energy is greater than the bandgap, the electron and the hole are often out of thermal equilibrium with the surrounding electrons and as such, they gain momentum and have to nonradiatively relax to dissipate it. However, even at the Γ point where the bandgap is at a minimum, the electron-hole pair is still out of equilibrium and so the pair radiatively recombines, the electron jumping across the bandgap back to the valence band to reoccupy the space of the hole. The energy lost in this translation is released as a photon of light with wavelength equal to the bandgap energy.

This is only the most basic example of the possible outcomes of the absorption of the incident photons. In practise, there are myriad possible electron energy states introduced by defects, dopants, ionised states and the formation of pseudo-particles such as excitons. These states provide different energy levels in both the valence and conduction bands, allowing transitions of greater and lesser energy on either side of the bandgap energy. Photons released by these transitions are recorded and counted for each wavelength in the investigated wavelength range.

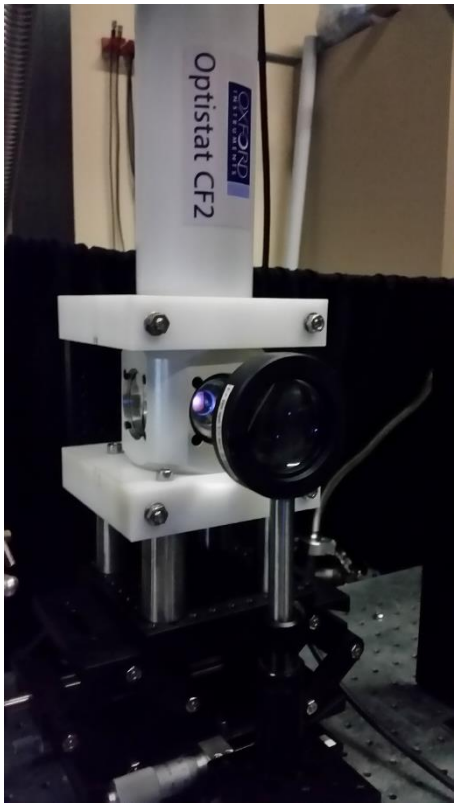

Figure 10: Dull violet luminescence from ZnO nanowires in the Optistat Cryostat.

Different materials luminesce more strongly than others and overall intensity count can be affected by external factors including the equipment, so absolute intensity is not important. Intensity is a raw count of incoming photons, so it has no units associated with it. The data gained from PL plots comes from the relative intensity and spectral positions of particular peaks and lines in the spectrum, compared to other features. These data are compared to existing plots in order to make inferences about the composition and structure of the sample being examined. It is important to note that current science is very far from knowing what all the peaks on a given spectrum are indicative of and indeed, within the study of ZnO, there is significant controversy over the exact causes of several rather significant features. Understanding of many of the features on PL plots that are known was derived empirically and it is an active and ongoing area of research to develop tests proving or disproving a possible cause for features in a material's PL spectrum.

Luminescence from a material can be caused by many other sources as well as photon absorption. Cathodoluminescence is the emission of photons from the absorption of electrons generating electron-hole pairs. Ionoluminescence is the emission of photons due to ion bombardment. However, an unavoidable form of contaminating luminescence in any such measurement is thermoluminescence, the emission of photons from thermally excited electron-hole pairs. Any amount of heat above absolute zero is capable of generating electron hole pairs spontaneously. The photons given off by this form a base layer of noise in any PL spectrum and even at room temperature, they can drown out subtle features. In order to reduce this noise floor, PL is often carried out at very low temperatures, using liquid nitrogen or liquid helium as a coolant. The setup used in this thesis uses liquid helium to lower the temperature to as low as 3K to obtain the sharpest lines and peaks possible.

The use of a cryostat sample holder also enables temperature dependent PL. Spectra can be measured at a low temperature, which can then be raised in increments and more measurements taken. This results in a plot showing the changes in the spectrum as the temperature rises and the noise floor increases. Various effects might become more or less prominent as the temperature changes and this data can provide important insight on their possible causes. Because the intensity is measured in arbitrary units, the spectra at each temperature can be separated vertically on a plot.

Light passing into the spectrometer is gated by an entrance slit that can be made wider or narrower to let more or less light in. A wider slit improves the luminescence count logarithmically, which is useful for scanning wavelengths where the sample luminesces only dimly, but also admits exponentially more noise into the signal. The operator therefore attempts to choose a slit width to produce high counts without introducing too much noise.

The equipment used in the University of Canterbury PL laboratory is configured as follows. The beam from the Kimmon 325 nm (3.815eV) laser arrives at the sample at an incidence angle of 40° to 60° from the normal. The sample itself is aligned opposite the Spex1700 Spectrometer with light emitted from the sample collected and collimated by a 100 mm high transmittance quartz lens focussed on the spectrometer slit for maximum intensity. Focussing of this lens is done manually by moving the lens incrementally back and forth until a maximum intensity is obtained. The signal arriving at the spectrometer is dispersed by a diffraction grating of either 1200 or 2400 lines/mm. The diffraction grating separates out the wavelengths of light comprising the total luminescence of the sample, allowing each wavelength to be counted by a water-cooled, Hamamatsu R943-02 photomultiplier tube (PMT). Because this diffraction grating is responsible for the selectivity of the machine, the maximum possible resolution is determined by how fine the control of the gratings is. In our setup, this is controlled by a stepper motor and has a minimum spectral step size of 0.001 nm. The maximum resolution is always traded off with scan time and in general, 0.01 nm steps were more commonly used.

The spectrometer is Horiba Jobin Yvon 1000M with a 1000 mm focal length. was carried out at the beginning of each experimental set. A mercury lamp with four well known transitions in the UV and visible regions was placed between the sample holder and the spectrometer and scanned. The error of the system in nm is known to be non-constant and is variable with the wavelength. Scanning multiple known points allows the operator to estimate a correcting function of first or second order, which ensures a good degree of accuracy throughout the relevant spectral range. The accuracy of this calibration method is estimated by Mendelsberg [7] to be 0.05 nm or better throughout the UV-Visible range of 300-630 nm.

The sample holder itself is a copper cold finger inside an Oxford Instruments Optistat CF2 cryostat. The sample is mounted by silver past adhesive to one end of the finger and liquid He is passed over the other end. This enables the sample to be cooled to very low temperatures without having to submerge the sample itself in the coolant. Temperature of the sample is measured by a thermocouple wrapped around the sample end of the finger and a PID controlled heater is also attached for raising the temperature by controlled amounts.

2.11 Transmission Spectroscopy

Transmission spectroscopy is an optical technique used to analyse which parts of the optical spectrum are absorbed and which are transmitted by a sample, revealing information about its structural and elemental composition. This method was used as a routine check for colloid morphology as peak transmission for a colloidal dispersion changes with colloid diameter, revealing any anomalies. Light from a source is measured against light from the same source passing through a sample. A graph can then be produced showing the parts of the spectrum that are filtered by the presence of the sample and from this, inferences can be drawn about the composition and crystal structure of the sample. The University of Canterbury operates an Agilent Cary 6000i at the department of Physics and Astronomy and a less sophisticated machine capable of scanning the UV-Visible (UV-Vis) wavelengths at the Department of Chemistry.

The spectrophotometer generates light from one of several possible sources, dependent on the area of the spectrum being investigated. The Cary 6000i has two lamps, a deuterium lamp for low wavelengths and a mercury lamp for higher wavelengths, with a total spectral range of 175 – 1800 nm. These lamps emit a spectrum of light that can be filtered to a high degree of precision using a monochromator, so that only a small wavelength range is emitted at once. By making small changes in the slit spacing of the monochromator, the machine can step up or down the spectrum in fine 0.01 nm increments. Once the scan reaches the edge of one lamp's useful emission spectrum, the machine automatically switches to the other one to continue scanning. At the opposite end of the sample chamber, a detector measures the intensity of light received.

The Cary 6000i is a twin beam system, so the monochromatic light is directed down two channels, one that passes through air uninterrupted and the other that passes through the sample holder. The sample holder in this machine has fittings for solid chips, liquid in cuvettes and a cryostat capable of taking measurements down to approximately 15 K.

Before any measurements can be taken of the samples, a baseline scan needs to be performed. If using a cuvette, this will be performed using an empty cuvette or a cuvette filled with whatever solvent (deionised water or methanol for example) the solution of interest is suspended in. If using a sample on a substrate, the baseline will be performed using a clean, bare substrate identical in thickness to the sample. If the cryo unit is used, it will need to be inserted and filled with coolant. The baseline scan represents the effective zero state of the system, before the sample is added.

With a baseline established, the sample can be inserted and the scan run again. The resulting graph can be configured to show either one of the two reciprocal outputs: Transmission, the percentage of light that passes through the sample at a given wavelength, or absorption, the percentage blocked by the sample. Of note is the fact that light registered as blocked is not necessarily absorbed. Factors such as scattering and reflection are not accounted for in the software of either machine, and can be as large as 3% according to Professor Reeves from the Department of Physics and Astronomy. The baseline scan does help to minimise the impact of this error however and further tests can be done if greater accuracy is required. Also considered is the possibility of emission: a sample could become excited by an incident photon and then decay, releasing a lower energy photon that might be absorbed by the detector. However, the light passing from the monochromator to the detector is coherent, whereas emitted photons can travel in any direction. Assuming the detector is sufficiently far from the sample and therefore represents a very small proportion of the available angles for emission, it can be assumed that the error introduced by this effect to be relatively small.

2.12 X-Ray Diffraction

X-Ray Diffraction (XRD) is a non-destructive method of crystal surface analysis often used to examine the crystallinity of bulk materials and thin films. Particularly useful data that XRD can provide includes the surface plane or planes of the material being measured. XRD measurements presented here were conducted using a Bruker D8 XRD machine at Callaghan Innovation in Lower Hutt. This machine uses a cobalt source for its x-rays, resulting in the characteristic wavelengths shown in Table 1.

Table 1: Characteristic wavelengths of Bruker D8 XRD Machine.

Parameter	Wavelength (Å)
Alpha-1	1.78900
Alpha-2	1.79289
Alpha (Average)	1.7905
Beta	1.6208

Two types of XRD curve are of interest, the θ-2θ curve and rocking curves around specific diffraction angles. θ-2θ curves are a broad scan across a wide range of angles to investigate which planes of which materials are present and peak positions are compared to a database of empirically gathered reference values. These are conducted by sweeping the angle of the incident x-ray (θ), while keeping the detector at an angle of 2θ from the incident beam. A peak at a given angle indicates constructive interference. This angle can be inserted into Bragg's law (Equation 1.4) to determine d, the interplane spacing. As this spacing is unique for each plane of each material due to different bond lengths, the interplane spacing can then be used to identify the plane.

$$n\lambda = 2d \sin\theta \qquad \textbf{[2.4]}$$

Rocking curves are focussed scans on single diffraction peaks from which information about the spread in orientation of the crystal domains on a given crystal plane can be gathered. Once a diffraction peak has been found, the x-ray source and the detector are fixed to that angle. The sample itself is then tilted, "rocking" to either side of the diffraction peak by an angle of Δω. As the sample tilts away from the diffraction angle satisfying Bragg's law, the intensity of the diffracted x-rays decays. In a perfect crystal, the peak would be an impulse of zero width, but strain and imperfect crystallinity cause a broadening of the peak. As the rocking curve peak tapers to a point, the width is recorded and compared as the full-width at half maximum (FWHM): the width of the peak at half of its maximum value. A sharp peak with a low FWHM is indicative of a near-perfect crystal with no impurities or defects causing strain. A broad peak with a high FWHM represents that the crystal plane being measured is under some form of strain, be it from impurities, poor epitaxy or defects in the crystal structure. Figure 9 shows a typical XRD θ-2θ curve with an inset rocking curve, published by Tseng *et al.* [17]. Note that the θ-2θ curve has units of 2θ, but the rocking curve has units of θ. As an additional note, the θ values are not always directly comparable as different XRD machines use different wavelength X-Ray sources. For example, Tseng *et al.*'s Philips PW3710 uses CuK, where the Bruker D8 used in this thesis uses Co.

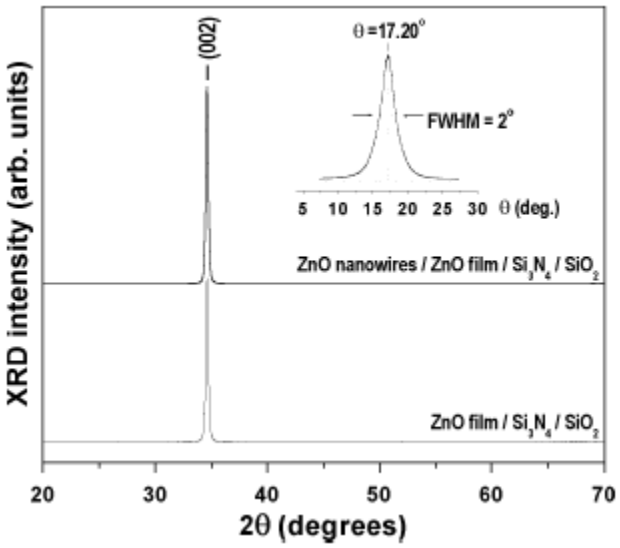

Figure 11: Typical θ-2θ curve for ZnO nanowires published by Tseng *et al*. [17] with inset rocking curve.

2.13 References

[1] Grabar, K.C., et al., *Preparation and characterization of Au colloid monolayers*. Analytical Chemistry, 1995. **67**(4): p. 735-743.

[2] Anderson, D.P., et al., *Chemically-synthesised, atomically-precise gold clusters deposited and activated on titania.* Physical Chemistry Chemical Physics, 2013. **15**(11): p. 3917-3929.

[3] Anderson, D.P., et al., *Chemically synthesised atomically precise gold clusters deposited and activated on titania. Part II.* Physical Chemistry Chemical Physics, 2013. **15**(35): p. 14806-14813.

[4] Weare, W.W., et al., *Improved synthesis of small (dCORE ≈ 1.5 nm) phosphine-stabilized gold nanoparticies [14]*. Journal of the American Chemical Society, 2000. **122**(51): p. 12890-12891.

[5] Wen, F., et al., *Crystal structure, electrochemical and optical properties of [Au 9(PPh3)8](NO3)3.* European Journal of Inorganic Chemistry, 2008(1): p. 106-111.

[6] Tachiki, M., et al. *Advanced pulsed laser deposition method (eclipse angel)*. in *Proceedings of SPIE - The International Society for Optical Engineering*. 1998.

[7] Mendelsberg, R., *Photoluminescence of ZnO Grown by Eclipse Pulsed Laser Deposition*, in *Department of Physics*. 2009, University of Canterbury.

[8] Tawil, S.N.M., et al., *Characterization of InGaGdN layers prepared by molecular beam epitaxy.* Physica Status Solidi - Rapid Research Letters, 2010. **4**(11): p. 308-310.

[9] Natali, F., et al., *Epitaxial growth and properties of GdN, EuN and SmN thin films*. Physica Status Solidi (C) Current Topics in Solid State Physics, 2012. **9**(3-4): p. 605-608.

[10] Xin, H.P. and C.W. Tu, *GaInNAs/GaAs multiple quantum wells grown by gas-source molecular beam epitaxy.* Applied Physics Letters, 1998. **72**(19): p. 2442-2444.

[11] Arthur, J.R., *Molecular beam epitaxy.* Surface Science, 2002. **500**(1-3): p. 189-217.

[12] Heinhold, R., *Hydrogen-related effects in the optical and surface electronic properties of ZnO*, in *Department of Electrical and Computer Engineering*. 2014, University of Canterbury.

[13] Reimer, L., *Scanning electron microscopy : physics of image formation and microanalysis*. 2nd ed. Springer series in optical sciences ; v. 45. 1998, Berlin; New York: Springer.

[14] Heinhold, R., et al., *Mobility of indium on the ZnO(0001) surface.* Applied Physics Letters, 2015. **106**(5).

[15] Heinhold, R., et al., *Influence of polarity and hydroxyl termination on the band bending at ZnO surfaces*. Physical Review B - Condensed Matter and Materials Physics, 2013. **88**(23).

[16] Allen, M.W., et al., *Polarity effects in the optical properties of hydrothermal ZnO.* Applied Physics Letters, 2013. **103**(23).

[17] Tseng, Y.K., et al., *Characterization and Field-Emission Properties of Needle-like Zinc Oxide Nanowires Grown Vertically on Conductive Zinc Oxide Films.* Advanced Functional Materials, 2003. **13**(10): p. 811-814.

Chapter 3: Growth of ZnO Nanowires from In-House Chemically Synthesised Gold Colloids

3.1 Motivation

Zinc oxide nanorods have been grown by catalytic, vapour-liquid-solid (VLS) pulsed laser deposition (PLD) by several groups [1-4]. This growth mechanism, as described in Chapter 1, relies upon the presence of nanoscale droplets of molten metal, most often gold, to catalyse the growth of individual nanorods or nanowires. A common method of applying this catalyst to the substrate is via the dewetting of thin, sputtered films [1, 3, 5, 6]. Heating these films under vacuum causes them to melt and separate into nanodroplets of molten gold. Whilst the sputtering and heating conditions used provide some control over the diameters of the resulting droplets [1], the limits of this control are usually a fairly wide distribution of sizes within a range.

Chemical synthesis of colloidal gold nanoparticles offers much tighter control over nanoparticle sizes, allowing the synthesis of gold nanoparticles and clusters with atomic precision [8]. The size of the catalyst seed droplet is known to be a determining factor in the morphology of a nanorod [5] and the morphology of the rods is important in determining its behaviour in device applications as well as affecting its emission and absorption properties in optical applications [9]. Chemically synthesised colloids have been used with some success for the growth of silicon nanowires [10] and are likely to be equally as effective in controlling the morphology of ZnO nanorods.

In this chapter, the treatment of substrates with gold colloids and the PLD growth of ZnO nanorods are optimised, in order to gain a better control over the morphology of the resulting nanorods.

3.2 Preparation of Au Colloids

13 nm diameter colloidal gold nanoparticles were chemically synthesised using the method described in Chapter 2 Section 1. The substrates used for ZnO nanorod growth were coated by drop coating: i.e. using a pipette to apply drops of the gold colloidal dispersion onto the surface of the substrate. Four drops were applied to each 10 x 10 mm substrate and allowed to evaporate in a clean environment in air until dry. This

method ensured a controlled amount of colloid was applied to each sample as it was reasonable to assume that all the gold nanoparticles in an evaporated droplet would precipitate onto the substrate.

The size of the synthesised colloids was measured using three methods: SEM, TEM and UV-Vis spectroscopy. SEM and TEM yield high quality direct measurements of the sizes of the nanoparticles but are time consuming to perform regularly. UV-Vis produces a known absorption curve for a typical batch of 13 nm colloids and can be performed quickly in the same laboratory as the colloids are prepared without the use of vacuum. While SEM and TEM were performed if the UV-Vis spectrum showed any anomaly, UV-Vis was always performed prior to drop coating in order to quickly confirm the quality of each batch of colloids.

Figure 1: A vial of freshly prepared 13 nm Au nanoparticles showing its characteristic scarlet hue.

The colloids used for the initial growth runs are shown in Figures 1 and 2. The diameters of these colloids were designed to be 13 nm and SEM imaging confirmed a good level of homogeneity around this size. A solution of these colloids appeared a deep crimson red as shown in Figure 1.

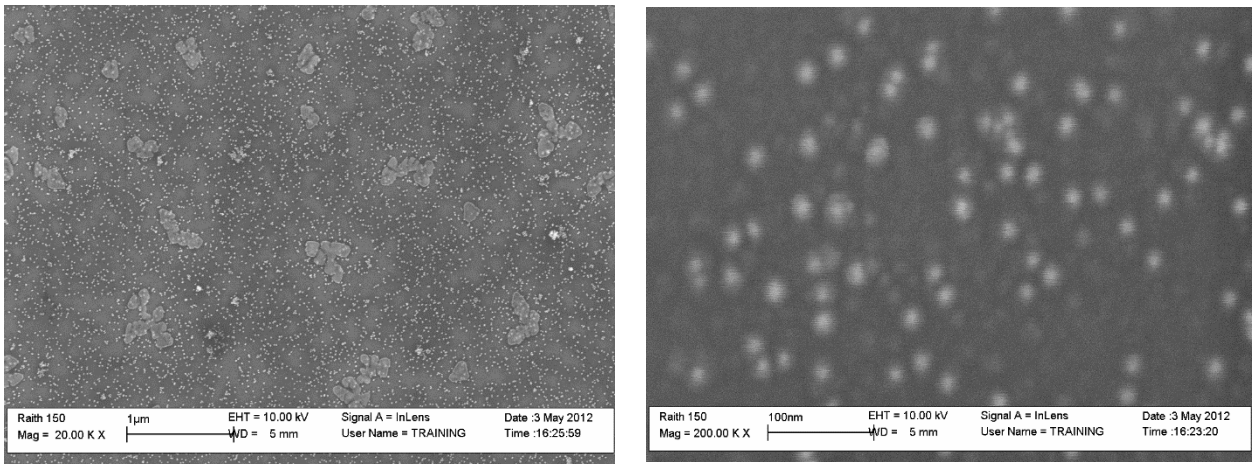

Figure 2: Colloidal gold nanoparticles deposited by drop coating on conductive silicon substrates, imaged at 20,000x (left) and 200,000x (right) magnification. The anticipated size of a single colloid is 13 nm and the particles are seen to be uniform in size. Note that imaging of colloids cannot be done on the sapphire growth substrates as their insulating nature causes too much charging to resolve the tiny nanoparticles.

3.3 Initial Growth Conditions

3.3.1 Target Selection

Previous work by Reuben Mendelsberg [11] in Chapter 4 of his PhD thesis documented the growth of ZnO nanorods by pulsed laser deposition. His work with the UC PLD system laid the foundation for the work conducted in this thesis, however the nanostructures formed were an unintentional disruption in his attempts to grow ZnO thin films using a metallic Zn PLD target. A search of available literature on ZnO nanowire growth by PLD showed that in growths where nanowires were the intended end product, most groups began with a ZnO target, rather than metallic zinc which is the approach adopted in this thesis. Through the course of the work presented in this thesis, in excess of 100 growths were performed and consequently PLD, targets were changed as they became worn down or cracked. The targets used were supplied by Kurt J Lesker (PA, USA) and Testbourne (Basingstoke, UK) and were of 99.99% purity or higher. Even a small amount of use roughens the surface of a PLD target, creating microscale features facing the direction of the laser. These features can then be removed and reformed in successive pulses, which introduces particulate matter into the ablation plume [12]. While the emission of these particulates is deleterious, especially for nanowire growth, the target surface reaches an equilibrium point of roughness, after which it can be considered that the surface exposed to each pulse is of the same roughness. To this end, a target which has been well used is actually more consistent than a fresh one. At the start of every growth, the target was pre-ablated to help ensure that the area of the target struck by the laser was in this pre-roughened condition and also to remove any surface contamination.

3.3.2 Sample Mounting

Another departure from Mendelsberg's work was the use of indium-tin alloy rather than silver paste for mounting the substrates, to provide better thermal contact with the substrate heater. Indium-tin alloy also does not outgas as much and oxidises less when exposed to oxygen at high temperatures than silver paste.

3.3.3 Temperature

ZnO nanowires have been grown by PLD with or without a catalyst and at a range of temperatures. Groups who performed their growths without a catalyst seemed to use a wider range of temperatures as their growths were not dependent on the melting of a metal catalyst. Growth temperatures of 500-800 °C [13, 14], 600 °C [15], 686-901 °C [16], 600 °C [17] have been reported. Catalytic growth was far more likely

to occur within the temperature range of 750-850 °C [2, 3, 18] where typical catalysts would start to melt in the presence of zinc vapour. An exception to the consensus that metal nanoparticles require high temperatures was only found when the nanoparticle were being used as solid growth nuclei rather as liquid catalysts [19]. In this case, the reported growth temperature of 150 °C is more correctly thought of as being non-catalytic, Vapour-Solid (VS) phase growth. Catalytic ZnO nanowires grown by other methods such as MOCVD also tended to use temperatures in the range of 750-900 °C [20]. Given these trends, 750 °C was chosen as a reasonable starting point for the PLD nanowire growth here. The University of Canterbury HV chamber requires external cooling if the temperature is raised higher than this, so 750 °C was a practical choice within both the desired temperature range and the limits of the equipment.

3.3.4 Oxygen Pressure

The choice of oxygen pressure for nanowire growth seemed more variable in the literature as its effects are more closely related to the geometry of the chamber via its effect on the mean free path of ablated material. An HV chamber can operate between atmospheric pressure (10^5 Pa) and 10^{-5} Torr (approx 10^{-3} Pa): eight orders of magnitude. Higher oxygen pressure linearly decrease the mean free path of plasma and ablated material according to the mean free path equation (Equation 1):

$$l = \frac{k_B T}{\sqrt{2}\pi d^2 p} \qquad \textbf{[1]}$$

Where k_B is Boltzmann's constant, T is the absolute temperature in Kelvin, d is the diameter of the gas particle in meters and p is the pressure in Pascals. So in order to achieve the maximum growth rate, ideally we would prefer a higher mean free path and lower oxygen pressure. However, there needs to be enough oxygen present at the sample surface to form ZnO nanowires from the Zn/Au droplets formed by the VLS process. The compromise between these opposing conditions is complex and most likely derived empirically by groups considering their own equipment. Mendelsberg used a pressure of 100 mTorr in the same system, although his target was metallic zinc and he saw scattering and a low mean free path as a desirable trait due to his use of an eclipse plate in his growths

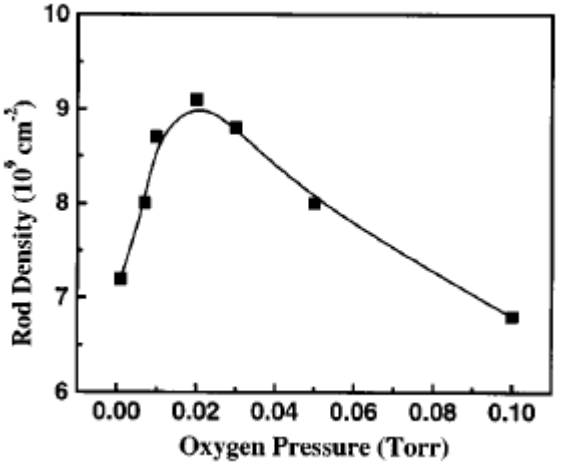

Figure 3: Data produced by Yan *et al*. [12] showing the effect of oxygen pressure on nanorod density.

[11]. Various groups growing from ZnO targets and using gold catalysts used background oxygen pressures of 1 Pa [21] and 0.02 mbar (0.015 Torr) [2]. Yan *et al.* [14] conducted a study growing catalyst free, gallium doped ZnO nanowires and concluded that oxygen pressure had an effect on the density of their nanowires. Their experiments covered the range between 10^{-3} and 10^{-1} Torr, with a maxima of nanorod density at 0.02 Torr as shown in Figure 3. While there could hardly be said to be a consensus from the literature, there were also equipment limitations to consider as described in Chapter 2. With the available setup, it was not possible to accurately measure pressure in the order of 10^{-3} Torr. The lowest pressure available was 1.27×10^{-2} Torr. A value of 5×10^{-2} Torr was selected such that any fluctuations would still be within the limits of measurement.

3.3.5 Laser Fluence

When researching the initial growth parameters, I discovered that the laser fluence is reported a disappointingly low proportion of the time in the literature on PLD nanowire growth, given its importance in determining the growth rate. Even highly cited articles often report only the pulse energy while neglecting to specify the spot size [14]. Those articles which did report laser fluence gave values in the order of 1-4 Jcm^{-2} [2, 21]. Mendelsberg used a fluence of 4 Jcm^{-2} on his Zn metal target and claimed this would also be appropriate for an oxide target [11]. The results of too high fluence in the literature were generally disordered nanorods and nanobelts, where insufficient fluence resulted in film growth [21]. With a proof of concept in mind, the high value of 4 Jcm^{-2} was chosen over a lower value, as overgrowth of nanorods was considered a more desirable and easier to diagnose error state than no nanorod growth at all.

Spot size, laser pulse energy and lens-target distance determine the laser fluence. The Lambda Physik KrF laser used in the PLD system can produce over 300 mJ of energy per pulse, but this is reliant on its internal gas pressure being sufficiently high. For ease of operation and maximum number of growths per fill, it was preferable to select a low pulse energy to minimise any dependence on high laser gas pressure. 100 mJ was selected as an easily maintainable output energy. Using a 750 mm lens to focus the laser, the required spot size was calculated to be 2.5 mm^2 and therefore the requisite lens to target distance followed as 687 mm.

For the initial experiments, the pulse rate and the duration of the growth were chosen fairly arbitrarily. It is usually assumed in the literature that the length of the nanowires is proportional to the growth time [14, 22]. It was also assumed here that the fixed, 25 ns pulses delivered by the laser represent a low enough duty cycle, even at high pulse frequency, that each pulse's ablation plume can be considered independent from the pulses before and after it. Therefore, it could be assumed that the frequency of pulses is not as relevant

as the total number of pulses. A 10 Hz pulse frequency for 60 minutes delivers 36000 pulses and was considered fairly standard for PLD growths in our chamber. This order of magnitude agrees with Lorenz *et al.*'s [4] choice for total pulse count of ZnO nanowire PLD growth.

3.3.6 Substrate

The choice of substrate for the first growth was made by conducting research into the principles of epitaxy, described in Chapter 1. Some groups have determined that the material SCAM ($ScAlMgO_4$ (0001)) presents the best epitaxial surface for growing ZnO [23-25], but this material is expensive to purchase for a long series of growths and the literature proves that it is not necessary in order to grow well aligned ZnO nanowires. Common and relatively inexpensive laboratory substrates include silicon, silicon dioxide, quartz and sapphire. Of these, sapphire has the lowest lattice mismatch with ZnO, with c-plane (0001) sapphire providing a lattice mismatch of 18.4% and it has been commonly used to grow high quality ZnO thin films [26, 27]. The literature concerning ZnO nanowire growth is divided over which plane of sapphire is optimal for nanowire growth. It is well accepted that the preferred growth direction for ZnO nanowires and films is in the (0001) direction, however ZnO does not perfectly align its (0001) direction with that of sapphire at the interface. It has been reported that this results in off-angled nanowires sprouting from the surface at a regular angle representative of the angle between the ZnO (0001) direction and the sapphire (0001) direction [28]. A more popular substrate for ZnO nanowire growth is a-plane (11-20) sapphire [14, 29, 30]. The rationale behind the use of a-plane sapphire is that the vertically growing (0001) c-axis of ZnO aligns with the (11-20) axis of sapphire, with the added advantage that there is no rotational symmetry with this mode of epitaxy so any off axis growth is non-commensurate [28]. This creates a strong tendency for nanowires to grow straight and parallel. Hence, for our initial growth, a-plane sapphire was selected.

3.3.7 Initial Growth Experiment

The first PLD growth was carried out using the conditions described in Table 1. 13 nm Au colloids were applied by drop coating. The gold nanoparticle coated a-plane sapphire sample was fixed to the PLD heater alongside an uncoated a-plane sapphire control sample using indium tin paste. The luminous purple PLD plume was monitored throughout the growth as shown in Figure 4. Table 1 shows the initial conditions for the PLD growth.

Table 1: Initial PLD growth parameters:

Substrate Temperature	750 °C
Oxygen Pressure	$5x10^{-2}$ Torr
Laser Energy	100 mJ
Pulse Frequency	10 Hz
Focussing Lens	750 mm
Lens-Target Distance	687 mm
Spot Size	2.5 mm^2
Laser Fluence	4J cm^{-2}
Growth Duration	60 mins
Total Pulse Count	36000
Substrate	A-plane sapphire

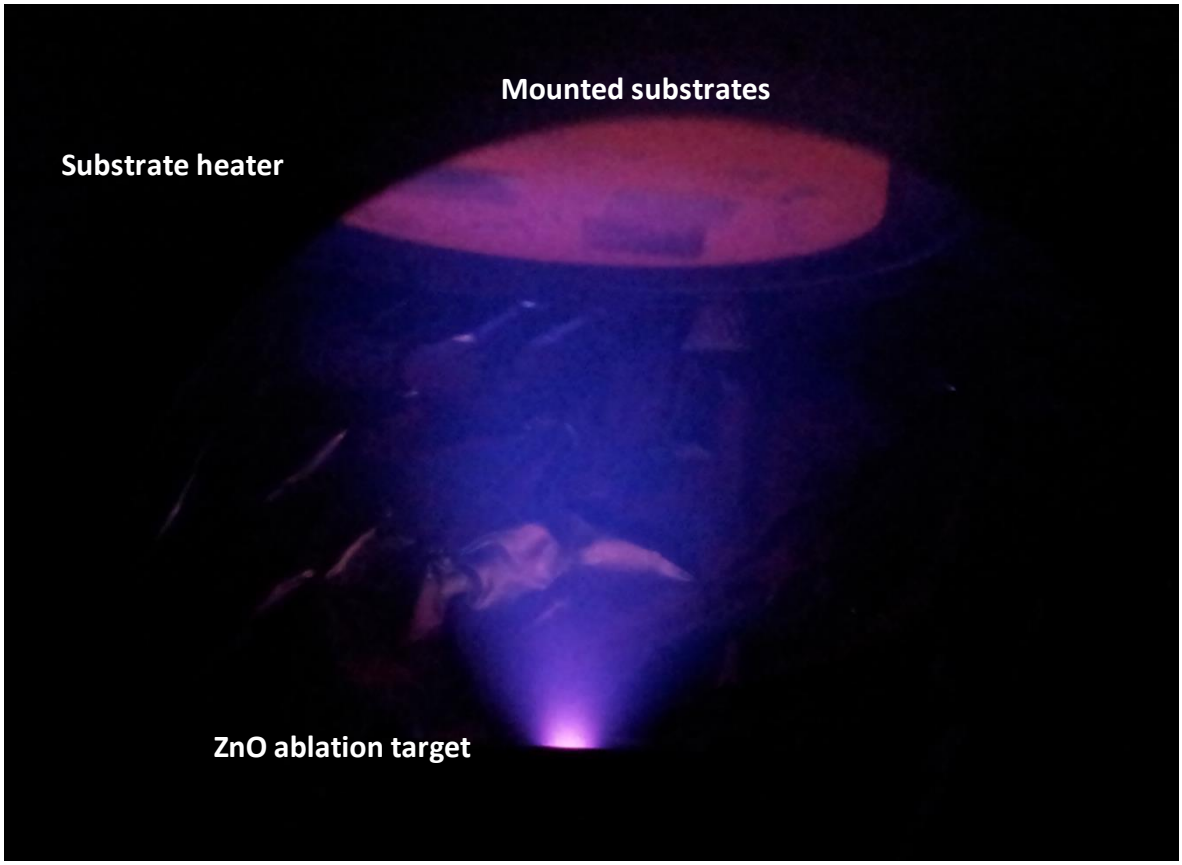

Figure 4: Laser ablation plume from ZnO target (bottom) transferring ablated material to the samples mounted on the glowing substrate heater (top). The separation distance is 6 cm, a factor determined by the geometry of the PLD chamber.

3.4 First Nanorod Growth

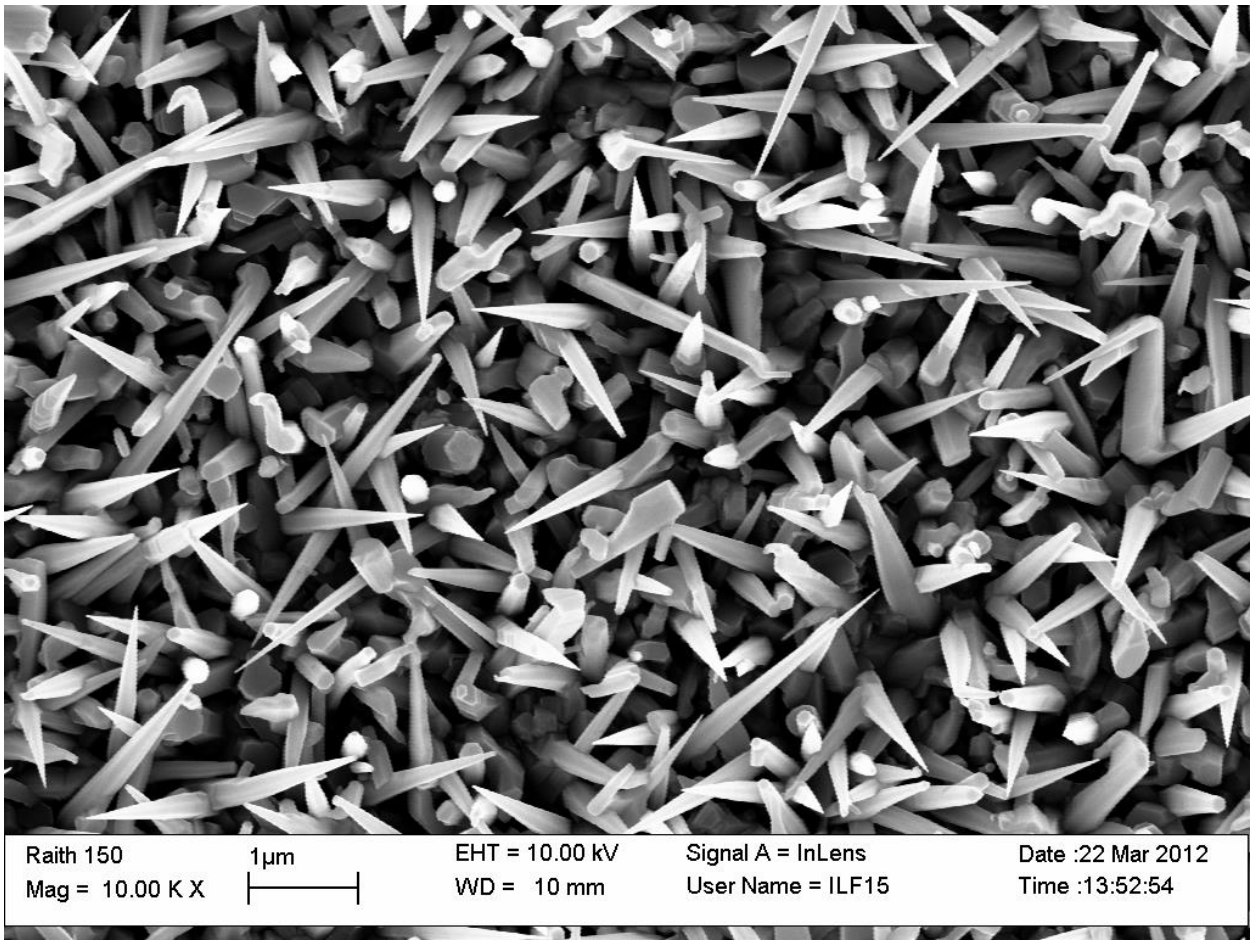

Figure 5: The first growth of ZnO nanorods on a-plane sapphire produced an array of tapering, needle-like rods, interspersed with flat, blade-like nanostructures and flat-tipped rods resembling the needle-rods if they had been sliced off at the tip. (Growth 1)

After the growth, the substrates were imaged using the Raith 150 SEM. ZnO nanostructures grew in a dense but disordered array on all parts of the substrate which had been coated with the Au colloid catalysts. Figure 5 is typical of all areas where Au colloids were present. Uncoated areas produced a thin, rough film and there was an extremely sharp discrimination between areas that had been coated with colloids and areas that had not, as shown in Figure 6 and Figure 7. At the boundary between the colloid coated area and the bare sapphire, a ridge had formed, which was most probably caused by the edge-bead of the colloid-containing water droplet depositing additional debris and is shown in Figure 7. The ZnO nanostructures comprised a mixture of morphologies, including heaxagonal nanorods and flat faced, blade like structures. While some of the nanorods terminated abruptly with flat tops, most of the nanostructures exhibited some degree of tapering, with diameters at the base of as large as 500 nm tapering down to points of 20-50 nm.

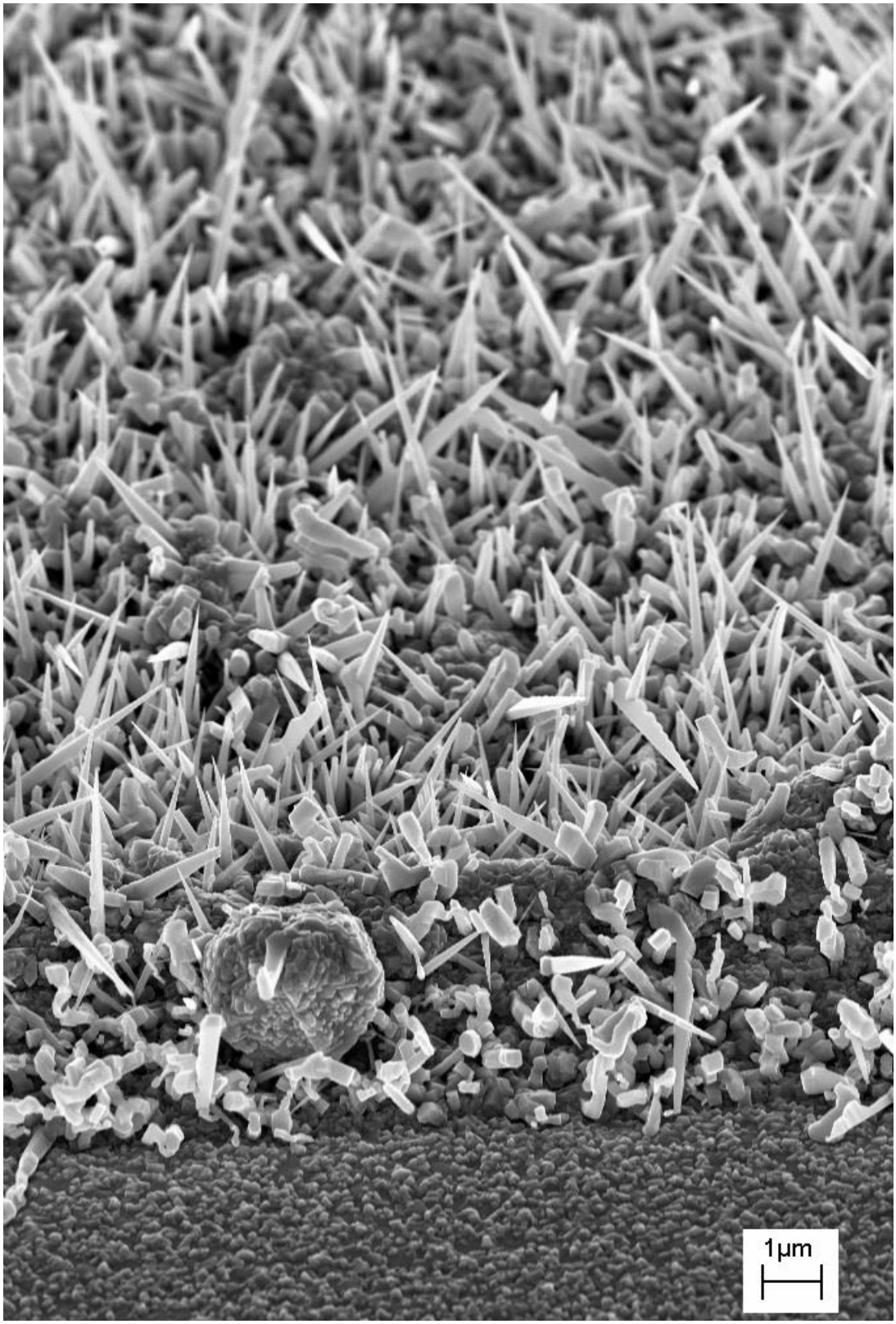

Figure **6** SEM view from a 45° angle showing the contrast between the area at the front with no gold nanoparticles and the area at the back with the nanoparticles. Also note the ridge of material including a large clump of matter, where the edge bead of the colloidal dispersion would have dried up. This region is also shown from above in Figure 7 (Growth 1)

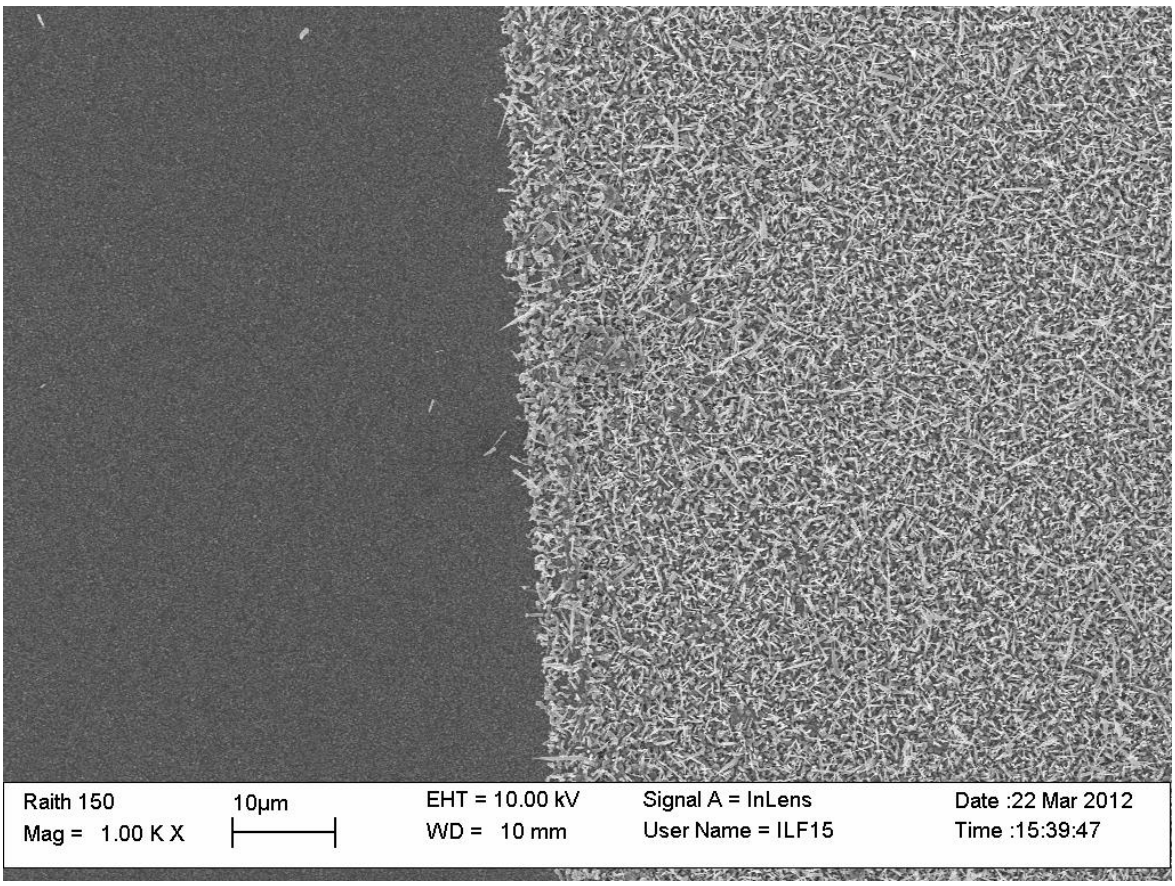

Figure 7: SEM image showing the stark discrimination between the dense array of nanorods grown to the right where gold nanoparticles were present and to the left, where the sapphire substrate was left bare. (Growth 1)

This tapering can be explained by the growth rates in each direction of the ZnO crystal structure: angled growth in the $(01\bar{1}1)$ direction is the second fastest growth direction after the (0001) direction, leading to growth out from the main core of the rod at 35.3° [3].

The bare a-plane sapphire control substrate grown alongside the colloid-treated substrate produced no nanorods at all. A thin film was produced as shown in Figure 8, with a high surface roughness identical in appearance to the colloid-free areas on the colloid-treated substrate (left half of Figure 7).

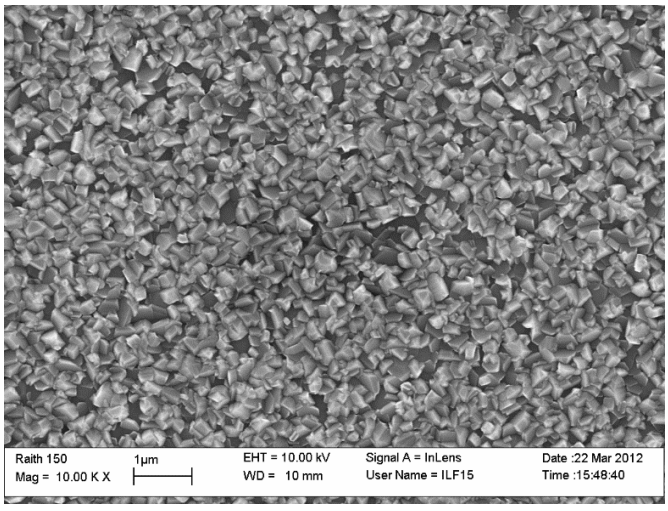

Figure 8: Growth on the colloid-free control sample produced only a rough textured film. (Growth 1)

These results were consistent with many of my expectations. ZnO nanowires grew only in areas where gold nanoparticles were present to catalyse the reaction. Gold capping particles at the tips of nanorods were observed in some of the SEM images as shown in Figure 9 and the extremely sharp discrimination between the dense nanostructures in the gold coated areas and the barren film of uncoated areas only a few microns away confirms that the nanoparticles were indeed acting as catalysts. The lack of alignment in the orientation of the nanorods was surprising. Some of the nanowires seemed to grow normal to the plane of the substrate as expected, but the majority did not. The nanorods that grew off-angle did not seem to grow at any consistent alternative angle. Angled elevation views of the nanorod array showed some rods growing nearly vertical, others at 60°, 45°, 30° and even a few which appeared to be lying nearly flat on the surface of the sample. This inferred that there was little epitaxial relationship between the nanostructures and the sapphire substrate or that if there was, it was not the most significant driving factor behind the nanorod growth direction.

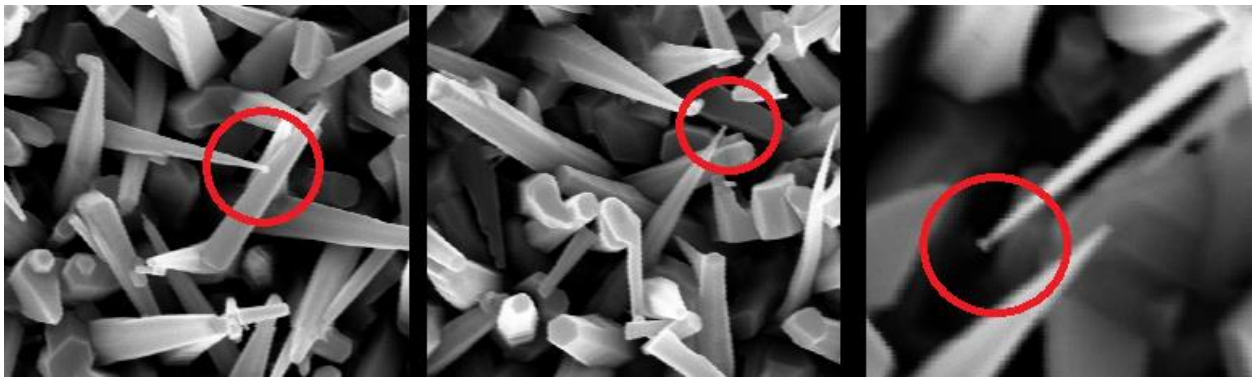

Figure 9: Gold colloid catalysts terminating the nanorods. (Growth 1)

The presence of multiple morphologies in the nanostructure array led to the unexpected conclusion that there were multiple modes of growth taking place in order to produce them. The common understanding of the preferred growth directions of the ZnO crystal predicts, under normal circumstances, a roughly hexagonal structure as observed in many of the nanostructures. This is because there are six m-planes that make up the outward facing walls of the ZnO crystal which grow at equal rates (the coordination tetrahedrons in these directions presenting faces and corners). In order to produce the flat 2D structures observed, at least two of these m-plane faces must have grown significantly slower than the other four. The same is still true if we assume that the rod's width is more correctly attributed to the angled $(01\bar{1}1)$ growth direction: this growth should still be of equal rate in all directions out from the nanorod. Research into other groups' reporting of non-standard nanostructures is complicated by the nomenclature used by each group reporting on a topic. Different groups may refer to the same structure by different names, for example, "nanospirals" vs. "nanosprings" or "nanoflowers" vs. "nanoroses" [31]. The flat faced nanostructures

among the nanorod array resemble knives or blades. "Nanoblades" similar in appearance to the structures that I observed have been reported in materials like tin oxide [32] and indium oxide [33], however these materials have the rutile and bixbyite crystal structures respectively, which have twofold rather than threefold rotational symmetry, so a flat, blade-like structure makes more intuitive sense in such materials than in trifold symmetric wurtzite ZnO.

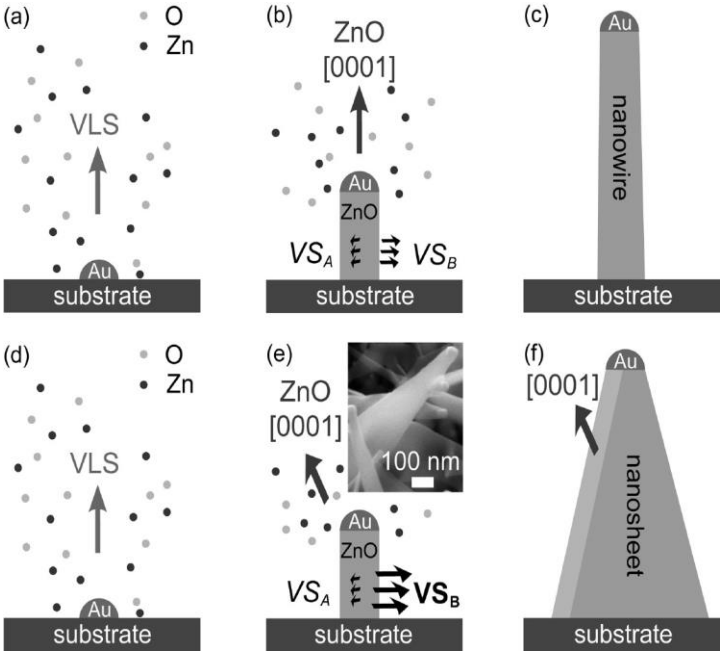

Figure 10: Weigand et al [3] propose this explanation for the presence of "nanosheets". In a) to c), the VLS growth proceeds normally. The growth of sidewalls VS_A and VS_B are equal. If the nanorod begins its growth inclined to the (0001) axis however, VS_B has facets of (0001) in it and grows faster than VS_A, producing a nanosheet.

Weigand *et al.* [3] have referred to similar structures simply as "nanosheets" and examined structure using Transmission Electron Microscopy (TEM). They observed that the nanosheets grew in plane with the expected (0001) growth direction but off angle by between 11-48° as shown by the labelled (0001) direction in Figure 10. This means that two of the nominally m-plane sidewalls of the nanorod include a small proportion of c-plane facets. Because the c-plane facets are preferential growth sites, these two side walls grow faster than the other four. In a normal nanorod, the six m-plane sidewalls to the hexagonal rod grow isotropically, but because two sidewalls incorporate fast growing c-plane facets, the growth becomes anisotropic. Any terracing is smoothed out by preferential deposition into concave spaces. They also report that growth in plane but inclined to the (0001) direction could be caused by high oxygen pressure creating a lower supersaturation point near the edges of the droplet of Zn/Au eutectic. This would cause terracing at the very tip of the growing nanorod rather than monolayer growth and the preference to fill in these terraces would compete with the preferred growth towards the (0001) direction. The fact that this could happen at any point around the edge of a droplet of the eutectic at any time during the growth also explains the kinks in growth angle seen in nanosheets.

Image processing using the SEM micrographs of the nanorods was attempted using the Gatan, Igor and ImageJ software packages in an attempt to produce quantitative data on the size, shape and orientation of the nanorods. Unfortunately these attempts were confounded by the irregularity of the nanorods as viewed by the SEM, as such computerised counting methods are only trivial where the object being counted or

measured has a common pattern in the 2-dimensional image. In this situation, a nanorod could appear as a hexagon if it were aligned perpendicular to the plane of the image, or it could appear as a triangular shape if it were aligned parallel to the plane of the image. Additionally, nanorods of similar shade often overlapped one another, without clear visual separation, which the software struggled to distinguish as multiple objects to be counted, rather than a single, large object. Communication with image processing experts Prof. Milane and Prof. Bones from the Department of Electrical and Computer Engineering recommended that while the task could be accomplished, the amount of work involved would be beyond the scope of this project.

These results produced an important proof of concept that the initial conditions of both the gold colloid treatment and the PLD system were within the ranges required to produce nanorods. However the nanorods were disordered indicating poor epitaxy with the substrate and showed unusual morphologies alongside more conventional nanorod structures.

3.5 Low Temperature and Low Rate Growths

Ms. Ke had previously performed research into growing carbon nanotubes using porous aluminium to control the spacing of gold nanoparticles and reduce aggregation. However, these substrates would melt at our 750 °C growth temperature so a lower temperature would be required to use them in ZnO PLD growth. A lower temperature growth below the temperatures required for VLS would also confirm if the nanorods were growing by the VLS mechanism, using the gold nanoparticles as catalysts, rather than just aggregation sites. If a non-catalytic VS mode was present, nanorods would still grow. A second growth was conducted using the same parameters as the original growth, but with a lowered temperature of 600 °C.

This growth failed to produce any real nanorods as shown in Figure 11. Rough textures and deformations which showed up brightly in the SEM images were observed, indicating that the Au colloids had caused local disturbances in the film growth, but had not been able to catalyse the nanorod growth that had been observed at 750 °C. This result combined with the previous very high level of nanorod growth discrimination observed between gold coated and bare sapphire areas, inferred that the growth mechanism of the nanorods involved the liquefied gold as a catalyst. Unfortunately this ruled out the use of metallic aluminium as a substrate as the temperatures required for VLS would destroy the sample.

Having established that the gold nanoparticles were indeed catalysing the growth of the ZnO nanorods, the largest uncertainty became the lack of order in the nanowire arrays. Assuming that the a-plane sapphire substrate was suitable and that the growth mechanism was indeed VLS, which the previous experiment had indicated, then the disorder must have been related to the growth conditions themselves. A potential cause of the observed disorder was the possibility that the ablated material was arriving too fast at the substrate surface. If supersaturation of the gold-zinc droplets happened too quickly, the atoms might not have sufficient time to arrange themselves in their preferential lattice locations before more material was added. A large surplus of material might also directly allow for the filling of less desirable lattice locations.

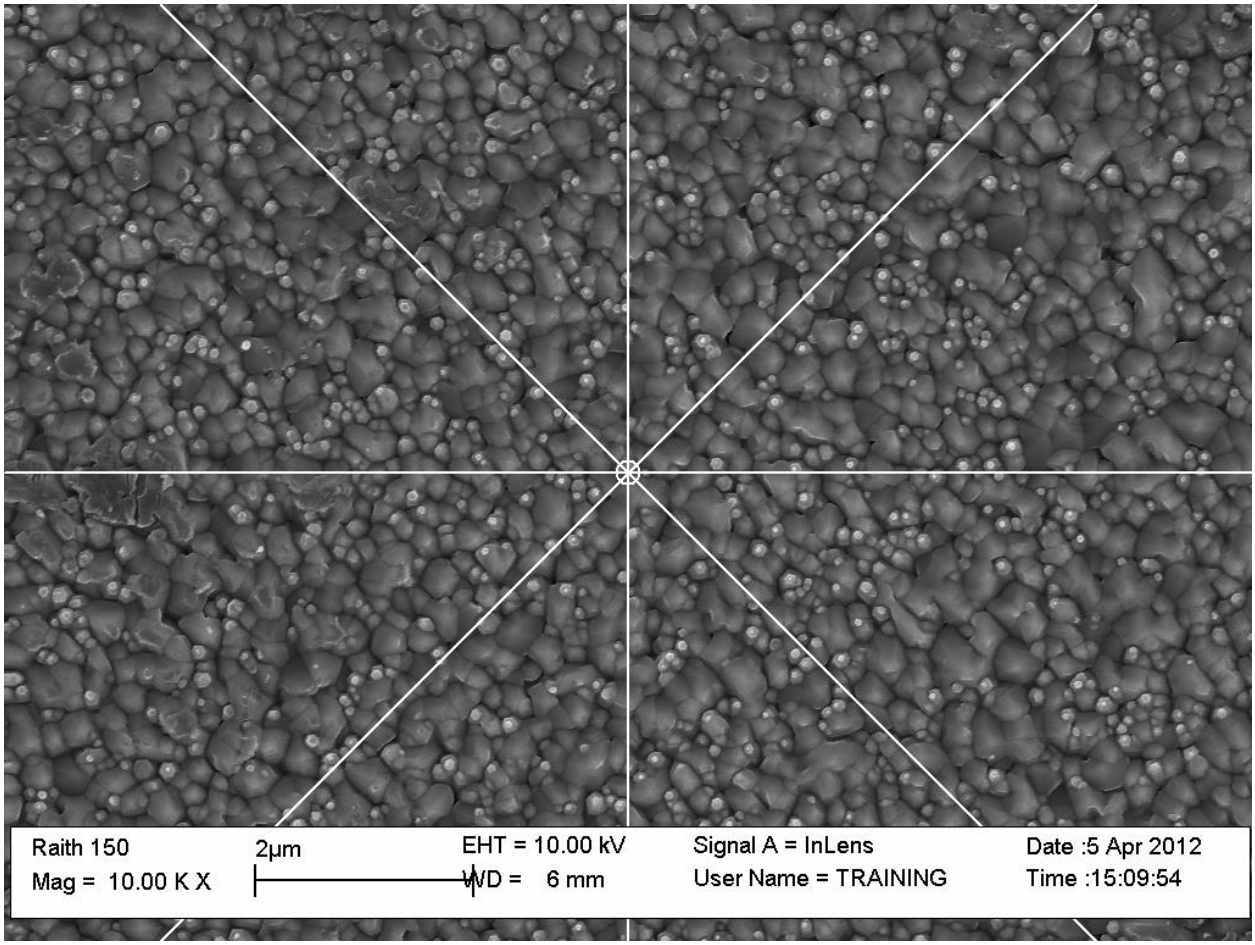

Figure 11: An attempted growth at a temperature of 600 °C, but with all other variables held constant. While there were clearly nucleation sites forming, potentially due to the gold nanoparticles, no actual nanorods were able to grow. (Growth 2)

The simplest way to test this hypothesis was to lower the laser fluence, which is easily accomplished by lowering the pulse energy. The minimum pulse energy available using the KrF laser was 68 mJ, so 70 mJ was selected as a round number close to this equipment limit. A ZnO PLD growth was conducted holding all other parameters constant.

The largest nanorods produced by this lower fluence growth were of similar morphology and shape distribution to the ones in the original growth, with tapered rods as long as 2-3 µm as shown in Figure 12. No visible increase in the order of the rods was discernible and in addition to the neatly hexagonal rods expected, the flat edged "nanosheet" structures described in Figure 10 were also visible. In addition, a dense layer of stubby, flat topped nanorod "stumps" was observed between the larger rods. These areas were unlike the areas of the chip that was not coated with the colloid solution, which variously produced either rough, mosaic-like films or relatively smooth films punctuated by irregularly shaped, rock-like defects as shown in Figure 13.

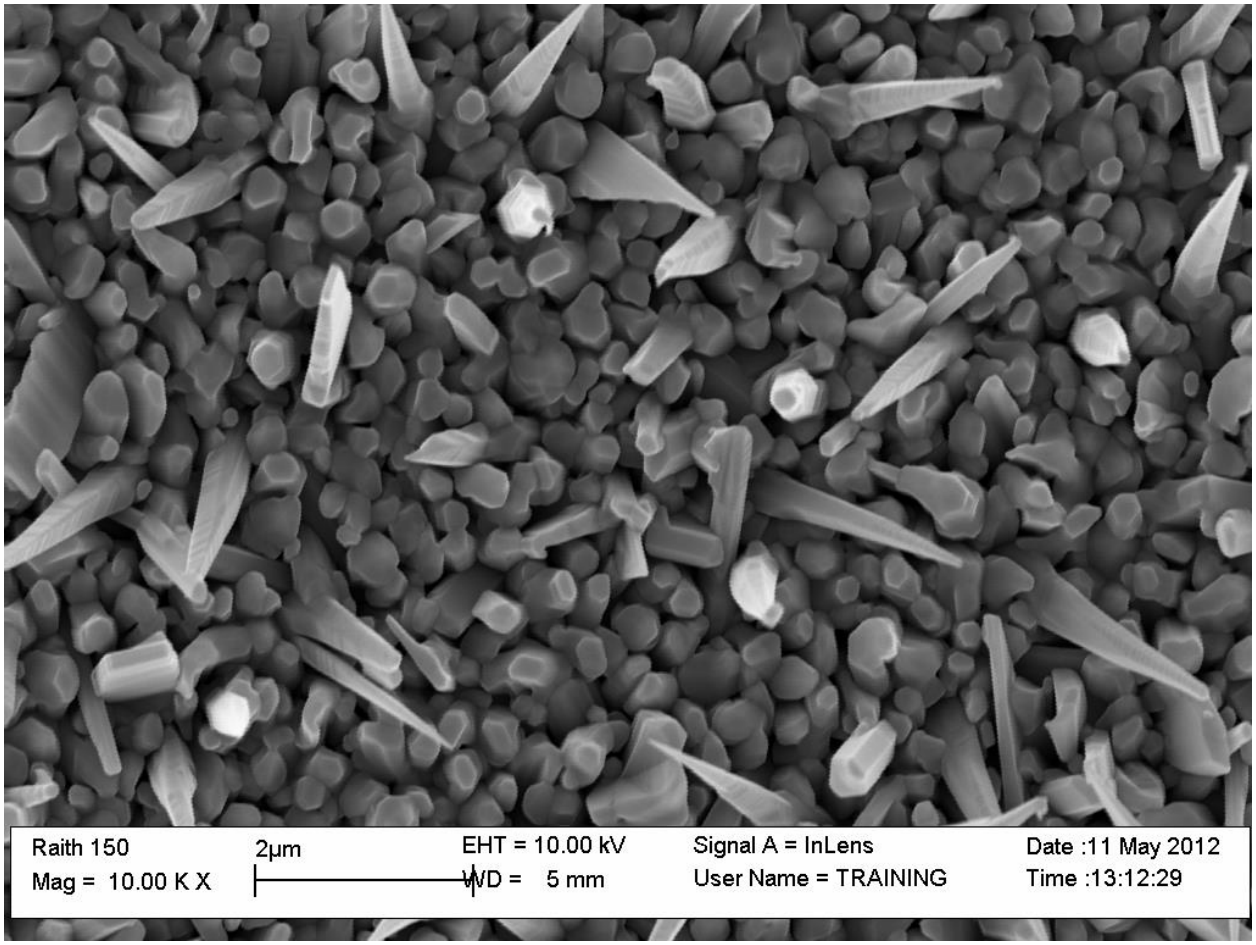

Figure 12: Nanorod growth conducted using a 70 mJ laser energy and hence a fluence of 2.8 J/cm^2. (Growth 6)

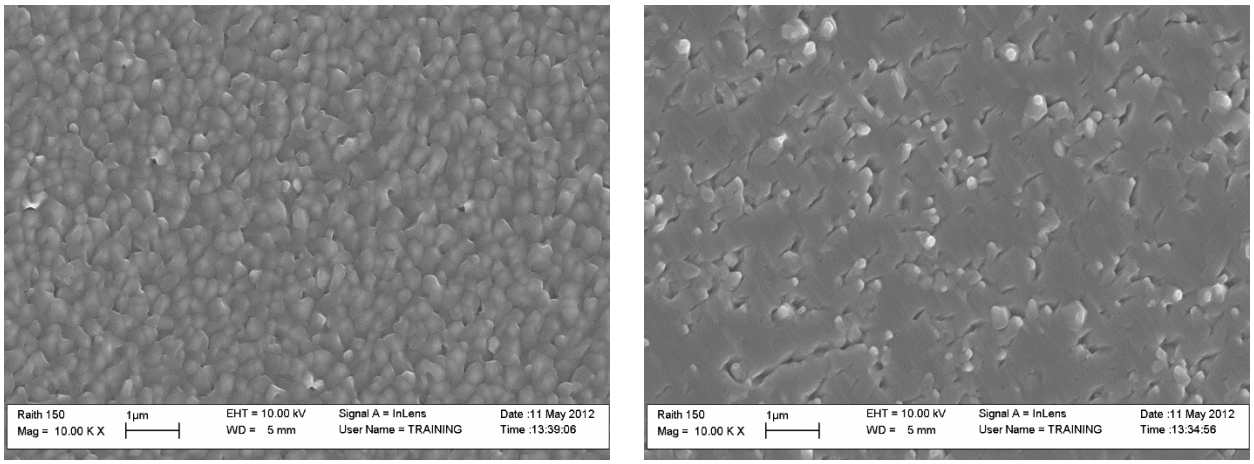

Figure 13: Areas outside the droplets of gold colloid took on one of two morphologies. A "rocky", nanotextured mosaic film (left) or a very smooth film with crevasse-like defects (right). (Growth 6)

Compared to the uncoated area, the stumpy rods seemed unlikely to be caused by a lack of available gold nanoparticles, but perhaps by some factor stunting the growth of a catalysed nanorod. Significantly, the fact that nanorods were still able to form and that their morphologies were similar to those grown at a higher fluence addressed a potential source of serious error in the growth equipment related to the laser window, which has been detailed in the experimental method. The window through which the laser passes to enter the vacuum chamber had been measured to have varied in transmittance between several growths, ranging from as low as 51% to its factory specified value of 90%. This seemingly very large variance was not mentioned in the work of Mendelsberg and was mentioned in passing by Dr. Farrell [34] although he concedes that even with his attempts to compensate for this error, he believes it still contributes a variation in fluence of as much as +/-20%. After this 70 mJ pulse energy growth, this specific laser window was found by Dr Farrell to have a very low transmittance of 51% and was replaced. Testing and replacing the window required a significant expenditure of effort on behalf of Dr Farrell and involved partial disassembly of the chamber, so it was unreasonable to test regularly. In this instance, I have a recorded number for the transmittance immediately after my growth, but knowing that this was a moment of lowest transmittance is useful. The fact that nanorods of equal size and morphology to those from the initial ZnO nanorod growth were able to form with a laser energy of 70 mJ, further reduced by a poor laser window transmittance suggests that even the lowest available laser fluence was no inhibitor to the growth of the nanorods. These growths laid the groundwork for this study of ZnO nanorods by showing that nanorods could be grown using our setup and that the Au colloids were indeed catalysing the growth of the nanorods by VLS.

3.6 Eclipse PLD

Eclipse PLD is a variant of the conventional PLD method which involves the use of an eclipse plate placed between the target and the substrate [11]. The purpose of the eclipse plate is to block the direct line between the target and substrate. The rapid superheating effect of the laser on the target can be quite explosive as the target rapidly heats up and expands and this can displace large macroparticles around the laser spot. These larger particles of ablated material ejected from the target travel directly on a ballistic trajectory to the substrate and are relatively unaffected by diffusion with the processing gas which affects smaller particles. These macro particles are undesirable as they are solid rather than gaseous and so are liable to form grains and produce defects in the material being grown. It has been shown that in the growth of MgO nanowires, an increased particle size in the ablation plume has a deleterious effect on the VLS process occurring at the substrate [35].

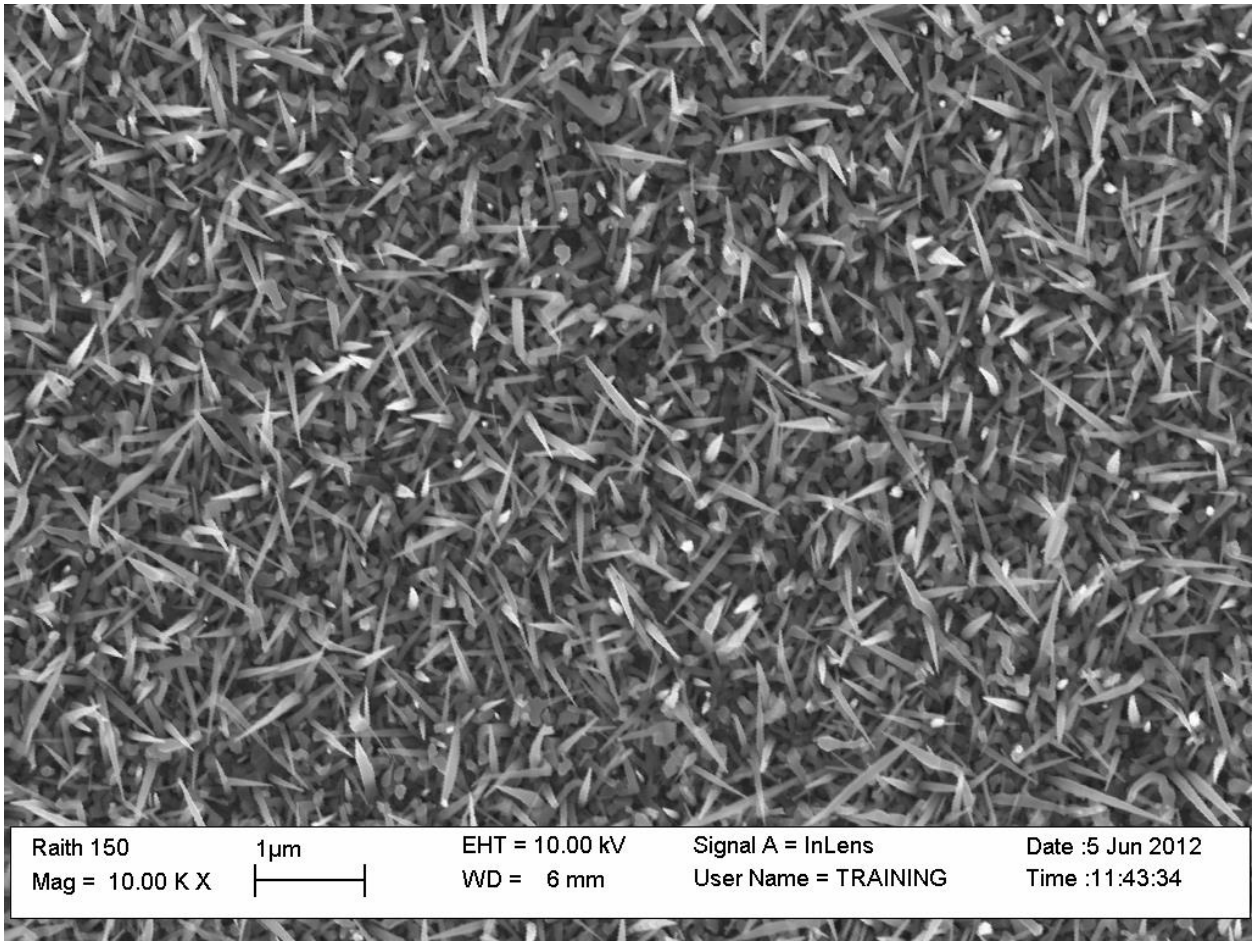

Figure 14: Nanorods grown by EPLD for 2 hours. Nanorod density was greatly enhanced by use of the eclipse plate. (Growth 9)

Placing an eclipse plate between the target and the substrate blocks solid macroparticles from travelling directly to the substrate, but allows vapour to diffuse around the edges of the plate and coalesce on the substrate. In film growth, this predictably lowers the deposition rate (as vapour which travels in a straight line is also deflected), but improves the quality of the resulting films [7]. A flat, square plate is most commonly used, although Mendelsberg also investigated various types of eclipse plate in his work including a spiral shaped wire [11]. The best material produced in his work was grown using the standard square plate. Consequently a new ZnO nanorod growth was conducted using the original growth parameters (see Table 1), but with a 10 mm x 10 mm copper eclipse plate placed 2 cm from the middle of the sample and 4 cm from the target. The eclipse plate was placed at the same height as the laser spot and substrate. To compensate for the predicted loss of deposition rate, the growth time was extended to 2 hours from the original time of 1 hour.

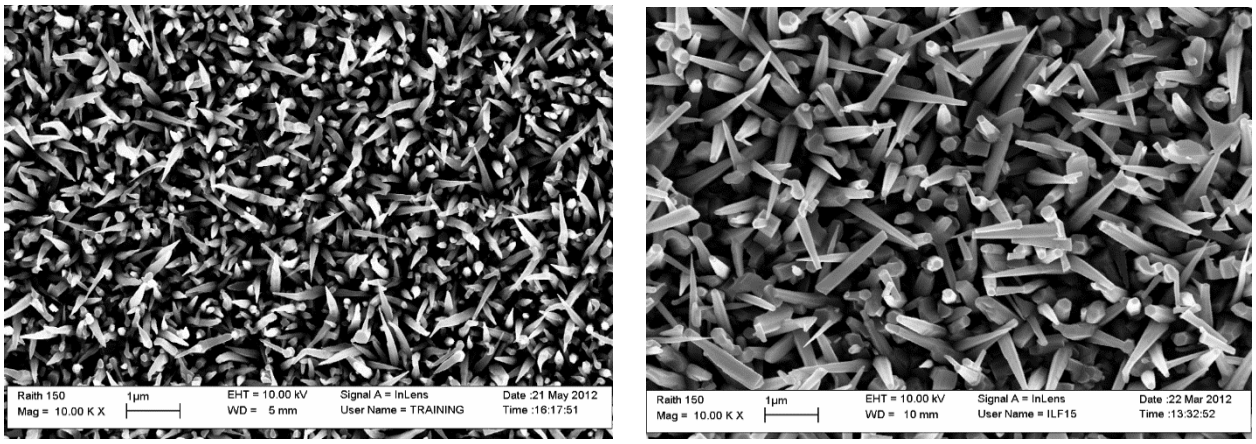

Figure 15: Comparison between EPLD using a square plate placed 2 cm from the substrate (Growth 9) (left) and standard PLD growth (Growth 1) (right). Approximate nanorod counts for each image are 651 for EPLD, 195 for PLD.

The nanorods grown using eclipse PLD were noticeably thinner and denser than those produced by conventional PLD. An approximate tally yields a density increase of 330% with 651 nanorods counted in Figure 15 (left) showing EPLD Growth 19, compared to 195 in PLD Growth 1 (See Appendix). Even with the additional hour of growth time, the resulting nanorods were still shorter than the rods grown without the eclipse plate, with lengths ranging up to about 1.5 µm. A follow up EPLD growth using the original one hour growth time was performed and the resulting nanorods shown in Figure 16. The increased density and thinness of the nanorods produce was found to be reproducible and the density of nanorods was much the same between the long and the short EPLD growth with 745 nanorods counted in Growth 10 (Figure 16). It is interesting to note that the correlation between nanorod length and deposition time reported by other groups was not observed between these two growths. The one hour growth produced nanorods of a very

similar length to the two hour growth, with an approximate average length of a fully formed rod of just under 1 µm in both cases.

In these EPLD growths, while there were fewer of the sheet like "nanoblades" found in conventional PLD growths, there were quite a few nanorods which appeared to bend or change direction midway along their length, sometimes with more than one bend in a single rod. Although these distortions were observed in each growth, the exact frequency of these occurrences was inconsistent. For example, approximately 10% of nanorods grown in Growth 9 shown in Figure 15 (left) show at least one deflection, but in Growth 10 shown in Figure 16, the rate of occurrence is approximately to 2%. The causes for this are unknown as one would assume that a nanorod growing upwards by the VLS process would essentially be growing upon itself in a homoepitaxial arrangement: each new layer of ZnO being added on top of the one immediately below it. A possible explanation for this could be that a large defect has occurred at the bend, causing the planes of the crystal at that point along the nanorod to reorient. This would change the (0001) direction relative to the rest of the nanorod and cause the growth to continue in that direction instead. Defects can be

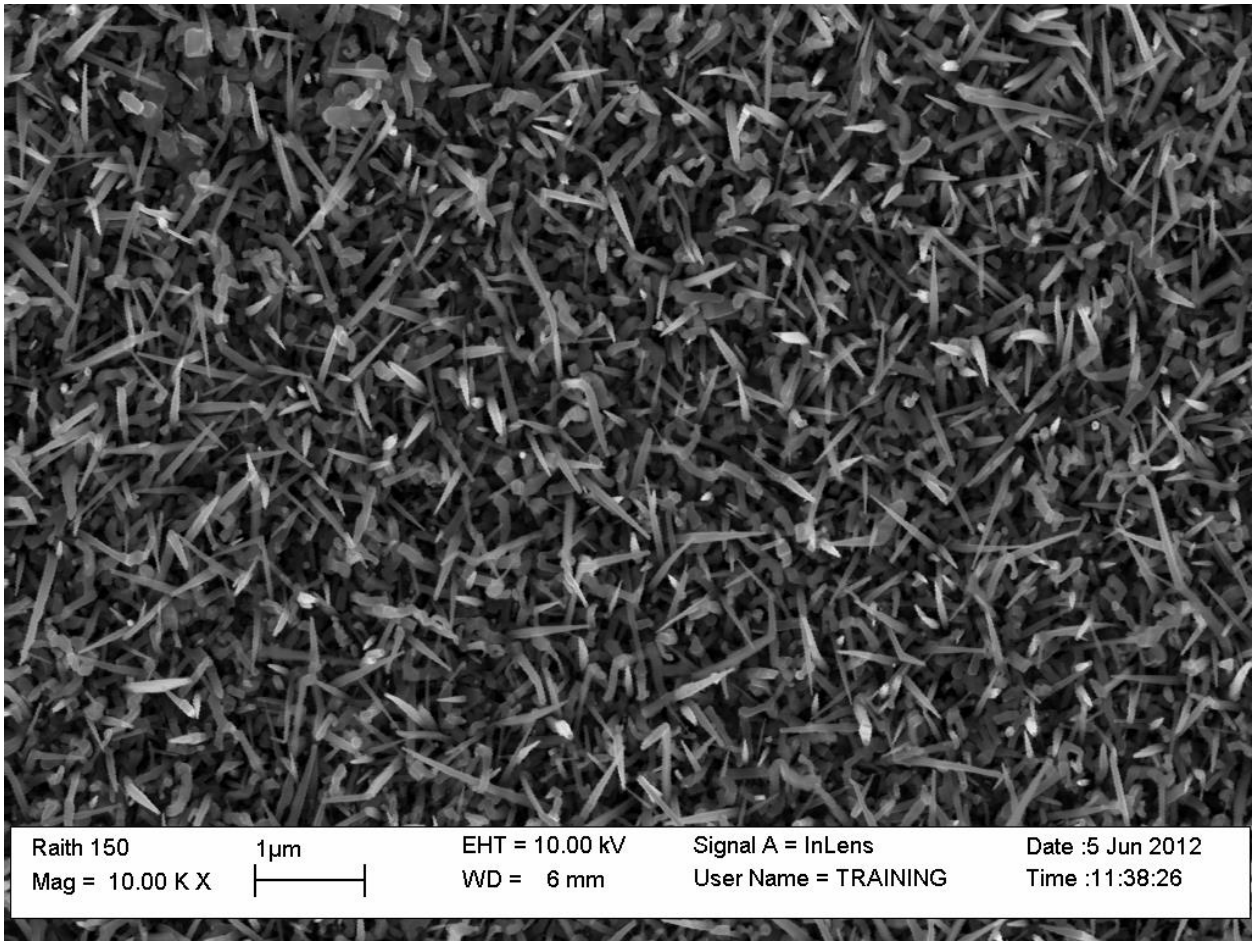

Figure 16: Growth conducted using the EPLD method and the standard 60 minute growth time. The number of rods is approximately 745 in this 10,000x magnification image. (Growth 10)

caused by many possible factors including contamination in the growth environment or the introduction of macroparticles from the target. Meticulous cleaning was done in order to minimise or eliminate contamination and the eclipse plate was employed primarily to reduce the amount of macroparticles reaching the sample. Another possible explanation was strain in the crystal. If the nanorods were strained due to a poor match to the substrate, then it is possible that they would seek to dissipate this strain through geometric transformations such as rotations. However, this explanation does not explain why the bending nanorods were not observed in the initial growths with the same substrate but without the eclipse plate.

Despite these disruptions to the morphologies of the nanorods, the EPLD technique was seen as a success. The threefold increase in nanorod density as well as the associated narrowing of the rods was more in keeping with expectations for rods grown from the high density of gold colloids deposited on the sample. Based on these results, it was decided that the standard growth parameters would be modified to use the eclipse plate at the position used in these exploratory EPLD growths (2 cm from the substrate, 4 cm from the target).

3.7 Sapphire substrate planes

An experiment was designed to test if the substrate was the cause of the disordered nanorod growth. The question of which plane of sapphire substrate was most conducive to ZnO nanorod growth had not been conclusively answered by reviewing the literature. While a-plane sapphire has been used by some groups [14, 29, 30], other groups have used c-plane sapphire with similarly favourable results [1, 36, 37]. Two ZnO EPLD growths were performed, using first c-plane sapphire and then m-plane and r-plane sapphire.

The EPLD growth on c-plane sapphire (shown in Figure 17) produced nanorods of similar size and morphology to those produced by the EPLD growth on a-plane sapphire. The nanorods were small and very densely packed with more of the blade-like nanosheet structures than the twisted rods that were observed in the initial EPLD growths on a-plane sapphire. While there was still a large degree of disorder, there seemed to be a greater proportion of vertically aligned nanorods. This suggested that the ZnO nanorods formed a better epitaxial relationship with the c-axis sapphire than they did to the a-plane sapphire.

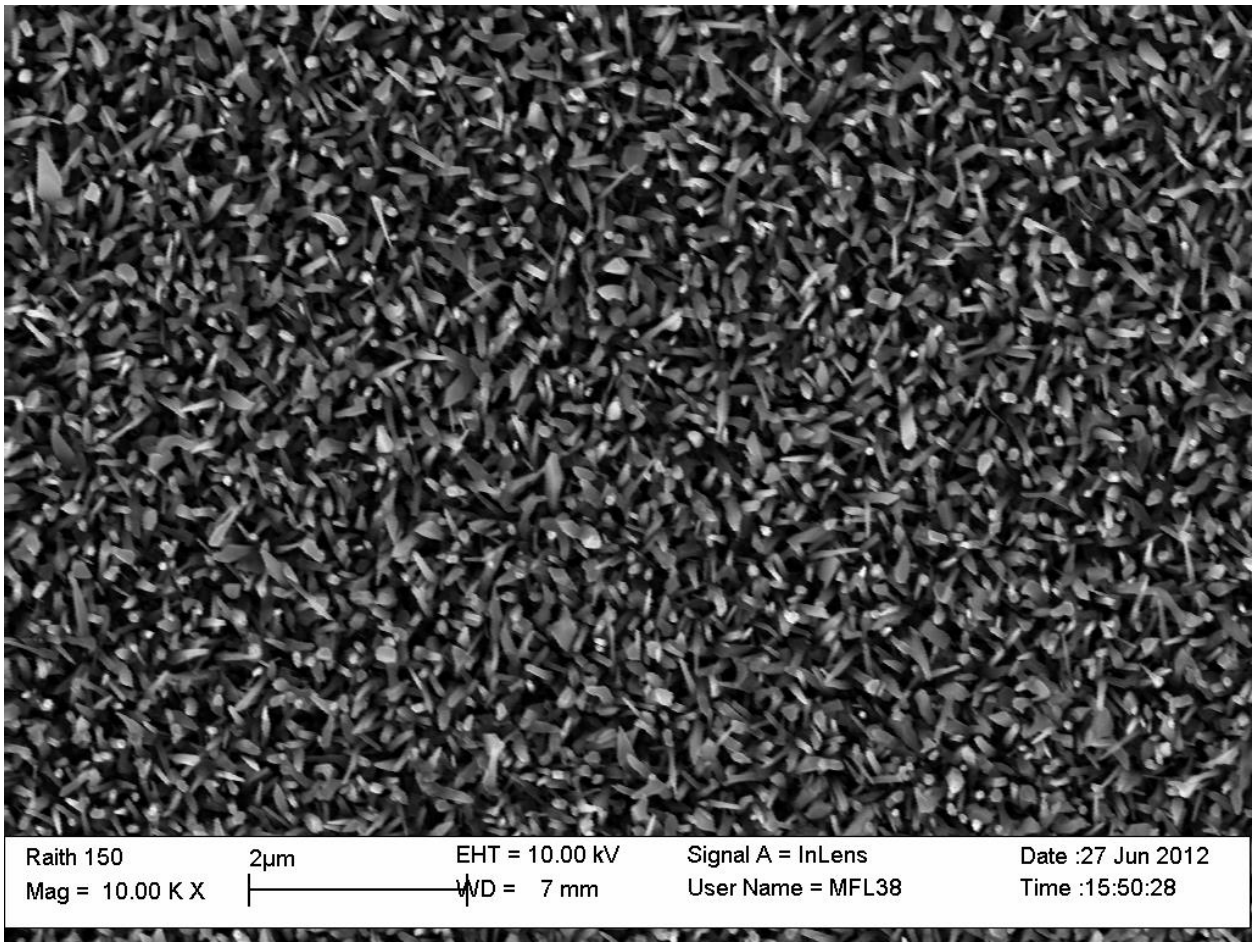

Figure 17: ZnO nanorods grown on C-axis sapphire. There are over 1000 nanorods in this image taken at the same 10,000x resolution as previous growths. Additionally, there appear to be a larger proportion of vertical rods present. (Growth 12)

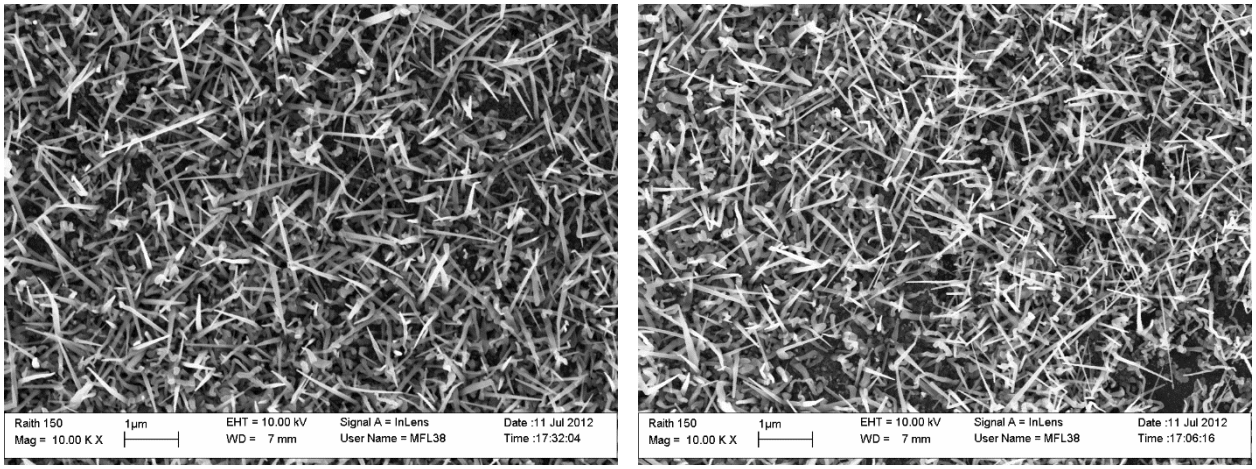

Figure 18: Growths on M-plane (left) and R-plane (right) sapphire. (Growths 15 and 16)

Nanorods grown on m- and r-plane sapphire had very high aspect ratios, producing tip diameters as small as 35 nm, with lengths of up to 3 µm. Disordered alignment prevailed almost completely, with no apparent preferential direction and many of the rods appearing to bend or change their growth direction partway along their lengths several times. Although the results were not reproducible in later attempts to recreate the same conditions, these two growths were both in line with expectation when using a substrate with a completely mismatched orientation. VLS growth appeared to be occurring but the direction of the nanorods appeared random, indicating little or no epitaxial relationship. It was also observed that the growth on the m-plane sapphire substrate also produced short nanorods outside the areas coated with gold colloids as shown in Figure 19. This did not occur in any other growth conducted in the course of this thesis.

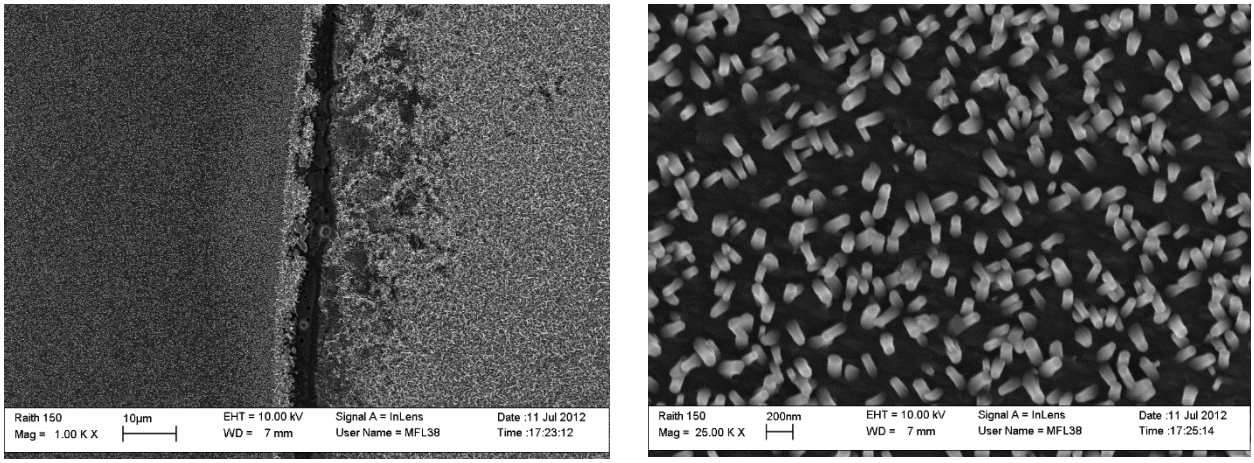

Figure 19: Nanorods grown outside the areas coated with gold on M-plane sapphire. Left: Low magnification view showing the boundary area and the difference between long, thin rods in the gold coated area and short stubby rods grown on bare sapphire. Right: High magnification view of short stubby nanorods grown without catalyst. (Growth 15)

Nanorods grown in areas of m-plane sapphire without gold colloids were short and squat, with a roughly hexagonal morphology. They did not appear to exhibit any tapering and grew in a seemingly random order, although with perhaps some preference to growing at approximately 60° from the substrate. Despite being in the chamber at the same time, the r-plane substrate did not produce any nanorods on the bare areas, so clearly this vapour solid phase growth was facilitated in some way by the m-plane substrate. A report in the literature by Moriyama and Fujita [38] reported unintentional ZnO nanorod growth on m-plane sapphire occurring during an attempted ZnO film growth, suggesting that untreated m-plane sapphire has a natural tendency to produce ZnO nanorods.

ZnO nanorods grown on m-plane sapphire by catalytic vapour transport have been reported by Ng *et al.* [39] who suggested that the incommensurate epitaxy between the ZnO (0001) plane and the sapphire (100)

plane would be overcome by a 30° tilt in the nanorods. Their experiment showed a relatively homogenous array of nanorods growing at a 60° angle from the substrate. While the gold catalysed areas of nanorod growth on our m-plane substrate did not demonstrate any regularity, the nanorods which appeared on the bare sapphire do seem to agree with this prediction.

Zúñiga-Pérez *et al.* [16] reported non-catalytic PLD growth of ZnO nanorods on m-plane sapphire at similar temperatures but much higher pressures (between 50-300 mbar) and produced similar results to Ng *et al.*'s [39] vapour transport grown nanorods. They observed that the presence of nanorods on m-plane sapphire was less dependent on temperature than on a- and c-plane sapphire. Nanorod growth occurred on bare m-sapphire at all temperatures between 686 °C and 901 °C, but that growth rate increased with temperature. The 750 °C growth temperature used here is at the cooler end of Ng *et al.*'s temperature range and our 6 cm eclipsed target-substrate distance was much greater than their unshadowed target-substrate distance of 2.5 cm, so it is consistent with their observations that short nanorods were observed growing on bare m-plane sapphire on our sample.

R-plane sapphire seems to have attracted very little attention in the literature, with only a few groups setting out to grow ZnO nanorods on it [37, 40]. Results from these groups infer that the substrate is not very suitable for nanorod growth, only producing inconsistent, block-shaped nanorods [37] as the preferred c-axis growth direction for ZnO is parallel to the surface of the substrate and therefore epitaxy is unlikely. This does however make it of interest for growing high smoothness films [38].

3.8 Dip Coating

The lack of good order and vertical alignment in the previous growths, despite substantial literature proof that ordered, vertical alignment of ZnO nanorods was attainable with the substrates being used, led to the conclusion that the method of colloid catalyst application needed improvement. Nanorod coverage over an area drop-coated with gold colloids was irregular and areas such as the edge bead of the droplets were predictably different to areas in the centre of the droplet. If the coating of the sample was not uniform, it would be unreasonable to expect uniform nanorod growth. In addition, drop coating was likely to precipitate any other carbonaceous chemicals or salts present in the colloid solution onto the substrate. 100% transfer of nanoparticles also means 100% transfer of any contaminants as well. Contamination of the surface could interpose itself between the Au colloids and the substrate, leading to very poor epitaxy. If this amount of contaminant varied, then it might be expected that rods would have varying degrees of alignment, determined by how much of their base was actually formed on clean sapphire. The result would be disorder and a high degree of randomness, consistent with our observations.

An alternative method of coating is dip coating, where the substrate is immersed in the colloid solution for a measured amount of time before being taken out and rinsed with deionised water. Colloids that become electrostatically attracted to the substrate will accumulate proportional to the immersion time. The follow-up rinse with high purity deionised water washes away larger organic molecules, resulting in a more uniform coverage of gold nanoparticles across the surface of the substrate.

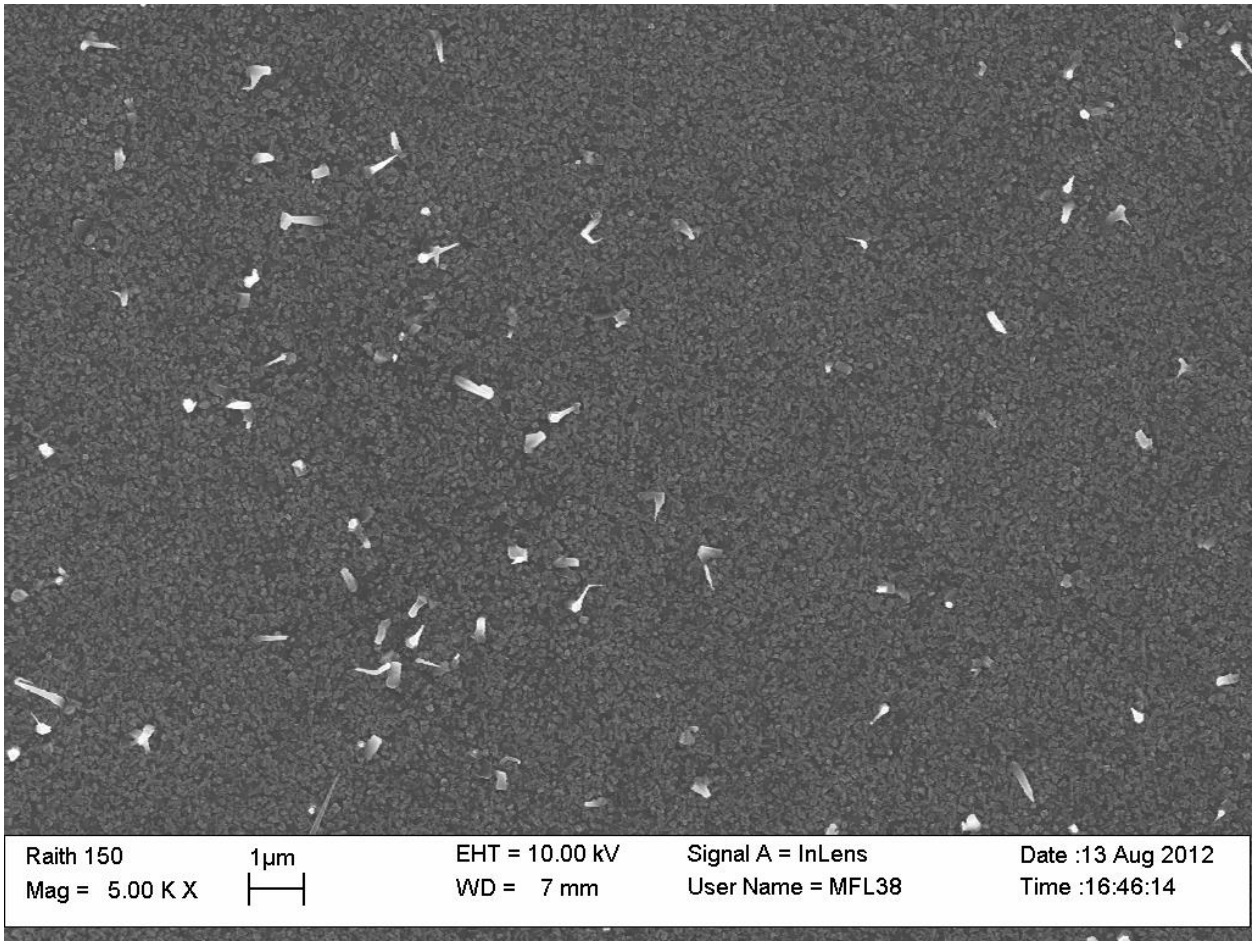

Figure 20: ZnO nanorods grown on C-Plane sapphire dip coated with gold colloids. The density of nanorods is extremely sparse, with rough film in between, indicating growth only occurred where gold was present. (Growth 20)

The potential issue with dip coating is that since it relies on incidental attraction to attach the gold colloids to the substrate, a much lower density of coverage would be expected. This is not necessarily as a bad thing as if nanorods are allowed to grow sufficiently far from their nearest neighbours, there would be no interference between rods growing near each other. It was reasonable to assume that, much like drop coating, the density of the colloids attached to the substrate would also be a function of the concentration of the colloids in solution. This could be easily adjusted by dilution, so an optimal concentration would need to be found.

A dip coated sample prepared using 0.25 mmol/l gold colloid was grown using our standard EPLD conditions, using c-plane sapphire substrates. A normal drop coated sample was placed alongside the dip coated one in order to control for any variation between growths. Typical results of this experiment are shown in Figure 20. The control sample produced ZnO nanorods typical of our previous c-plane growths (see Figure 17). The growth of nanorods was extremely sparse, indicating a poor coverage of the substrate with colloids, although this was not entirely unexpected. Unfortunately, the nanorods grown in their widely spaced locations were not ordered or well aligned and displayed a similar degree of random disorder and bending to any of the previous samples. While a few rods did appear to grow approximately vertically, the ratio of vertical nanorods was no different to that seen on any other denser growth.

Although this method did not correct the issue of disorder and random growth direction, it did eliminate the edge beads associated with drop coating and it reaffirmed our assumption that our growth mode was catalytic (as the sparseness of the nanorods reflected the sparseness of the colloids). This growth clearly showed that the nanorod density could be controlled by the density of the Au colloids. This conclusion was significant in that it validated the possibility of using patterning to apply Au colloids in different densities to different areas of a single substrate in order to control the density of nanorods in each area.

Additional increases in concentration were also tried. Our initial dip coated sample was coated with Au colloids of 0.25 mmol/l concentration. This concentration was doubled to 0.5 mmol/l and then doubled again to 1 mmol/l. However growths conducted with substrates coated with these higher concentrations showed little difference in nanorod growth to the original 0.25 mmol/l colloid coated substrate. Nanorod growth was extremely sparse and still disordered. The adhesion rate had effectively saturated and additional concentration was not resulting in more nanoparticles arriving at the surface. A method was needed to radically improve the gold colloid adhesion to the sample.

3.9 Nanosphere Lithography

While improvements to the dip coating technique were being considered, an idea was explored to create a patterned array of nanoscale gold islands using a special solution of polystyrene beads which adhere to the substrate surface. This commercial product was designed to be deposited onto a substrate, effectively masking it with a monolayer of spheres. The sample could then be sputtered with metal, in our case the gold catalyst. After deposition, exposure to acetone would dissolve the beads, leaving a repeating pattern of metal islands deposited on the c-plane sapphire. The beads could be purchased commercially, pre-deposited on substrates from Sigma Aldritch, MO, USA and a group in the literature had used this "nanosphere lithography" to pattern an ordered array of silicon nanorods using molecular beam epitaxy [41]. Figure 21 shows the beads after being sputter coated with 10 nm of Au. It can be noted that the beads form a good approximation to a monolayer, with only a few irregularities in size and defects in the regular 2D lattice. This was expected to produce small sites of gold on the substrate, essentially triangular, with edges of approximately 100 nm and arranged in a roughly hexagonal pattern.

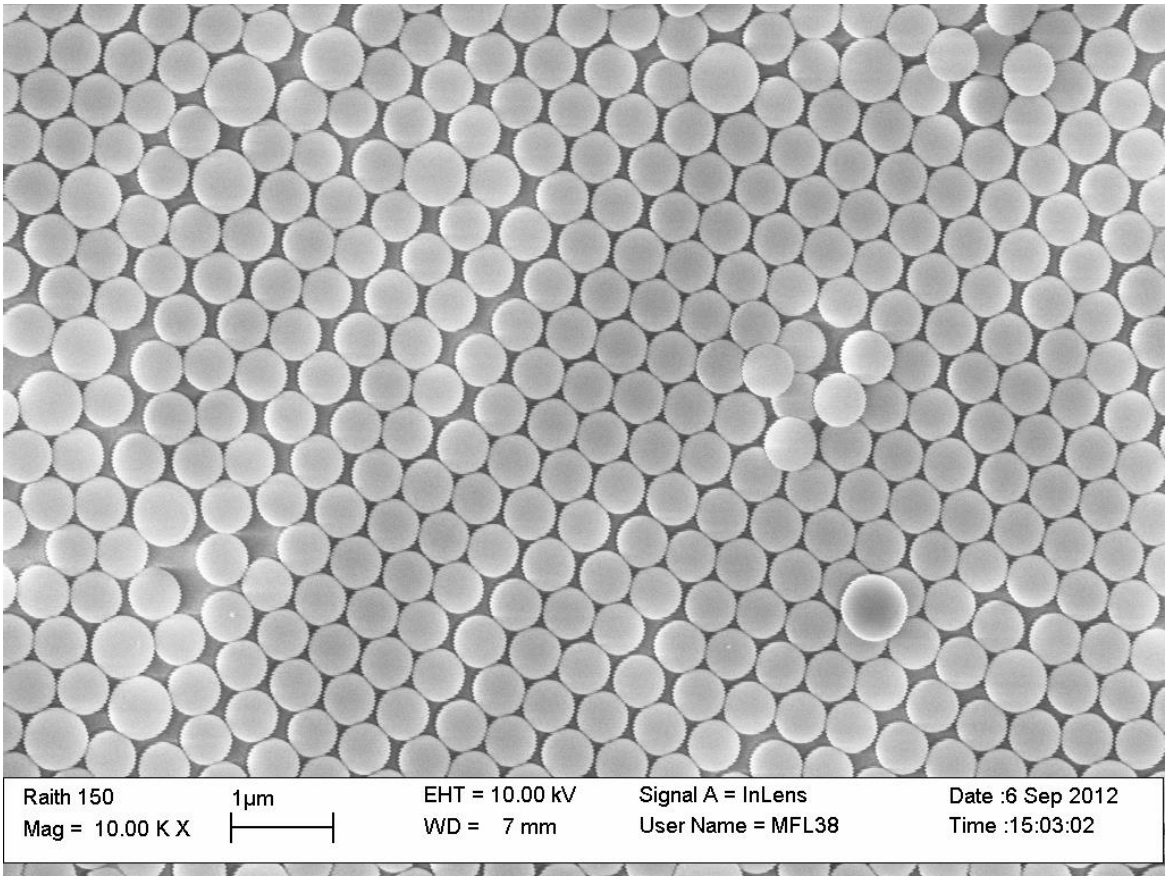

Figure 21 Sigma-Aldritch 500 nm polystyrene beads applied to sapphire substrate and sputter coated with 10 nm of Au. Diameter of the beads is approximately 500 nm and the coverage is approximately a monolayer with a few outliers in each criteria.

Difficulties occurred when the polystyrene spheres were dissolved. After soaking in acetone for 2 hours, the spheres appeared to disappear from the sample, although the poor ability of the SEM to resolve 3-dimensional objects made it difficult to determine if the spheres had actually been removed, as a sphere would appear almost the same as the hole left by a sphere. Small circles of residue appeared to remain on the sample concentric with the circles, which suggested that the spheres were no longer present. Figure 22 shows the patterned substrate after the dissolution of the spheres. In some images, it was ambiguous whether the spheres had been fully removed, so in order to make certain, the samples were treated to a brief oxygen plasma ashing which appeared to remove the debris noted in the middle of the circles.

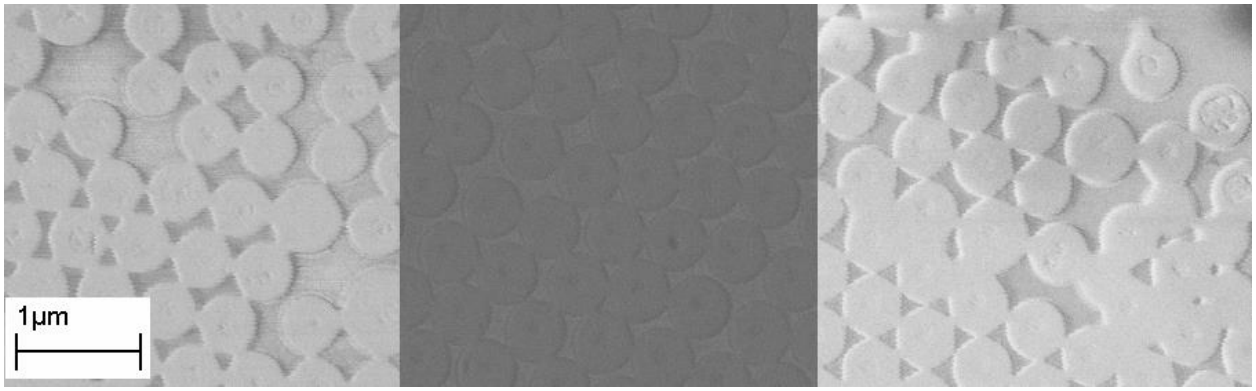

Figure 22: Nanosphere lithography patterned gold on sapphire substrate. All three images show the same sample, but note how the contrast settings of each image appear to show either the circles or the gaps as raised up. Also note the circles of debris inside the middle of some of the circles.

EPLD growth was performed on the patterned substrates alongside a normal drop coated control sample and typical results are shown in Figure 23. The results were again unexpected. There is no visible translation of the very clear pattern shown in Figure 22 and nanorods grew all over the substrate, even though previous results have shown that the nanorods will not grow in areas without gold present. There are several potential explanations for this, firstly that it was incorrect to assume that the nanospheres had been properly removed. The spheres could have remained, coated with gold on the substrate throughout the growth, or even been burned up in the high temperature environment of the PLD chamber, depositing their gold coating on the substrate below. The 10 nm of gold deposited could have been too thick and at high temperature could have melted and dewetted across the sample, forming a thin liquid film across most of the substrate. By whatever mechanism, the growth was unsuccessful and the technique did not offer enough potential for improvement to warrant investigating further.

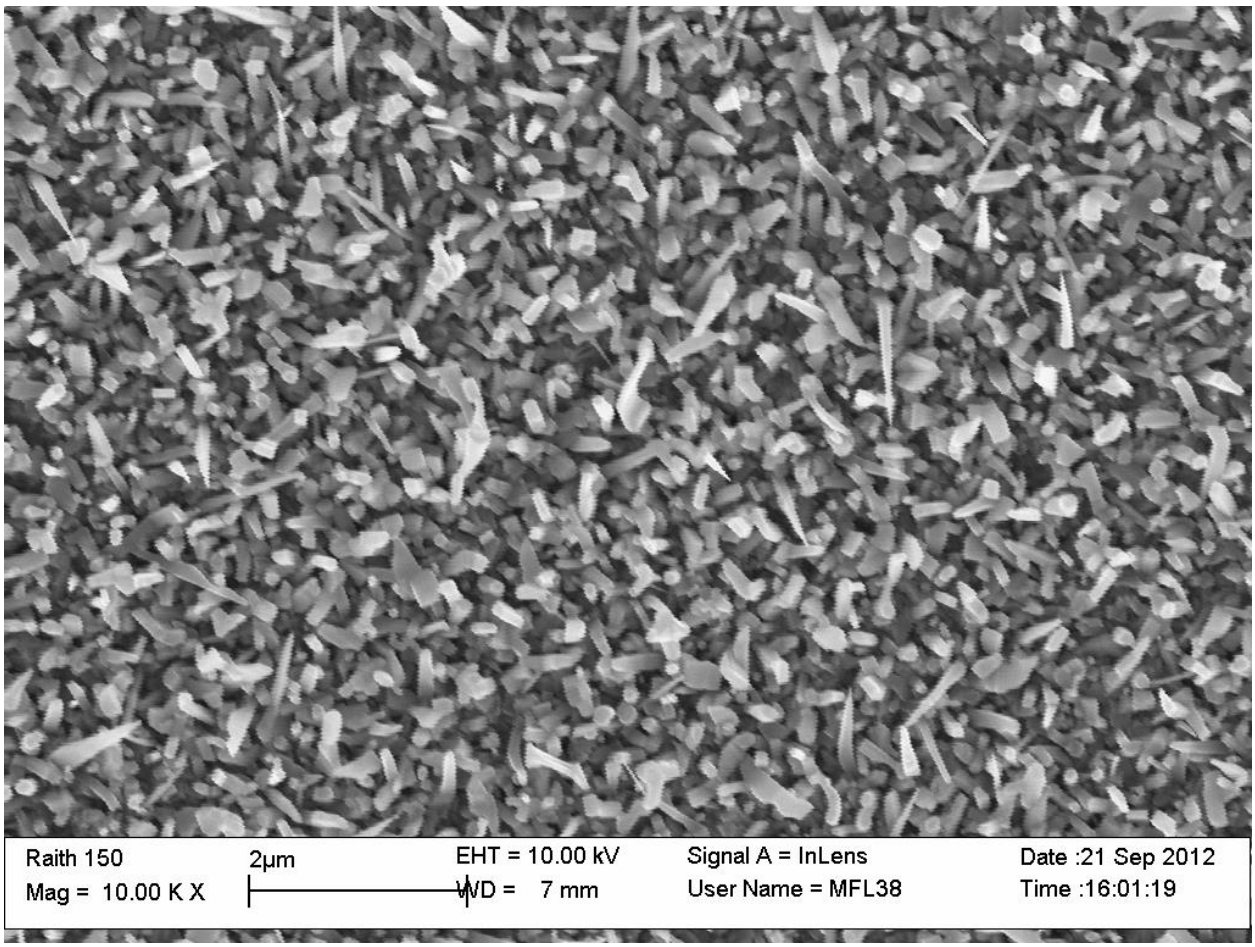

Figure 23: ZnO nanorod growth on nanosphere lithography patterned sapphire substrate. (Growth 22)

3.10 Sputtered Gold

The distinct lack of order in the nanorods grown by EPLD compared to those reported in the literature showed that there must be a problem in either one of the two phases involved with the growths: the colloid deposition onto the substrates or the PLD process. In order to determine where the problem lay, a ZnO nanorod EPLD growth using a simple sputtered Au film on c-plane sapphire as catalyst was performed. Well aligned arrays of ZnO nanorods have been grown on c-plane sapphire by PLD using this type of catalyst by several different groups [1, 2, 4].

A sapphire sample was prepared by sputtering gold onto the surface of a c-plane sapphire substrate for 10 s. TEM images show that this resulted in the formation of gold nanoparticles of various sizes from 2-3 nm up to approximately 10 nm as shown in Figure 24. A ZnO EPLD growth was performed using this substrate as well as a drop-coated c-plane sapphire control substrate.

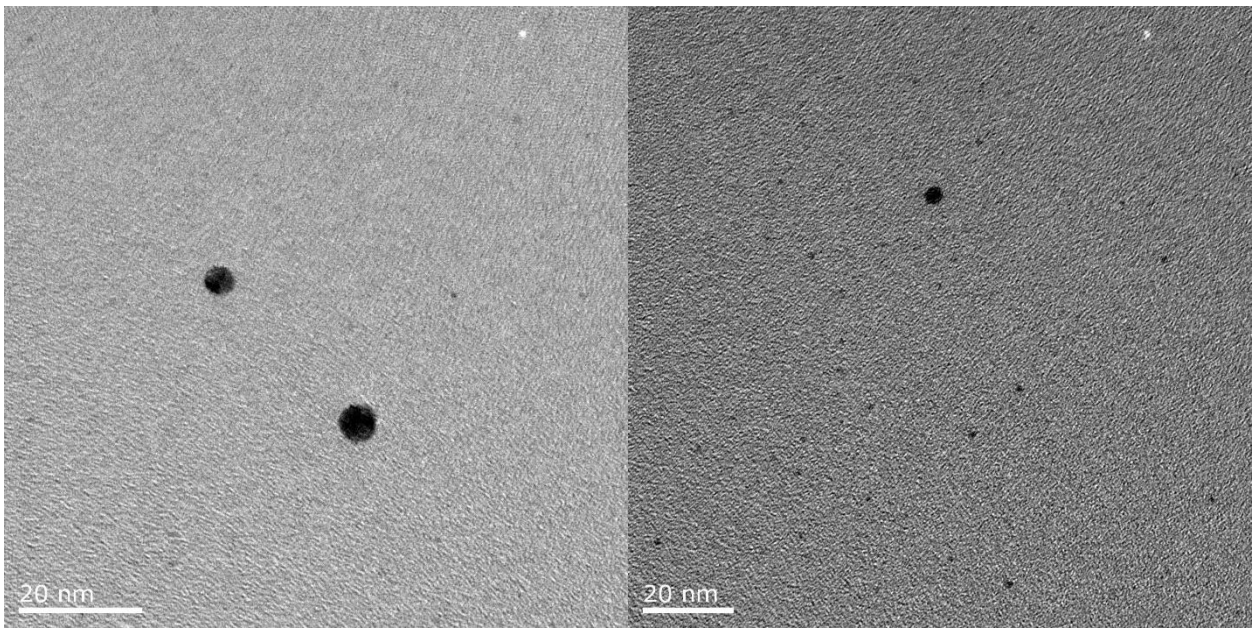

Figure 24: TEM scans showing sputtered gold nanoparticles. Because they are not created from the high precision technique used on the colloidal gold, they exhibit significant variation in diameter.

The results of the sputtered gold growth were "textbook" ZnO nanorods narrow enough to be considered "nanowires". The nanorods grew in a well aligned array of narrow, vertical rods all over the substrate as shown in Figures 25 and 26. As well as being well aligned, many of the rods tapered down to extremely small tip diameters. Figure 26 shows the tips of several nanorods under very high magnification. When compared to the TEM images in Figure 24, the 10 nm dimensions measured at the tips of the nanorods are close to the size of the sputtered gold nanoparticles from which they are seeded. This is logical, as the growth from the Zn/Au eutectic should only be precipitating down onto the substrate (or onto the forming nanorod). If the catalyst is not consumed, then the Zn/Au droplet should stay the same size. Only after the rod has formed from the eutectic will growth in other directions cause the rod to grow outwards. The nanorods grown using the sputtered Au film also showed a large variety of diameters, which is also consistent with the wide distribution of nanoparticle sizes observed in figure 24.

The results of this growth provided a strong indication that our PLD growth parameters were effective for growing ordered ZnO nanorods with tip diameters determined by the size of the catalyst particles on c-plane sapphire. The fact that the Au colloids were unable to produce this morphology was therefore an issue concerning the colloids themselves and either their ability to function as catalysts or their method of application to the substrates.

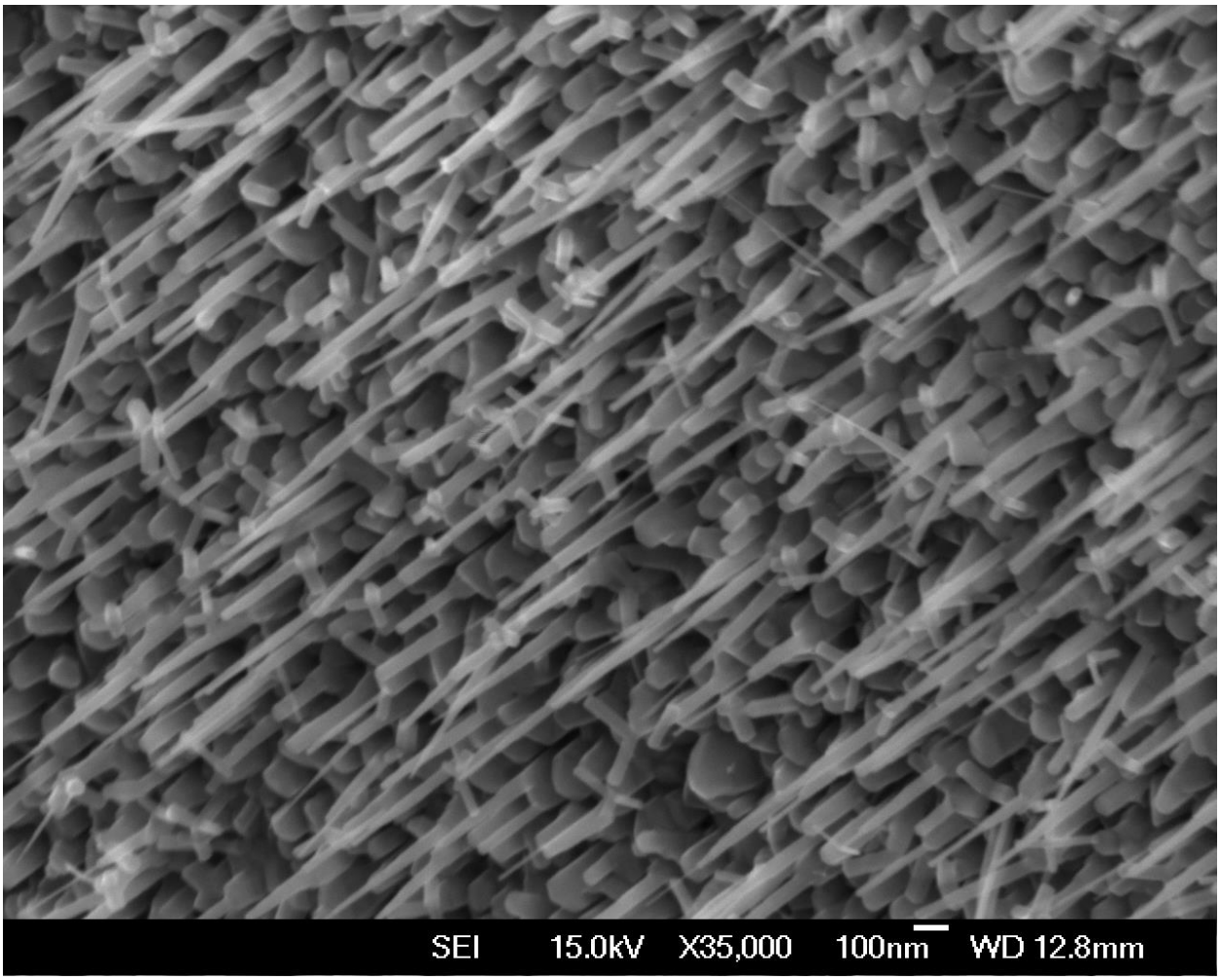

Figure 25: Side view from 30° of ZnO nanorods grown using sputtered Au catalyst. (Growth 40)

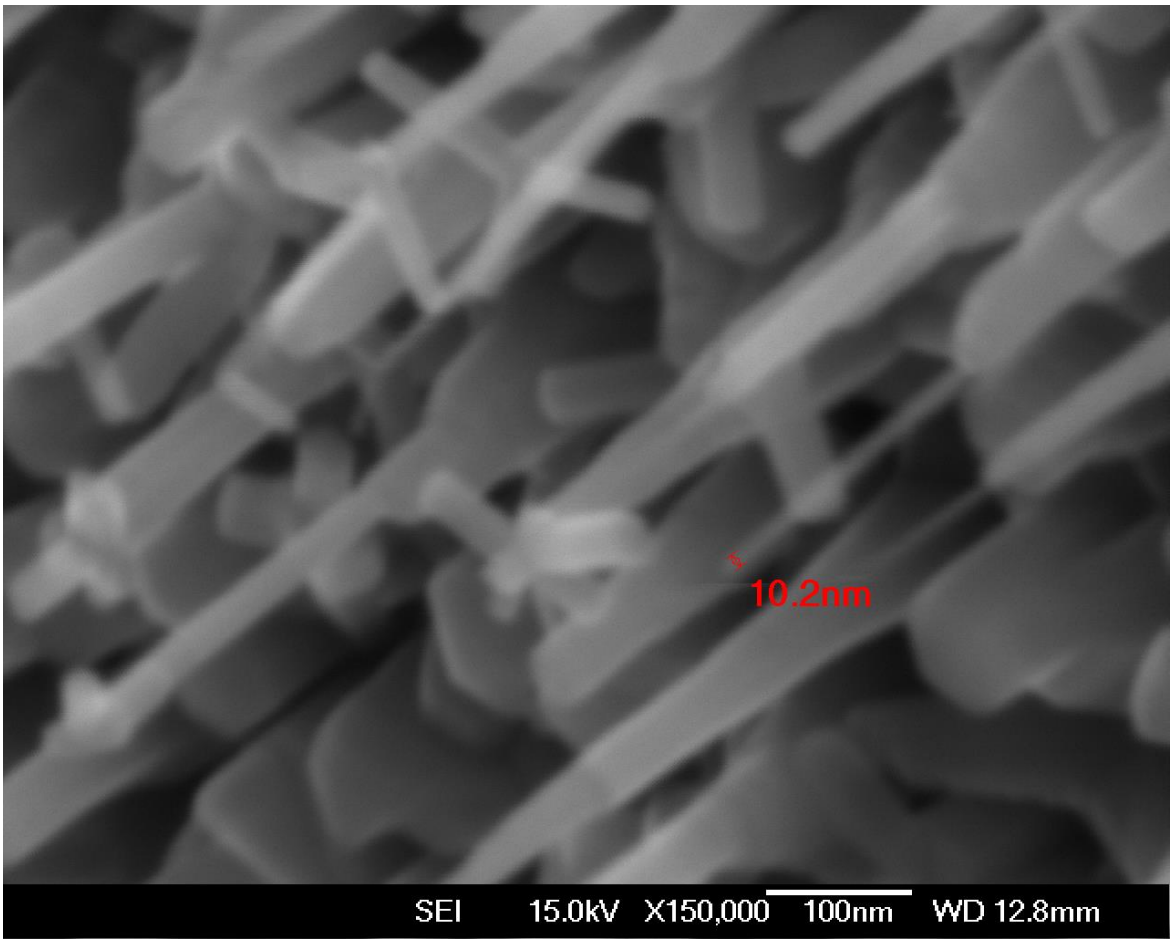

Figure 26: Very high resolution SEM image showing the tip of a nanorod measured using the SEM software. The accuracy of this measurement is not particularly good at this scale, but is probably accurate to within 5nm (Growth 40).

3.11 APTMS

3.11.1 Citrate Ligand

A proposed solution to the problem of Au colloid adhesion to the sapphire substrate was to treat the substrates with a surface modifier that would effectively tether individual colloids to the substrate. A chemical known for this property is 3-aminopropyl trimethoxysilane (APTMS). APTMS is a relatively small organic molecule which features two important

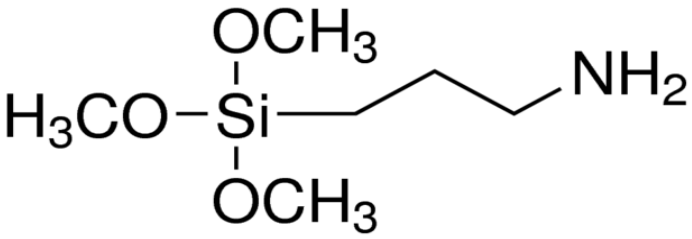

Figure 27: 3-Aminopropyl Trimethoxysilane (APTMS) molecular diagram. Notable are the three alkoxy (methoxy) groups bonded to the silicon atom and the amine group at the end of its propyl chain.

active groups: an amine group at one end and methoxy groups attached to a silane group at the other. Sapphire is a form of aluminium oxide (Al_2O_3), but the surface of the crystal, (as with many other oxide crystals including ZnO) is terminated with a layer of hydroxyl groups, adsorbed from the atmosphere [42]. The hydroxyl groups on the surface of a substrate react with the methoxy groups in the APTMS, displacing them and in the case of sapphire, forming a covalent Al-O-Si bond. This reaction is well documented and is regularly used to increase the hydrophobicity of materials such as glassware [43-45].

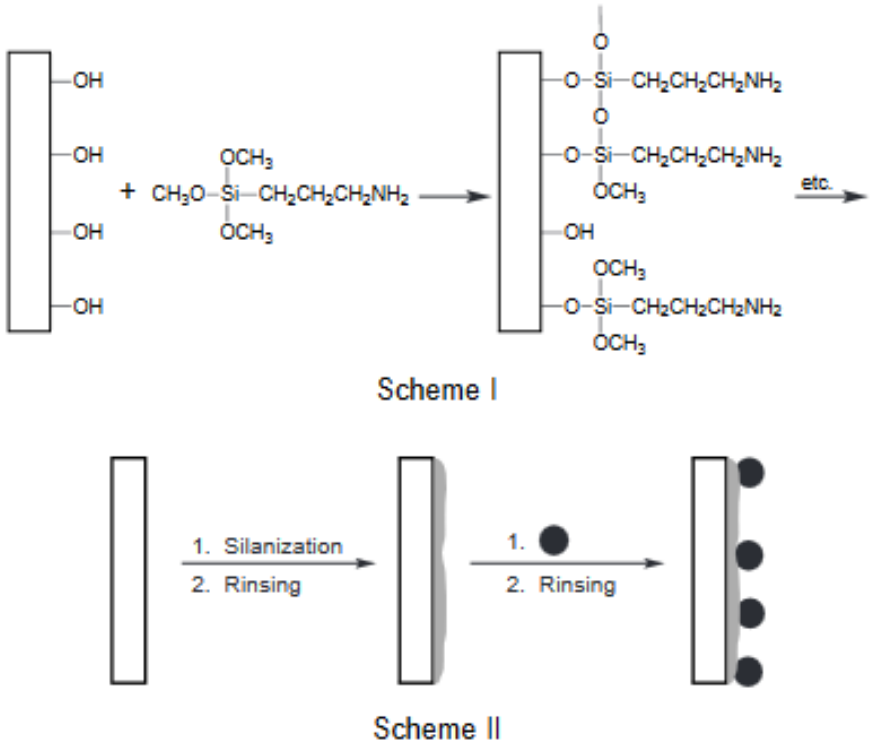

Figure 28: Tethering of gold nanoparticles to a hydroxylated substrate via the use of APTMS. The substrate can then be rinsed thoroughly in deionized water without disruption. Image by Keating *et al.* [46]

Gold and silver nanoparticles are attracted to the amine group at the opposite end of the APTMS molecule and bond covalently [46] as shown in Figure 29. This has the effect of tethering the nanoparticle to the substrate in such a way that it is resistant to being dislodged, even by vigorous rinsing in deionised water. The use of APTMS as a chemical tether for the gold nanoparticles served three purposes. Firstly, tethering would increase the attraction of the Au colloids to the substrate and therefore increase the number of colloids on each substrate. Secondly, the strength of the bond would enable more rigorous washing of the substrates after the application of the colloids. Thirdly, it may help to improve coverage homogeneity and reduce any aggregation, as colloids would be more strongly attracted to the APTMS than to each other.

3.11.2 APTMS Growth

Substrates were treated with APTMS via the method described in Chapter 2, Section 1. An immersion time of 30 minutes was expected to deposit a complete layer of APTMS on the surface of the sapphire substrate [47]. SEM images of colloids applied to APTMS coated silicon by dip coating for 5 minutes indicated a good coverage of the colloids, comparable to that obtained by drop coating. Additionally, a correlation was observed between colloid density on the surface of the substrates and colloid concentration in the dip coating solution as shown in Figure 29.

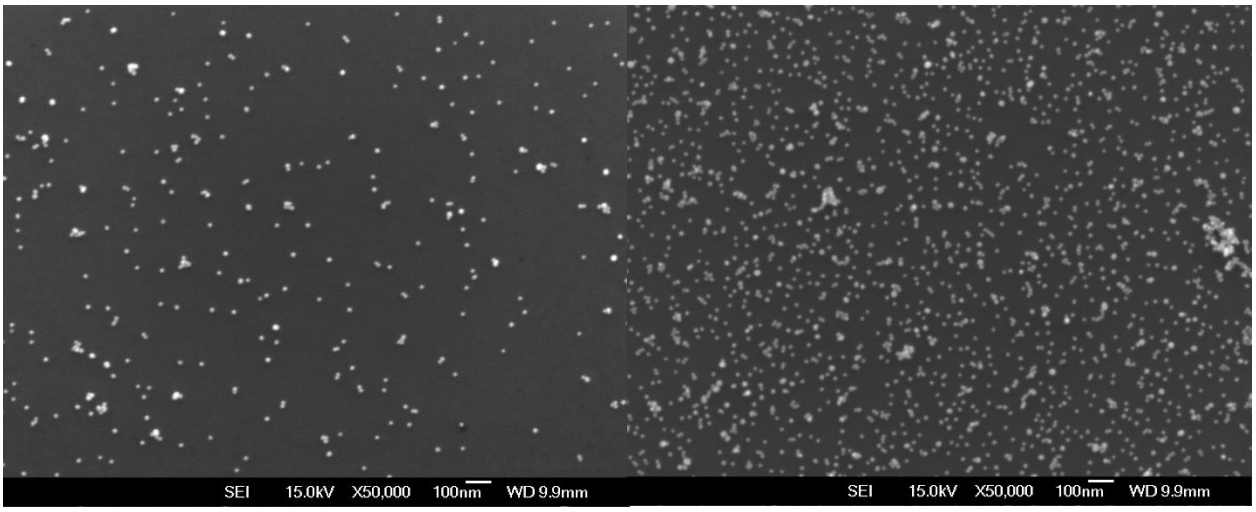

Figure 29: 13 nm gold colloids deposited on APTMS treated silicon substrates. Left: 8.5 mM colloid concentration. Right: 17 mM colloid concentration. The higher concentration shows more aggregation, but the majority of colloids are not aggregated.

A sample of c-plane sapphire was treated with APTMS and Au colloids were applied by dip coating in 17 mM colloid solution for 5 minutes. A ZnO nanorod growth was conducted using this substrate with the standard parameters, including the eclipse plate, alongside a control sample prepared by drop coating.

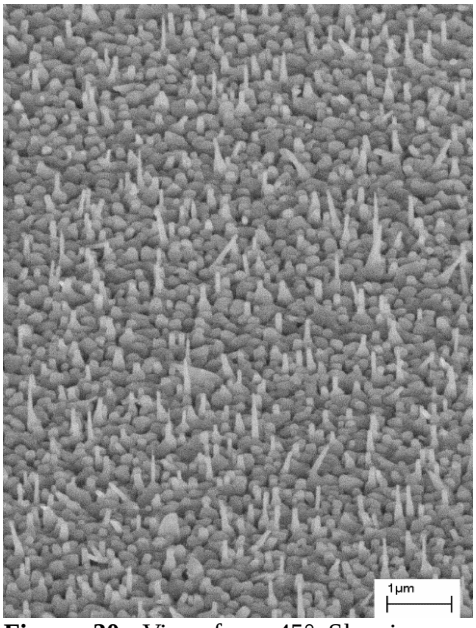

Figure 30: View from 45° Showing good vertical alignment of nanorods. (Growth 43)

The nanorods produced by this growth, although not as thin and well-ordered as those catalysed by the sputtered gold, were significantly better aligned than previous growths without the APTMS. Rods which grew from the block-like, textured surface tended to align themselves vertically, as would be expected from good epitaxy. A small proportion of

nanostructures resembled blade shaped nanosheets which grew at odd angles from the substrate, potentially indicating some manner of defect in the growth mode. Nanorods grown on the control sample matched previous growths indicating that there had been no errors in the PLD deposition.

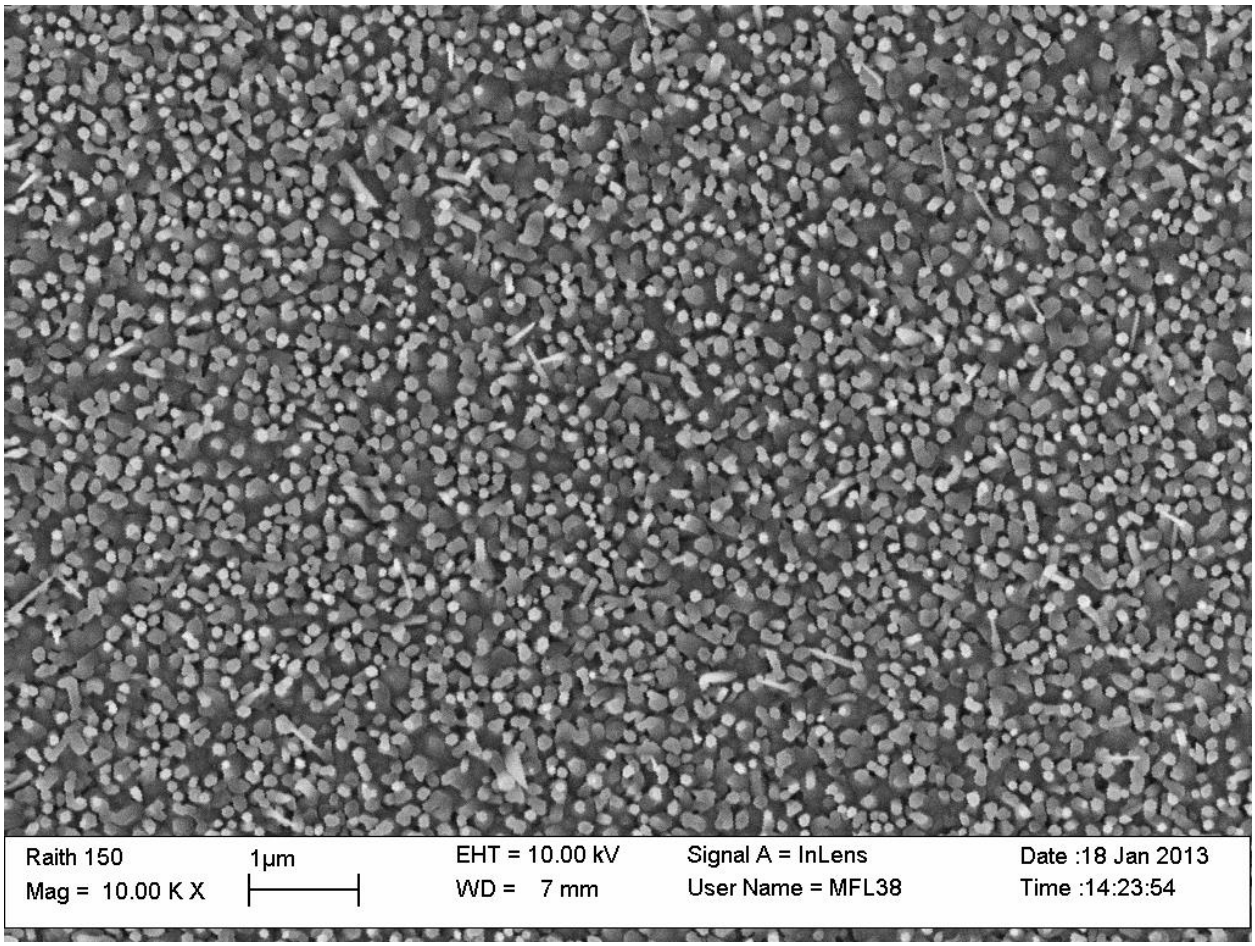

Figure 31: Top view of ZnO Nanorods grown using APTMS dip coating. The dot-like pattern shows a high proportion of nanorods standing vertical on the substrate and represents good epitaxy between the rods and the sapphire. (Growth 43)

This was very significant as although the nanorod ordering was not perfectly vertical as hoped, it was now significantly better than all previous growths. Nanorod counts from SEM images such as Figures 31 and 32 show that approximately 95% of nanorods grew normal to the substrate or deviated by only a few degrees. This confirmed one of our initial expectations, which was that ZnO nanorods could be grown in ordered arrays using colloidal gold, but a further question remained. In the sputtered gold growth, the nanorods tapered down to the approximate size of the gold particles which seeded them, but even using APTMS to anchor the particles, the nanorods displayed fairly broad, flat tips of 50-100 nm despite being catalysed by gold colloid nanoparticles of only 13 nm diameter.

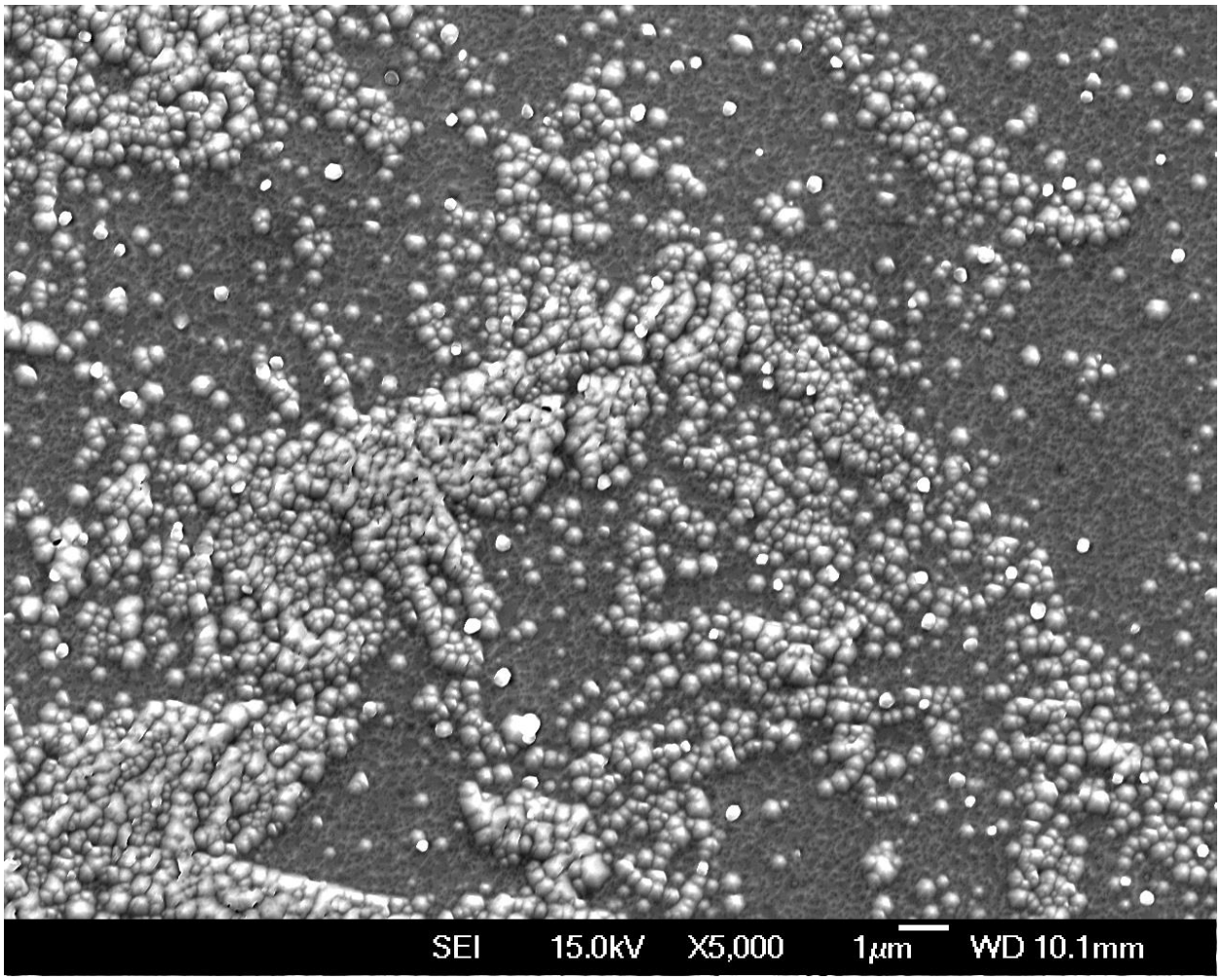

Figure 32: Sapphire sample treated with APTMS but no Au colloids after ZnO growth. There are clearly micron-scale disruptions in the film, presumably caused by residual organics accreting ZnO around them.

In a repeat of this growth conducted to ascertain reproducibility, an additional control sample was added to the chamber which had been treated with the APTMS, but had no gold colloids added. As expected, there were no nanorods grown on this sample, however there was some manner of accretion and disruption visible in some areas on the substrate as shown in Figure 32. In deploying the APTMS, our assumption had been that the 750°C substrate temperature, combined with the oxygen processing gas would have either evaporated or oxidised most of the organic residue left by the APTMS on the surface. Unbonded APTMS has a boiling point of 194°C, so this assumption was not unreasonable. Unfortunately Figure 32 shows that this was not the case. Disruptions in the film were on the order of hundreds of nanometres, indicating that significant organic contamination remained. In order to address this, a small change in the operation of the

PLD chamber was adopted and was found to yield a significant improvement in nanorod quality. The standard operation procedure had been to mount the samples using indium-tin at approximately 170 °C and continue heating while the chamber was being pumped to its base pressure of approximately 1.5 x 10^{-5} Torr. As heating and pumping both took approximately 80 minutes, performing these in parallel was expedient for time efficiency. Oxygen was introduced into the chamber once the temperature had reached the growth temperature of 750 °C and the growth commenced one the oxygen pressure had stabilised. Pure oxygen at high temperature would act as a powerful oxidant and it was proposed that allowing the oxygen more time to oxidise residual organics before the growth started would reduce their contaminating effects on the growth. A growth was therefore conducted using the standard EPLD parameters, in which the chamber was pumped to base pressure at 170 °C after mounting the samples. Oxygen was only then added and heating to 750 °C was performed over the usual 80 minutes while oxygen was present in the chamber.

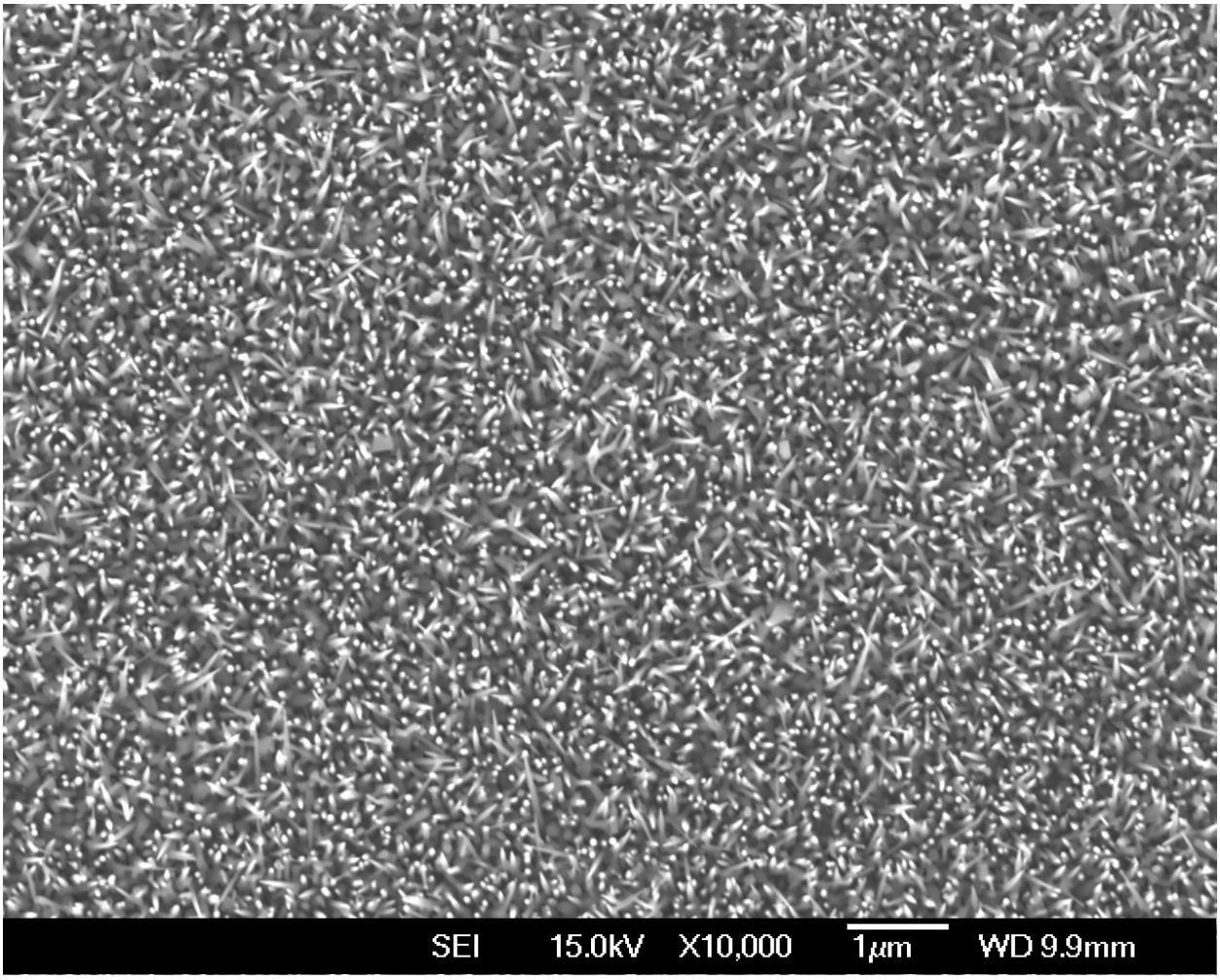

Figure 33: Growth performed by adding oxygen before heating in order to minimize the amount of organic contamination. (Growth 55)

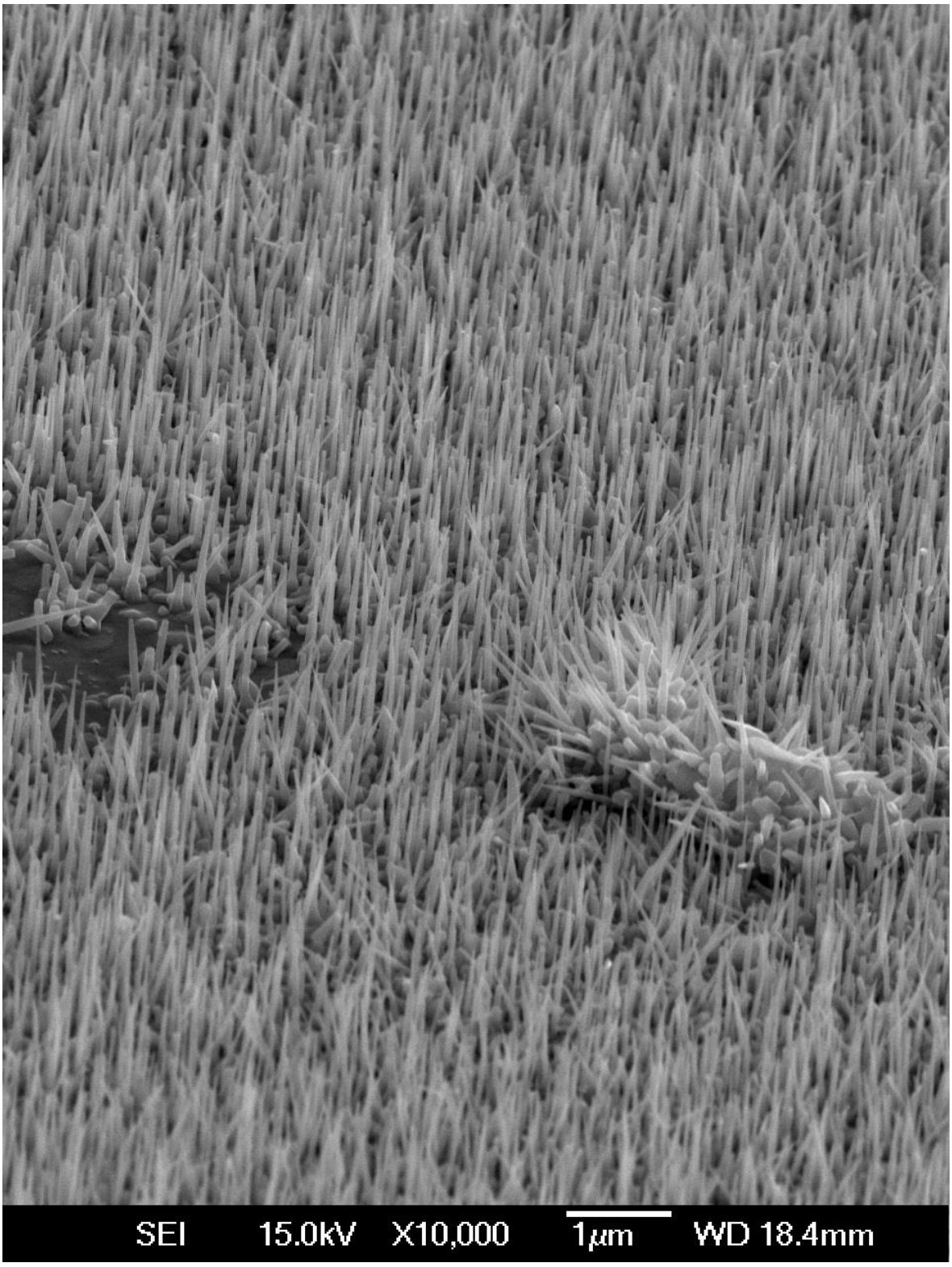

Figure 34: Detailed SEM image showing a highly ordered nanorod array punctuated by defects which allow vision of the underlayer of ZnO between the rods. (Growth 55)

This growth was extremely successful as shown in Figures 33-35. The resulting nanorods were very densely packed and while there was some disorder in their orientations, they mostly formed a parallel array normal to the substrate. It was difficult to observe if the rock-like underlayer was present between the rods unless the array was viewed from an angle (as in Figure 34).

For the first time with using the gold colloids as catalysts, the resulting nanorods ended in pointed tips of approximately the same dimensions as the 13 nm colloids themselves as shown in Figure 35. This was an important development, as the potential for precise control of nanorod dimensions was part of the motivation for the investigation of colloids for ZnO nanowire growth. Subsequent reproductions of this growth confirmed the effectiveness of the modified EPLD process (see Appendix 1 for complete growth list).

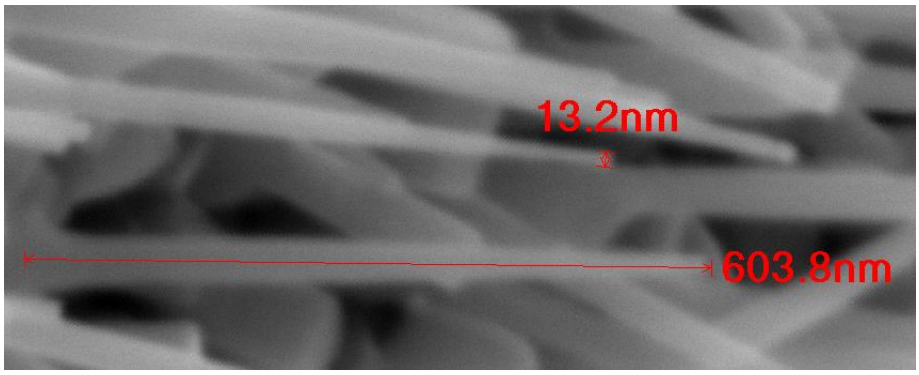

Figure 35: Measurements made by the SEM show a nanorod length of approximately 600nm and a tip diameter of 10-15nm. (Growth 55)

3.12 Pulse Frequency Effects

A single pulse from the KrF excimer laser lasts approximately 25 ns. Although observation of the plume with the naked eye shows it flickering rapidly, the pulses do not actually overlap even at high pulse frequency. At the substrate however, it was possible that the nanorod morphology and specifically the tapering might be different if the same quantity of material was delivered over a longer time period. Exposed to the high temperature of the substrate, it was reasoned that perhaps the material arriving would be mobile enough to move to preferential growth sites.

Two growths were performed, scaling the original 10 Hz pulse rate by 2.5x in either direction while keeping the total pulse count the same. The first growth was at 4 Hz for 150 minutes and the second at 25 Hz for 24 minutes. Both of these new growths would therefore comprise 36000 pulses, the same number as the standard 10 Hz for 60 minutes growth, resulting in the same total quantity of ablated material.

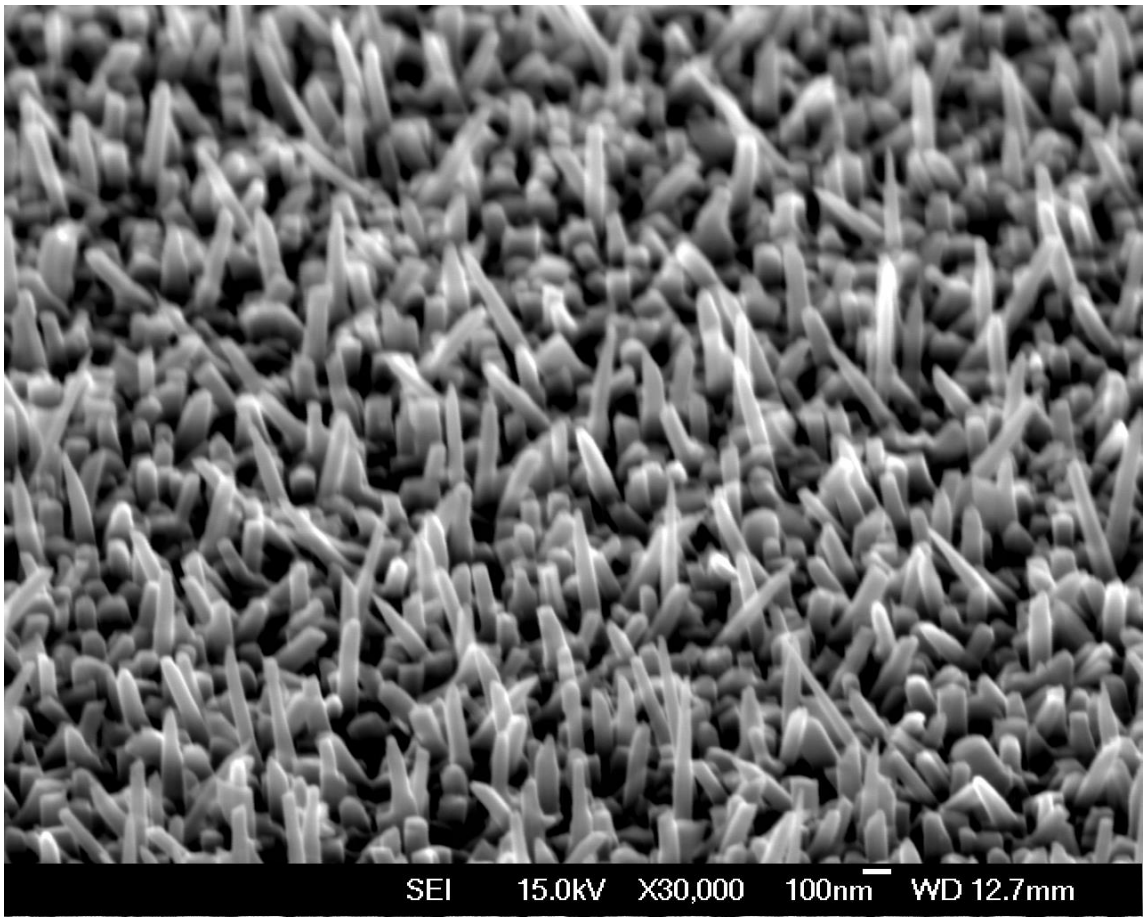

Figure 36: Nanorods grown at low frequency for an extended time, viewed from 30° angle. (Growth 59)

Figures 36 and 37 show typical nanorods from the 4 Hz, 2.5 hour growth, with all other parameters kept the same. The nanorods are poorly ordered, short and very thick, often with multiple slight bends and changes in thickness along their lengths. Interestingly, the tapering has more or less vanished, but so has all diameter correlation with the 13 nm gold colloids used to catalyse the growth. The block-like, underlayer growth is highly textured and seems to blend with the wide nanorods, making it difficult to differentiate between large blocks of underlayer

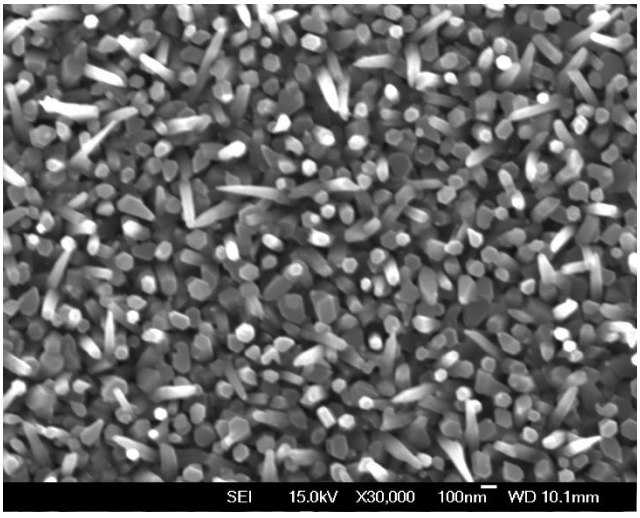

Figure 37: Top-down view of ZnO nanorods grown by low-frequency PLD. (Growth 59)

and fully formed nanorods. Viewed from the top in Figure 33, it can be seen that these nanorods still maintain an approximately hexagonal shape. Presumably the strong emission from the long rods is what gives the fully formed nanorods the ability to stand out in the SEM image.

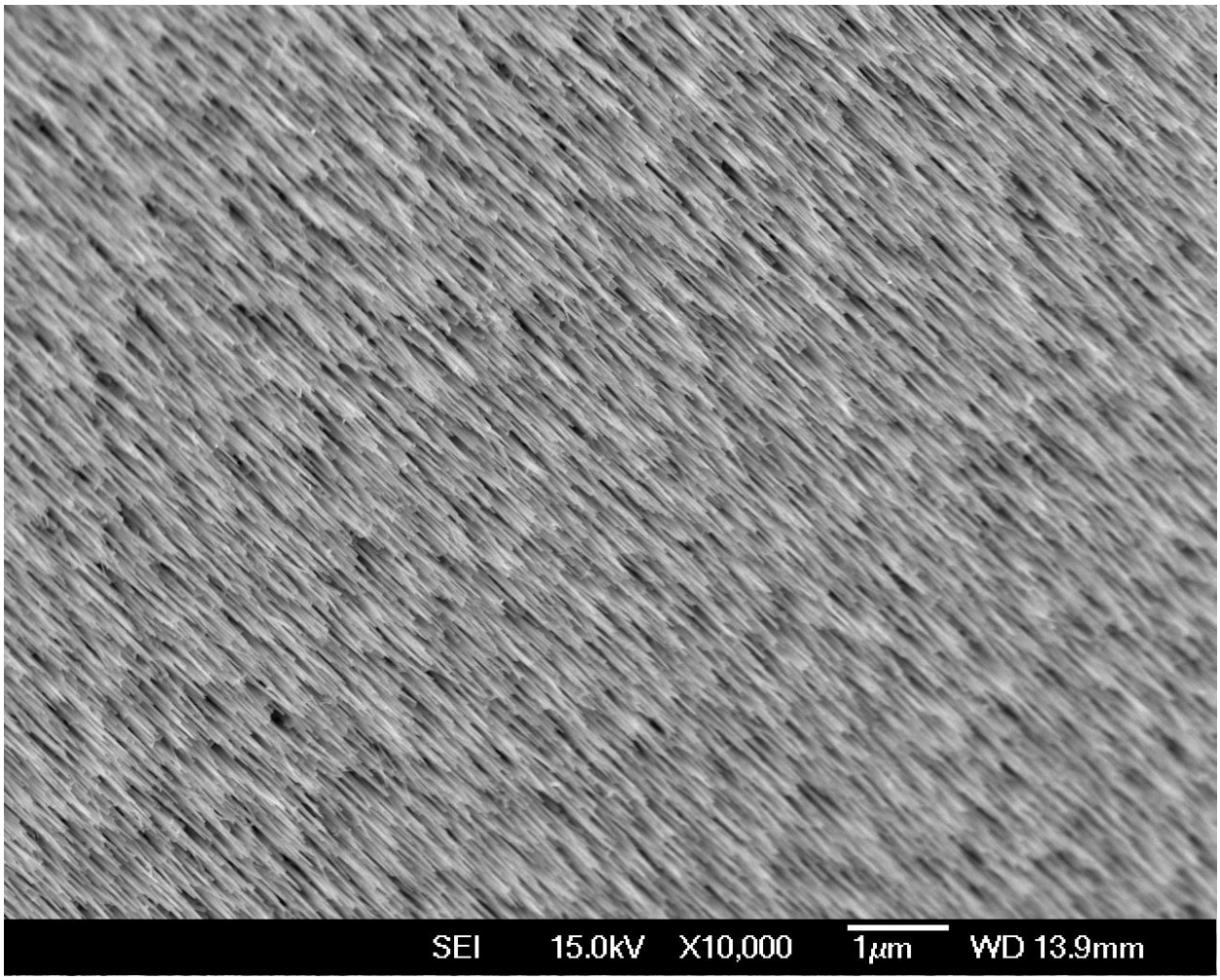

Figure 38: 30° elevation showing extremely high density and well-ordered ZnO nanorods grown by high frequency PLD. (Growth 63)

In contrast, the high frequency growth produced even finer and sharper nanorods than even the best growths at the standard 10Hz, shown in Figure 38. The nanorods were extremely long and thin, as long as 1 μm and tapering to a point approximately the same diameter as the 13 nm colloid catalysts, with excellent uniformity and order.

These results suggested that a higher deposition rate actually improved the morphology of the resulting ZnO nanorods. A possible reason for this may be that the extended growth time and wider gap between pulses could function like the annealing of a film, allowing the lattice to rearrange itself for greater

electrostatic balance. The preferred growth direction in the c-direction as discussed previously is due to the lower energy required to essentially start a new layer building in that direction. Most incoming atoms accumulate in the c-axis, but we have no reason to assume that this growth builds up one complete monolayer at a time as it might in an MBE growth. It is known that the growth in non-preferred directions is nonzero, so during each pulse, an incomplete monolayer could build up on these non-preferred planes, as well as a several layers in the preferred (0001) direction. An incomplete monolayer is electrostatically unfavourable, so given the time and energy to migrate (which the relatively long inter-pulse period of heating provides), atoms might migrate to the incomplete monolayers on the side walls of the nanorod in order to complete the layers. Even though the primary growth direction still grows the fastest, the comparatively long periods of heating between pulses could allow this preference to be diluted.

3.13 Eclipse Plate Geometry Effects

3.13.1 EPLD Thickness Gradient

When using the eclipse plate in our growths, a gradient of morphologies between nanorods assembled on different areas of the substrate/s was observed. This is logical because the amount of material being deposited by a PLD system varies with angle from the centre of the plume. Chrisey and Hubler [12] modelled the thickness of a film deposited by PLD as $\cos^{p+3}\theta$, where p is an exponent related to the tendency

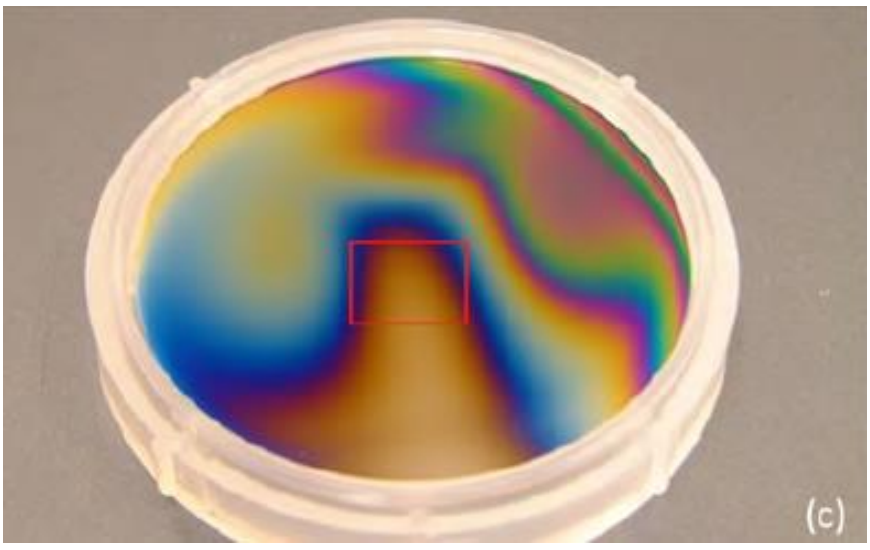

Figure 39: IrO_x film on silicon grown by Mendelsberg [11] showing the thickness gradient caused by the eclipse plate (position indicated by a red square). The pattern is asymmetrical because the laser strikes the target at an angle from the right. Note that the eclipse plate is supported on a small tower, so the area directly beneath the plate is also shadowed.

of the plume to be concentrated in the direction normal to the target. With the addition of an eclipse plate, the thickness gradient changes significantly. Figure 39 shows an iridium oxide (IrO_x) test film grown by Mendelsberg [11] on a silicon wafer using EPLD in the same system as the previous nanorod growths. The red square outlines the approximate position of the eclipse plate and variations in thickness can be observed both in the area shadowed by the plate and outside it. Mendelsberg notes that the asymmetry in the pattern outside the shadowed area is due to the laser striking the target at an angle, creating a slight directional bias. In my growths, a 10 mm x10 mm plate placed 2 cm from the substrate and 4 cm from the target shadows an area 15 x 15 mm behind it. If two 10 mm x 10 mm samples are placed on the heater side by side, centred immediately behind the eclipse plate, the outer 2.5 mm of each will still be exposed to direct line of travel to the target.

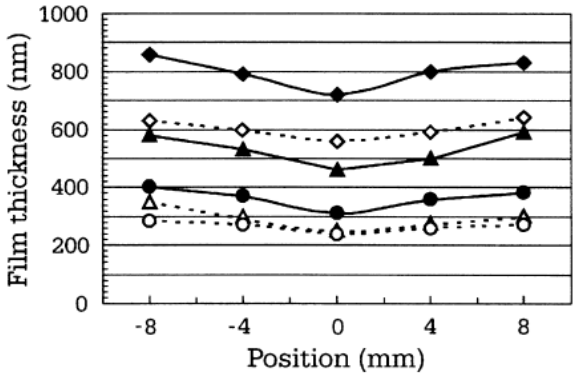

Figure 40: Marcu *et al*.[7] produced this data showing the thickness of several YBCO films as a function of its position behind an eclipse plate. It stands to reason that ZnO nanorod growths experience a similar pattern of material arriving at different areas.

Behind the eclipse plate, the arrival of ablated species is governed by diffusion. Marcu *et al.* [7] confirmed that the thickness of a film decreases to a minimum when moving from the area behind the edges of the plate to the area behind the centre as it is further to reach this area by random diffusion. Growing YBCO films, they measured a thickness difference of between 12.5 - 28.5% between these regions for a variety of different growth conditions shown in Figure 40.

3.13.2 Position dependent EPLD growth

In light of the previous growths, this positional thickness gradient was important, because while Marcu *et al.* were primarily concerned with film thickness, the total amount of material deposited also governs the growth rate, which was seen in the 4 and 25 Hz growths to have a significant effect on the nanorod morphology. A growth was conducted with three identical c-plan sapphire substrates, prepared at the same time using APTMS tethered Au colloids and placed in the PLD chamber as shown in Figure 41 and 42. The orientation of the samples was carefully recorded and care was taken not to lose track of their rotation during handling.

SEM images from near the corners of each of the substrates were taken as shown in Figure 43. The morphology of the nanorods showed a significant variation across the three samples. In this growth and in

subsequent repetitions, it was consistently found that the optimum area for thin nanorods consistent in tip size with the colloid particle diameters was the area most strongly shadowed behind the eclipse plate (the bottom right of Sample 1 and the bottom left of Sample 2).

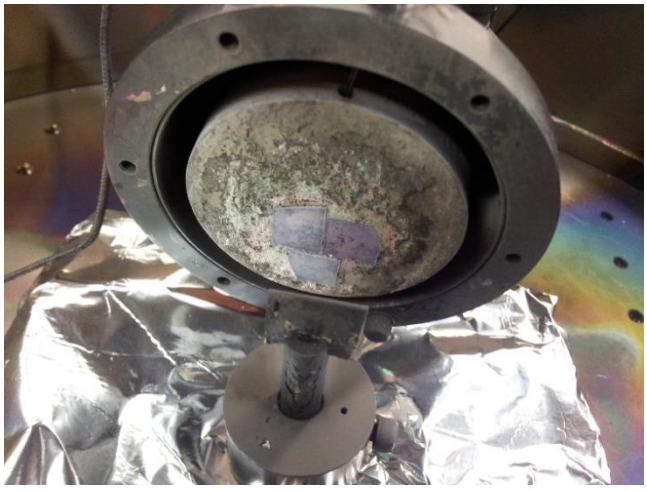

Figure 41: The eclipse plate and substrate heater as used in nanorod growth experiments.

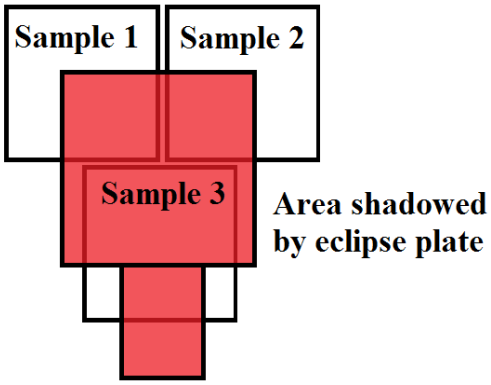

Figure 42: Explanation of nomenclature used for sample positions.

Moving upwards away from the centre of the plate produced larger and sparser rods and in the case of Sample 1, quite significantly so. The far left of the system, the left edge of Sample 1 showed thicker, less well ordered nanorods and a rougher sublayer, but the far right showed less variation from the centre and in fact, the top right produced nanorods as fine and as dense as those in the centre (although this was not reproducible). Although the displacement from the centre point was similar in images taken at the outside edges of the two samples, the morphology in those areas was quite different. This difference is not completely unexpected, considering Figure 40 of Mendelsberg's IrO_x growth using the same chamber. The film thicknesses in the areas beyond the top corners of the eclipse plate are quite different on either side. The laser ablation plume has a tendency to turn back towards the laser slightly, as the laser cuts a trench at an angle into the target [12]. It is likely, therefore, that the top right corner of Sample 2 experienced a higher deposition rate than the top left corner of Sample 1, resulting in thinner, denser nanorods as seen in the frequency controlled growths.

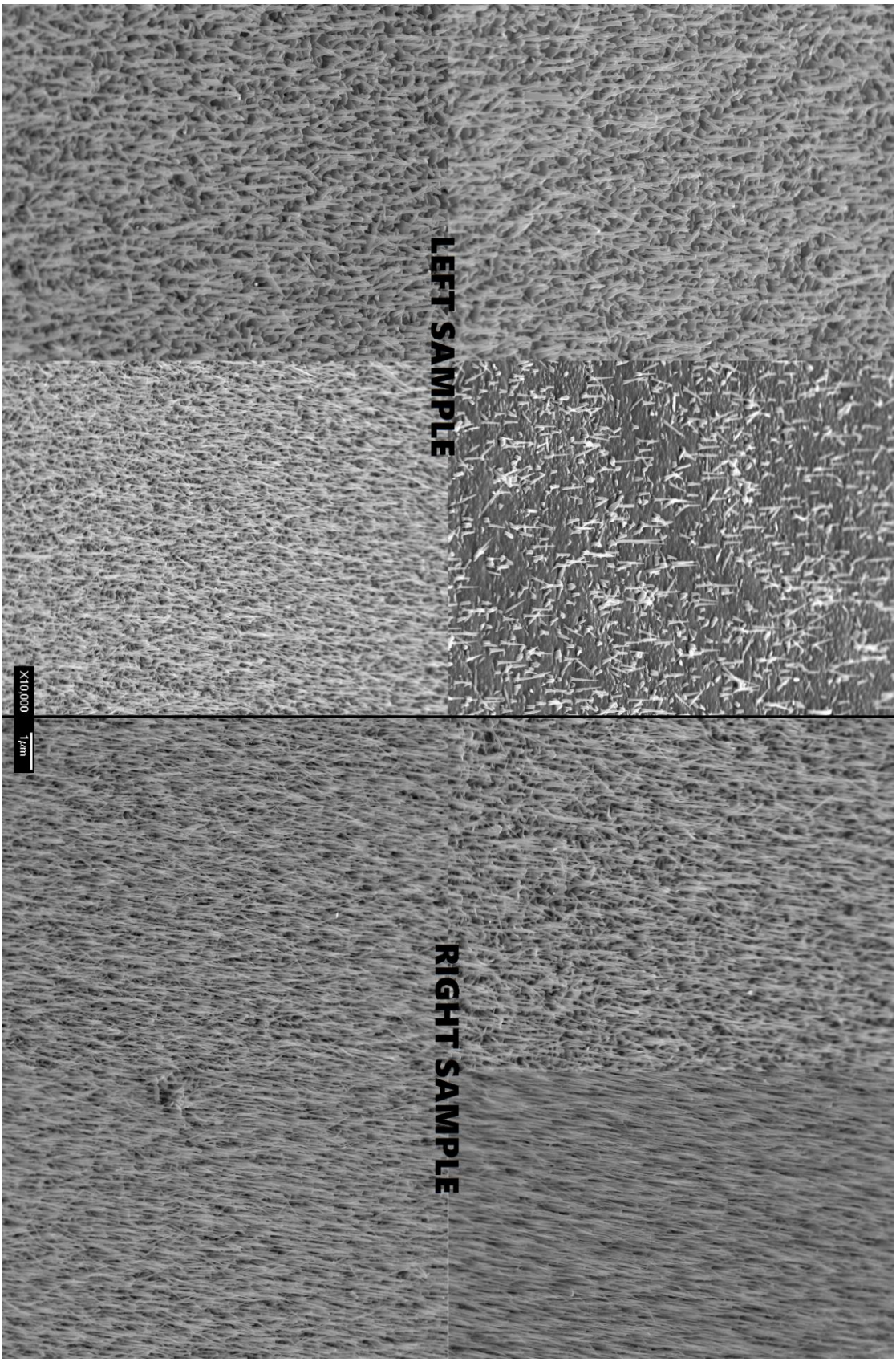

Figure 43: ZnO nanowires grown on two substrates side by side, imaged at eight locations. (Growth 60)

Sample 3, mounted below the others and in the centre produced unusual growth as shown in Figure 44. A potential oversight in Mendelsberg's discussion of Figure 39 is that he does not mention that the eclipse plate, outlined in red, is supported by a small pillar, almost as wide as the plate itself as shown in the photo of the chamber setup in Figure 40. This means that much of Sample 3 was in fact shielded by the pillar of the eclipse plate. Covered by the pillar, the nanorods grown on this sample were relatively uniform, with a small drop in density moving downwards, away from the centre of the eclipse plate and the centre of the ablation plume.

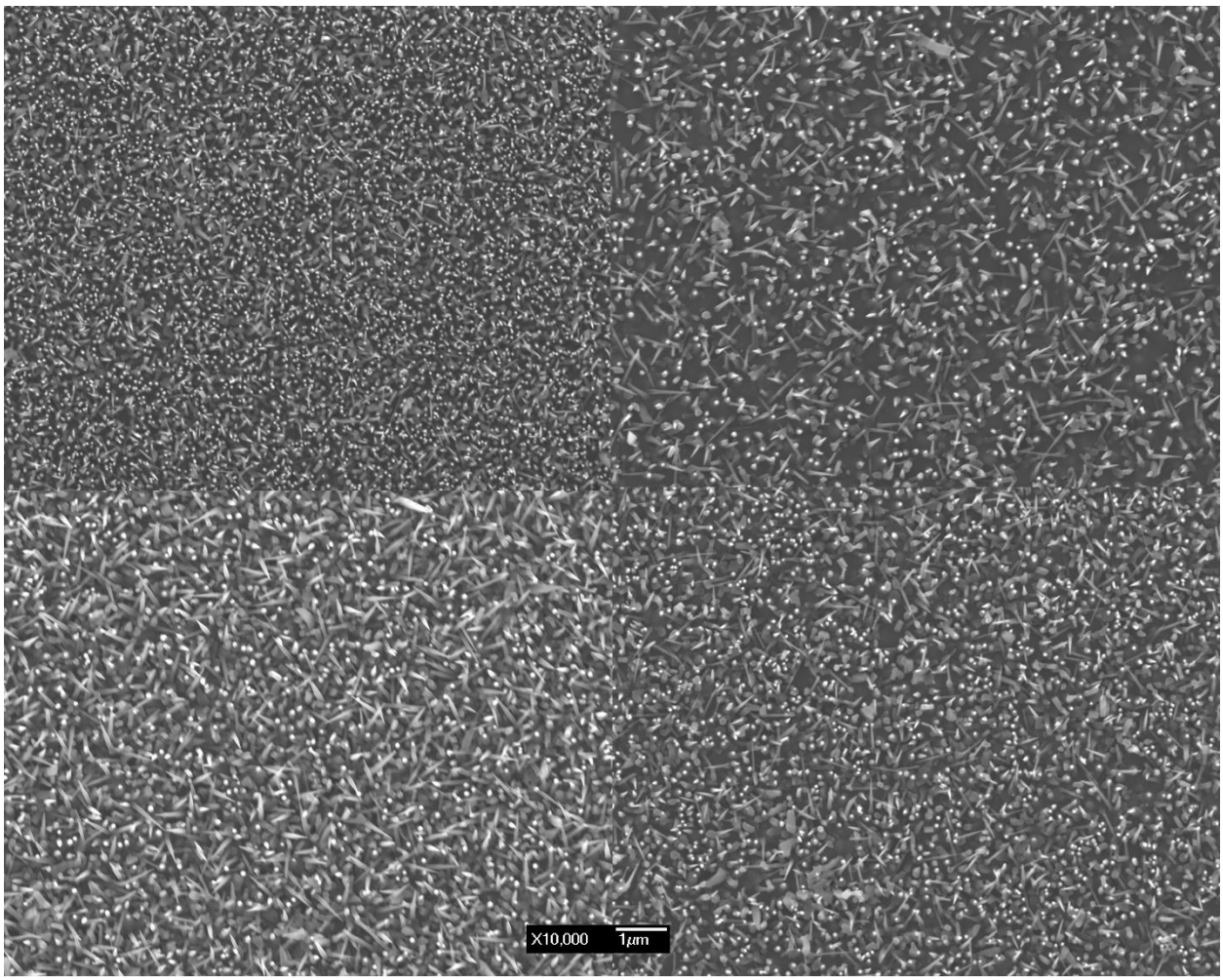

Figure 44: SEM images taken the four corners of substrate 3 in the position dependent EPLD growth. (Growth 60)

Many of the areas in this growth exhibited unexpected and unusual results. The top right of Sample 1 and the top right of Sample 3 were expected to produce much better results and the top right of Sample 2 was expected to produce significantly worse results. By far the most consistent result however, was the "sweet spot" immediately behind the centre of the eclipse plate would generally produce the thinnest

nanowires most representative of the Au colloids catalysing the growth. Consistency in nanorod growth in areas other than this was significantly poorer in subsequent repeats. There are clearly a multitude of factors involved with determining the amount of material reaching each part pf the substrate. Additionally, while the heater on the PLD unit purported to have a variation of only 5 °C , the surface had aged considerably and become rougher, potentially setting up small temperature gradients. In future growths, the orientation of samples would be carefully controlled and all measurements noted as to which area of the heater they were taken from.

3.14 Summary

Chemically synthesised gold colloids proved effective for catalysing the growth of ZnO nanorods and nanowires via eclipse PLD. The colloid deposition method and EPLD growth parameters were optimised.

- A novel method for preparing a sapphire substrate for catalytic nanorod growth using APTMS to position the colloidal gold nanoparticles on the surface such that organic contamination could be washed off without affecting nanoparticle coverage was optimised.
- A-, c-, r- and m-plane sapphire were trialled and only a- and c- plane were found to give consistent results, concurrent with our understanding of the epitaxial relationship between the nanorods and the substrates.
- Eclipse PLD was found to be significantly more effective than standard PLD without an eclipse plate and the growth conditions for EPLD were optimised within the limits of operation of our equipment. It was found that the order of operations in loading the PLD chamber was important to remove carbon based contaminants from the substrates and this had a significant effect on the order and density of the nanorods.
- Increasing the laser pulse frequency resulted in a moderate improvement of the nanowires morphology and order. Decreasing laser pulse frequency resulted in a significant degradation of nanowire morphology and ordering. This indicated that there is a lower limit to the flux of incoming material required for the growth of ZnO nanowires.
- The nanowires grown by EPLD varied in morphology depending on their position relative to the eclipse plate. The finest nanowires with the most ordered morphology were typically found on the areas of the substrate directly shadowed by the eclipse plate.

3.15 References

[1] A. Marcu, L. Trupina, R. Zamani, J. Arbiol, C. Grigoriu, and J. R. Morante, "Catalyst size limitation in vapor-liquid-solid ZnO nanowire growth using pulsed laser deposition," *Thin Solid Films,* vol. 520, pp. 4626-4631, 2012.

[2] B. Q. Cao, J. Zúñiga-Pérez, C. Czekalla, H. Hilmer, J. Lenzner, N. Boukos, *et al.*, "Tuning the lateral density of ZnO nanowire arrays and its application as physical templates for radial nanowire heterostructures," *Journal of Materials Chemistry,* vol. 20, pp. 3848-3854, 2010.

[3] C. C. Weigand, M. R. Bergren, C. Ladam, J. Tveit, R. Holmestad, P. E. Vullum, *et al.*, "Formation of ZnO nanosheets grown by catalyst-assisted pulsed laser deposition," *Crystal Growth and Design,* vol. 11, pp. 5298-5304, 2011.

[4] M. Lorenz, E. M. Kaidashev, A. Rahm, T. Nobis, J. Lenzner, G. Wagner, *et al.*, "Mgx Zn1-x O ($0 \leq x < 0.2$) nanowire arrays on sapphire grown by high-pressure pulsed-laser deposition," *Applied Physics Letters,* vol. 86, pp. 1-3, 2005.

[5] M. H. Huang, Y. Wu, H. Feick, N. Tran, E. Weber, and P. Yang, "Catalytic growth of zinc oxide nanowires by vapor transport," *Advanced Materials,* vol. 13, pp. 113-116, 2001.

[6] P. K. Giri, S. Dhara, and R. Chakraborty, "Effect of ZnO seed layer on the catalytic growth of vertically aligned ZnO nanorod arrays," *Materials Chemistry and Physics,* vol. 122, pp. 18-22, 2010.

[7] A. Marcu, C. Grigoriu, W. Jiang, and K. Yatsui, "Pulsed laser deposition of YBCO thin films in a shadow mask configuration," *Thin Solid Films,* vol. 360, pp. 166-172, 2000.

[8] M. N. Martin, J. I. Basham, P. Chando, and S. K. Eah, "Charged gold nanoparticles in non-polar solvents: 10-min synthesis and 2D self-assembly," *Langmuir,* vol. 26, pp. 7410-7417, // 2010.

[9] N. Pan, H. Xue, M. Yu, X. Cui, X. Wang, J. G. Hou, *et al.*, "Tip-morphology-dependent field emission from ZnO nanorod arrays," *Nanotechnology,* vol. 21, 2010.

[10] J. D. Holmes, K. P. Johnston, R. C. Doty, and B. A. Korgel, "Control of thickness and orientation of solution-grown silicon nanowires," *Science,* vol. 287, pp. 1471-1473, 2000.

[11] R. Mendelsberg, "Photoluminescence of ZnO Grown by Eclipse Pulsed Laser Deposition," Doctor of Philosophy PhD, Department of Physics, University of Canterbury, 2009.

[12] D. B. Chrisey and G. K. Hubler, *Pulsed Laser Deposition of Thin Films*: Wiley, 1994.

[13] L. C. Tien, D. P. Norton, S. J. Pearton, H. T. Wang, and F. Ren, "Nucleation control for ZnO nanorods grown by catalyst-driven molecular beam epitaxy," *Applied Surface Science,* vol. 253, pp. 4620-4625, // 2007.

[14] M. Yan, H. T. Zhang, E. J. Widjaja, and R. P. H. Chang, "Self-assembly of well-aligned gallium-doped zinc oxide nanorods," *Journal of Applied Physics,* vol. 94, pp. 5240-5246, // 2003.

[15] A. B. Hartanto, X. Ning, Y. Nakata, and T. Okada, "Growth mechanism of ZnO nanorods from nanoparticles formed in a laser ablation plume," *Applied Physics A: Materials Science and Processing,* vol. 78, pp. 299-301, 2004.

[16] J. Zúñiga-Pérez, A. Rahm, C. Czekalla, J. Lenzner, M. Lorenz, and M. Grundmann, "Ordered growth of tilted ZnO nanowires: Morphological, structural and optical characterization," *Nanotechnology,* vol. 18, 2007.

[17] Y. Sun, R. P. Doherty, J. L. Warren, and M. N. R. Ashfold, "Effect of incident fluence on the growth of ZnO nanorods by pulsed excimer laser deposition," *Chemical Physics Letters,* vol. 447, pp. 257-262, // 2007.

[18] A. Marcu, F. Stokker, R. R. Zamani, C. P. Lungu, and C. Grigoriu, "High repetition rate laser ablation for vapor-liquid-solid nanowire growth," *Current Applied Physics,* vol. 14, pp. 614-620, 2014.

[19] A. O. Dikovska, N. N. Nedyalkov, and P. A. Atanasov, "Fabrication of ZnO nanorods using metal nanoparticles as growth nuclei," *Materials Science and Engineering B: Solid-State Materials for Advanced Technology,* vol. 176, pp. 1548-1551, // 2011.

[20] F. Falyouni, L. Benmamas, C. Thiandoume, J. Barjon, A. Lusson, P. Galtier, *et al.*, "Metal organic chemical vapor deposition growth and luminescence of ZnO micro- and nanowires," *Journal of Vacuum Science and Technology B:Nanotechnology and Microelectronics,* vol. 27, pp. 1662-1666, 2009.

[21] A. Marcu, M. Goyat, T. Yanagida, and T. Kawai, "ZnO nanowire mophology control in pulsed laser deposition," *Journal of Optoelectronics and Advanced Materials,* vol. 11, pp. 421-424, 2009.

[22] M. Madel, Y. Xie, I. Tischer, B. Neuschl, M. Feneberg, R. Frey, *et al.*, "Catalytic growth of hexagonally aligned zno nanorods," *Physica Status Solidi (B) Basic Research,* vol. 248, pp. 1915-1918, 2011.

[23] A. Ohtomo, K. Tamura, K. Saikusa, K. Takahashi, T. Makino, Y. Segawa, *et al.*, "Single crystalline ZnO films grown on lattice-matched ScAIMgO4(0001) substrates," *Applied Physics Letters,* vol. 75, pp. 2635-2637, 1999.

[24] J. S. Liu, C. X. Shan, S. P. Wang, F. Sun, B. Yao, and D. Z. Shen, "A route to single-crystalline ZnO films with low residual electron concentration," *Journal of Crystal Growth,* vol. 312, pp. 2861-2864, 2010.

[25] S. F. Chichibu, A. Tsukazaki, M. Kawasaki, K. Tamura, Y. Segawa, T. Sota, *et al.*, "Photoreflectance spectra of a ZnO heteroepitaxial film on the nearly lattice-matched ScAlMgO4 (0001) substrate grown by laser molecular-beam epitaxy," *Applied Physics Letters,* vol. 80, pp. 2860-2862, 2002.

[26] Y. Chen, D. M. Bagnall, Z. Zhu, T. Sekiuchi, K. T. Park, K. Hiraga, *et al.*, "Growth of ZnO single crystal thin films on c-plane (0 0 0 1) sapphire by plasma enhanced molecular beam epitaxy," *Journal of Crystal Growth,* vol. 181, pp. 165-169, 1997.

[27] A. R. Hyndman, M. W. Allen, and R. J. Reeves, "Growth of epitaxial ZnO films on sapphire substrates by plasma assisted molecular beam epitaxy," in *Proceedings of SPIE - The International Society for Optical Engineering,* 2015.

[28] J. B. Baxter and E. S. Aydil, "Epitaxial growth of ZnO nanowires on a- and c-plane sapphire," *Journal of Crystal Growth,* vol. 274, pp. 407-411, // 2005.

[29] Ü. Özgür, Y. I. Alivov, C. Liu, A. Teke, M. A. Reshchikov, S. Doğan, *et al.*, "A comprehensive review of ZnO materials and devices," *Journal of Applied Physics,* vol. 98, pp. 1-103, 2005.

[30] M. H. Huang, S. Mao, H. Feick, H. Yan, Y. Wu, H. Kind, *et al.*, "Room-temperature ultraviolet nanowire nanolasers," *Science,* vol. 292, pp. 1897-1899, 2001.

[31] Z. L. Wang, "Zinc oxide nanostructures: Growth, properties and applications," *Journal of Physics Condensed Matter,* vol. 16, pp. R829-R858, 2004.

[32] Y. C. Her, J. Y. Wu, Y. R. Lin, and S. Y. Tsai, "Low-temperature growth and blue luminescence of SnO2 nanoblades," *Applied Physics Letters,* vol. 89, 2006.

[33] R. Yang, J. Zheng, J. Huang, X. Z. Zhang, J. L. Qu, and X. G. Li, "Low-temperature growth of vertically aligned In2O3 nanoblades with improved lithium storage properties," *Electrochemistry Communications,* vol. 12, pp. 784-787, 2010.

[34] I. L. Farrell, "Growth of Metal-Nitride Thin Films by Pulsed Laser Deposition," Doctor of Philosophy PhD, Department of Physics, University of Canterbury, 2010.

[35] A. Marcu, C. Grigoriu, C. P. Lungu, T. Yanagida, and T. Kawai, "Ablation particles parameters influences on VLS oxide nanowire growing," *Physica E: Low-dimensional Systems and Nanostructures,* vol. 44, pp. 1071-1073, 3// 2012.

[36] A. M. Lord, T. G. Maffeis, A. S. Walton, D. M. Kepaptsoglou, Q. M. Ramasse, M. B. Ward, *et al.*, "Factors that determine and limit the resistivity of high-quality individual ZnO nanowires," *Nanotechnology,* vol. 24, 2013.

[37] J. P. Kar, S. N. Das, J. H. Choi, T. I. Lee, and J. M. Myoung, "Study of the morphological evolution of ZnO nanostructures on various sapphire substrates," *Applied Surface Science,* vol. 256, pp. 4995-4999, 6/1/ 2010.

[38] T. Moriyama and S. Fujita, "Growth behavior of nonpolar ZnO on M-plane and R-plane sapphire by metalorganic vapor phase epitaxy," *Japanese Journal of Applied Physics, Part 1: Regular Papers and Short Notes and Review Papers,* vol. 44, pp. 7919-7921, 2005.

[39] H. T. Ng, B. Chen, J. Li, J. Han, M. Meyyappan, J. Wu, *et al.*, "Optical properties of single-crystalline ZnO nanowires on m-sapphire," *Applied Physics Letters,* vol. 82, pp. 2023-2025, 2003.

[40] K. Shi, A. L. Yang, J. Wang, H. P. Song, X. Q. Xu, L. Sang, *et al.*, "The effect of different oriented sapphire substrates on the growth of polar and non-polar ZnMgO by MOCVD," *Journal of Crystal Growth,* vol. 314, pp. 39-42, 2011.

[41] B. Fuhrmann, H. S. Leipner, H. R. Höche, L. Schubert, P. Werner, and U. Gösele, "Ordered arrays of silicon nanowires produced by nanosphere lithography and molecular beam epitaxy," *Nano Letters,* vol. 5, pp. 2524-2527, 2005.

[42] R. Heinhold, G. T. Williams, S. P. Cooil, D. A. Evans, and M. W. Allen, "Influence of polarity and hydroxyl termination on the band bending at ZnO surfaces," *Physical Review B - Condensed Matter and Materials Physics,* vol. 88, 2013.

[43] W. Chen, A. Y. Fadeev, M. C. Hsieh, D. Öner, J. Youngblood, and T. J. McCarthy, "Ultrahydrophobic and ultralyophobic surfaces: some comments and examples," *Langmuir,* vol. 15, pp. 3395-3399, 1999.

[44] D. Öner and T. J. McCarthy, "Ultrahydrophobic surfaces. Effects of topography length scales on wettability," *Langmuir,* vol. 16, pp. 7777-7782, 2000.

[45] J. B. Brzoska, I. Ben Azouz, and F. Rondelez, "Silanization of solid substrates: A step toward reproducibility," *Langmuir,* vol. 10, pp. 4367-4373, 1994.

[46] C. D. Keating, M. D. Musick, M. H. Keefe, and M. J. Natan, "Kinetics and Thermodynamics of Au Colloid Monolayer Self-Assembly Undergraduate Experiments in Surface and Nanomaterials Chemistry," *Journal of Chemical Education,* vol. 76, pp. 949-955, 1999.

[47] A. V. Krasnoslobodtsev and S. N. Smirnov, "Effect of water on silanization of silica by trimethoxysilanes," *Langmuir,* vol. 18, pp. 3181-3184, 2002.

Chapter 4: Size Control of ZnO Nanowires by Catalyst Particle Size

4.1 Motivation

The work presented in Chapter 3 described the optimisation of the University of Canterbury eclipse PLD (EPLD) system for the growth of ZnO nanowires catalysed by colloidal Au nanoparticles tethered to sapphire substrates using APTMS as catalysts for VLS growth. The reliable production of nanowires with tip diameters close to the size of the 13 nm Au colloids used to catalyse their growth was demonstrated. In this chapter, these investigations are extended to explore the possibility of modulating the tip diameters of nanowires by changing the size of the Au colloid catalysts. Atomically precise Au clusters are then explored as catalysts to investigate whether a lower limit exists on the diameter of Au nanoparticles that can catalyse the VLS mechanism responsible for EPLD nanowire growth.

4.2 Commercial Au Colloids

4.2.1 Experimental Limits of In-House Synthesised Colloids

After the departure of collaborator Ms. Ke at the conclusion of her study, the direct supply of the Au colloids used to catalyse ZnO nanowire growth was reduced and the quality and homogeneity of available colloids decreased. This caused a decline in the reproducibility of the nanowire growths. Figure 1 shows a high resolution SEM image of inhomogeneous Au colloids overlaid with measurements of the particle sizes, taken using the point to point measurement tool on the Raith 150 SEM.

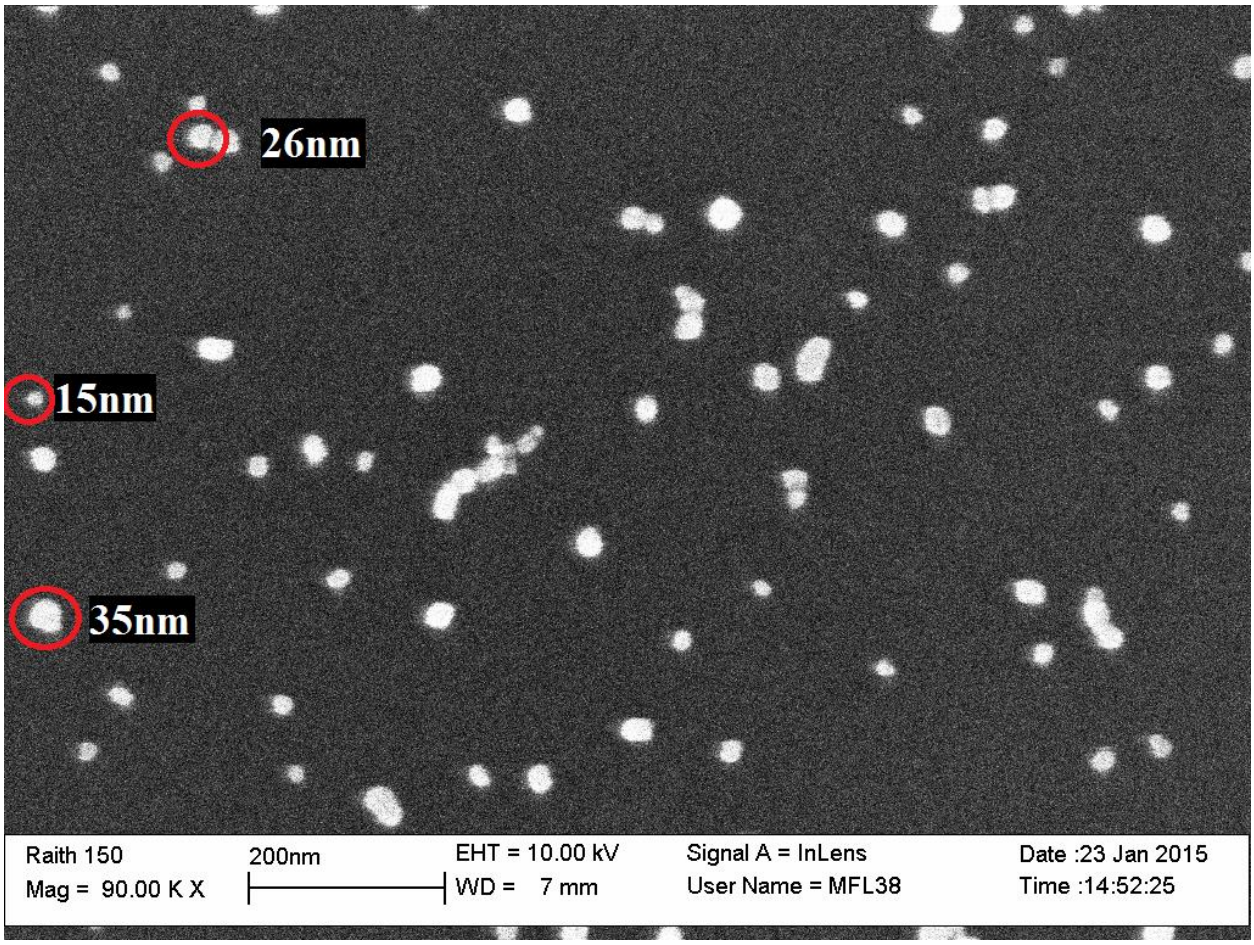

Figure 1: Poor homogeneity of gold colloids which are nominally supposed to be 13 nm in diameter. Measurements were performed using the point-to-point measurement tool of the Raith 150 SEM.

These colloids, which were intended to be closely distributed in sizes around 13 nm in diameter, included particles as large as 35 nm. Nanowires grown using these colloids showed a similar range of tip diameters as shown in Figure 2. This variation in colloid size was unhelpful for assessing the role of colloid size on nanowire morphology. Adjusting key parameters of the colloid deposition such as the immersion time for both the APTMS and the colloids themselves proved ineffective at improving the nanowire uniformity, indicating that the size inhomogeneity was not due to aggregation or accretion of other material around the colloids. To improve the size homogeneity of the catalyst nanoparticles, a selection of commercially prepared gold colloids suspended in a citrate buffer were purchased from Sigma-Aldrich, MO, USA. Gold colloids in sizes 5 nm, 10 nm, 20 nm, 30 nm, 40 nm and 60 nm were purchased as shown in Figure 3.

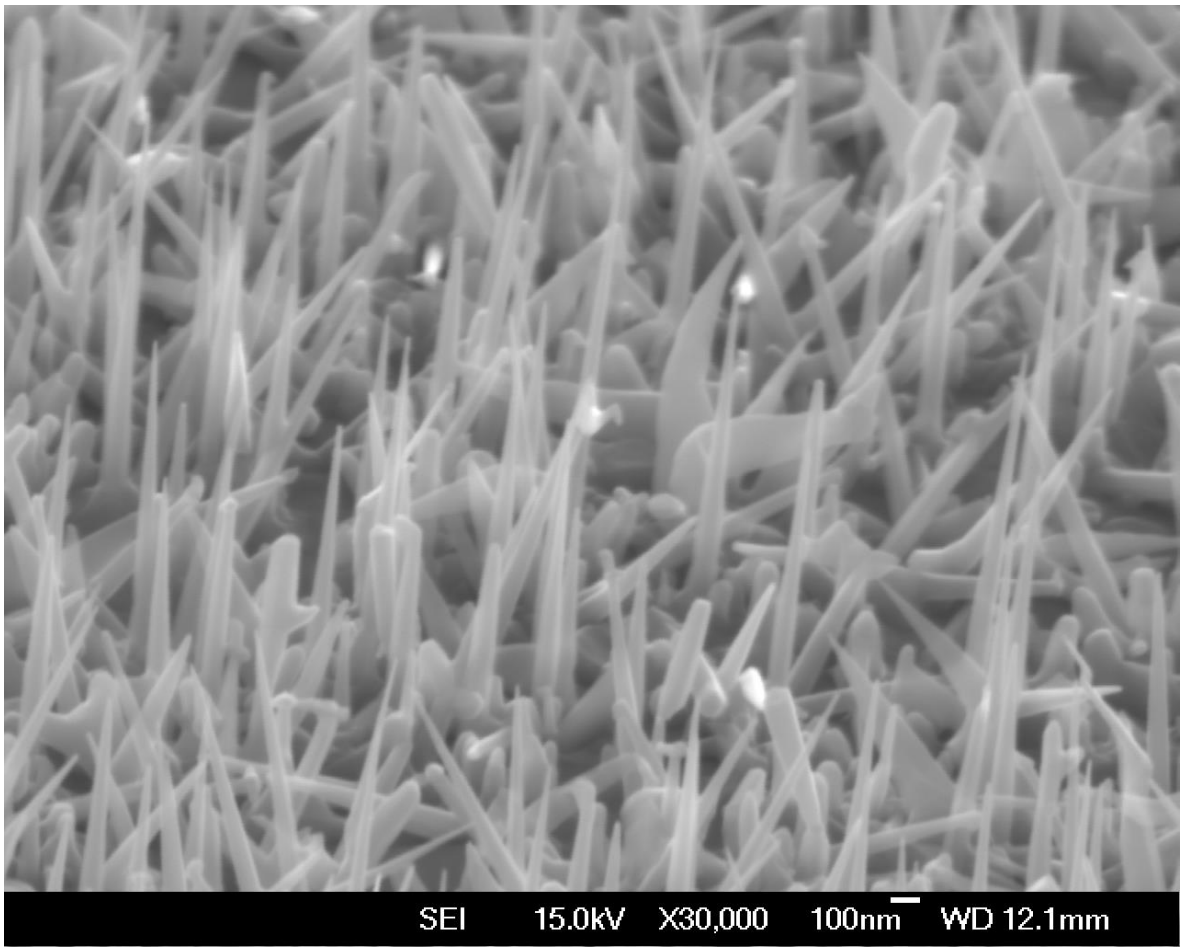

Figure 2: ZnO nanowires grown using inhomogeneous gold colloids as catalysts. There is good vertical alignment and many of the nanowires are very fine, however the tip sizes and morphology of the nanowires varies significantly between individual wires. (Growth 71)

Figure 3: Commercially produced gold nanoparticles supplied by Sigma-Aldrich. From left: 5 nm, 10 nm, 20 nm, 30 nm, 40 nm, 60 nm and 80 nm.

The commercial colloids were applied to conductive silicon samples by simple drop coating to examine the homogeneity of the nanoparticle sizes. Figure 4 shows SEM images of these colloids. Owing to the small size of the colloids and the extreme magnification required to view them, image quality was poor.

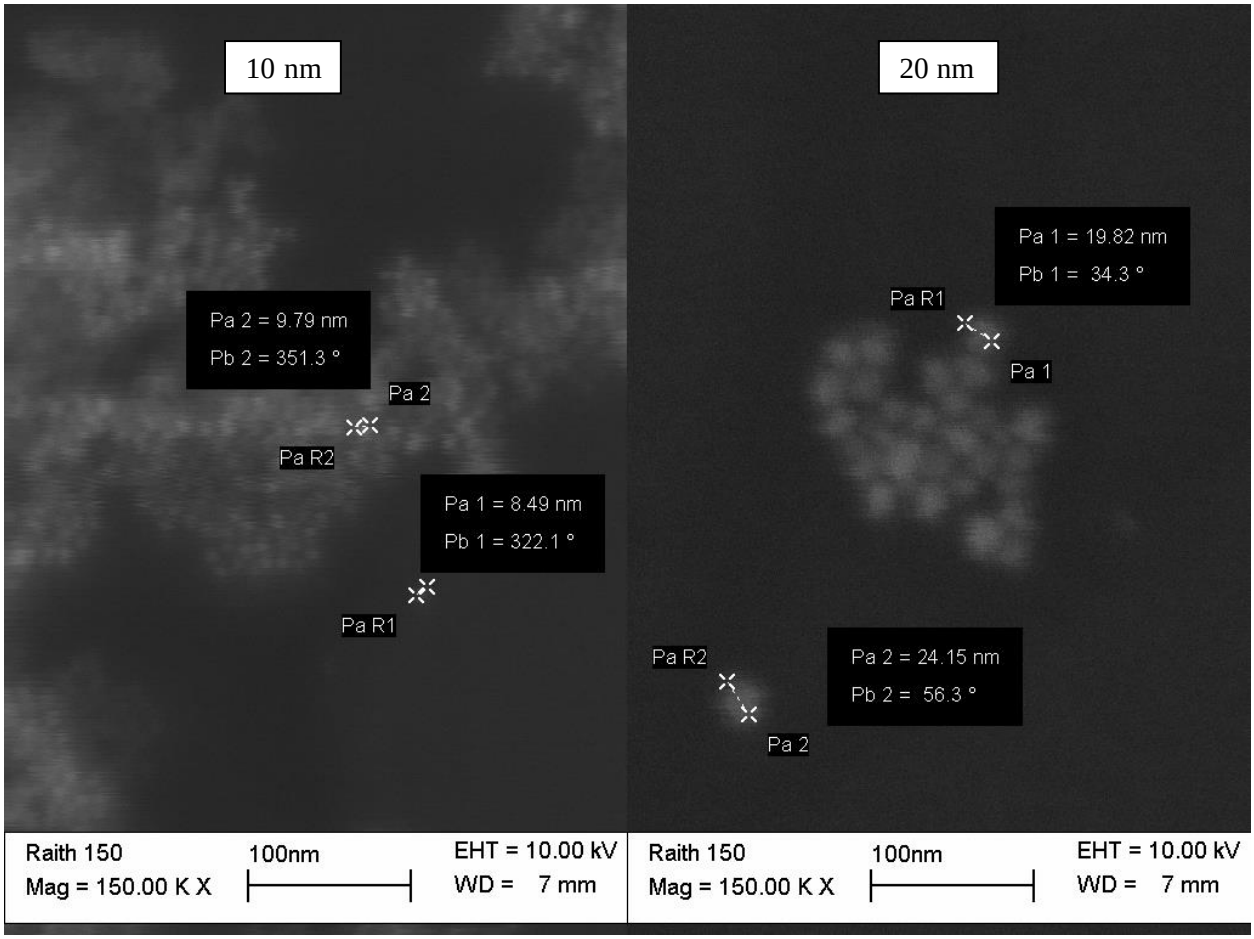

Figure 4: High resolution SEM image of commercially produced 10nm (left) and 20nm (right) colloids.

These medium-small colloids (10 nm and 20 nm) were of greatest interest, as their sizes were close to the 13 nm nominal size of the colloids produced by the chemical synthesis method. Using simple drop coating and no APTMS, there was significant aggregation of the colloids, but their individual diameters were relatively uniform. Point to point measurement using the Raith 150 indicated that their diameters were close to the prescribed values (± 2 nm for the 10 nm colloids and ±5 nm for the 20 nm colloids). Figure 5 shows images of 30 nm, 40 nm, 60 nm and 80 nm gold colloids. The larger colloids seemed to show greater inhomogeneity than the smaller colloids. The larger size nanoparticles also seemed to be less prone to aggregating, even without APTMS tethering.

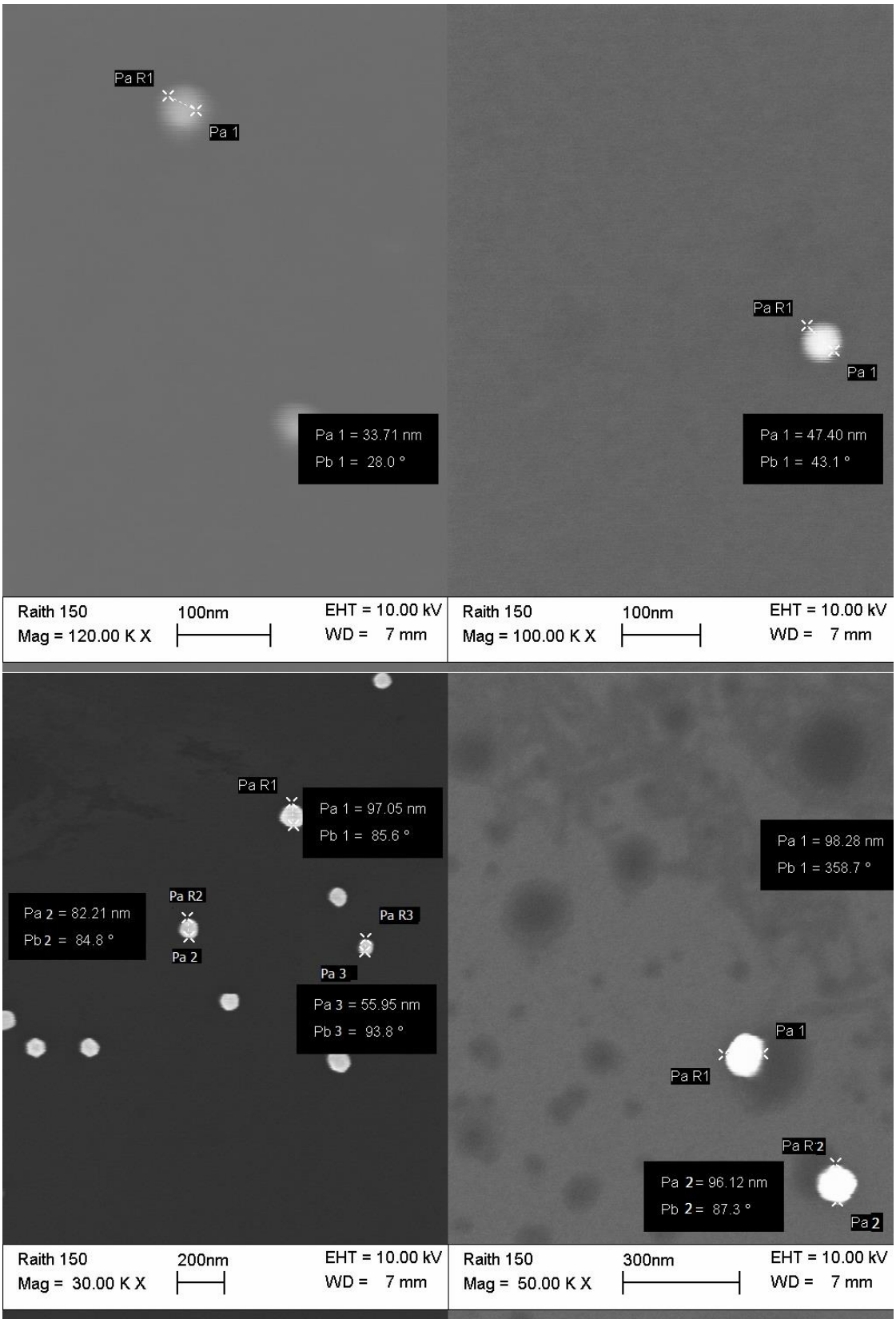

Figure 5: Larger gold colloids showed more significant deviations in diameter. Top left: 30 nm, Top Right: 40 nm, Bottom Left: 60 nm, Bottom Left: 80 nm.

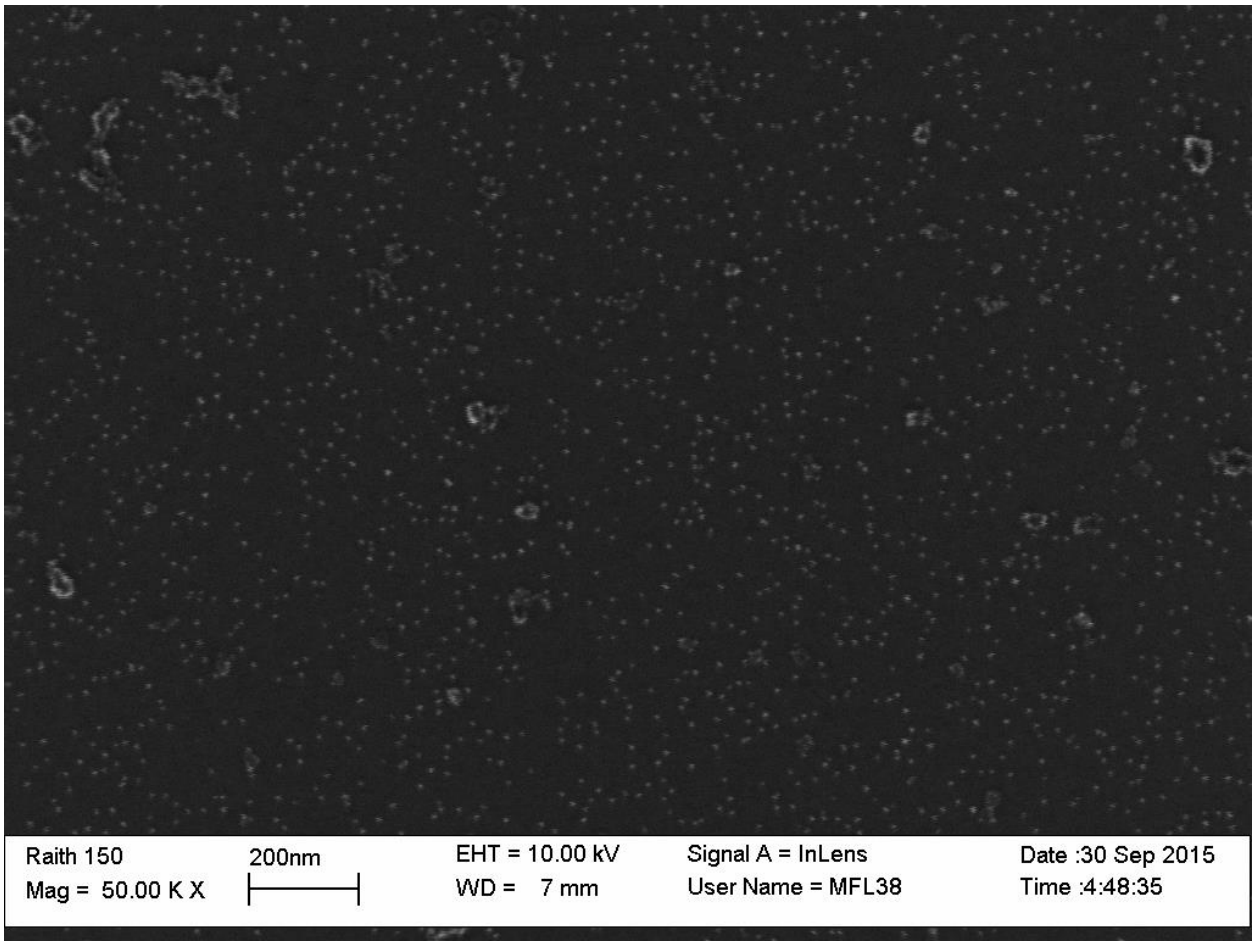

Figure 6: Commercially produced 5 nm Au colloids on a silicon substrate.

The 5 nm Au colloids were extremely difficult to measure due to their size and are shown in Figure 6. However, the size of these colloids appeared to be homogeneous.

4.2.2 Enhanced Drop Coating and Density Experiments

The commercially prepared Au colloid solutions were expensive compared to the cost of colloids routinely produced by Ms Ke. Consequently, it was not feasible to use the dip coating method to coat the substrates as this method produced a large amount of waste solution. The more efficient drop coating method was therefore re-evaluated and optimised. A drawback of the drop coating method was the formation of edge beads and uneven coating of colloids across the sample. This could be reduced using a single, large droplet, such that the drop covered the entire sample and was held in place by surface tension. The droplet could be left to completely dry, or it could be washed off after a certain deposition time had elapsed. This represented a compromise between dip coating and drop coating. This method was also combined with the standard application of APTMS to reduce the colloid aggregation observed in Figure 4. To determine an appropriate

length of time for this hybrid colloid deposition method, an experiment was conducted by applying 10 nm colloids to two clean, conductive silicon substrates. The remaining colloid solution was rinsed off the substrates after one and three hours' deposition respectively. Figure 7 shows the difference in colloid density between these two samples.

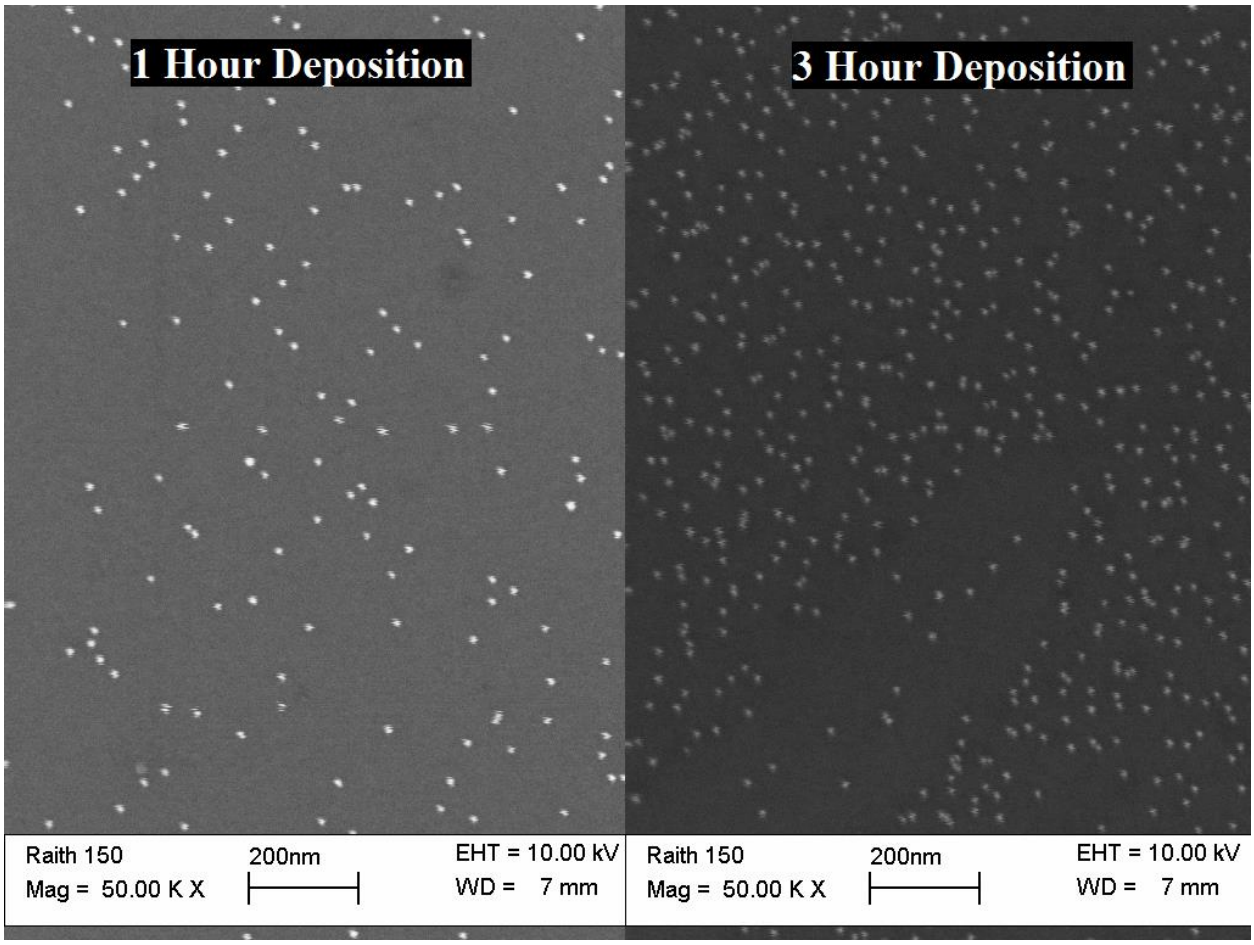

Figure 7: An increase in deposition time from one hour (left) to three hours (right) caused an increase in density of almost 400%.

Comparing the number of colloids shown on the left and right hand sides of Figure 7 shows an increase in the number of colloids from 147 to 559. This represents a 380% increase in density, similar to that expected if the deposited colloid density increased linearly with deposition time. After three hours, the droplet of colloid on the surface of the substrate began to evaporate and visibly decreased in volume. A silicon substrate coated with APTMS and colloids and left overnight to evaporate completely is shown in Figure 8. This complete evaporation resulted in a further increase in colloid density compared to the 3 hour colloid deposition, but significant aggregation occurred even with APTMS treatment.

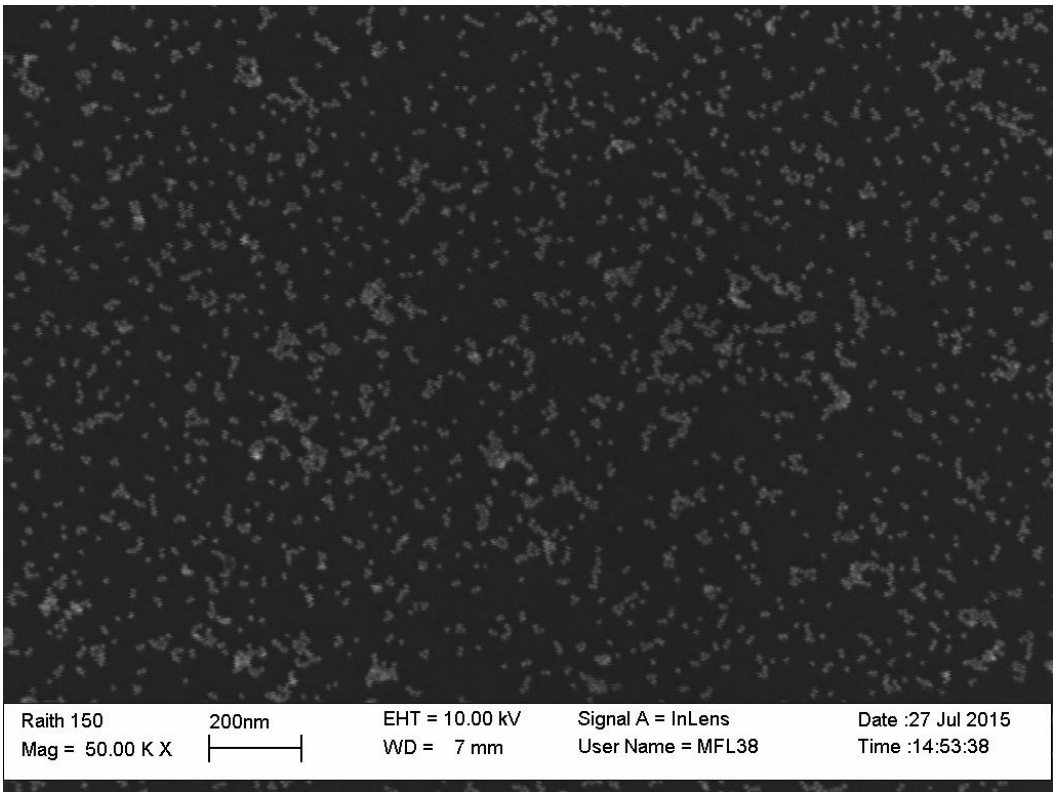

Figure 8: SEM image showing a droplet of 10 nm gold colloids left to evaporate overnight on a silicon substrate

The colloids are expected to liquify during the VLS process and therefore an aggregation of colloids will merge to provide one larger growth nucleus for a single large nanorod. The space between neighbouring groups of aggregated colloids was similar on the completely evaporated substrate to the space between neighbouring single colloids in the three hour deposition. It can therefore be assumed that the real density of nanowire growth sites (and thus, the resultant density of nanowires) is not significantly improved by depositing colloids for more than three hours. As little to no aggregation was seen after 3 hours, but the density of sites was similar to overnight, 3 hours was considered appropriate for growth using this method.

4.3 Commercial Colloid Nanowire Growth

4.3.1 Size Selectivity Growth

A ZnO nanowire EPLD growth was conducted to determine if colloids of different sizes would produce different tip sizes in the resulting nanowires. Three c-plane sapphire substrates, treated with APTMS were coated for one hour with commercial gold colloids of diameters 10 nm, 20 nm and 40 nm respectively and nanowires were grown by EPLD using our standard method as optimised in Chapter 3. With reference to

Figure 9 illustrating the positions on the sample heater, the 10 nm Au colloid sample was placed in position 1, the 20 nm Au colloid sample in position 2 and the 40 nm Au colloid sample in position 3. The resulting nanowires were imaged in the optimal area immediately behind the eclipse plate as discussed in Chapter 3.

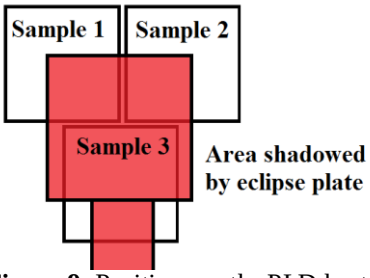

Figure 9: Positions on the PLD heater with reference to the eclipse plate.

Figure 10 shows a trend of decreasing nanowire density with increasing Au colloid size. A significant result of this growth was that the tips of the nanowires in each sample could be regularly observed to be the same diameter as the colloids that catalysed their growth. Figure 11 shows higher magnification SEM images of the nanowire tips themselves with measured diameters attached. Using 40 nm colloids, there was only sparse growth, due to the large separation between the colloids. Where nanowires did grow, there was often a visible gold droplet attached to the end of each wire. The sample grown using the 10 nm Au colloids displayed the greatest amount of order, with most of the nanowires growing normal to the substrate surface as shown in a 45° side view image in Figure 12.

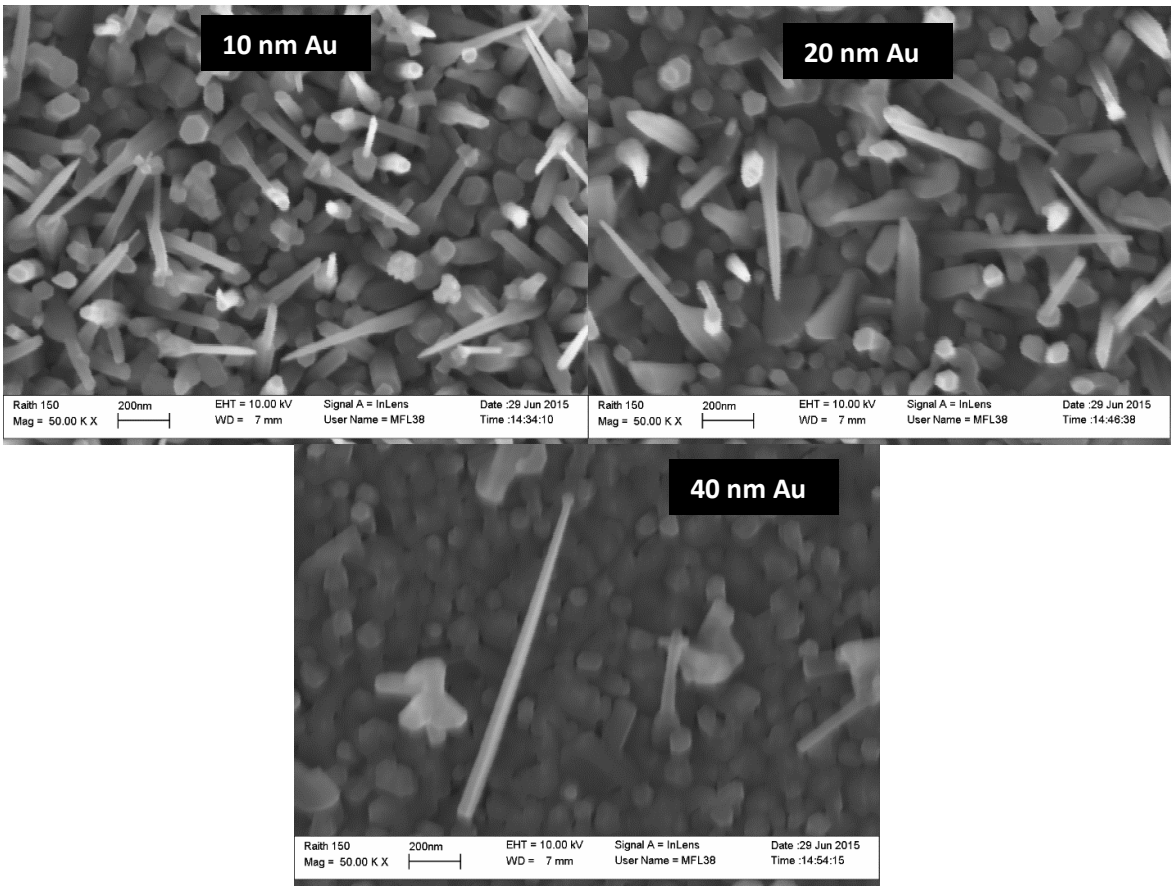

Figure 10: ZnO nanowires grown using different size gold colloids as catalysts. Left: 10 nm, Right: 20nm, Bottom: 40 nm. (Growth 80)

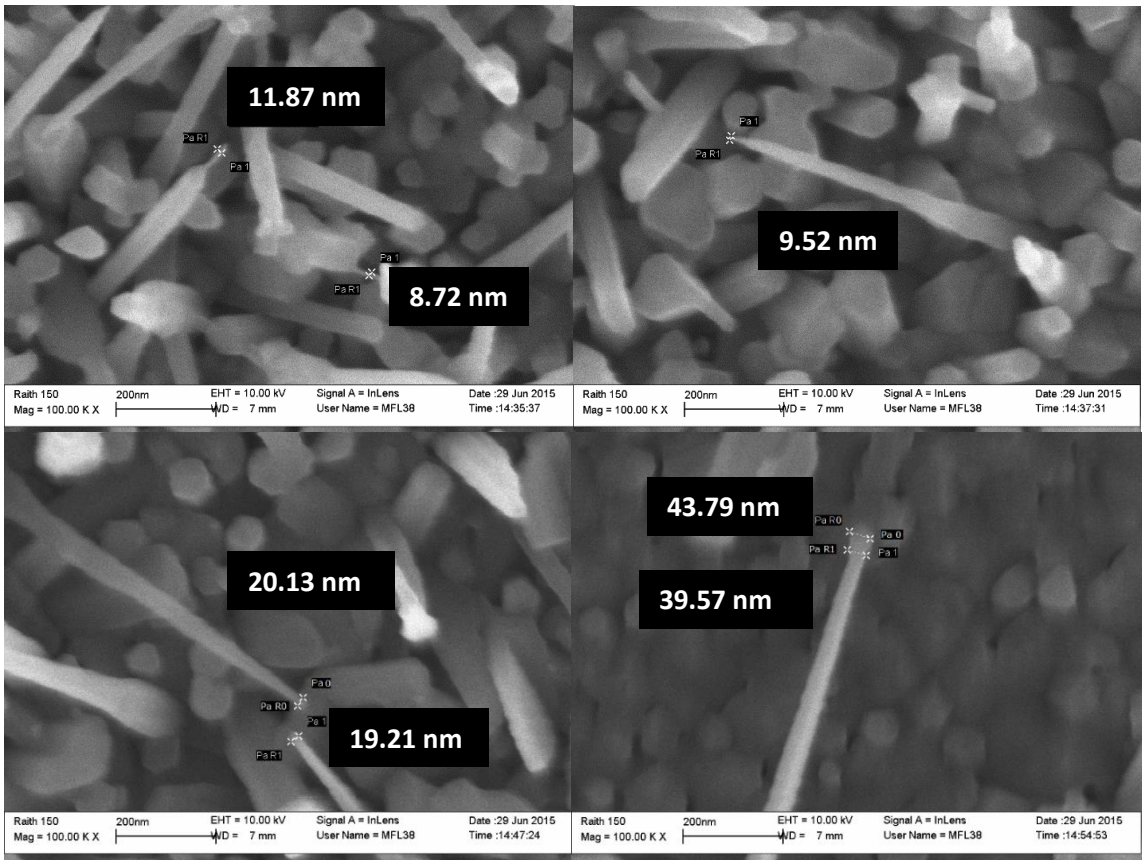

Figure 11: High resolution SEM images showing the tip diameters of ZnO nanowires catalysed by different sized gold colloids. Top Left: 10 nm "aerials", Top Right: 10 nm tapered tip, Bottom Left: 20 nm, Bottom Right: 40 nm with measurements of the droplet and the nanowire tip. (Growth 80)

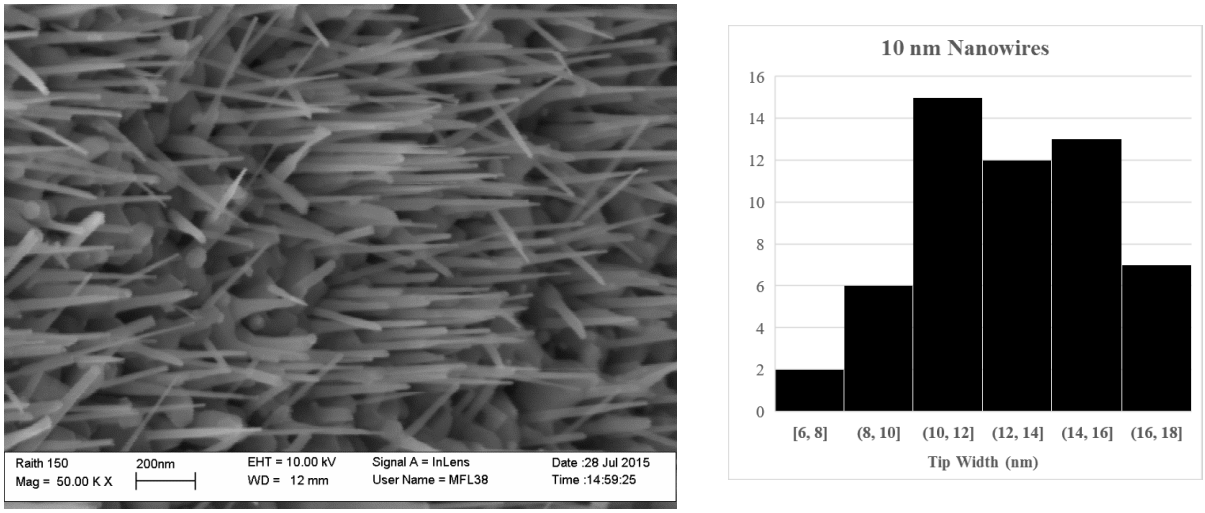

Figure 12: Left: Highly ordered nanowires grown using 10 nm gold colloids viewed from side view of 45°. Right: Histogram showing the distribution of tip diameters. The mean was 12.9 nm, with a standard deviation of 2.5 nm.

These growths clearly showed that there was a direct link between the size of the Au catalyst colloids and the tip diameter of the resulting nanowires as commonly predicted by the literature [1, 2]. Manual measurements of the nanowire tip diameters from SEM micrographs of the 10 nm colloid catalysed growth (Figure 12) found that the fully formed nanowires (those that displayed the dominant, tapered morphology down to a point) had a mean tip diameter of 12.9 nm and a standard deviation of 2.5 nm, slightly larger than the 10 nm colloids, but within the range of measurement error. A further explanation for this error is the fact that a spherical colloid melting into a droplet as expected in VLS, can flatten out into a hemisphere, potentially increasing its diameter by approximately 25% if the volume remains constant. This size selection phenomena was reproducible and was repeated in several subsequent growths. The alignment and ordering of the nanowires increased inversely with the size of the Au colloids. This was not unexpected as the larger colloids, especially the 40 nm colloids, were much thicker than the 1-10 nm thin-films which are often used in the literature to grow ZnO nanowires [1-4].

4.3.2 An Unusual Nanostructure Morphology

In several areas of the substrates coated with 10 nm gold colloids, the growth of an unusual type of nanostructure morphology was observed. At the end of many of the nanowires, a terminating nanostructure was formed consisting of three short nanowire stubs extending at 120° from a junction in a tetrahedral shape. Figure 13 shows a top down and a 45° side view of these structures. These structures tended to occur close to the centre but above the eclipse plate. With reference to Figure 9, these nanostructures were found at the top right of Sample 1 and the top left of Sample 2 where the flux of incoming material and the likely

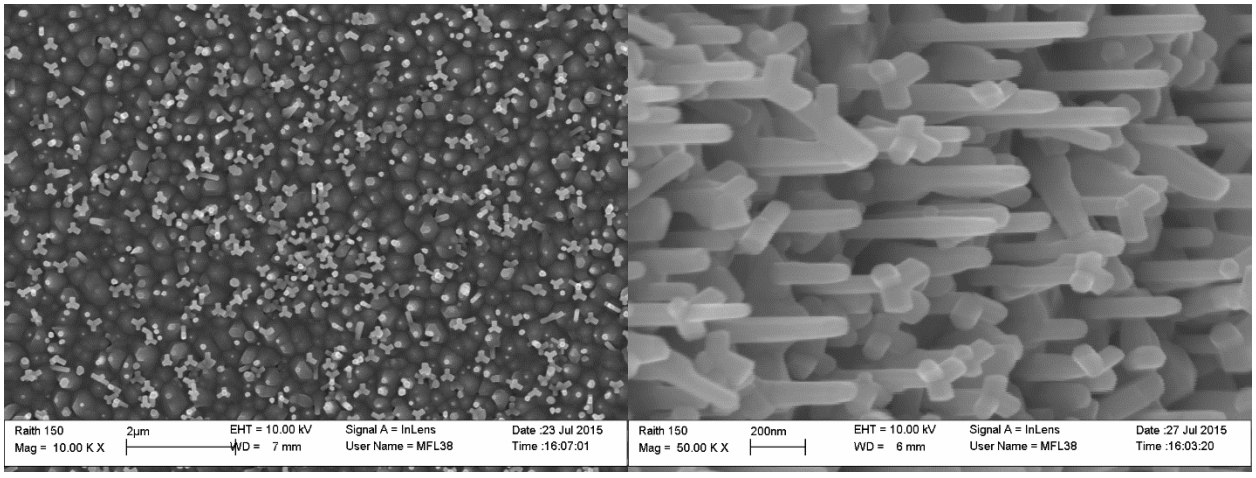

Figure 13: Tetrahedral nanostructures observed in some areas of a growth using 10 nm gold colloids from top-down (left) and from 45° (right). Note that the scale of each elevation is different to better convey the density and morphology of the nanostructures.

presence of macroparticles would be higher than in the optimal area directly behind the eclipse plate. These tetrahedral, terminating nanostructures were observed in several growths using the 10 nm gold colloids.

4.3.3 Low Diameter 5 nm Au Colloid Catalysed Growth

Following the success of the 10, 20 and 40 nm colloids, a growth was performed using APTMS-tethered 5 nm colloids. These colloids are the smallest available from Sigma-Aldrich and are smaller than the droplets produced by the sputtering of an Au target, even when sputtered for less than ten seconds as described in Chapter 3, Section 10.

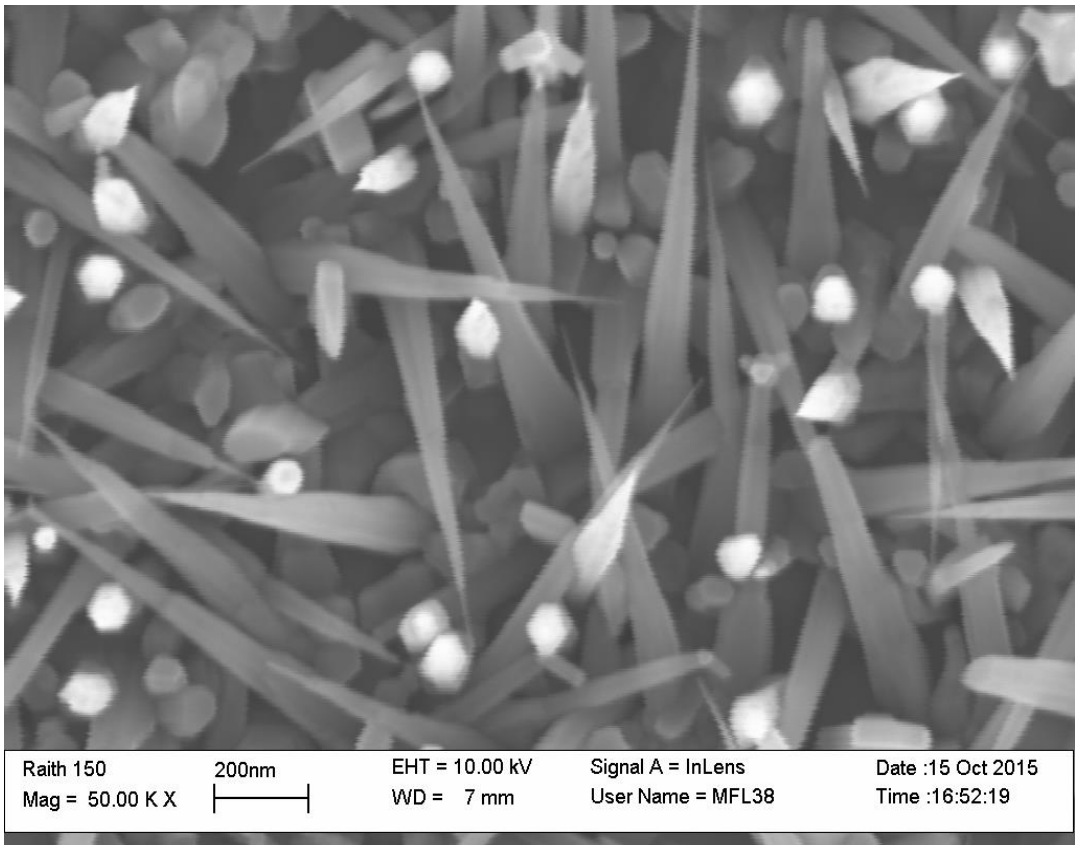

Figure 14: ZnO nanowires grown from 5 nm commercial gold colloids. (Growth 92)

Figure 14 shows the resulting nanowires produced in this growth. Although very tapered, the tips of these nanowires were incredibly fine and consistent with the 5 nm expected diameter. The extreme magnification required to examine the tips was just within the operational limits of the Raith 150 SEM, but manual counts of the nanowires shown in Figure 15 estimate the man at approximately 8.5 nm, with a standard deviation of 2 nm. This error is proportionally similar to that found in measuring the 10 nm catalysed nanowires.

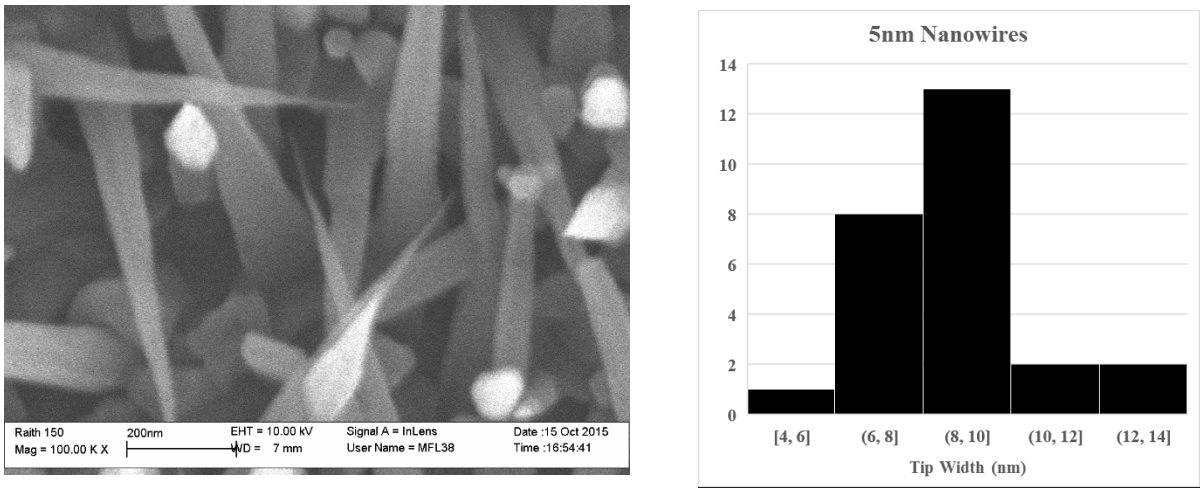

Figure 15: Left: SEM image showing the extremely fine tips of the 5 nm colloid catalysed nanowires. Right: Histogram showing the approximate tip diameters. Mean: 8.5 nm, Std. Dev: 2 nm.

4.3.4 Bending and Welding of Ultra-Fine Nanowires in an SEM Beam

A strange phenomena was observed while imaging these nanowires that has not been previously reported. When the SEM beam was focussed on the fine tips of these nanowires and scanned for a few seconds, occasionally the finest nanowires would spontaneously bend. The movement was very fast, often within a single high speed scan, so that in one frame the wire would be straight and in the next frame it would be bent. The effect was reproducible and likely candidates could be found by selecting especially narrow wires. Further observation revealed that the nanowires were not bending at random, but rather a nanowire would bend in order to connect itself to the tip of another nearby nanowire. The two wires would then become

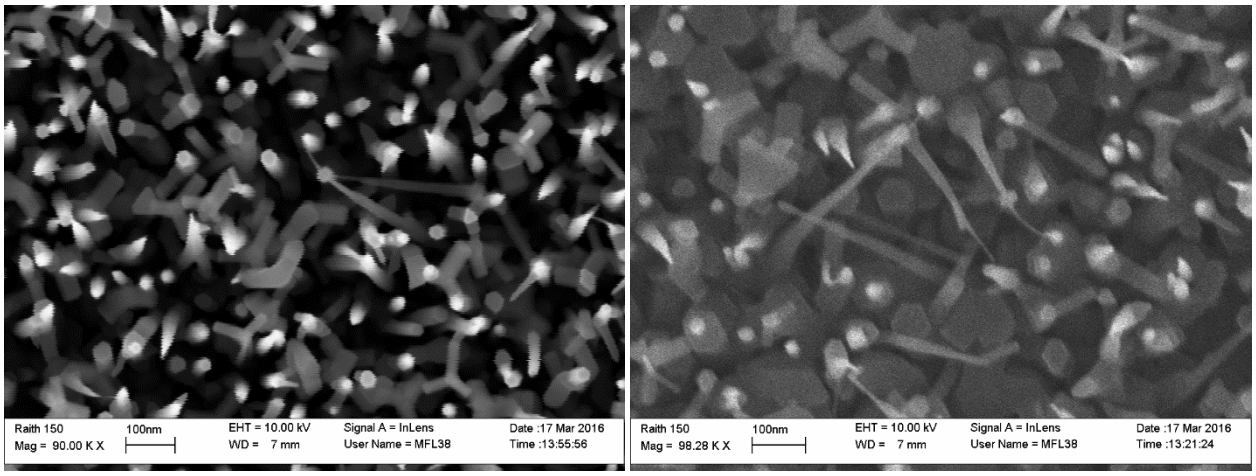

Figure 16: Ultra-fine nanowires which have bent under excitation from the SEM electron beam. The wires fused to the tips of other nanowires nearby and to all observation, this change seemed permanent.

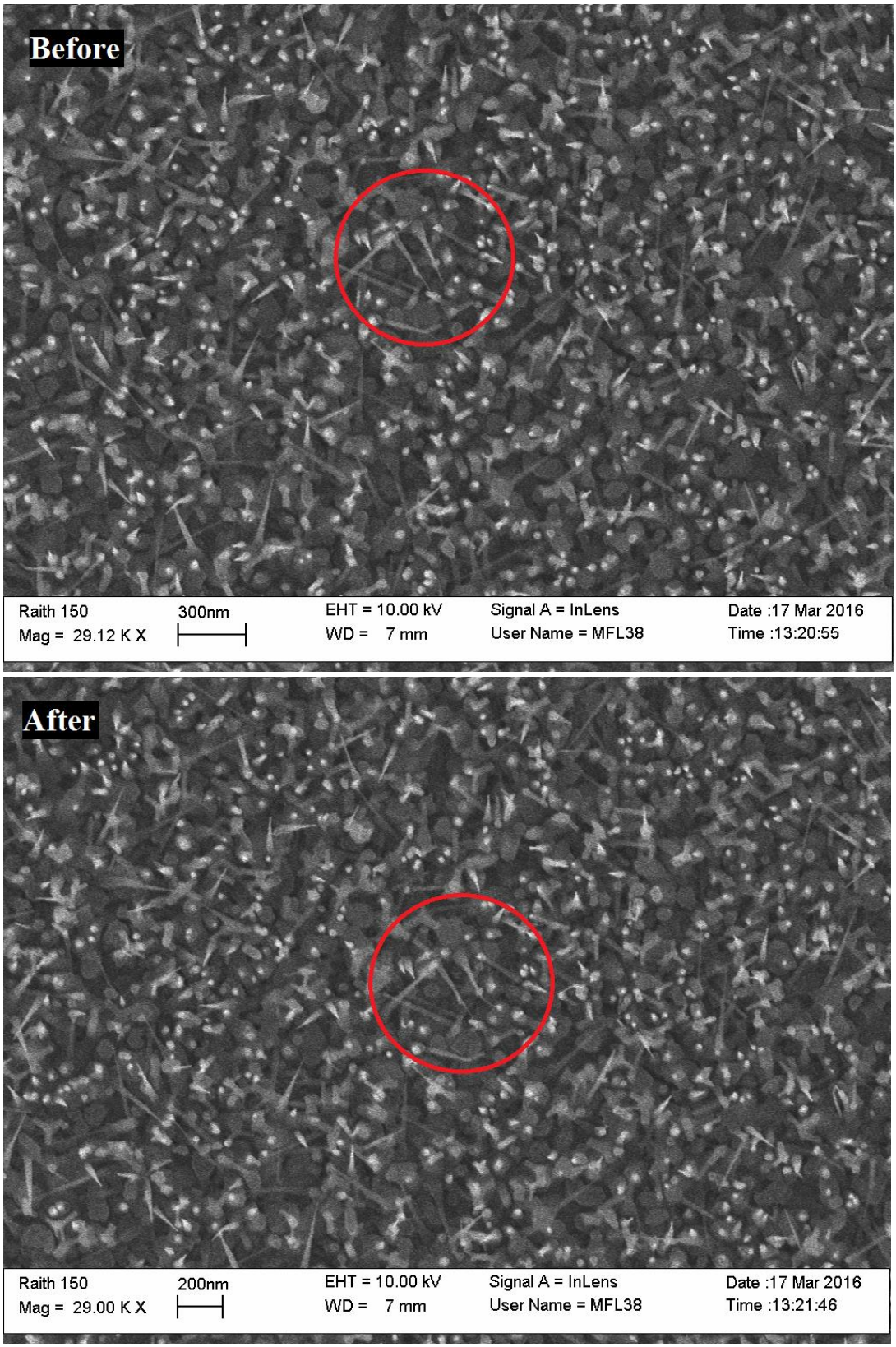

Figure 17: Before and after image of a straight nanowire bending to make contact with a nearby wire. The nanowire on the right bends and attaches at the top to a vertical wire to the right of its tip.

fused together at their tips and no further movement would be observed. This process appeared to be permanent and irreversible. Figures 16 and 17 show the results of this process. Only a few seconds of scanning was needed to cause a narrow wire to bend and so it was rather difficult to obtain a high resolution "before" image of a wire that was likely to bend.

The marking of substrates and nanowire samples by continuous viewing of a single location using the SEM had previously been observed in this work. This usually took the form of a change in the brightness of the area being imaged and would be visible as a darkened rectangle when the magnification was lowered. As described in Chapter 2 Section 3, the SEM uses a beam of electrons to create a profile of the sample surface. The resulting image is not a pattern of photon reflections like our eyes perceive, but rather a picture of the electrical interactions between the beam and the surface [5]. A change in the brightness of a surface therefore indicates a change in its electrical properties caused by the beam. The beam could directly implant electrons or generate secondary electrons in the sample, building up a static charge. It is also possible that the beam current passing through the sample could generate heat by resistive heating.

Local heating of individual nanowires via beam current conduction could explain the bending of the wires, but this heating would be expected to produce a gradual rather than a sudden movement. The fact that bending wires always suddenly attach to another nearby wire suggests a charge-based explanation with one wire becomes negatively charged by absorbing electrons from the beam. Electric fields are strongest at sharp points and so very large fields may occur at the tips of the ultra-fine nanowires. The presence of a large negative charge density near the tips of the nanowires repels free electrons from neighbouring nanowires, creating an induced positive charge that attracts the negatively charged wire. Once the magnitude of these charges reaches a certain level, the electrostatic attraction overwhelms the lateral strength of the weakest nanowire which then snaps to the stronger wire, allowing the accumulated charge to dissipate. Energy released by this neutralisation of charge could be responsible for the wires fusing. A TEM cross-section of a bent nanowire would be extremely useful in assessing how this bending affects the lattice structure of the nanowire, however it would be very difficult to transfer these bent wires and their neighbours onto a TEM grid.

4.4 Au Clusters

4.4.1 Au101 Clusters

The success of the 5 nm gold colloids in catalysing ZnO nanowire growth raised the question of "how small is too small?" Gold is usually a metal, but below a size of approximately 2 nm, Au nanoparticles lose their

metallic nature [6-8]. This is because when the number of atoms in a cluster of metal atoms falls below a certain limit, the bonding structure moves away from metallic bonding (with a lattice of positive nuclei and a sea of free valance electrons) and becomes more like a covalently bonded molecule. In such a cluster, gold atoms bond covalently into a centred-icosahedral structure with a specific number of atoms, much like a C_{60} bucky-ball. Gold clusters of this size are of interest to chemists for their properties in catalysing chemical reactions such as the selective oxidation of styrene [9]. As well as the colloids used in Chapter 3, My collaborator Ms Ke's supervisor, Dr Golovko has done a lot of work in the production and analysis of gold clusters, ranging in size from 6 atoms to 101 atoms [6, 7, 9-11].

In searching for a lower limit of gold nanoparticle size for ZnO nanowire catalysis, it was reasonable to start from the largest available clusters and work down, i.e. Au101 (101 Au atoms). These clusters were prepared by Dr Golovko as a solid powder and could be dissolved in chloroform. Au101 is approximately 1.5 nm in diameter, just below the 2 nm critical diameter for metallic behaviour [6]. These are shown in Figure 18. The enhanced method of drop coating was employed to deposit the Au101 clusters onto the sapphire substrates, but in order to ensure that a comparable amount of Au was being applied to the substrates as in previous growths, an appropriate concentration needed to be calculated. To do this, the mass of Au colloids used in previous growths was estimated as follows:

- The bulk density of gold is 19,282 kg/m^3.
- A spherical, 10 nm diameter gold colloid has a volume of 5.23 x 10^{-25} m^3.
- Therefore one 10 nm diameter gold colloid has a mass of 1.01x10^{-20} kg.
- Figure 7 (earlier) shows an approximate colloid density after an hour's deposition of approximately 5.75x10^{14} colloids/m^2.
- Therefore a 10 mm x10 mm sapphire substrate coated with 10 nm colloids contains approximately 5.75x10^{10} colloids.
- The total mass of gold applied to the substrate is therefore 0.58 µg.

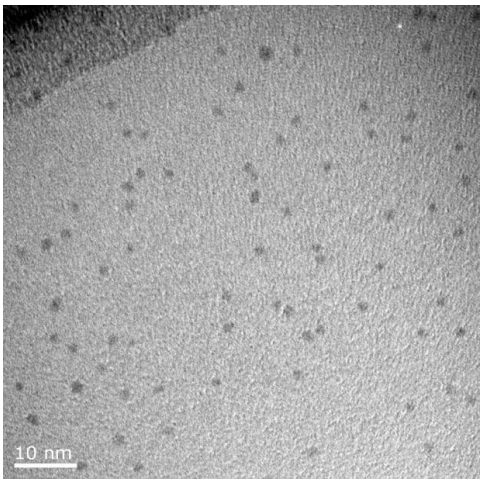

Figure 18: TEM image from Anderson *et al.* [6] showing Au101 clusters.

All gold clusters are stabilised with additional organic chemicals. The formula for Au101 is $Au_{101}[P(C_6H_5)_3]_{21}Cl_5$, which contributes to the weight of the powder. As gold makes up only 77% of the mass of the powder, 0.75 µg was measured to provide the required 0.58 µg of gold.

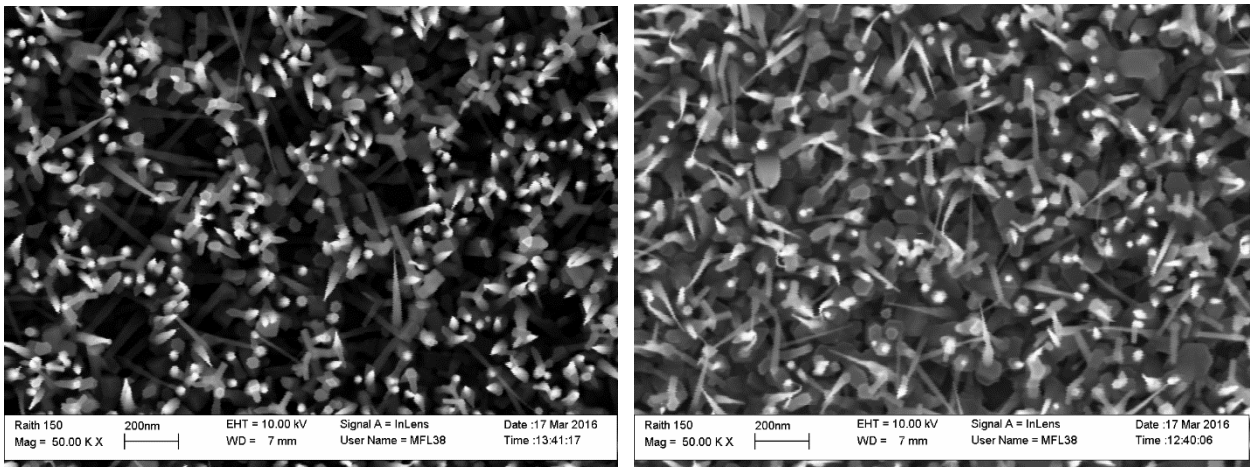

Figure 19: ZnO nanowires catalysed by Au101 clusters on c-plane sapphire without (left) and with (right) APTMS surface modification. The magnification is very high in these images as the fine tips of the wires are very hard to resolve. (Growth 101)

The interaction between APTMS and the Au101 clusters was not certain, so two c-plane sapphire substrates were prepared, one with and one without the standard APTMS coating. The ZnO nanowire growth was conducted using our standard EPLD method described earlier. Both samples produced extremely fine nanowires with tip diameters of the order of 2-4 nm. Figure 19 shows a typical image of each sample. Figure 20 shows attempts to measure the tip diameters which were at the extreme limit of the Raith 150's imaging capability, with 3.79 nm and 2.6 nm measured. These nanowire tips were much smaller than the features the SEM was designed to measure, so the images are of low quality and measurements made are only estimates of the tip diameters. Figure 21 shows two 30° side views of the nanowires.

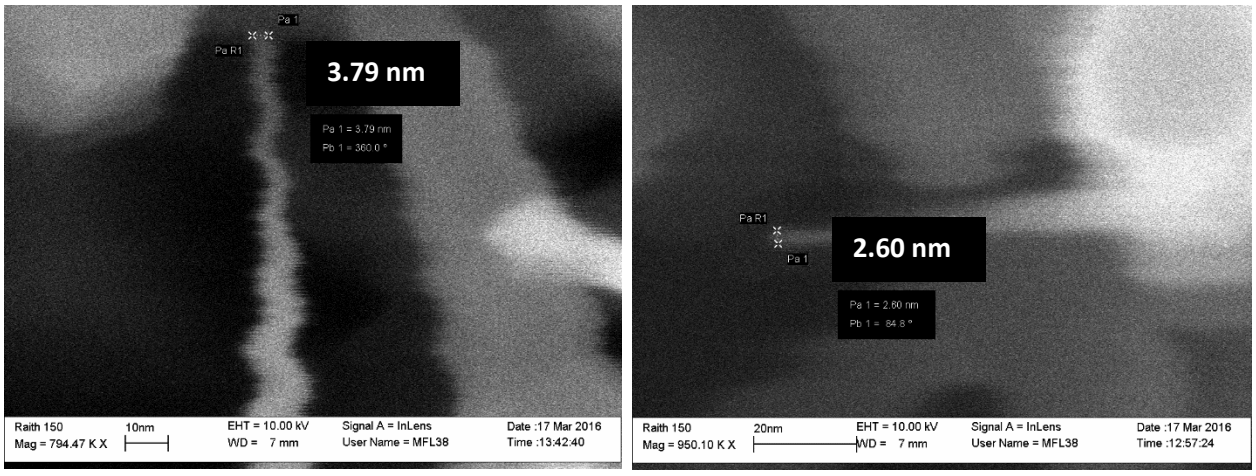

Figure 20: Attempted measurement of the tip diameters of ultrafine nanowires showing 2-4 nm thickness. At over 750,000x magnification, it is extremely difficult to resolve anything without significant distortion. Note that blurriness is likely to result in a measurement which is greater than the true value rather than lesser.

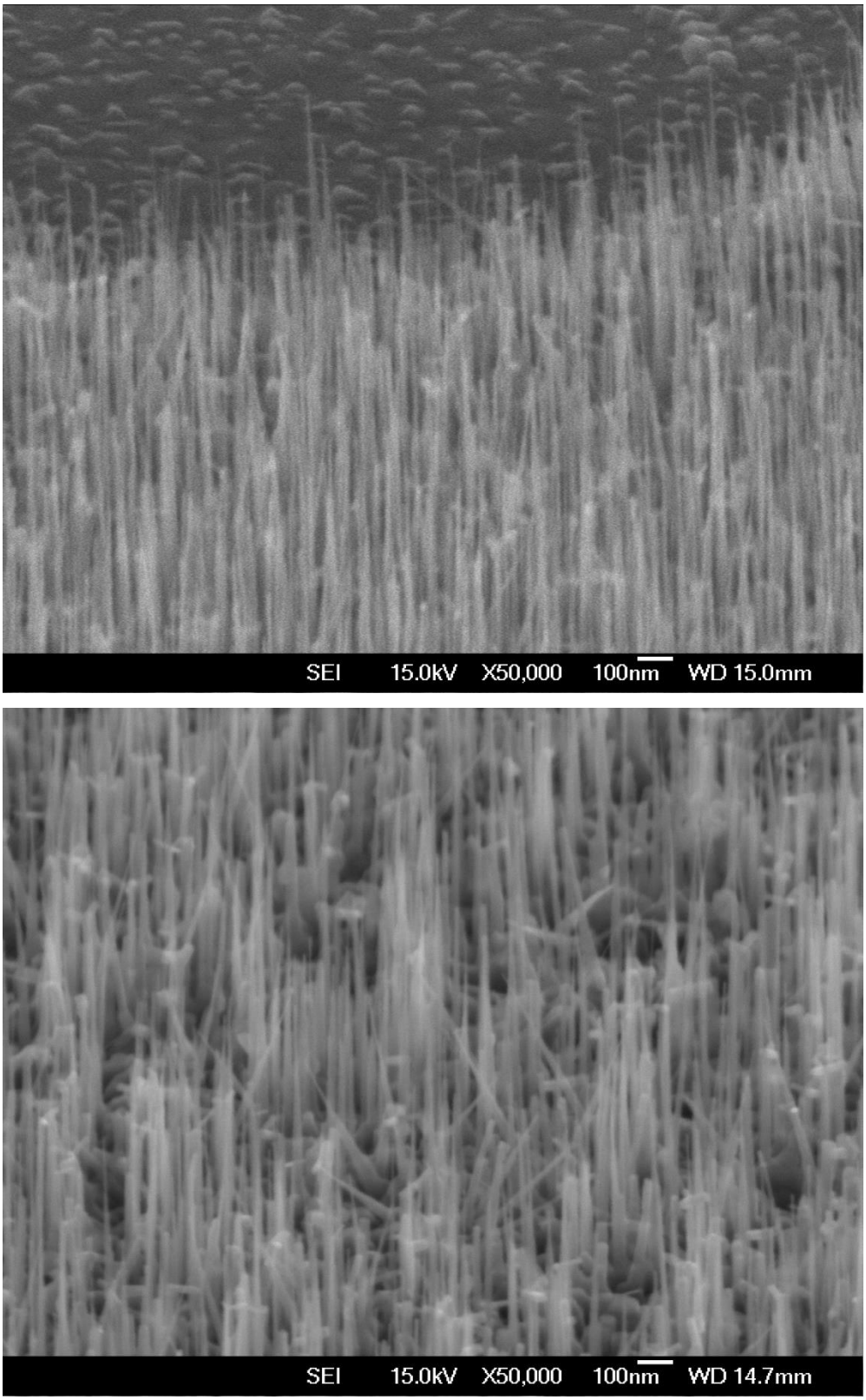

Figure 21: 30° side views of Au101 cluster catalysed ZnO nanowires grown without (top) and with (bottom) APTMS substrate modification.

Figure 20 shows that the tip diameter of these nanowires is less than 3-4 nm although their exact dimensions could only be approximated due to insufficient resolution of the SEM. This is not as small as the 1.5 nm diameter of the Au101 clusters. This small discrepancy can be explained by a number of factors, most importantly the inaccuracy of the measurements taken at such high magnification. The upper limit of the Raith 150's magnification is approximately 950,000x, but the image quality degrades rapidly above 50,000x as ambient vibrations introduce image blurring that cannot be compensated for. A blurred, moving image of an object invariably appears larger than a stationary image of the same object, so the measured 3-4 nm tip diameters can be considered as an upper estimate. It is known that the tip of a gold catalysed ZnO nanowire is a eutectic mixture of gold and zinc. At the extreme scale where the gold behaves as a single molecule such as in the Au101 clusters, the addition of a few Zn atoms could significantly increase the size of the cluster or even induce a shift to a different electronic state, closer to that of a bulk, metallic lattice. Even with the use of APTMS, aggregation might have also occurred. It is possible that a 3-4 nm tip nanowire could have been grown from an aggregate of several clusters, however the regularity of the small nanowire tip sizes makes this an unlikely explanation.

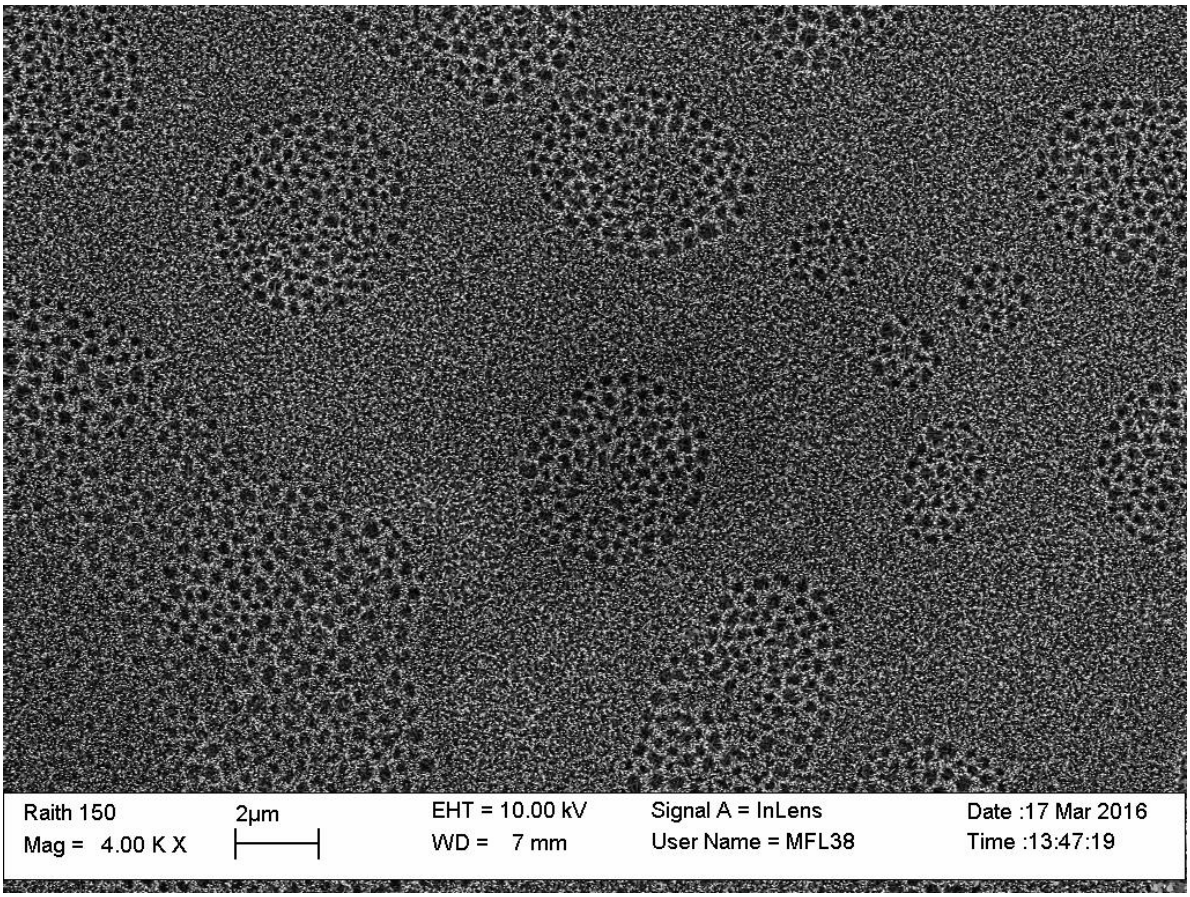

Figure 22: Honeycomb patterns in the nanowires grown without APTMS. These are possibly caused by inhomogeneous drying of the colloid solution as applied to the substrate.

An unusual pattern was observed on the Au101 sample without APTMS that had not been seen on any of the previous growth. On some areas of the substrate, the resulting ZnO nanowires had grown in a honeycomb pattern as shown in Figure 21. It is likely that this was caused by the rapid drying of the chloroform solvent used to disperse the Au101 clusters. The morphology of the nanowires inside these honeycomb patterns did not differ from that of nanowires outside them, suggesting that if inhomogeneous drying was the cause, it did not produce any additional aggregation.

Assuming that these ZnO nanowires grown were catalysed by single Au101 clusters and that the 3-4 nm tips are actually capped by a single cluster, then this is a very significant result. This suggests that ZnO nanowires can be catalysed by non-metallic, molecular gold and not just from metallic gold colloids and films. This suggests that the catalytic action is not due to the metallic nature of gold and is due solely to its atomic interaction with the incoming zinc atoms. These are the first ZnO nanowires grown from non-metallic gold clusters.

4.4.2 Au9 Clusters

Having discovered that non-metallic Au101 nanoclusters were effective at catalysing ZnO nanowire growth, the question of "Is there a lower limit on catalyst size?" remained unanswered. Dr Golovko provided a sample of Au9, clusters of just nine gold atoms that were less than a single nanometre in diameter. The preparation method used is described by Wen *et al.* [12]. The Au9 clusters also contain other stabilising groups and their full chemical formula in powdered form is $[Au_9(P(C_6H_5)_3)_8](NO_3)_3$. It was intended to repeat the same calculations made when using Au101 to ensure that the same amount of gold was applied to the growth substrates, however a mistake was made in calculating the molecular mass of the Au9 cluster. The mass percentage of Au in the Au9 clusters in the powder was assumed to be 69.26% instead of the actual value of 43.70%. Correspondingly, the mass of Au applied to the substrate was less than the mass of Au101 used in the Au101 catalysed ZnO nanowire growth.

As with the previous Au101 experiment, two c-plane sapphire samples were prepared, one treated with APTMS and one without. However, it was found that when deposited by pipette and allowed to dry, the Au9 in chloroform did not dry evenly on the sample prepared without the use of APTMS. The droplet of liquid applied to the surface dried in a non-uniform manner, leaving a ring of residue on the substrate. The two substrates were then used to grow ZnO using the standard EPLD method.

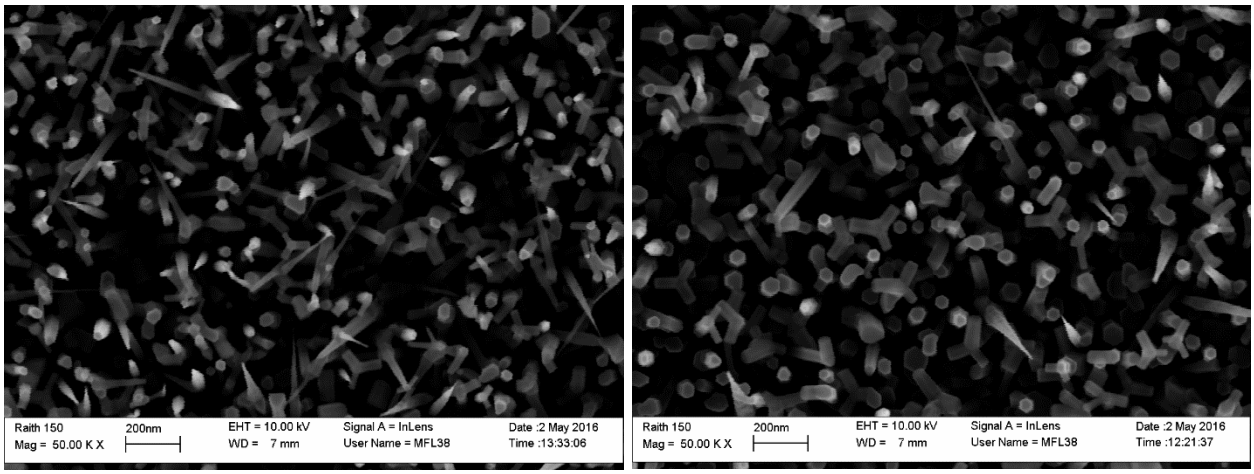

Figure 23: ZnO nanowires catalysed by Au9 clusters on substrates without APTMS treatment (left) and with APTMS treatment (right) (Growth 102)

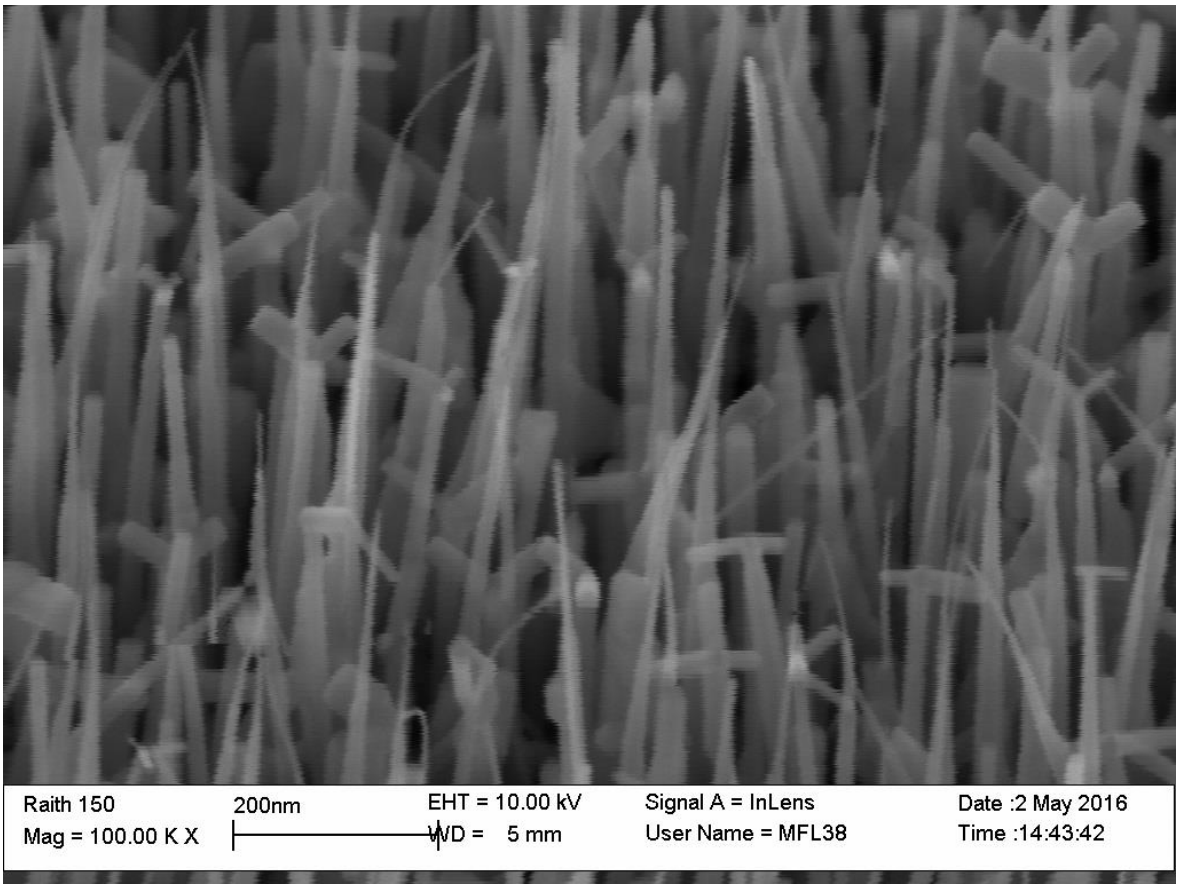

Figure 24: 45° side view of Au9 catalysed ZnO nanowires showing significant bending due to the SEM electron beam.

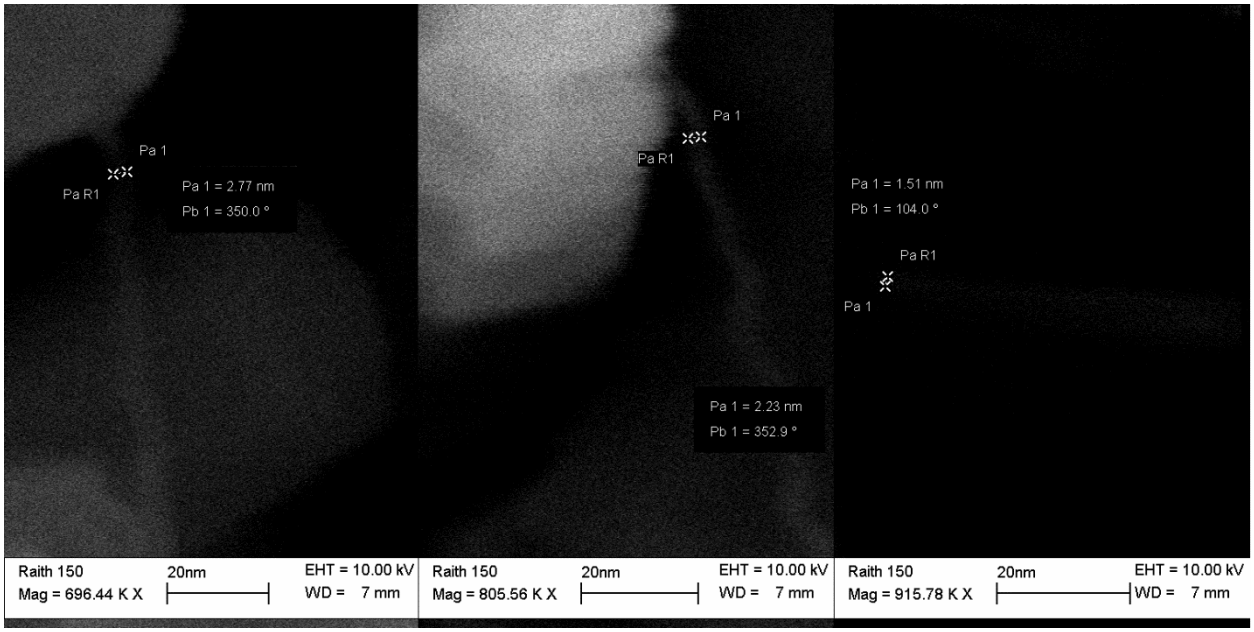

Figure 25 Three ultra-high resolution SEM images measuring the tip diameter of the finest ZnO nanowires.

Both the treated and untreated substrates produced ZnO nanowires with tips finer than any previously observed, either in this research or in the literature as shown in Figure 23 and Figure 24. As with the Au101 growth, efforts to measure the tip sizes of the ZnO nanowires were limited by the ability of the Raith 150 SEM to resolve the extremely small dimensions involved. Figure 25 shows several measurements showing tip diameters of 1.5-2.5 nm, but as before, these measurements are likely to represent an upper limit.

The density of ZnO nanowires shown in Figures 23 and 24 is similar to that observed in the Au101 catalysed growth. Considering that the same mass of gold in the form of Au9 represents over 11x more discrete clusters compared to Au101 of the same mass, the fact that a total mass of 36 µg was erroneously applied to the substrates rather than 58 µg was probably not significant. With this amount of gold on the substrates, we expect approximately 7x more clusters to be present per substrate for Au9 compared to Au101. A corresponding increase in ZnO nanowire density might also be expected, but this was not observed.

It is impossible to tell if the finest nanowires grown using Au9 as a catalyst are truly terminated at a nine atom point. It is possible that the tips are nine gold atoms combined with several zinc atoms or that the clusters have simply aggregated into larger gold nanoparticles. However, in these growths using Au9 clusters, nanowires with tips of 1.5 nm diameter were measured. Even with the unlikely assumption that the tip of the nanowire consists entirely of gold with no additive zinc, a 1.5 nm gold cluster would exhibit non-metallic behaviour [6-8]. Even if each nanowire was grown from an aggregate of ten Au9 clusters, this

still represents fewer gold atoms than a single Au101 cluster which is expected to be non-metallic. It is therefore concluded that non-metallic gold clusters are still capable of catalysing the VLS nanowire growth method in ZnO. If a lower limit for the size of gold clusters for VLS catalysis does exist, then it is beyond the measurement limit using the SEM equipment that was available in this thesis.

4.5 Summary

In this chapter, various EPLD nanowire growths were conducted to investigate the potential of tuning the tip diameter of ZnO nanowires using selecting different sized Au catalyst nanoparticles. Commercially prepared Au colloids of various sizes as well as atomically precise Au clusters of 101 and 9 atoms were used.

- EPLD ZnO nanowires were grown on c-plane sapphire substrates treated with APTMS-tethered, commercially produced Au colloids of 5 nm, 10 nm, 20 nm and 40 nm diameters. The resulting nanowires had tip diameters that matched the colloid size indicating a direct link between the diameters of the colloid catalysts and the tips of the ZnO nanowires.
- Ultra-fine nanowires with tips of ≤ 5 nm diameter displayed an unusual behaviour when imaged using the SEM. Repeated scanning of an ultra-fine nanowire caused it to become attracted to a neighbouring nanowire and suddenly bend towards it. The two nanowires would then fuse together at the tips. This is likely due to the SEM's electron beam generating electric charges in the nanowires that were strong enough to bend them by electrostatic attraction.
- Atomically precise, non-metallic Au clusters of 101 and 9 atoms were substituted for the Au colloids and used to catalyse ZnO nanowire growth. Tip sizes as small as 1 nm were observed, indicating that non-metallic Au clusters can still catalyse the VLS growth of ZnO nanowires.

4.6 References

[1] A. Marcu, L. Trupina, R. Zamani, J. Arbiol, C. Grigoriu, and J. R. Morante, "Catalyst size limitation in vapor-liquid-solid ZnO nanowire growth using pulsed laser deposition," *Thin Solid Films,* vol. 520, pp. 4626-4631, 2012.

[2] M. H. Huang, Y. Wu, H. Feick, N. Tran, E. Weber, and P. Yang, "Catalytic growth of zinc oxide nanowires by vapor transport," *Advanced Materials,* vol. 13, pp. 113-116, 2001.

[3] A. M. Lord, T. G. Maffeis, A. S. Walton, D. M. Kepaptsoglou, Q. M. Ramasse, M. B. Ward, *et al.*, "Factors that determine and limit the resistivity of high-quality individual ZnO nanowires," *Nanotechnology,* vol. 24, 2013.

[4] F. Falyouni, L. Benmamas, C. Thiandoume, J. Barjon, A. Lusson, P. Galtier, *et al.*, "Metal organic chemical vapor deposition growth and luminescence of ZnO micro- and nanowires," *Journal of Vacuum Science and Technology B:Nanotechnology and Microelectronics,* vol. 27, pp. 1662-1666, 2009.

[5] H. R. Khan and H. Frey. (2015). *Handbook of Thin Film Technology (1 ed.)*. Available: http://canterbury.eblib.com.au/patron/FullRecord.aspx?p=972953

[6] D. P. Anderson, J. F. Alvino, A. Gentleman, H. A. Qahtani, L. Thomsen, M. I. J. Polson, *et al.*, "Chemically-synthesised, atomically-precise gold clusters deposited and activated on titania," *Physical Chemistry Chemical Physics,* vol. 15, pp. 3917-3929, 2013.

[7] D. P. Anderson, R. H. Adnan, J. F. Alvino, O. Shipper, B. Donoeva, J. Y. Ruzicka, *et al.*, "Chemically synthesised atomically precise gold clusters deposited and activated on titania. Part II," *Physical Chemistry Chemical Physics,* vol. 15, pp. 14806-14813, 2013.

[8] R. Jin, Y. Zhu, and H. Qian, "Quantum-sized gold nanoclusters: Bridging the gap between organometallics and nanocrystals," *Chemistry - A European Journal,* vol. 17, pp. 6584-6593, 2011.

[9] M. Turner, V. B. Golovko, O. P. H. Vaughan, P. Abdulkin, A. Berenguer-Murcia, M. S. Tikhov, *et al.*, "Selective oxidation with dioxygen by gold nanoparticle catalysts derived from 55-atom clusters," *Nature,* vol. 454, pp. 981-983, 2008.

[10] J. F. Alvino, T. Bennett, D. Anderson, B. Donoeva, D. Ovoshchnikov, R. H. Adnan, *et al.*, "Far-infrared absorption spectra of synthetically-prepared, ligated metal clusters with Au6, Au8, Au9 and Au 6 Pd metal cores," *RSC Advances,* vol. 3, pp. 22140-22149, 2013.

[11] B. G. Donoeva, D. S. Ovoshchnikov, and V. B. Golovko, "Establishing a Au nanoparticle size effect in the oxidation of cyclohexene using gradually changing Au catalysts," *ACS Catalysis,* vol. 3, pp. 2986-2991, 2013.

[12] F. Wen, U. Englert, B. Gutrath, and U. Simon, "Crystal structure, electrochemical and optical properties of [Au 9(PPh3)8](NO3)3," *European Journal of Inorganic Chemistry,* pp. 106-111, 2008.

Chapter 5: ZnO Nanowire Devices

5.1 Motivation

Having grown well-aligned arrays of vertical ZnO nanowires, it was necessary to examine their electrical properties and assess their viability for incorporation into electrical circuits. In order to do this, an individual nanorod (or several nanorods) needed to be physically connected to a testing circuit such as a parameter analyser or an oscilloscope. Owing to the extremely small dimensions involved, this was a significant challenge.

Different research groups have approached this challenge using various methods, influenced by the equipment available to them and the morphology of their nanorods or nanowires. Some groups have the facilities available to measure nanorods without forming a permanent contact, using movable electrical probes. Lord *et al.* [1] have used a four point STM probe measuring system mounted to their Gemini SEM column to measure the resistances of individual ZnO nanowires. Nakayama *et al.*[2] have used a multiple-probe AFM system to accomplish the same result. These techniques provide valuable characterisation data but any practical device involving ZnO nanorods or nanowires requires permanent contacts be made.

Where nanowires are grown in a large array, a popular method of contacting them involves macro-contacting, where layers of contact are deposited onto the array, separated by a "templating membrane" which is either insulating so as not to affect measurements or able to be later removed [3-5]. This allows a single contact to be made to the top of the entire nanowire array while another is made to the bottom and the whole array is then tested in parallel. The average electrical properties of the nanowires can then be investigated. A hybrid of this method and the temporary contact method can also be used, in which a macro-contact is applied to the bottom of the array and then a conductive AFM tip is applied to a single nanowire [6]. Macrocontacting has promising applications for transistor arrays, as in many applications one end of the channel of each transistor will be simply tied to an electrical supply or to ground. In addition, MOSFETs have been fabricated using gates which wrap around vertically standing nanowires like collars [7, 8].

Contacts can also be fabricated onto both ends of a nanowire using various forms of lithography. This usually first involves the transfer of nanowires from a vertical array onto a flat, insulating substrate where contacts can be deposited to either end. Usually, this transfer is achieved either by direct physical contact: running the nanowire array face-down across the surface of the substrate, or by using sonication in a suitable solvent to separate the wires, after which the solution is applied to a substrate and the solvent removed by evaporation [1]. For the latter process, isopropyl alcohol (IPA) is as a sensible choice of solvent for ZnO

nanowires as it has been shown that IPA has a minimal effect on the electrical properties of the wire, provided that the exposure time is kept short [9]. Nanowires longer than several microns which are large enough to be seen under an optical microscope can be contacted using simple photolithography [10] but nanowires too small to see through the viewfinder of a photolithographic mask aligner require a different approach. Electron Beam Lithography (EBL) is a fine-scale lithographic technique in which an SEM is used for viewing and alignment. EBL has been used to define electrical contacts onto individual nanowires [11] as well as the gate insulating regions of nanowire MOSFETs [12]. As the nanowires produced in this thesis were of the approximate order of 1µm long, EBL was the most practical means of contacting them.

With this method selected, we were interested in fabricating devices using both ohmic and rectifying contacts. The University of Canterbury's Metal Oxide Semiconductor group has considerable experience in the deposition of both types of contacts onto bulk ZnO and ZnO thin films [13-18], using bilayers of Ti/Au and AgO_x/Au to produce excellent ohmic and Schottky contacts respectively on ZnO. Ohmic contacts are the most basic metal-semiconductor contacts and these were attempted first.

Contacting nanowires using EBL is an extremely difficult task and our research into creating ZnO nanowire contacts attracted interest from two overseas collaborators, Dr Alex Lord from Swansea University, UK and Professor Simon Watkins from Simon Fraser University, Canada, who each sent us samples of their ZnO nanowires to analyse with our contacting experiments.

5.2 Substrate Preparation

5.2.1 Contact Pad Arrays

A significant challenge of using EBL to contact individual nanowires was the difficulty of making the nanoscale contacts large enough at one end to apply standard, millimetre scale electrical probes. In addition, it seemed logical to design a systematic search pattern when looking for suitable nanowires to contact. An array of 100 x 100 µm contact pads, arranged in pairs, was designed and written onto a standard chrome-coated glass photomask. This array could be patterned with Ti/Au layers of approximately 50 nm thickness onto the nanowire transfer substrate using conventional lift-off photolithography as shown in Figure 1. Each pair of contact pads was separated by an 11 µm gap. Nanowires that fell into this gap could then be contacted by EBL, with each end connected to a contact pad. When searching for nanowires, these contact pads would also serve as co-ordinate markers and provide a well-defined search area.

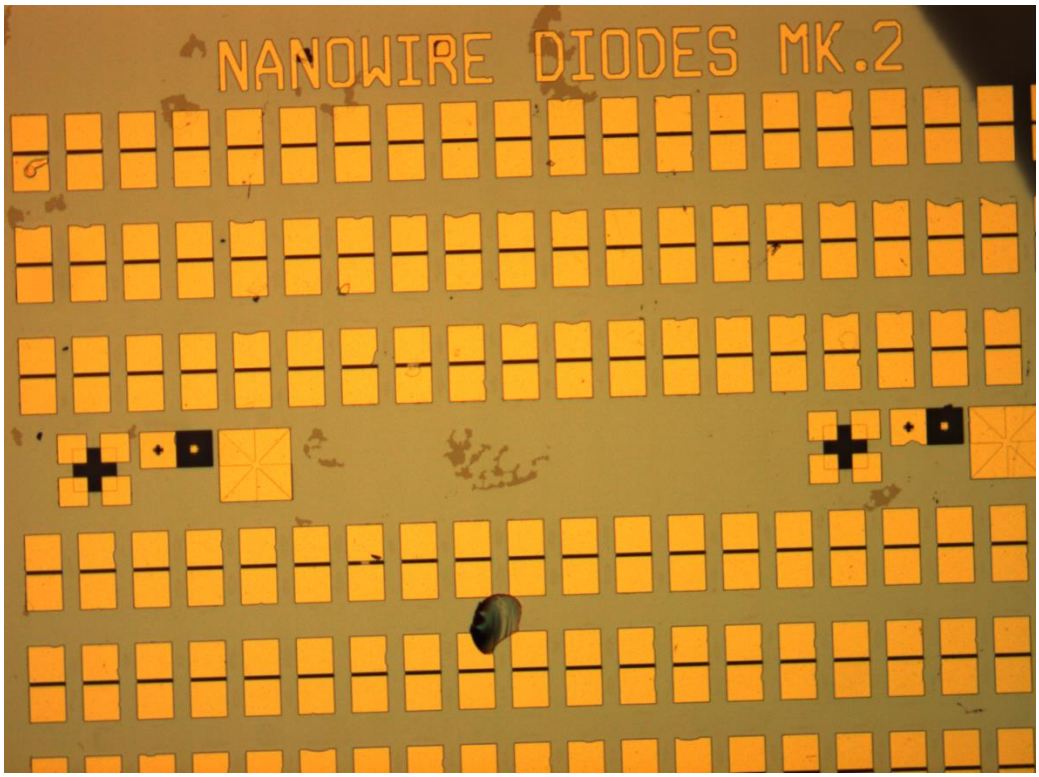

Figure 1: Completed array of contact pads for nanowire contacting. Each individual pad is 100 µm x 100 µm, with an 11 µm gap between them. The bright areas are Ti/Au contacts and alignment markers, the dark black regions between the pairs of pads are etched trenches and their alignment markers.

5.2.2 Nanowire Trenches

In order to increase the concentration of nanowires in the gaps, a second photomask was produced defining a trench between each pair of contacts that was dry-etched using reactive ion etching. This trench occupied 10 µm of the 11 µm gap and was etched to a depth of about 200 nm. It was intended that this would help to localise the distribution of the applied nanowires between the contact pads. Quartz was selected as the nanowire transfer substrate due to its insulating properties and relatively low cost, however its hardness made etching the trenches challenging. Reactive ion etching with sufficient strength to etch quartz required the use of chromium as a physical mask. Chromium was selected because it is easily removed by acid etching. Chromium was deposited onto to the quartz substrates by thermal evaporation, with a measured thickness of 40 nm. A layer of 4% High Molecular Weight PMMA (Poly-Methyl Methacrylate) EBL photoresist was applied to the surface by spin coating at 3000 rpm for 60 s, followed by a soft bake for 30 minutes at 185 °C. The trench array pattern was exposed into the resist using the Raith 150 EBL system as described in Chapter 2, Section 5. The exposure dose was set at 200 µAs/cm^2, double the usual 100 µAs/cm^2 dose in order to ensure complete exposure as the possibility of underexposure leaving residual resist behind was of greater concern than the fabrication of high precision features.

The exposed trench arrays were developed in 1:3 MIBK:IPA for 30 s and were inspected under an optical microscope. Chrome etch was applied to the developed arrays for 20 s, resulting in the complete removal of chromium from the PMMA defined trenches. The samples were reactive ion etched for 10 mins using 50/30 CHF_3/Ar at 200 W and 253 K (-20 °C). Any remaining PMMA was rinsed off with acetone, methanol and IPA and the remains of the chrome mask were dissolved with chrome etch for 40 s until no chrome was visible. The trenches were measured using the DEKTAK surface profiler and found to have an approximate depth of 270 nm.

Using alignment markers patterned on the trench layer, the contact pad layer was then defined on top of the trench layer. AZ1518 photoresist was spin coated onto the sample for 60 s at 4000 rpm. The Karl Süss MA6 mask aligner was used to position the exposure, which was set for 12 s using soft contact mode. The resist was then soft baked for 30 mins in an oven at 95 °C. The resist was developed immediately before metallisation for 30 s using MIF328 developer and rinsed with de-ionised (DI) water. A layer of 20 nm thick Ti was first deposited by electron beam evaporation, followed by 30 nm of Au, without unloading the sample or exposing to air. The metallised substrates were then placed in a beaker of acetone to lift off the Ti/Au layers, leaving the contact pad patterns behind.

5.3 Nanowire Dissociation

5.3.1 Ultrasonic Dissociation

Tests were conducted to demonstrate the viability of using sonication to displace nanowires from the substrates on which they were grown and to transfer them onto the surface of the contact pad array chip. A 10 x 10 mm sample of ZnO nanowires from the position-dependence growth (Growth 61, Appendix 1) was sonicated for 3 mins in approximately 25 ml of IPA. The IPA solution containing the suspended nanowires was then applied by means of a clean pipette to a blank, low-resistivity silicon chip which was then inspected using SEM. Nanowires were observed on the silicon chip after solvent evaporation as shown in Figure 2. Before and after SEM observations of the high density as-grown nanowire substrate showed no visible change in the density or quality of the nanowires, indicating that only a tiny fraction had been transferred. It is interesting to note that some of the wires shown in Figure 2 have lengths as long as several microns, whereas the as-grown nanowires on their original substrates were never observed with this length. This could be due to several reasons. SEM images of as-grown nanowires show a layer of material growing between the wires. This material could be relatively thick and conceal the true length of the nanowires, although this seems unlikely as this layer would need to be several microns thick. It is possible that the long wires were multiple wires aggregating together, but the long wires observed were very straight and

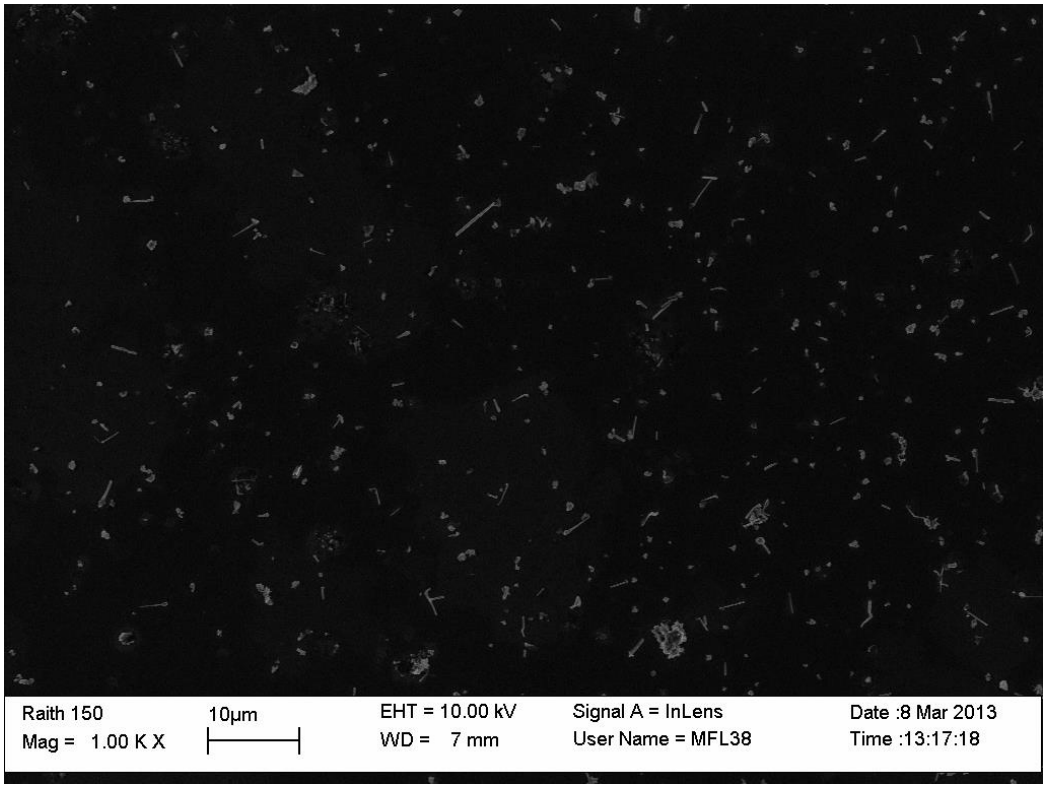

Figure 2: ZnO nanowires transferred onto a silicon chip by ultrasonic in isopropyl-alcohol.

enhanced magnification showed no sign of agglomeration or discontinuities as shown in Figure 3. A more likely explanation is that any SEM image of the as-grown nanowires is essentially a random sample of several hundred nanowires from a total numbering in the tens of billions. However, dissociation by physical agitation will have a greater effect on the longest wires, making them more likely to become detached from the substrate. An SEM micrograph of the as-grown nanowires could be considered a fair sample of the nanowire morphology, where ultrasonication could produce a systematically biased sample, favouring the very longest wires from the entire substrate. Due to the astronomical number of nanowires on each substrate, if these long wires simply occur with extremely low frequency, they could reasonably go unnoticed even in a hundred SEM micrographs.

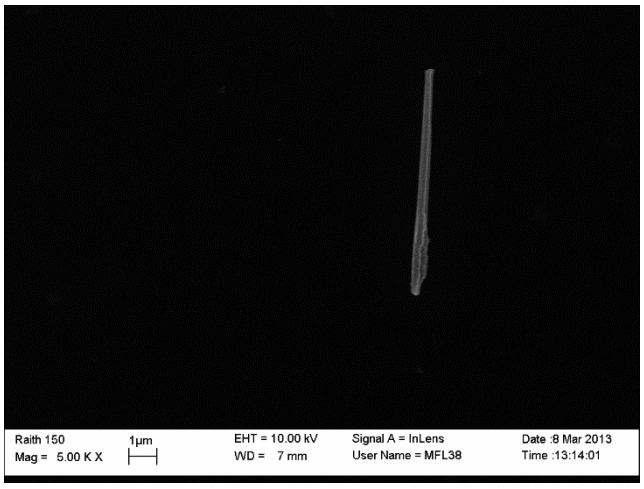

Figure 3: Higher magnification of a long nanowire dissociated onto silicon. There are no visible discontinuities.

5.3.2 Substrate Re-Evaluation and Treatment

Quartz had been initially selected as an insulating substrate for the nanowire devices. However, when nanowires were dispersed onto these substrates it was discovered that their insulating nature created too much charging interference for the SEM to be able to resolve individual nanowires, even with the conducting gold pad arrays present on the surface. As the electron beam from the SEM penetrates some distance into solid materials, a thin layer of insulating silicon dioxide on top of conductive silicon was chosen to replace the quartz. In this design, the SEM beam could penetrate through to the conducting silicon layer, avoiding the build-up of static charge interference while imaging, while the nanowire contacts on the surface would remain electrically isolated. Any trapped or accumulated charge in the insulating layer would also have a short path back to the electrically grounded, conducting silicon layer. By etching one corner of the silicon dioxide layer to the bare silicon and placing an SEM grounding clip here, the electrical resistance to ground encountered by the beam could be further reduced as shown in Figure 3. Silicon substrates with 300 nm thick silicon dioxide layers were chosen as this would be thick enough to provide good insulation at the low nanowire device test voltages (<10 V).

A wafer was prepared by growing 300 nm of silicon dioxide on a low-resistivity *n*-silicon wafer from MTI Corp, CA, USA. Although the surface of the silicon was thoroughly cleaned before oxidation, when the oxide layer was grown, many small bumps were observed across the surface as shown in Figure 4. These did not affect the insulating properties of the oxide, so these samples were used in the early contacting experiments. A commercially produced wafer of pre-grown 300 nm SiO_2 on silicon was acquired from MTI Corp and this was used in subsequent experiments. The silicon dioxide layer was etched to the bare silicon at the corner of each sample using hydrofluoric acid until the green oxide hue was replaced by the steely silver of bare silicon, a process usually taking approximately 3 mins.

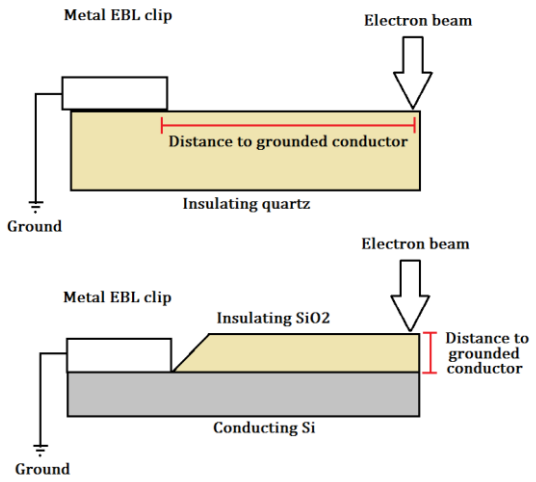

Figure 4: Diagram showing the advantages of a short insulating path between the surface of the substrate and a conductor tied to ground.

5.4 Electron Beam Lithography Calibration

5.4.1 Titanium Lift Off on PMMA

The electron beam lithography technique was calibrated/optimised before any contacting experiments using actual nanowires were carried out. The vast majority of EBL exposures conducted at the University of Canterbury have been using pre-made mask files, not custom contacts of variable size, so the operating parameters had to be first extracted empirically. The method of operation is also described in Chapter 2, Section 3. Typical photoresist settings could still be used, so Poly-Methyl Methacrylate (PMMA) was used in a bilayer, with a high molecular weight layer on top of a low molecular weight layer to deliberately create an undercut during development. Spin speeds of 4000 rpm and 3000 rpm respectively for 60 s produced a bilayer of approximately 250 nm thickness.

Initial attempts at using electron beam evaporation to metalise test patterns imprinted on a PMMA bilayer by EBL were unsuccessful. The standard ohmic contact used for ZnO is a Ti/Au bilayer. Titanium is used as it has a high affinity for oxygen and so it draws oxygen from the ZnO lattice creating a high density of near-surface oxygen vacancies, which increases the local carrier concentration, thereby producing an enhanced ohmic contact. The inert capping layer of Au prevents further oxidation of the Ti layer by the atmosphere. Surprisingly, Ti deposited by electron beam evaporation (the standard deposition method) would not lift off from the thin bilayers of PMMA, even when only a few nanometers of Ti was deposited. It was concluded that the electron beam evaporated Ti had too much thermal energy and was hard baking the PMMA resist.

DC sputtered titanium was found to lift off effectively, however this required venting the chamber to atmosphere before the capping layer of Au could be deposited by electron beam evaporation, which lead to unwanted oxidation of the Ti layer. Thermal evaporation of Ti, though similar in principle to electron beam evaporation, was also found to be successful and did not bake the photoresist. As the Au capping layer could also be thermally evaporated, thermal evaporation was selected as the optimal method of depositing ohmic contacts onto the ZnO nanowires.

5.4.2 Beam Current and Aperture Size Calibration

With the metallisation step working, a test exposure was set up, creating a small pattern of crosses and squares intended to test the minimum line size in both the X and Y directions. EBL exposure parameters were estimated at the standard instrument conditions of a 30 µm aperture and a 10 kV beam voltage. The writefield was moved blind, using the EBL's coordinate system without SEM imaging in order not to

expose the PMMA. At each location where a pattern was to be written, a single SEM scan was performed to confirm that the location was correct. After PMMA development and Ti/Au metalisation by thermal evaporation, it was found that a rectangular area around each pattern had been exposed, even by the single scan. This is shown in Figure 5. Rather than the expected squares and crosses of the test pattern, the pattern displayed in the exposed resist was simply a large rectangle the size of the writefield at each point where the pattern had been written, indicating that even a single scan with these settings was enough to expose the entire writefield, resulting in the loss of the intended pattern.

In order to address this problem, the 30 µm aperture size was reduced to 10 µm. This has the effect of reducing the electron beam current from the 200 pA range to the 20 pA range. Exposure of the PMMA is determined by the electron dose and this is calculated by the instrument software. As the dose represents the total number of electrons per unit area, a lower current could be offset by simply increasing the exposure time. A single scan used for navigation or alignment however, will receive a proportionally lower dose, reducing the risk of unintentional exposure. On a large scale, writing several mm^2 of exposed areas,

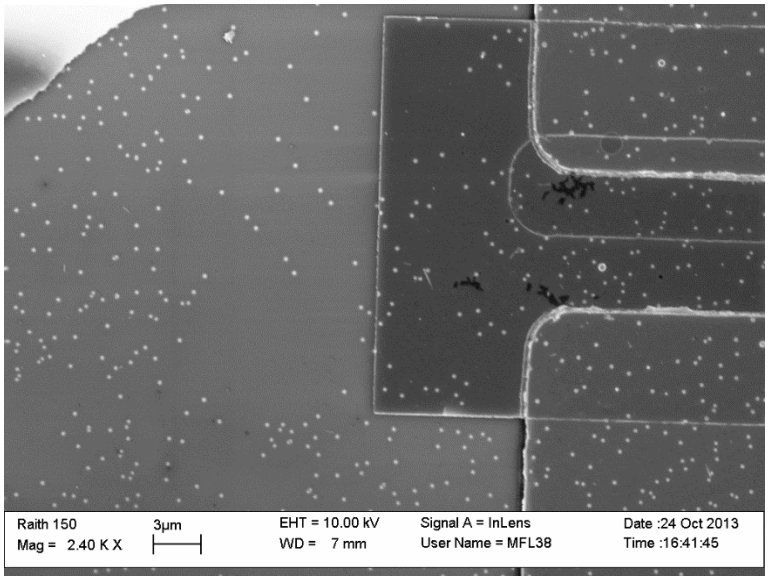

Figure 5: A large metal rectangle between two contact pads caused by a single scan of the electron beam with 30 µm aperture size.

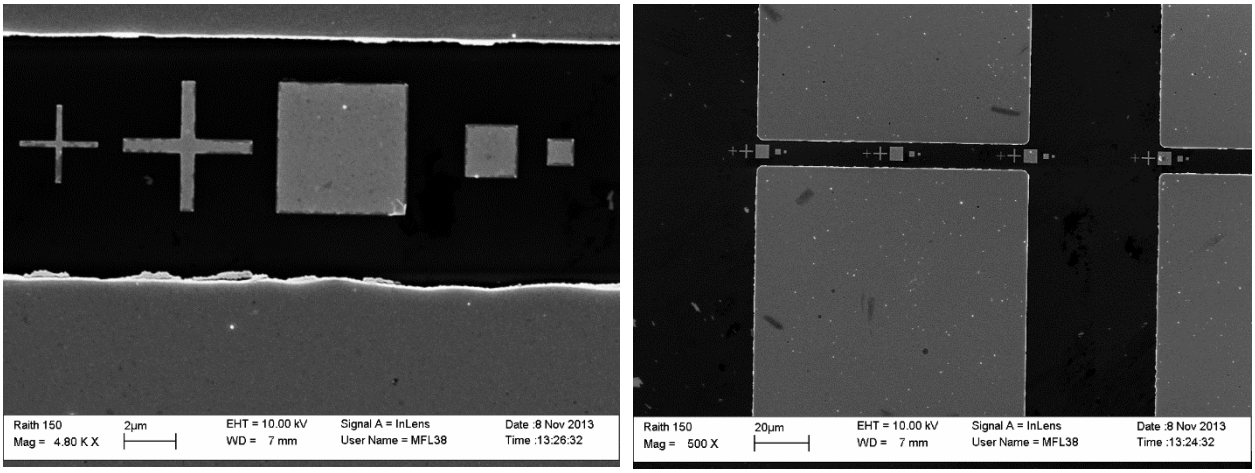

Figure 6: Test patterns exposed by EBL and metallised by thermal evaporation of Ti/Au. The squares are 3 µm, 2µm and 1µm respectively. The large and small cross have critical dimensions of 50nm and 20nm respectively.

this decrease in beam current could decrease throughput by an unacceptable level, but these nanowire contacts and test patterns had a total area of only a few hundred square nanometres and took on the order of 5-10 s to write, so this was not an issue. A repeat of the test exposure with a 10 µm aperture size was carried out and this time the pattern was successfully transferred onto the PMMA. The Ti/Au metallisation was also successful as shown in Figure 6.

5.5 Attempted Nanowire Contacting

5.5.1 Discarding the trench etching step

Nanowires were again applied to a freshly prepared array of contact pads on a SiO_2 coated silicon substrate chip. Figure 7 shows a chip with etched trenches that has been dispersed with nanowires, circled in the figure. It can be seen that as many of the wires were found outside the trench as inside it, suggesting that the use of these trenches had a limited effect on nanowire position. These trenches would also require the actual contacts to curve down from the contact pads to reach the nanowires in the trench. This could potentially weaken the thin, EBL-defined Ti/Au contacts and lead to breakages, or higher resistance between the nanowire and the large contact pads where the probes would be placed. The etched trenches were therefore discarded. Reactive ion etching of the substrate corners to enable the grounding clip of the SEM to be directly applied to the conductive silicon layer was retained.

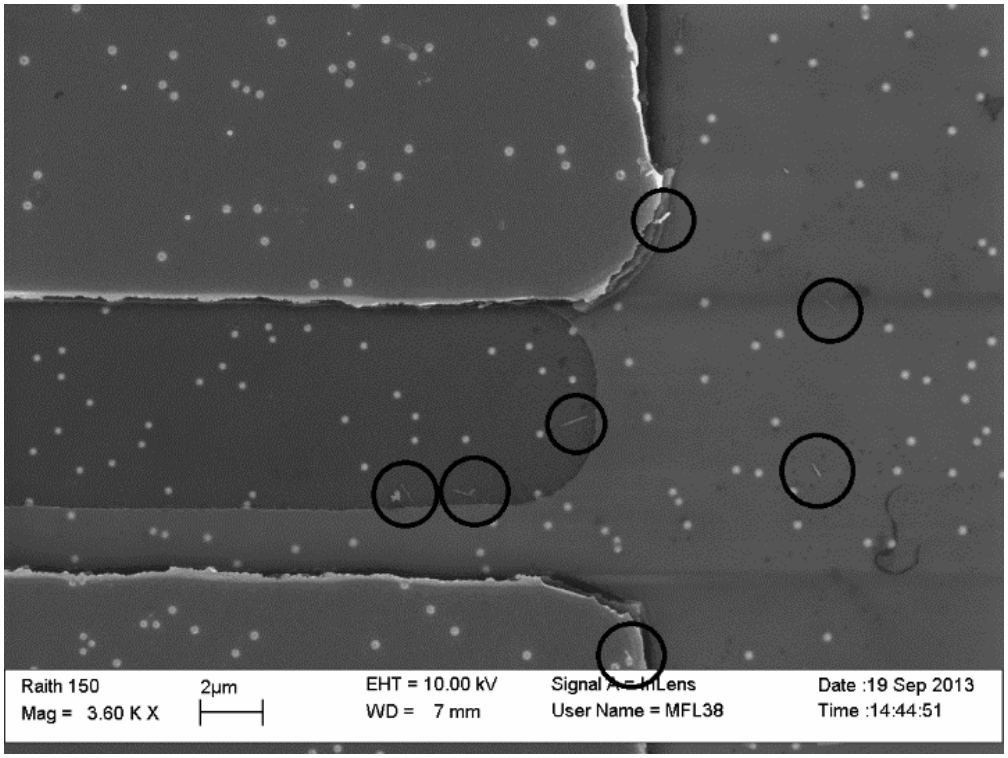

Figure 7: Nanowires dispersed near the etched trench. The trench does not seem to concentrate the circled nanowires.

5.5.2 First Contact Attempts

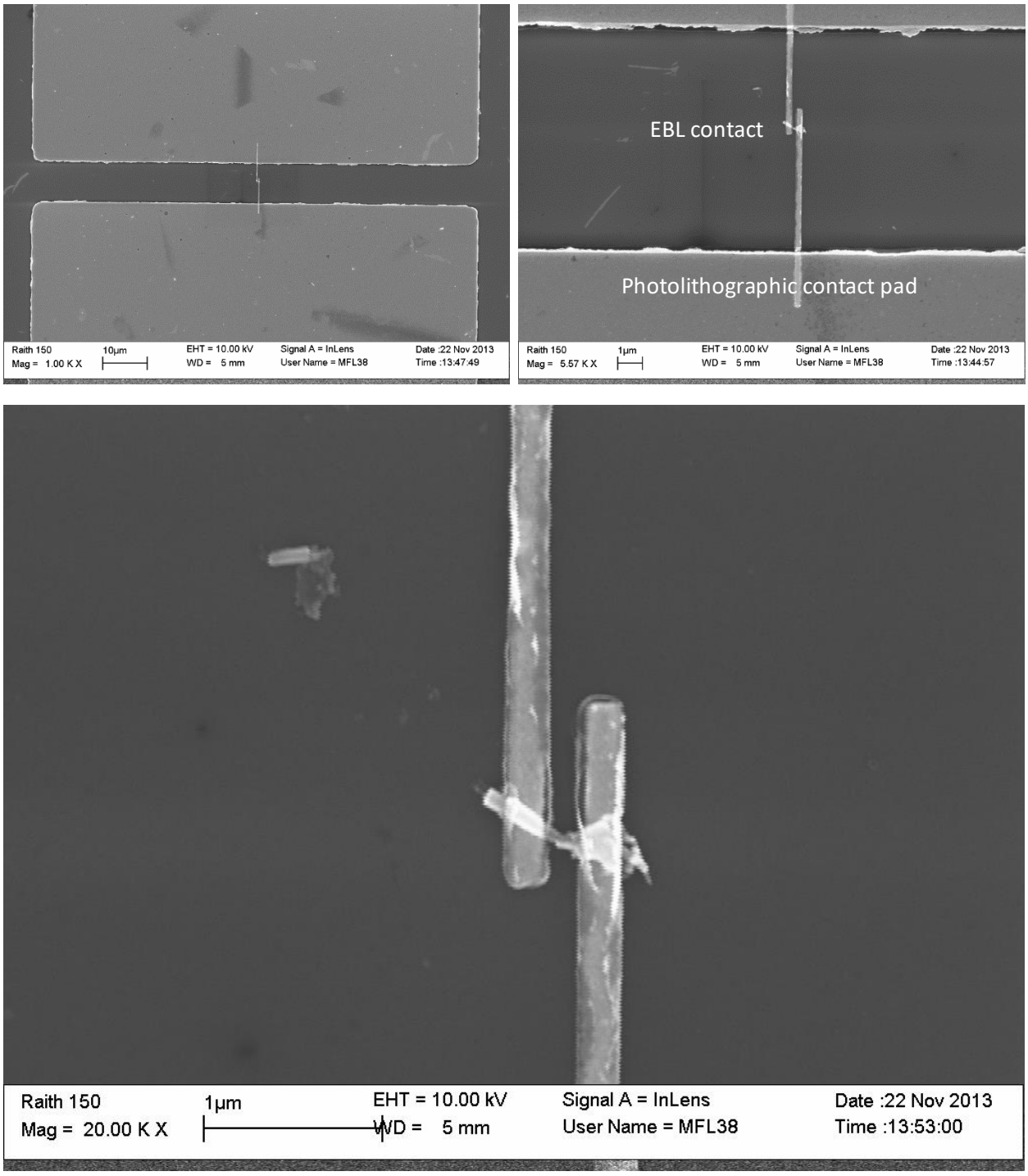

Figure 8: Contacted ZnO nanowire shown at increasing resolution. There is quite a lot of detritus around the nanowire and under the contact pad. Also note the slight darkening of the area around the contact caused by EBL exposure.

The layer of non-conductive PMMA applied to the substrate surface for the EBL step made it difficult to identify a single nanowire on the substrate, even when the beam was perfectly focussed and aligned. A methodical search pattern was therefore developed. The contact pad array comprised 90 pairs of 100 µm wide pads. The size of a single scan window was 25 µm x 25 µm, therefore starting in the centre of one edge, each pair of pads could be easily inspected at the 0, 50 and 100 µm positions with no possibility of overlapping scans causing premature exposure. This gave 270 possible sites for nanowires to be found on a single silicon substrate so the potential yield was quite high even if nanowires were sparsely distributed and difficult to see. Nanowires from some of the finest growths (Growth 63, Appendix 1) were dispersed on a chip and several contacts were made to individual nanowires. The contacted wires were examined under SEM as shown in Figure 8.

Despite its promising visual appearance, the contact shown in Figure 8 did not work when electrical probes were applied to the larger contact pads. No current could detected above the parameter analyser noise level when a bias of 5 V was applied to probes on either side of the nanowire, even after exposure to UV light, which is known to significantly increase the carrier concentration of ZnO. There were several possible explanations for the failure of this device, including the poor quality of the contact on the right hand side of the nanowire as shown in Figure 8. It was also possible that the contacts were effective, but that the nanowire was simply too insulating. In his work on GaN nanowires, Kendrick [19] stressed the importance of thick nanowire contacts, on the basis that deposited Au can fail to adhere to the side of a rounded nanowire as illustrated in Figure 9, causing the contact layer to break. The Ti/Au layer used in the contact shown in Figure 8 was 25/30 nm thick, giving a total thickness of 55 nm, approximately the same thickness as the nanowire. There are other points of potential failure on the contact geometry, including the junction between the large, photolithographically defined contact pad and the smaller EBL contact. As resistance is inversely proportional to the contact area, the resistance of the long, thin EBL contact could have simply been too large. A second chip was prepared, using long nanowires from the r-plane sapphire growth (Growth 15, Appendix 1) performed without APTMS. The methodology was the same, with the objective of achieving a cleaner contact to the wire itself, free from the debris and potential contact breakage shown in Figures 8 and 9. EBL contacts were enlarged wherever possible in order to reduce the overall contact resistance. Three wires were contacted on this chip as shown in Figure 10.

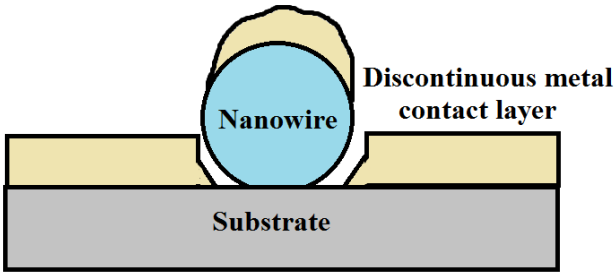

Figure 9: A mechanism for nanowire contact failure caused by insufficient metal thickness proposed by Chito Kendrick [19].

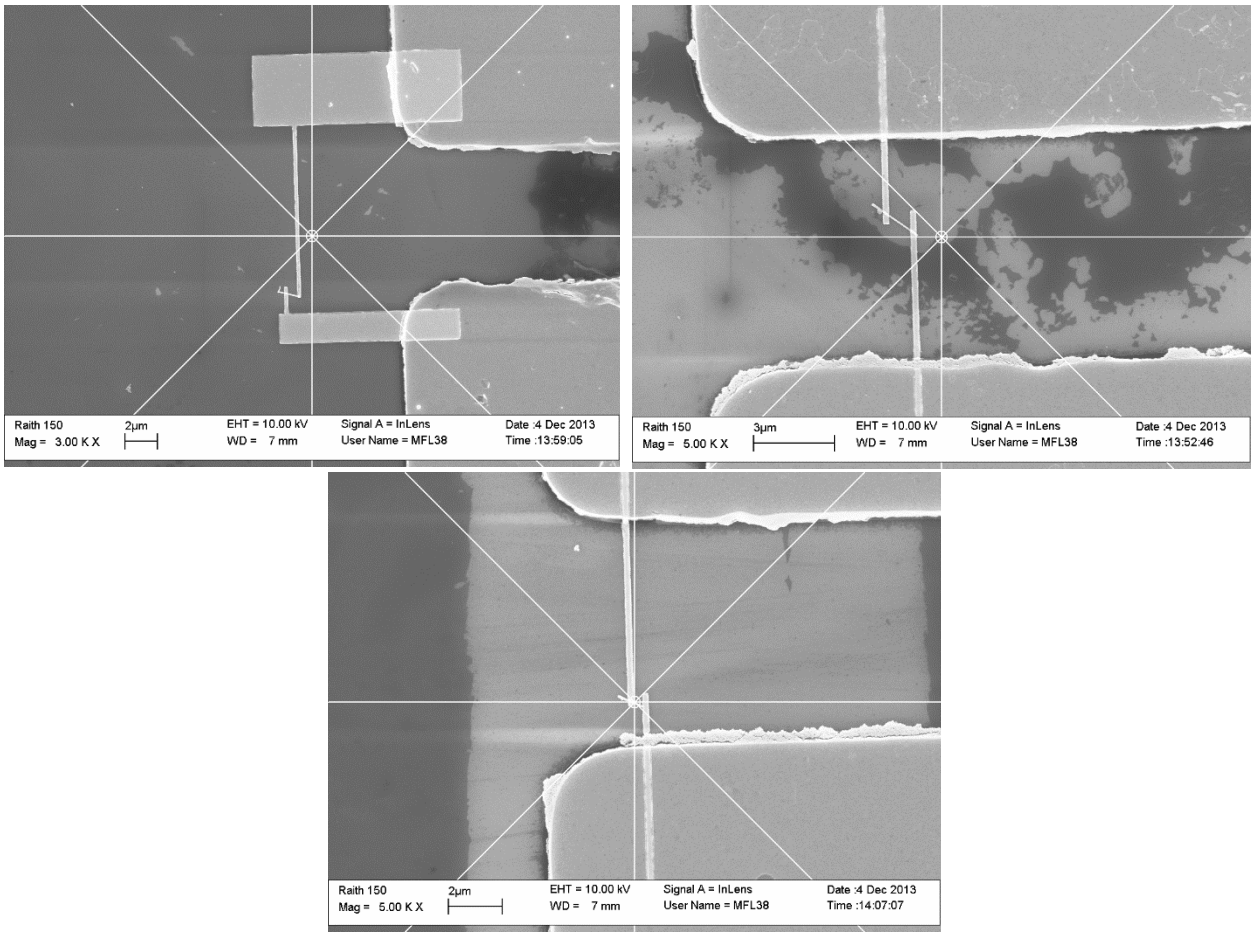

Figure 10: Three nanowire contacts on a single chip coated with nanowires from the R-plane growth (see Appendix 1, Growth 15 for information on these wires).

An attempt was again made to apply electrical probes to the large contact pads connected to each of the nanowires and again, each attempt failed to measure any current, despite exposure to 365 nm UV light and the application of voltage biases up to 5 V. Enhanced magnification provided by the JEOL-7000 SEM (Figure 11) showed that the contact onto each of the nanowires was mechanically sound. However, a close inspection of the junction between the EBL-defined contact and the large, photolithographically-defined probe pad showed signs of breakage due to a ridge of material protruding from the probe pads as shown in Figure 12. This material appeared to be produced by the poor/incomplete lift off of Ti/Au around the exposed probe pad during the photolithography process. Figure 10 and 12 show that this ridge of metal is very thick compared to the 50 nm thick contacts. On the micron scale where photolithography is typically used, such a disruption is less important, but at the ultra-thin interface between the pads and the tiny EBL contacts, this could cause a critical contact breakage.

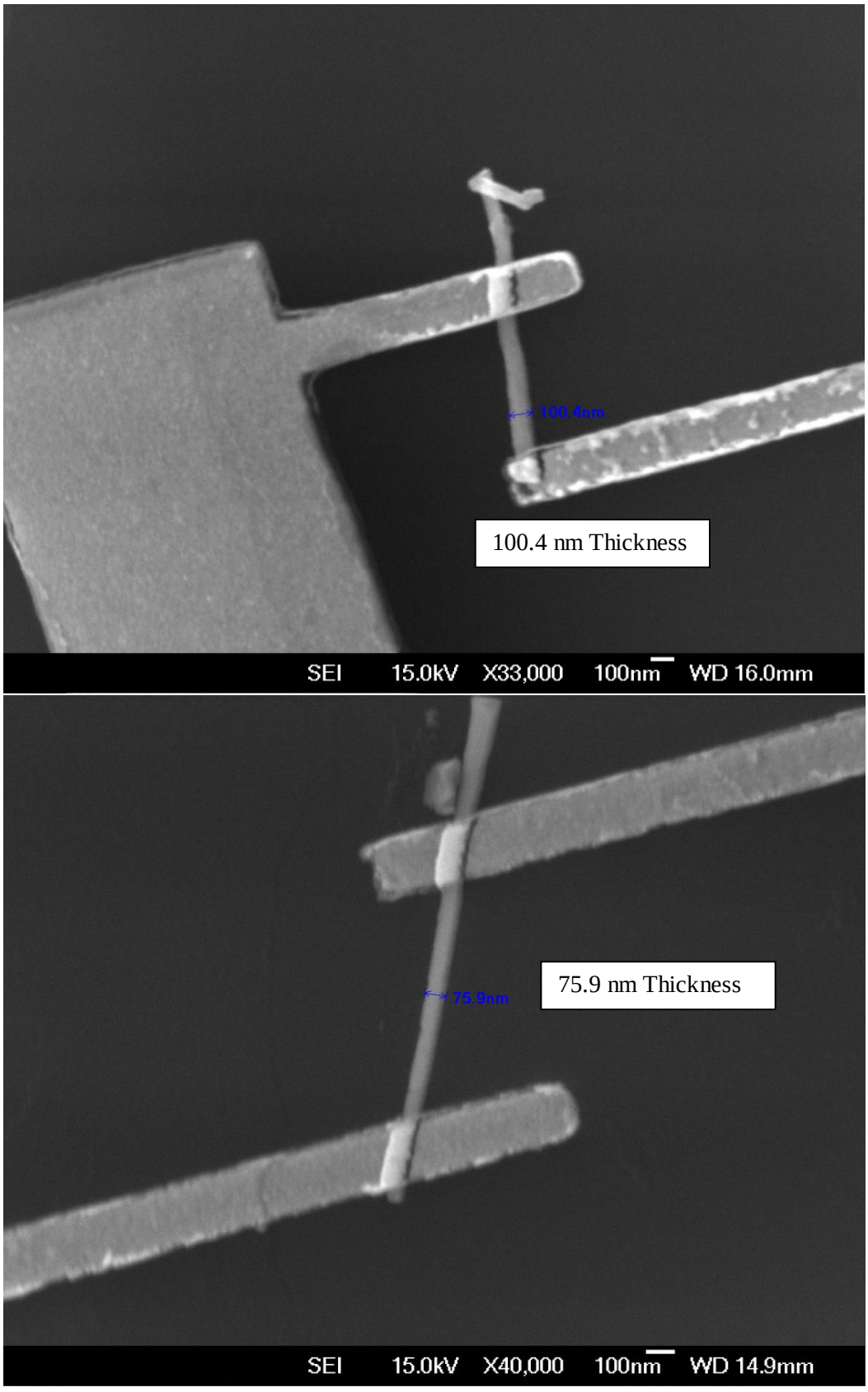

Figure 11: High magnification SEM imaging showing the contacted nanowires. To this inspection, the mechanical join between the wire and the contact appears to be solid.

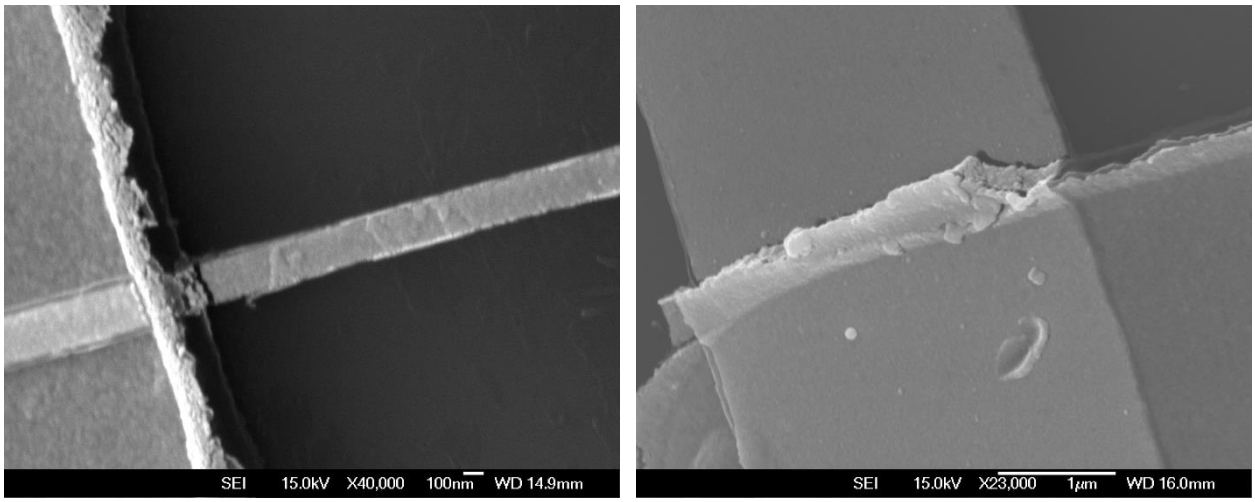

Figure 12: Interface between the large contact pads and the much smaller EBL defined nanowire contacts showing signs of breakage. Note that the size of the ridge of material around the edge of the pad is much larger than the thickness of the metal.

5.5.3 Pad-Contact Interface Patching and Pad Enlargement

The ridge of material could also have been caused by the large difference in thickness between the AZ1518 photoresist and the deposited Ti/Au layer. Ti/Au could have become attached to the sidewall of the resist profile, especially if it was not vertical. This metal could then either be removed with the photoresist, or adhere to the edge of the pad, depending on where it was most strongly anchored, illustrated in Figure 13.

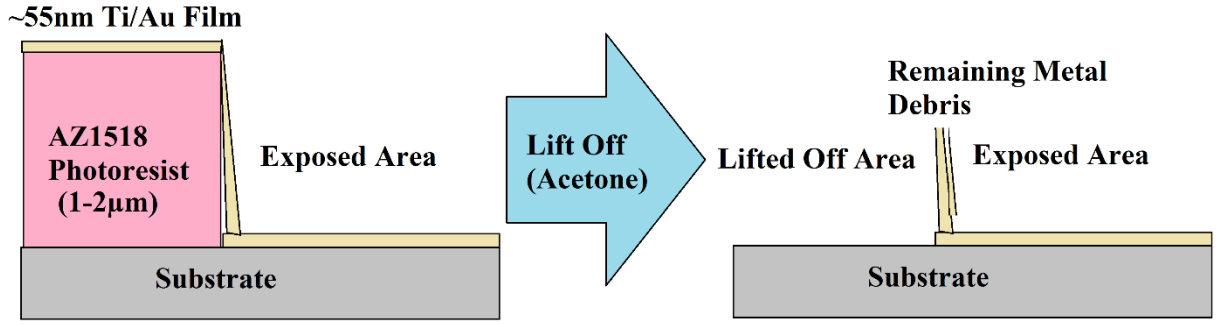

Figure 13: A potential explanation for the large ridge of metal debris appearing at certain points around the edges of the large contact pads.

An EBL-defined, 50 nm thick "patch" was fabricated over the ridged junctions between the contact pads and the nanowire contacts as shown in Figure 14, but this was not successful at completing the circuit and

there was still no measurable current. This was likely due to the fact that the ridge was much taller than the thickness of metal deposited. This was not a total failure however, as it proved that a second layer of EBL could be successfully performed over the contacted nanowires without damaging the existing contacts.

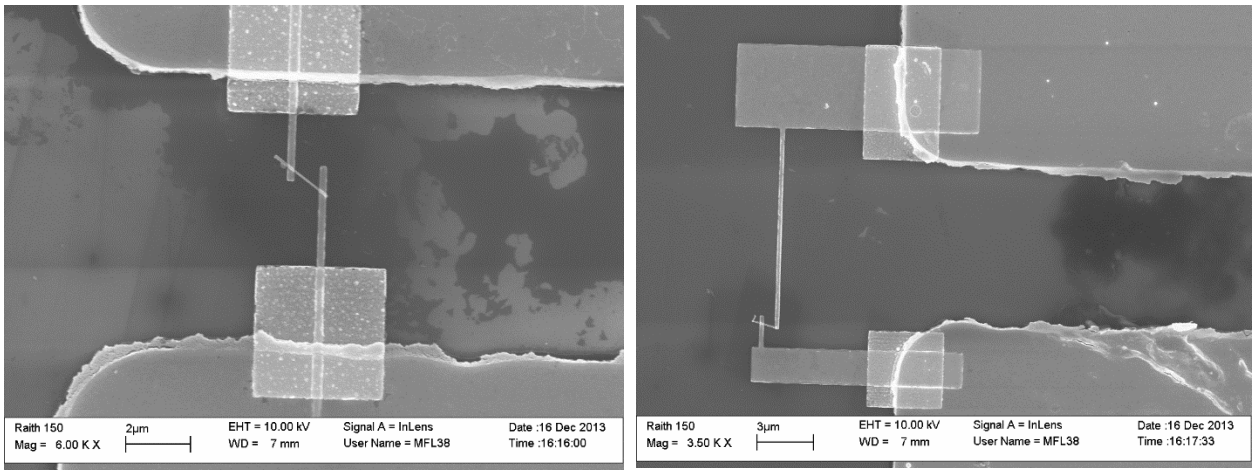

Figure 14: Patches of 50 nm Ti/Au applied to the interface between the large pads and the EBL contacts.

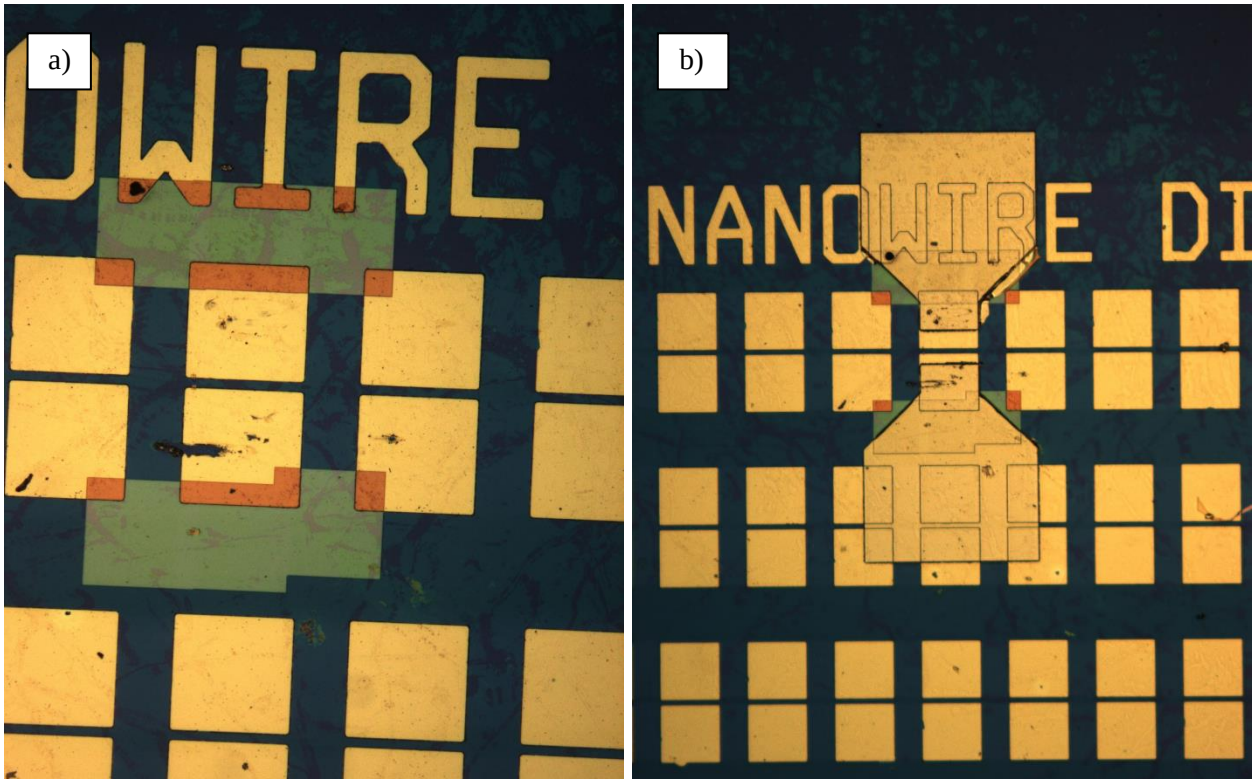

Figure 15: Enlargements of the 100µm pads by a) EBL and b) Photolithography. These add-ons increase not just the area but also the thickness of the pads, making them more resistant to damage from the sharp tipped probes. Note probe scratch in a).

A final attempt was made to repair the contacts on this chip. A common issue with probing electrical contacts on thin film devices is movement of the probes while testing causing damage to the pads. Some scratching was observed on one of the large contact pads, exposing the bare SiO_2. EBL was used to expand these pads as well, in order to enlarge the area able to be contacted by the probe as shown in Figure 15.

The expanded pads connected neighbouring pads together, but as there was no nanowire between the neighbouring pads, this was not electrically significant. Unfortunately these expanded pads did not improve the nanowire connection and once again electrical probing yielded no signal. The process of expanding the pads was retained and improved to avoid the shorting of neighbouring pads, as it was much easier to ensure that the probes were placed correctly with a larger contact area available.

5.5.4 EBL Defined Pad Arrays

It is of note in Figures 14 and 15 that neither the EBL contacts, nor the EBL-defined patches showed evidence of the tearing and ridging that was present on the photolithographically defined pads. In light of the explanation for tearing, this improvement is most likely due to the fact that PMMA is much thinner than AZ1518. EBL was therefore used to create the full array of pads. Because this pattern could be simply programmed into the EBL system and run automatically without having to perform single observation scans at each area, the larger aperture of 30 µm (and hence higher beam current) was used. The 3 mm x 3 mm pattern represents a relatively large exposure area by EBL standards and required approximately 14 hrs to complete, compared to a few minutes using photolithography but fortunately this exposure could be run overnight.

Contact pad arrays defined by EBL were crisp, with sharp edges visible as shown in Figure 16, giving cleaner lift off of the Ti/Au layer than before. Text and alignment markers were retained in the design because they proved useful for writefield alignment and focussing of the microscope during EBL.

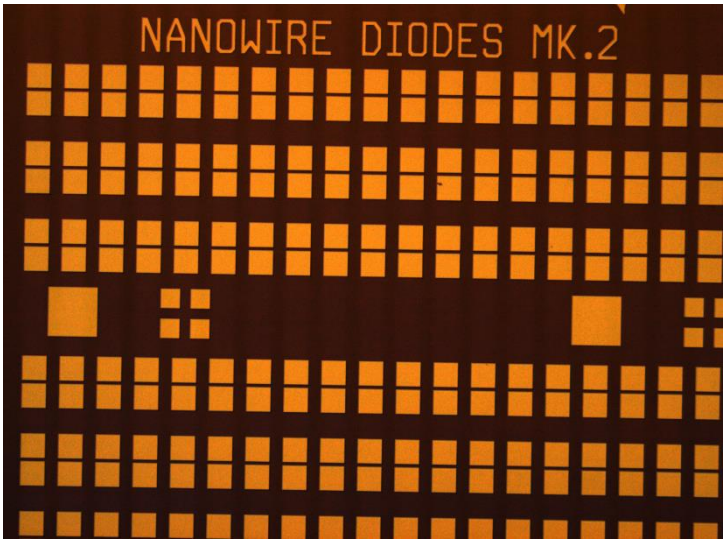

Figure 16: EBL defined pad array viewed with optical microscope.

5.6 Nanowires from Collaborators

Owing to the difficulty of directly contacting nanowires and the usefulness of the potential data from direct electrical measurements on nanowires, news of this research attracted the interest of several other ZnO nanowire groups. The opportunity to engage with these collaborators presented several potential advantages. Firstly, it was possible that the failures to measure current through the contacted nanowires was due to the nanowires themselves- the EPLD grown nanowires I had produced might simply have been of too high resistance to measure, a possibility with precedent for ZnO nanowires in the literature [1]. Secondly, the nanowires offered by these collaborators were larger than the ones I had previously been attempting to contact. The difficulty in locating the very small, EPLD grown nanowires through the EBL resist significantly increased process times and decreased throughput of devices. Being able to fabricate devices quicker, even if none were functional would increase the likelihood of a workable solution being arrived at. Thirdly, if a workable solution could be found and data gathered reliably from the contacted nanowires, it would be interesting to compare the electrical characteristics of nanowires grown by different methods, especially with reference to spectroscopic methods discussed in Chapter 6. If device applications are to be considered for ZnO nanowires, it would therefore be important to investigate which methods of growth produce the best devices.

5.6.1 Vapour-Phase Nanowires from Swansea University

Dr Alex Lord's group [1, 20-24] from Swansea University have published several papers on their vapour-phase ZnO nanowires. Their nanowire growths have included both gold-catalysed and non-catalytic

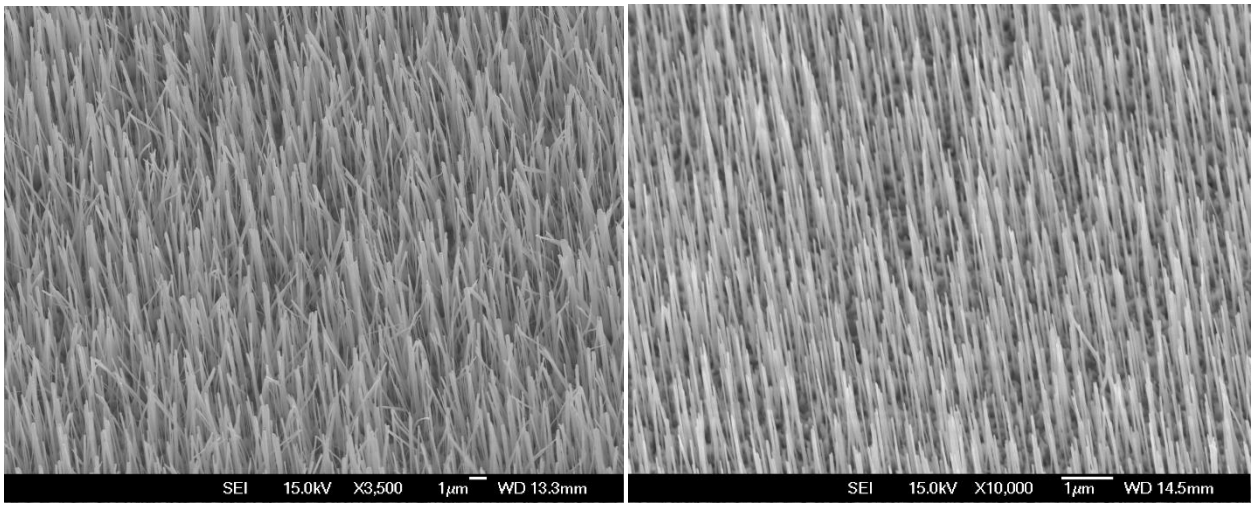

Figure 17: Non-catalytic (left) and gold-catalysed (right) ZnO nanowires grown by a vapour-phase method by A.M. Lord *et al.* and imaged at the University of Canterbury. The non-catalytic nanowires are longer (note the scale bars), more disordered and show greater variation in diameter than the catalytic nanowires. Note the different scale bars.

methods. A sample of each was sent to us for contacting and photoluminescence (PL) measurements (see Chapter 6). These wires were first examined using SEM as shown in Figure 17. Lord *et al.*'s nanowires, especially those grown without catalysts were significantly longer than any of my own PLD grown nanowires, with some wires being more than 10 µm in length. This made them easier to see under the PMMA resist when fabricating contacts.

5.6.2 MOCVD Nanowires from Simon-Fraser University

Professor S. Watkins' group [25-27] from Simon Fraser University in Vancouver, Canada has been growing ZnO nanowires of different sizes using Metal Oxide Chemical Vapour Deposition (MOCVD) and his group have published a number of papers on the behaviour of donors in ZnO nanowires. Their wires were implanted with dopants in varying concentrations, which affected their electrical and optical properties as well as their physical morphologies. We were supplied with six samples, to be imaged, characterised using photoluminescence and electrically contacted if possible. These are shown in Figure 18.

These MOCVD nanowires varied greatly in morphology. Wires with added dopants such as those in Figure 18 c) and d) were notably wider in diameter than undoped samples such as a) and b). This was somewhat unfortunate, as it made contacting them using EBL difficult. Using PMMA to deposit 45 nm of Ti/Au contact metal onto a rod or wire of 1000 nm thickness would almost certainly result in the previously discussed problem of incomplete contacting of the sides of the nanowires (see Figure 14). Such a large difference between contact thickness and nanowire thickness significantly reduces the likelihood of forming a successful electrical contact. Nevertheless, samples a), b), e) and f) provided thin enough wires to make good contacts to, with their extra length making them easier to find.

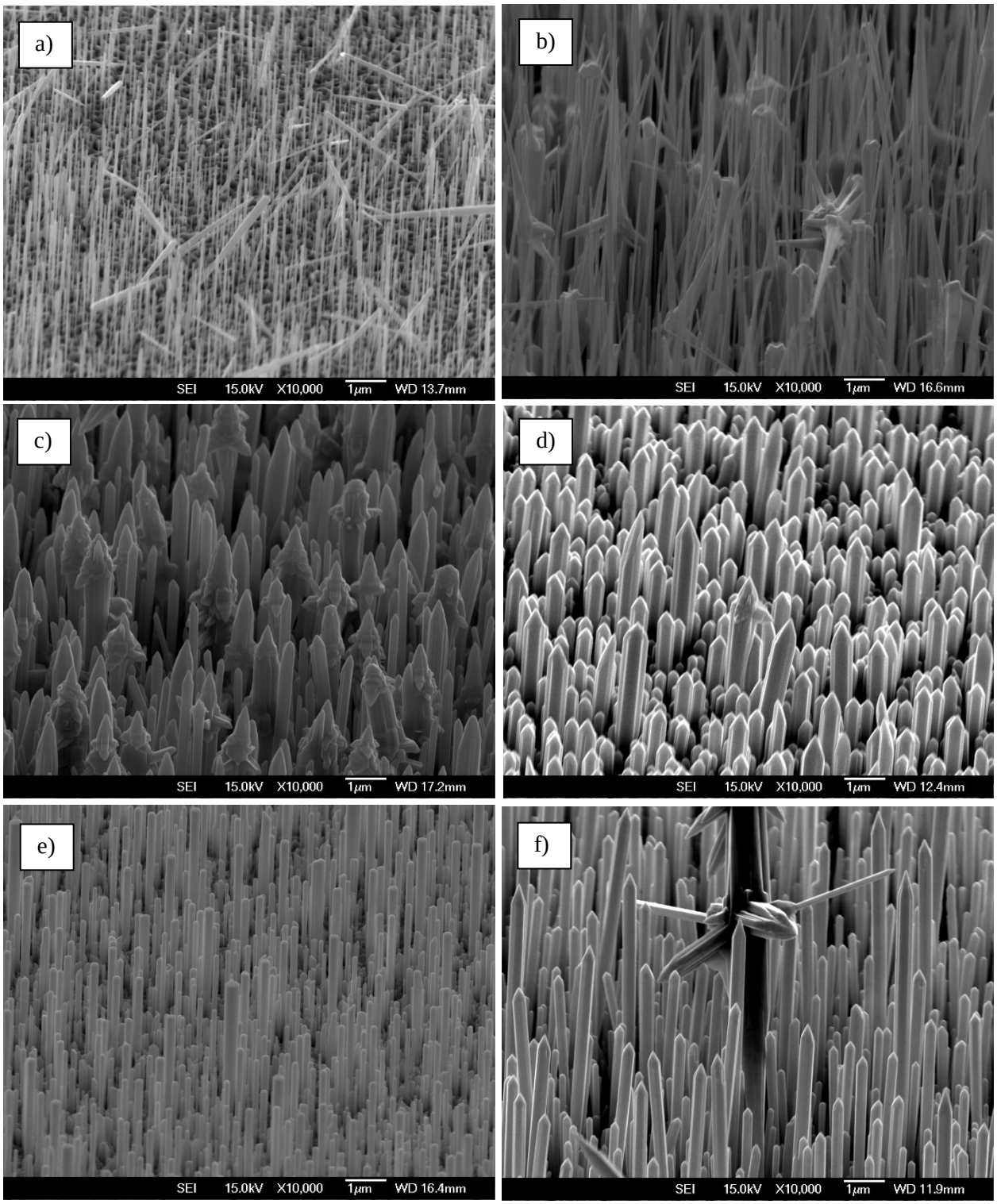

Figure 18: MOCVD grown ZnO nanorods and nanowires from Simon Fraser University demonstrating vastly different morphologies to each other and to my own PLD grown nanowires. From top left: **a)** Undoped wires grown at 750 °C on GaN, **b)** Undoped extra-long wires, **c)** 50 sccm Ga doped wires grown on sapphire at 605 °C, **d)** 100 sccm Ga doped wires grown on sapphire at 605 °C, **e)** Undoped wires grown on GaN at 650 °C **f)** 50 sccm Ga doped extra-long wires.

5.7 Swansea University Nanowire Contacting

5.7.1 Physical Contact Nanowire transference

A new method was also trialled for transferring nanowires from their as-grown substrates to the contact pad arrays by simply brushing the surface of the nanowire substrate gently across the contact pad array chip. This method resulted in a significant increase in the number of nanowires transferred onto the contact pad array chips. Care had to be taken to not scratch the gold pads as overly vigorous scraping could damage them as shown in Figure 19. A chip such as this would not necessarily be unusable because of the high number of pad pairs, but would decrease the number of opportunities for good contacts to be made.

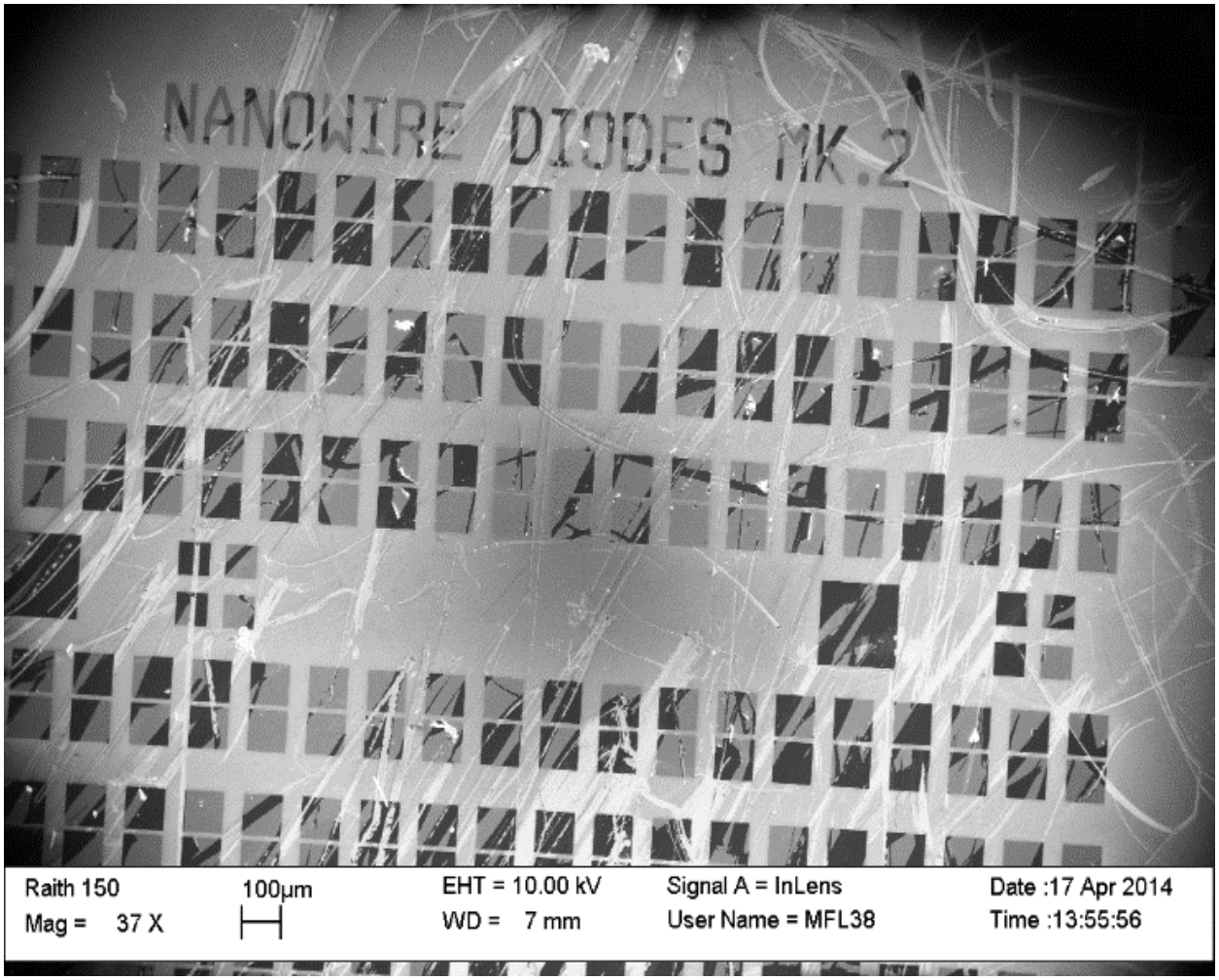

Figure 19: Contact pad chip damaged by rough handling. The dark areas of pads are where the light gold layer has been displaced from the darker titanium layer underneath.

5.7.2 Swansea Nanowire Contacting

The long, wispy, non-catalytic nanowires from Swansea University were the first to be contacted using EBL to make both the contacts and the contact pad array chips. As expected, the extra length made locating and writing contacts to these wires easier and several contacts were successfully made to the wires from the contact pad pairs. The physical transfer method of transferring the wires to the chips produced many opportunities for contacting, often with several choices of nanowires to make contacts to from a single pair of pads. Figure 20 shows the best contacts made to these wires.

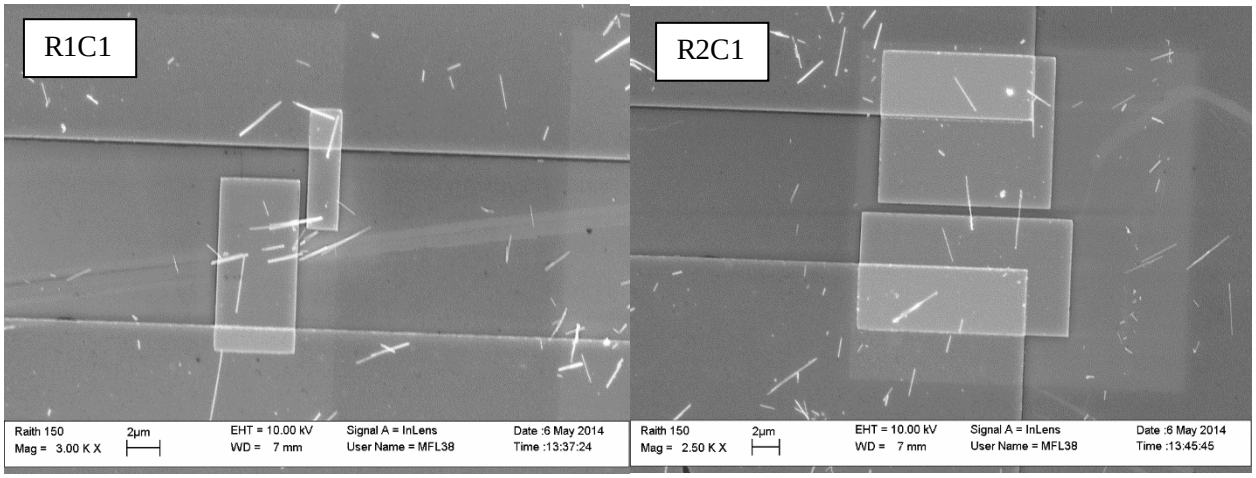

Figure 20: Contacted ZnO nanowires from Swansea University's non-catalytic growth. Note the high density of nanowires all over the area from the physical contact transfer. Contacted nanowires were named according to their position on the pads array. These contacts are left: row 1, column 1 (Referred to as R1C1) and right: row 2, column 1 (referred to as R2C1).

Larger, block shapes were used to contact these wires rather than the previous thin contact lines in order to minimise the resistance of the contact lines. It is still assumed that the nanowire itself is much less conductive than the Ti/Au contacts and comprises the majority of the total resistance of the current path. If this is true, then we can assume that the width differences between the block contacts on R1C1 and R2C1 have negligible effect on the total resistance if the length of the actual nanowire interface remains approximately the same. R2C1 contacts two nanowires at once and there appear to be several nanowires bundled together in R1C1. Photolithography was retained for depositing the expanded contact pads onto the chip. The patterning

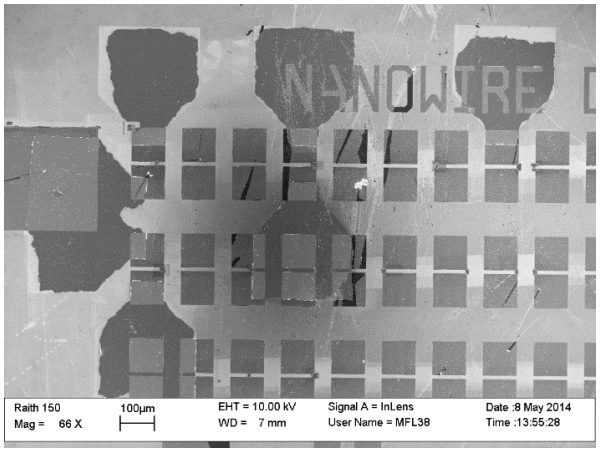

Figure 21: Expanded contact pads on R1C1, R2C1 and also on R1C4. Despite their rough appearance, these pads did not seem to cause any problems.

in this particular case appeared to be particularly rough as shown in Figure 21, but this did not seem to affect the contacts.

5.7.3 Silver Paste Parameter Analyser Connections

A different probing system was used to measure the electrical properties of these nanowires. This involved mounting the nanowire chip onto a metal sample holder and using permanent wire connections from the pads on the chip to separate pins on the sample holder which were then accessed by the parameter analyser. A single strand of fine aluminium wire was used to make these connections. At the sample holder pin end, the contacting wire was wrapped around the pin and soldered, but at the chip end a more delicate approach was needed. The connecting wire was bonded to the expanded contact pads using Electrical Sciences Inc. silver paste, which was applied via a needle with the aid of an optical microscope. Even with the larger size ~200 µm contact pad, this task was extremely difficult and over-application or application in the wrong area could easily short out a wire, destroying the device completely. Figure 22 shows the bonded contact pad array. The prober had three active measurement pins, so one pad was used to access both the bottom contact of R1C1 and the top contact of R2C1. R1C1 was then measured using pins 1 and 2 and R2C1 measured using pins 2 and 3.

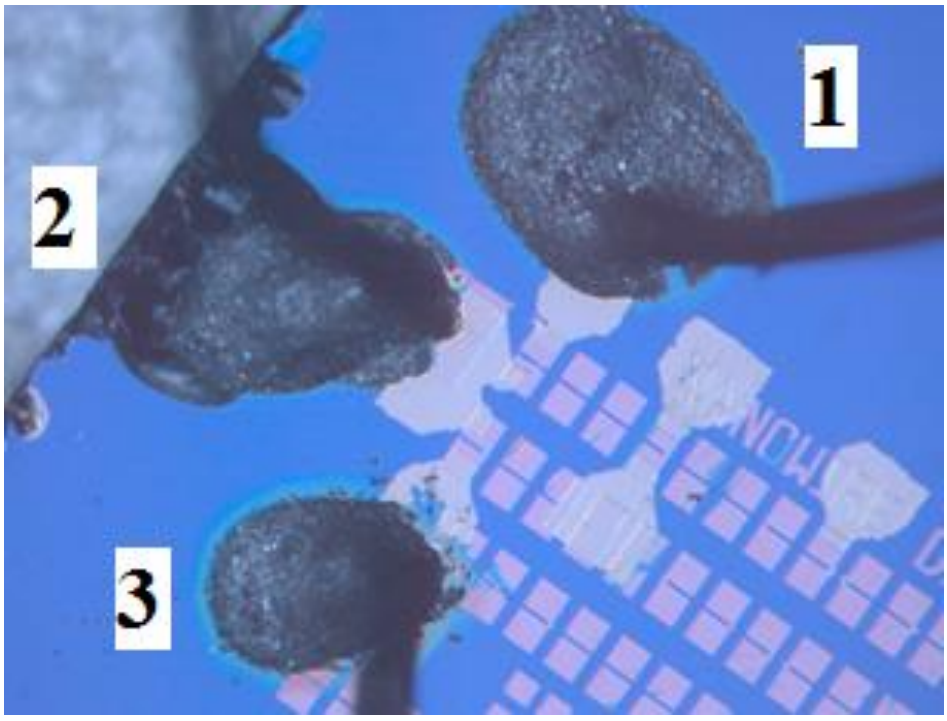

Figure 22: Silver paste bonded wires connected to the expanded contact pads. Even with the aid of a microscope, the silver paste is difficult to control.

5.7.4 Resistance Measurements of Swansea Non-Catalytic Nanowires

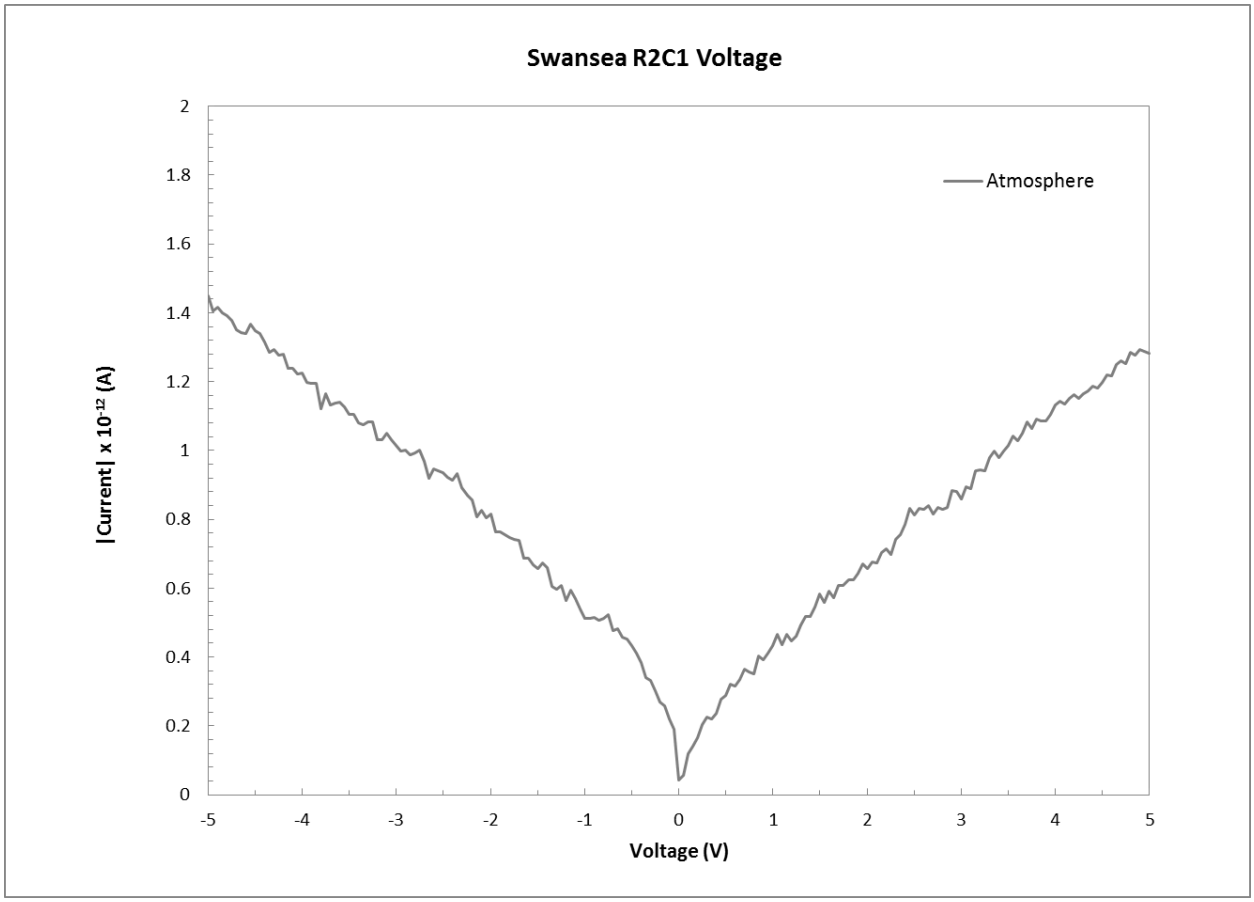

Figure 23: Voltage sweep of Swansea nanowire R2C1 showing very high resistance.

The non-catalytic Swansea nanowires were the first nanowires which gave a detectable current signal with applied voltages of ±5 V as shown in Figure 23. Figure 23 shows very weak ohmic I-V characteristics, recorded at room temperature, in atmosphere on the two nanowire contact, R2C1. 1.2 pA at -4 V gives an approximate resistance of 3.3×10^{12} Ω. This is massively larger than the approximate resistance of 200 kΩ that Lord *et al.* [1] reported on similar nanowires using their four point probe system with a similar probe spacing of at 1 µm. Other researchers who have used lithographically defined nanowire contacts similar to those fabricated here have measured currents much closer to my results than to Lord *et al.*'s. While Lord *et al.* report approximately 5×10^{-6} A in vacuum at 1V, Bao *et al.* [28] report 5×10^{-9} A in air, Liao *et al.* [29] report 4×10^{-12} A in air and Cammi and Ronning [30] report approximately 10^{-9} A in vacuum.

Other groups whose contacted nanowires have shown higher currents than those measured here have taken various additional steps in order to improve the quality of their contacts. Lord *et al.* used ethanol to activate the surface of their nanowires and stressed the importance of cleaning their probes with a piranha

etch. Liao *et al.* [29] annealed their Ti/Au contacts for 3 minutes at 500°C in N_2. Bao *et al.* [28] also used a thermal treatment for 10 minutes in a forming gas mixture of 5% hydrogen and 95% helium. Cammi and Ronning [30] did not report any additional treatment of their contacts. Other groups have used oxygen plasma treatment to prepare the surface of nanowires prior to ohmic contacting (discussions at the 8th International Workshop on Zinc Oxide, Niagara Falls, 2014).

It is possible that Lord *et al.*'s pre-treatment regime and probe system is the cause of the superior nanowire conductivity measured in their experiments. Their justification for the use of ethanol is that it readily binds to both the pristine surface of the nanowires and also to any adsorbed species. Ethanol also readily desorbs under UHV, thereby carrying any adsorbates away from the nanowire surface. They propose that this is the cause of an order of magnitude decrease in resistivity as shown in Figure 24. However, their results differed from those measured using lithographically defined pads by much more than a single order of magnitude. At this point in my experiments, I was unable to explain this very large difference in the resistances of the nanowires measured using Lord *et al.*'s in-situ four point probe system and my EBL contact pad methodology. I will propose an explanation after discussing persistent photoconductivity effects in Section 7.7 of this Chapter.

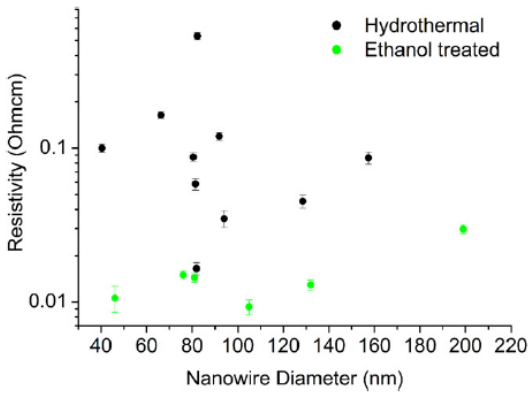

Figure 24: An order of magnitude decrease in resistivity caused by use of ethanol to activate the surface of nanowires demonstrated by Lord *et al.* [1] Note that while this graph compares hydrothermally grown nanowires rather than vapour-phase nanowires, Lord *et al.* also concluded that there was no statistically meaningful difference between the two methods in terms of resistivity.

5.7.5 Swansea Nanowires Vacuum Response

The surface of ZnO is known to be electrically active and is naturally terminated by hydroxyl groups bound to the outer plane of the surface truncated crystal lattice. Further, any defects on this surface layer act as sites where O_2 and H_2O molecules can adsorb to the surface, accepting and immobilising electrons from the conduction band to become O^{2-} and H_2O. This "charge trapping" reduces the number of carriers to the point where a depletion region forms near the ZnO surface [1, 28, 29]. Due to the high surface area to volume ratio, this effect is expected to be much more pronounced in nanowires and a significant fraction of their cross sectional area could become non-conductive due to the formation of this adsorbate induced depletion region.

Adsorbed oxygen and H_2O are only weakly bound to the crystal surface and some of these can be removed by vacuum pumping. This reduces the electrical depletion of the surface and releases trapped electrons increasing the free carrier concentration and therefore lowering the sample resistance. As before, this effect should be more pronounced in nanowires [28, 29]. The I-V characteristics of the non-catalytic Swansea nanowires were measured in atmosphere and then in vacuum at a pressure of 6 x 10^{-5} mbar using a -5 V to +5 V applied voltage sweep. As shown in Figure 25, the effect was the opposite of that expected with the measured current significantly less in vacuum than in atmosphere.

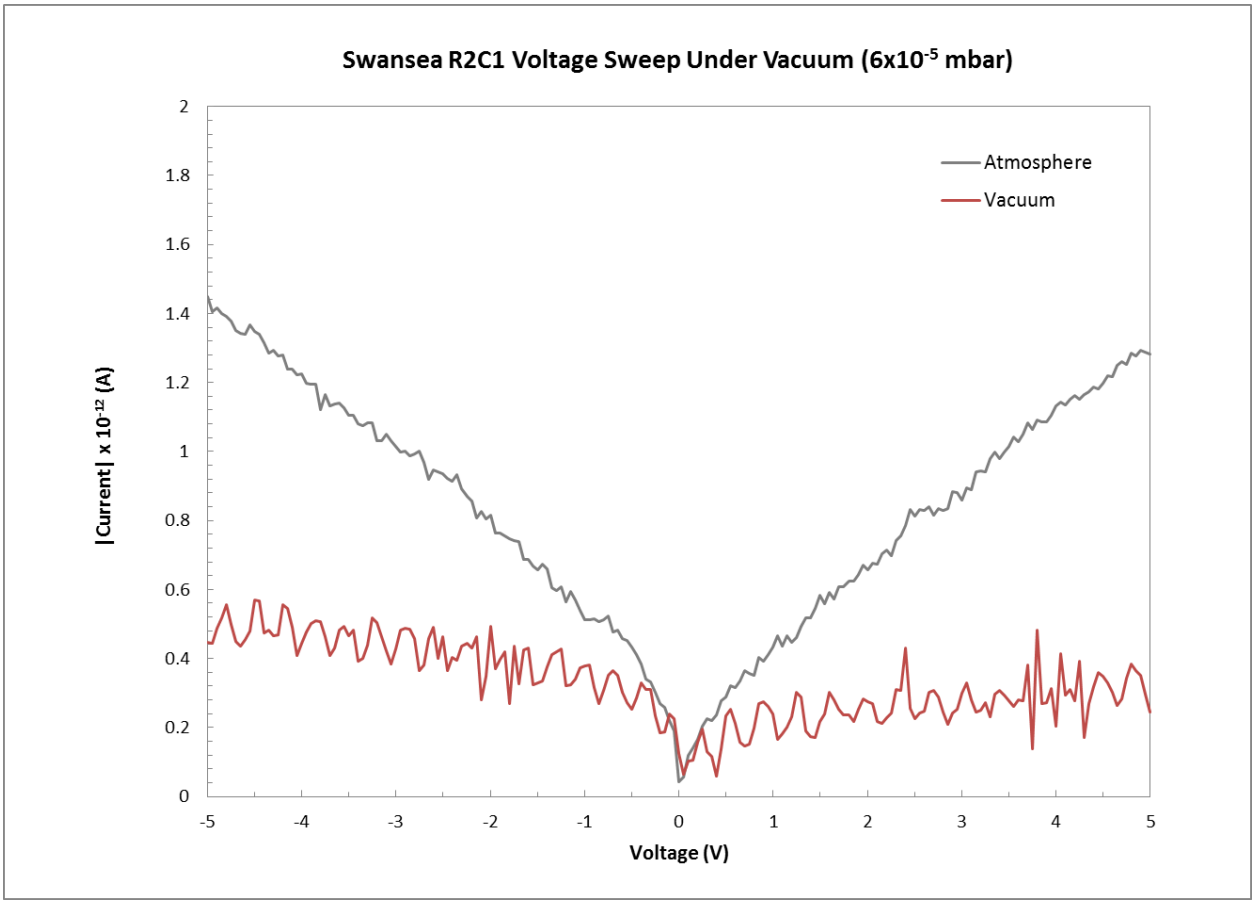

Figure 25 Swansea nanowire R2C1 voltage sweep in air and in vacuum.

5.7.6 Swansea Nanowires UV Response

To test whether the current signal recorded by the prober was coming from the contacted ZnO nanowire and not from some other leakage source, the I-V characteristics of the nanowire were re-measured after exposure to 365 nm ultraviolet light. UV photons of energy greater than the bandgap (3.37 eV for ZnO) create electron-hole pairs by exciting valence band electrons into the conduction band. This increases the carrier concentration of the material, which in turn, increases its conductivity. In addition, the energy

supplied by the photons assists in the desorption of atmospheric surface adsorbates from the crystal. It has also been proposed that above-bandgap irradiation can also create oxygen vacancies [28], but this theory is contentious. This potentially creates a two stage effect, with fast desorption of surface adsorbed oxygen combined with the slow release of oxygen from the lattice. It was expected that the former, being a surface effect, would be particularly pronounced in nanowires due to the high surface-area to volume ratio [29]. The contacted nanowires were exposed to 365 nm UV radiation for 30 s with a voltage of 1 V maintained across the contacts. The effects of the UV excitation were then monitored until the current signal returned to its initial, pre-excitation level as shown in Figure 26. This UV photocurrent effect took an extremely long time to decay, even with such a brief 30 s exposure to the 365 nm UV light.

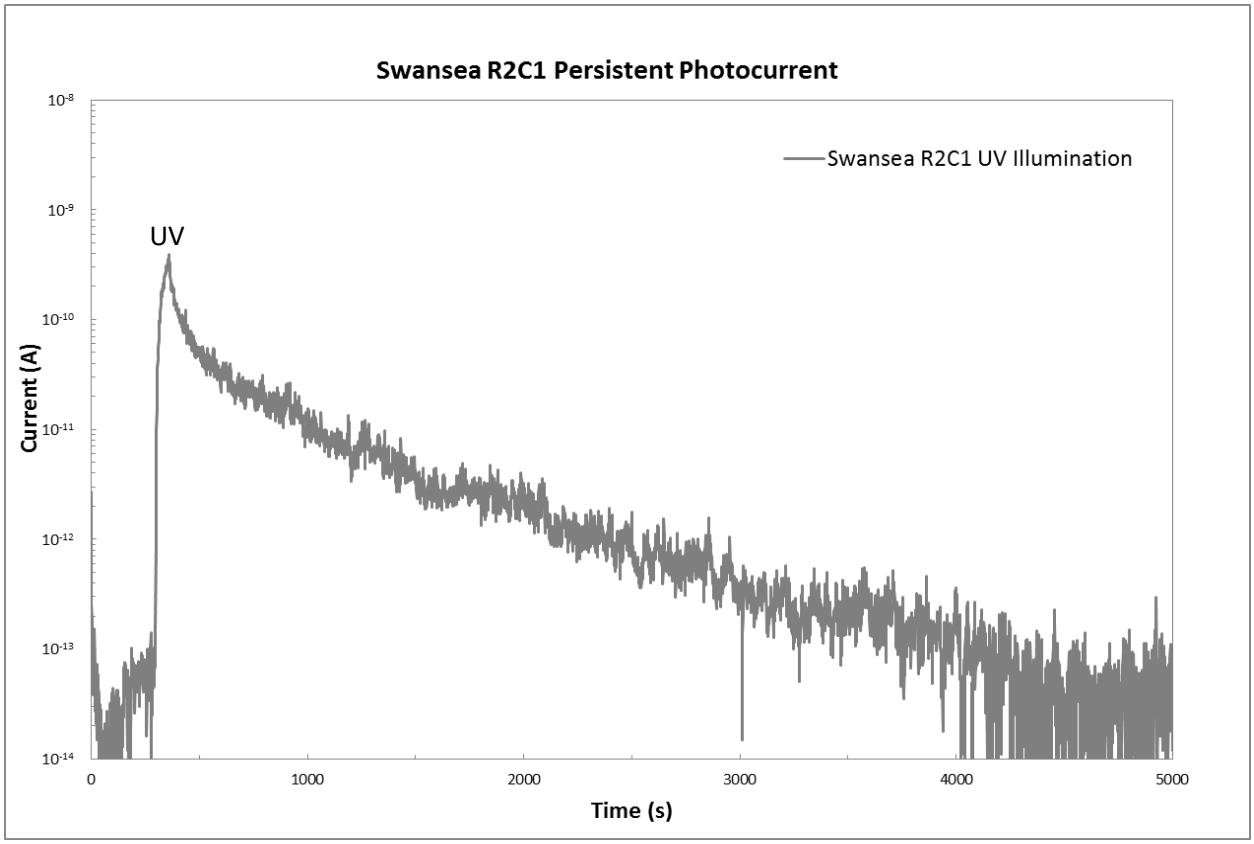

Figure 26: UV exposure of Swansea nanowires in atmosphere. Over 30s of illumination, the current rose 4-5 orders of magnitude due to photogenerated carriers and desorption of surface oxygen. This effect gradually decayed over 5,000 seconds.

5.7.7 Swansea Nanowires Persistent Photocurrent in Vacuum

Much of the persistent photocurrent produced by UV exposure is related to the removal of oxygen from the nanowire surface, followed by the slow re-adsorption of oxygen back onto their surface sites. Oxygen adsorbates deplete the surface of the nanowire as seen in Figure 27. Photogenerated holes are attracted to the oxygen adsorbates and are neutralised on the surface, leaving free electrons in the lattice [1, 31, 32]. If oxygen desorption and re-adsorption is responsible for these long-lived changes in conductivity, then it would be reasonable to assume that the re-adsorption process would be retarded or eliminated by completely removing oxygen from the test environment. The UV exposure test was repeated with the sample pumped to a vacuum of 5 x 10^{-6} mbar with the results shown in Figure 28.

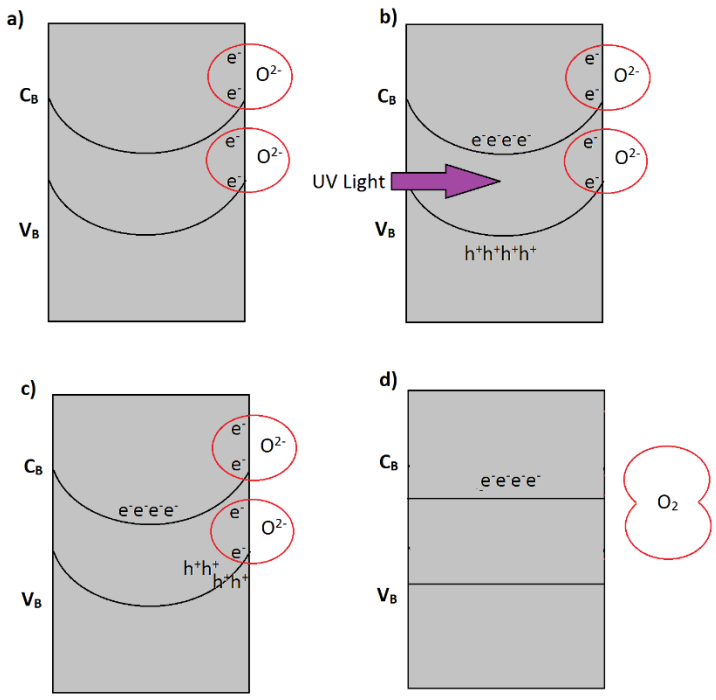

Figure 27: a) Oxygen adsorbs to the side of a nanowire, taking electrons from the suface Zn atoms and creating a surface depletion layer (and upward band bending). b) UV illumination generates electron-hole pairs in the lattice. c) The holes move up the valence band towards the surface of the nanowire. d) Some of the holes recombine with the surface electrons, releasing oxygen. The photogenerated electrons are now free carriers in the conduction band, contributing to a persistent, higher conductivity.

As expected, the absence of oxygen in vacuum conditions prevented the recovery of the current signal to its initial value. Even after 5000 s, the sample exposed to UV in vacuum did not recover to its intial pre-illumination current when biased at +1 V. A current decay was observed immediately after UV illumination, similar to that in atmosphere. This is consistent with the assumption that the UV irradiation both drives off surface adsorbates and generates photocarriers. The photocarrier component decays exponentially and is mostly gone after 1000 s, but the decrease in nanowire resistivity due to the removal of surface adsorbates remains due to the absence of oxygen in the high vacuum environment.

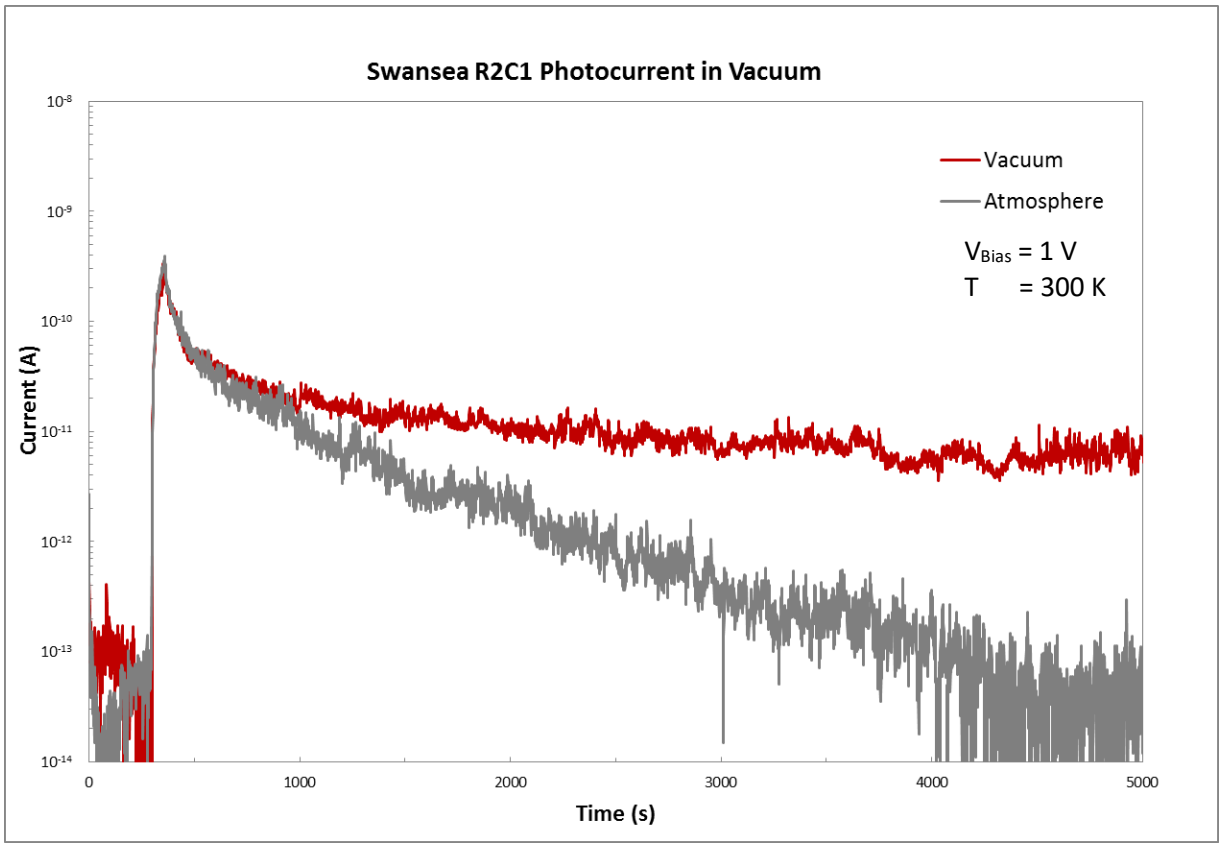

Figure 28: Swansea nanowires exposed to UV irradiation in atmosphere and in vacuum. Both exposures generate similar amounts of photocurrent, but the exposure in vacuum does not decay back to its original levels after 5000s.

An interesting effect was observed when the contacted nanowires were exposed to UV irradiation in vacuum and then exposed to air by venting the system to atmosphere while the photocurrent was slowly decaying. Figure 29 (overleaf) shows a "quenching" effect, where venting to atmosphere causes a sudden decrease in photocurrent. It is surprising that this "quenching effect" results in a significantly shorter time for the photocurrent to decay back to pre-illumination levels compared to being allowed to decay solely in atmosphere (about 1000 s from exposure to dark current levels, compared to over 4000 s).

From this, it can be inferred that it is the change in atmosphere causes the current to suddenly decrease. The turbulent inrush of air when the chamber was vented could have allowed more oxygen to flow over the nanowire surface than being simply exposed to still air. A test for this could be to measure the decay of photocurrent in a steady flow of air or gas.

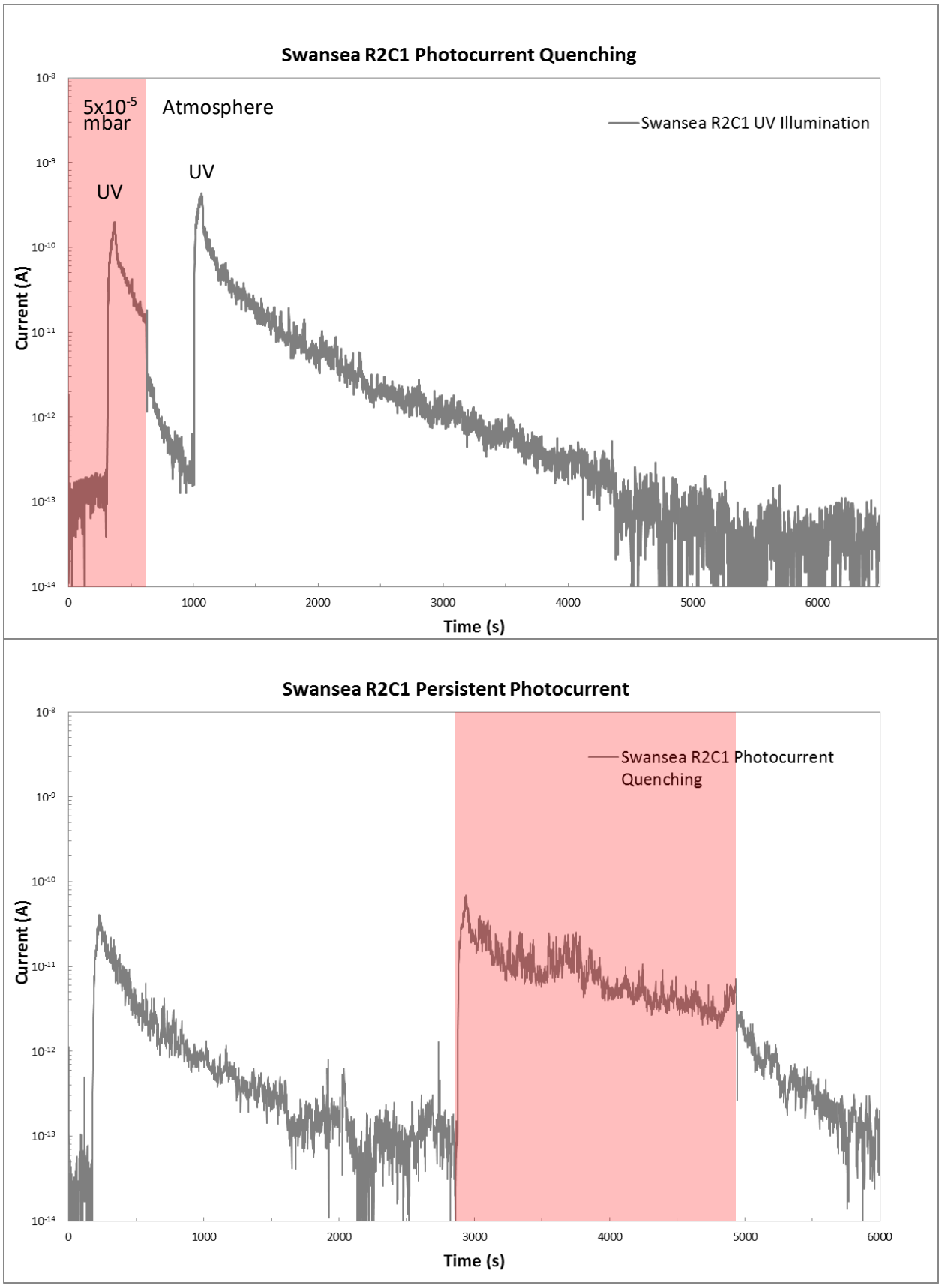

Figure 29: A photocurrent "quenching" effect was seen when a sample which had been exposed to UV irradiation in vacuum was vented quickly to atmosphere.

5.7.7 Nanowire Charging and A Possible Explanation for Lord *et al.*'s low resistance

In Chapter 3, the growth of ultra-fine nanowires catalysed by sub-nanometre gold clusters was described and their bending when exposed to the electron beam of the Raith 150 SEM is discussed in Section 4.3.4. When combined with the results from the UV exposures of nanowires, we can now propose an explanation for why Lord *et al.*'s nanowires have a significantly lower resistivity when measured using their four-point probe system than when measured using EBL-defined permanent contacts [1].

As discussed in Chapter 4, Section 3.4, the bending and fusing of ultra-fine nanowires when exposed to normal SEM scanning is most likely due to some form of charging effect, even though the wires are in electrical contact with one another and there is a current path to ground through the clip to the SEM stage. From this we infer that even when connected to an electrical ground, the electron beam of the SEM is capable of imparting some charge to a ZnO nanowire.

The electron beam provides an injection of electrons, so any charging of the nanowire by exposure to the electron beam is likely to increase the concentration of majority carriers in the n-type wire, especially if the outer shell of the wire is depleted as some authors have proposed [1, 29]. In addition, the electrons in the SEM beam were accelerated using a voltage of 10 kV, giving them an energy well above the bandgap of ZnO, allowing them to create electron-hole pairs in the nanowire. The persistence of UV-induced photocurrent in ZnO nanowires as demonstrated above in Section 7.7 of this chapter and elsewhere [28-30] shows that carriers generated in a nanowire, by whatever mechanism, can persist for hours, or perhaps indefinitely if maintained in vacuum. This generated photocurrent can be as large as 3-4 orders of magnitude as shown in Figures 26 and 28.

Lord *et al.*'s four-point probe measurements were made in vacuum, using an SEM column to image and guide the tips of the probes onto the nanowires, with multiple measurements of resistance made on a single nanowire with the probes moved to different positions each time. If the SEM electron beam used to image the nanowire while the probes were being moved were to generate or inject carriers into the nanowire in the UHV environment of the SEM chamber, these carriers are unlikely to have decayed by the time the resistance was measured. Furthermore, the nanowire would have no path to ground while the probes were being moved as the substrate was electrically insulating. An increased density of free electrons in the nanowire will decrease its measured resistance. If the effect of electron beam illumination is comparable to that of UV illumination, the resistance could have decreased by 3-4 orders of magnitude as observed in Figure 26. Consequently, Lord *et al.* could have observed a current in their nanowires of the order of 10^{-9}

A if they had used permanent contacts, which would be more consistent with my results and those of others previously mentioned [28-30].

Due to the quenching effect of venting from vacuum to atmosphere shown in Figure 29 and the persistence of photocurrent in vacuum conditions, it would be difficult to test such a hypothesis without venting the main SEM chamber after the probes had been applied to the sample. Similarly, a nanowire contacted using EBL, loaded into an SEM and scanned would likely experience significant photocurrent decay when it was unloaded from the SEM vacuum chamber.

There is a certain amount of support in the literature for the idea that carriers can be injected into semiconducting materials using an SEM beam. Liu *et al.* [33] demonstrated that one minute scanning with an SEM beam could improve the conductivity of a ZnS nanowire by two orders of magnitude, as shown in Figure 30. This result is significant due to the fact that ZnS is intrinsically insulating. The authors referred to the current measured before the electron injection as being due to leakage in the system, so it is possible that a two orders of magnitude increase in conductivity is a conservative estimate.

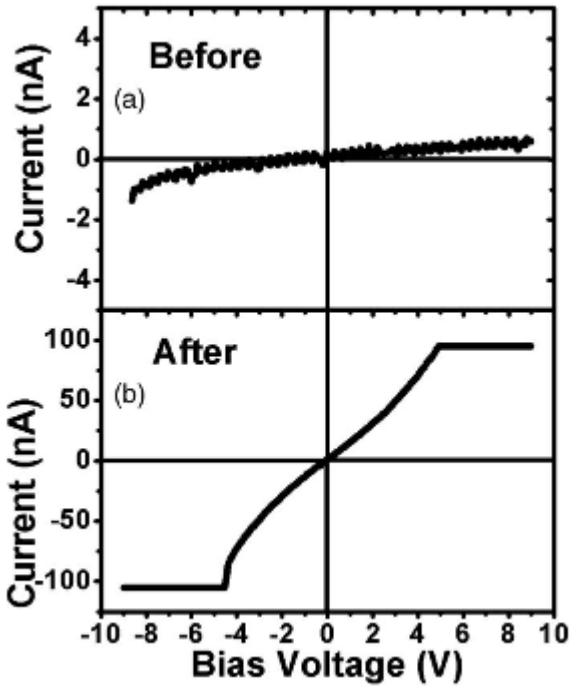

Figure 30: Liu *et al.* [31] exposed an insulating ZnS nanowire to electron beam injection via SEM beam. They saw a negligible current of less than 1 nA (which they ascribed to leakage) increase to over 100 nA with 1 minute of exposure.

In an example using a ZnO nanowire, Zhang *et al.* [34] investigated the effect of an electron beam on a nanowire contacted with probes that formed Schottky contacts and with probes that formed Ohmic contacts. They found that the electron beam did introduce carriers into the nanowire and suggested that the effect was similar to light-induced photocurrent. While the nanowire was exposed to the beam, the current measured was significantly higher, however their conclusions were mainly concerned with the lowering of the Schottky barrier-height by scanning the electron beam across the probes themselves rather than the nanowire.

Ichimiya *et al.* [35] conducted experiments where ZnO:Zn microcrystals were exposed to an electron beam during the measurement of cathodoluminescence. They discovered that they could observe emission

from the free-exciton band at room temperature, which is not usually possible due to the large green emission from defects. The emission of UV photons is caused by the recombination of electron-hole pairs, which means that the electron beam was generating these free carriers in the sample in a similar manner to UV irradiation. The signal was strongest with an accelerating voltage between 9-12 kV as electrons with this energy appeared to maximise the production of electron hole pairs in the microcrystals. The acceleration voltage normally used in SEM systems is 10 kV which is in the middle of this range.

The lack of surface preparation for the Swansea nanowires contacted in this thesis is likely to have resulted in a missed opportunity for achieving a lower measured resistance and I do not doubt Lord *et al.*'s conclusions about its effectiveness. However I feel that the evidence presented here enough to question the applicability of comparing resistance measurements of nanowires using an SEM probe system to those made using permanent contacts.

5.8 Simon-Fraser University Nanowire Contacting

5.8.1 Device Fabrication

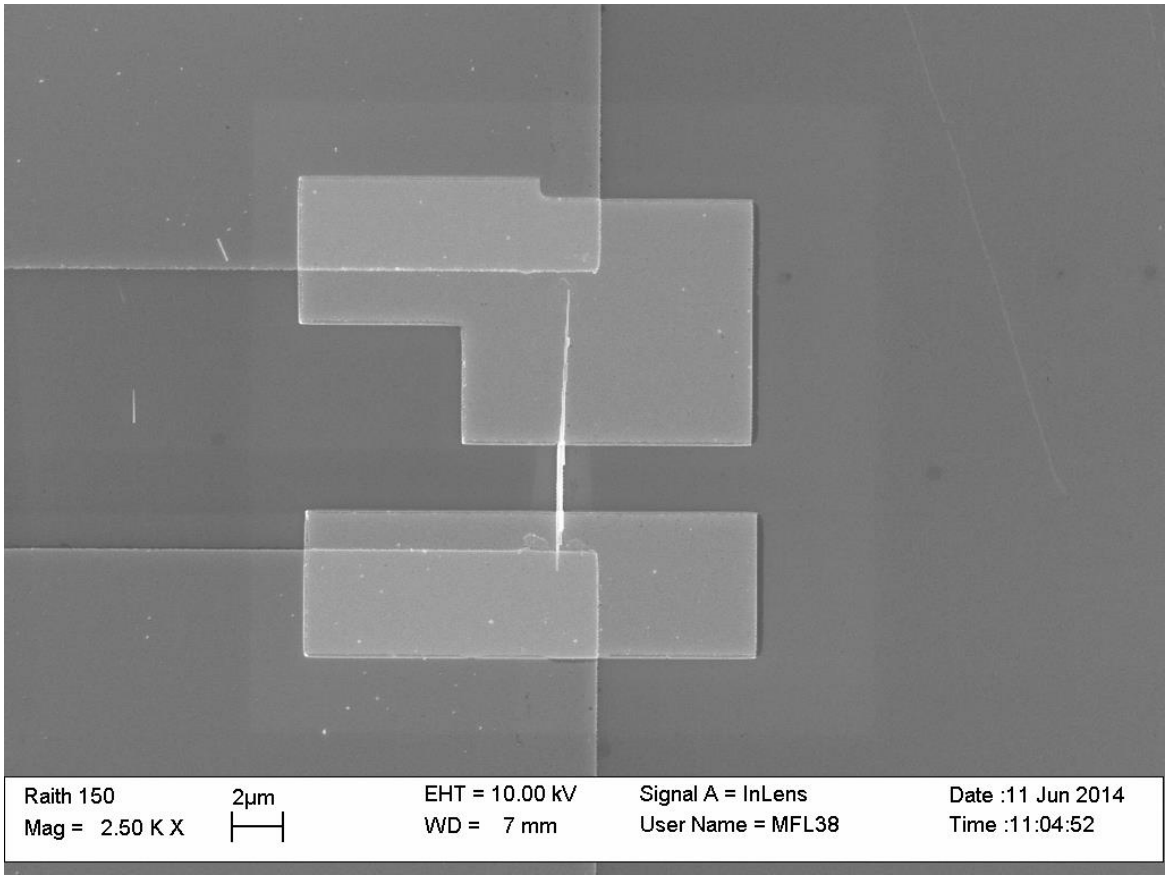

Figure 31: SFU H825 nanowire contacted at position R9C10 by electron beam lithography. There seem to be more than one nanowire contacted here, but at least one spans the approximately 2µm gap.

Following success in contacting the Swansea University nanowires, the same fabrication techniques were used to apply contacts to nanowires supplied by Simon-Fraser University (SFU). The undoped extra-long nanowires shown in Figure 18b, designated H825 by SFU researchers, were chosen for their length and high aspect ratio. A successful contact is shown in Figure 31. These nanowires on their as-grown substrates were as long as 10µm, almost long enough to span the entire gap between a pair of contact pads without any additional lithography steps.

5.8.2 Wire Bonding

Using silver paste as a means of manually connecting the large contact pads to the test pins of the prober was a difficult procedure requiring a high level of manual dexterity. Many mistakes were made using this process and these mistakes often irreparably damaged the sample by shorting two pads together or covering a contacted nanowire with paste. Wire bonding was used to replace this technique as it could precisely bond

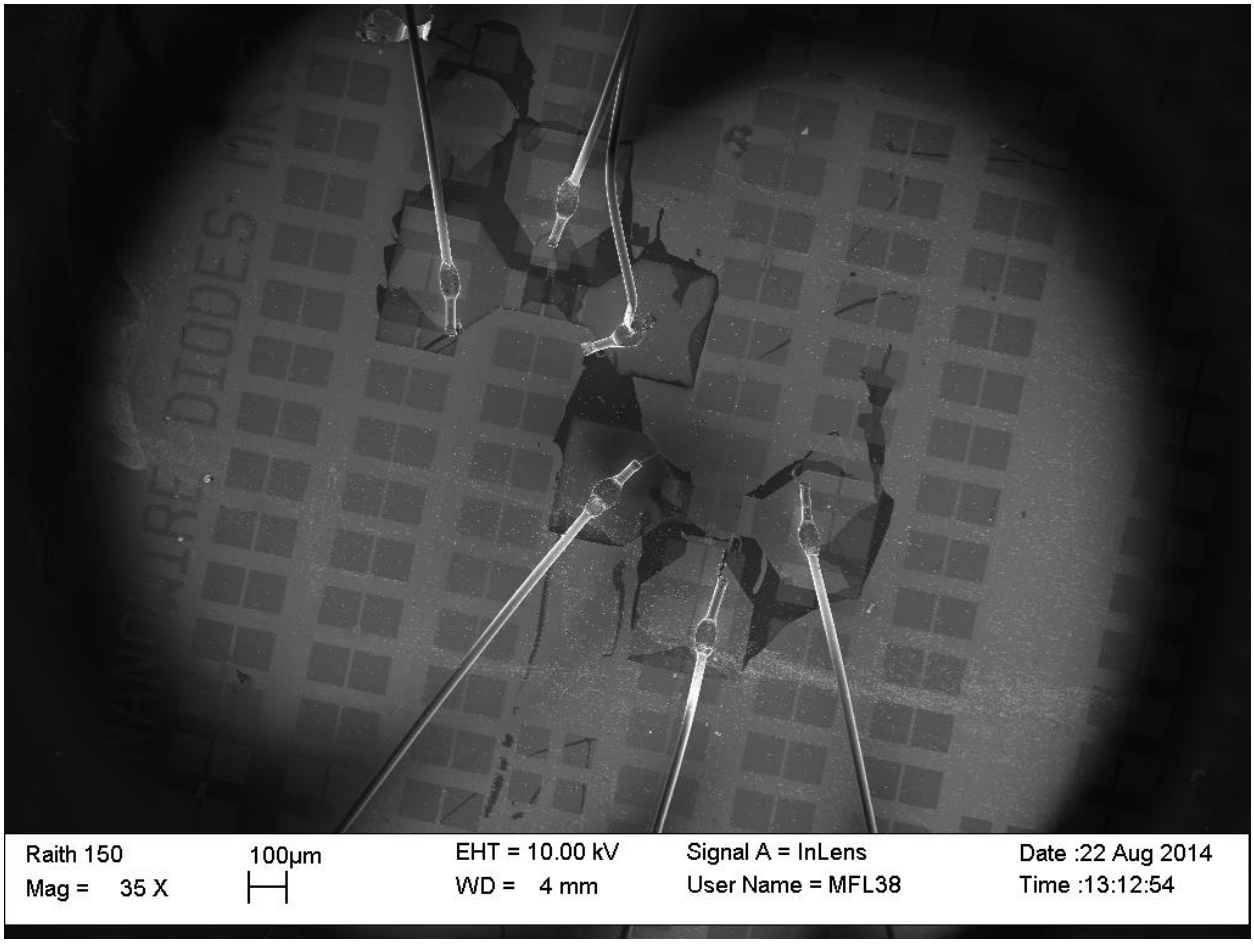

Figure 32: Wire bonding used to easily contact two nanowire devices in close proximity to one another without the potential to accidentally short out the device.

a thin wire from a targeted point on the contact pad to the metal pins on the sample holder. Figure 32 shows how two devices close to one another could be connected without interference. Although the wire-bonds proved to be more fragile than the silver pasted wires, their ease of fabrication and significantly lower risk of damaging the contacts made them a superior choice.

5.8.3 Schottky Contacting

The long length of these nanowires made them a suitable choice for adding a third Schottky contact, between the two ohmic contacts of the nanowire with the aim of making a nanowire MESFET. The University of Canterbury ZnO research group has had considerable success in fabricating AgO_x Schottky contacts on ZnO bulk crystals and thin films [15, 18] so this material was chosen and a Schottky contact was patterned using EBL and deposited using reactive RF sputtering and electron beam evaporation for the AgO_x Schottky contact and its gold capping layer respectively. The fabrication of the Schottky gate appeared successful as shown in Figure 33. All the deposited material lifted off rapidly when the photoresist was washed off with acetone leaving clean lines and features of less than a micron wide.

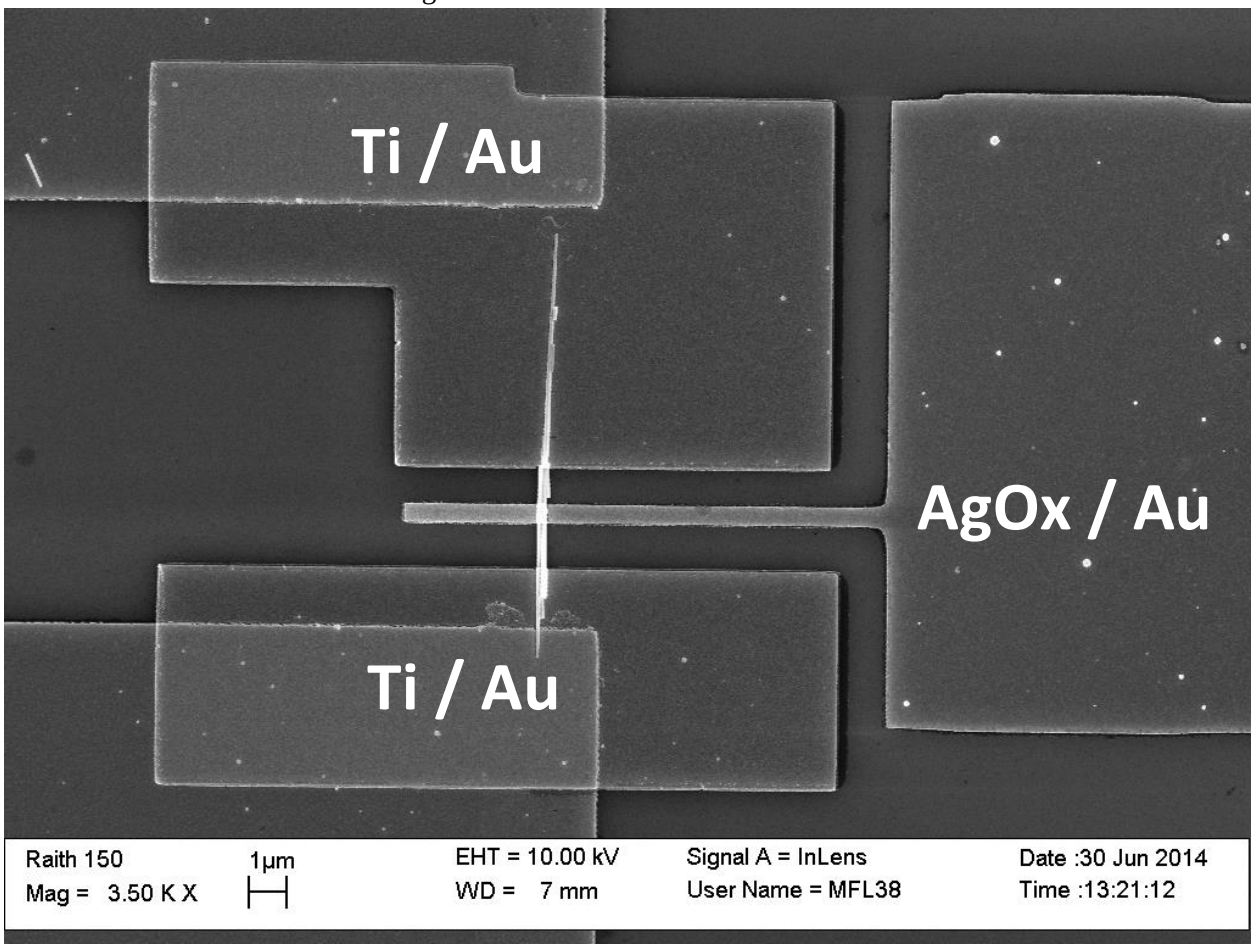

Figure 33: Gold capped AgO_x Schottky contact deposited onto already contacted nanowire R9C10. The close proximity of the gate contact to the ohmic contacts is a testament to the precision of EBL as a patterning technique.

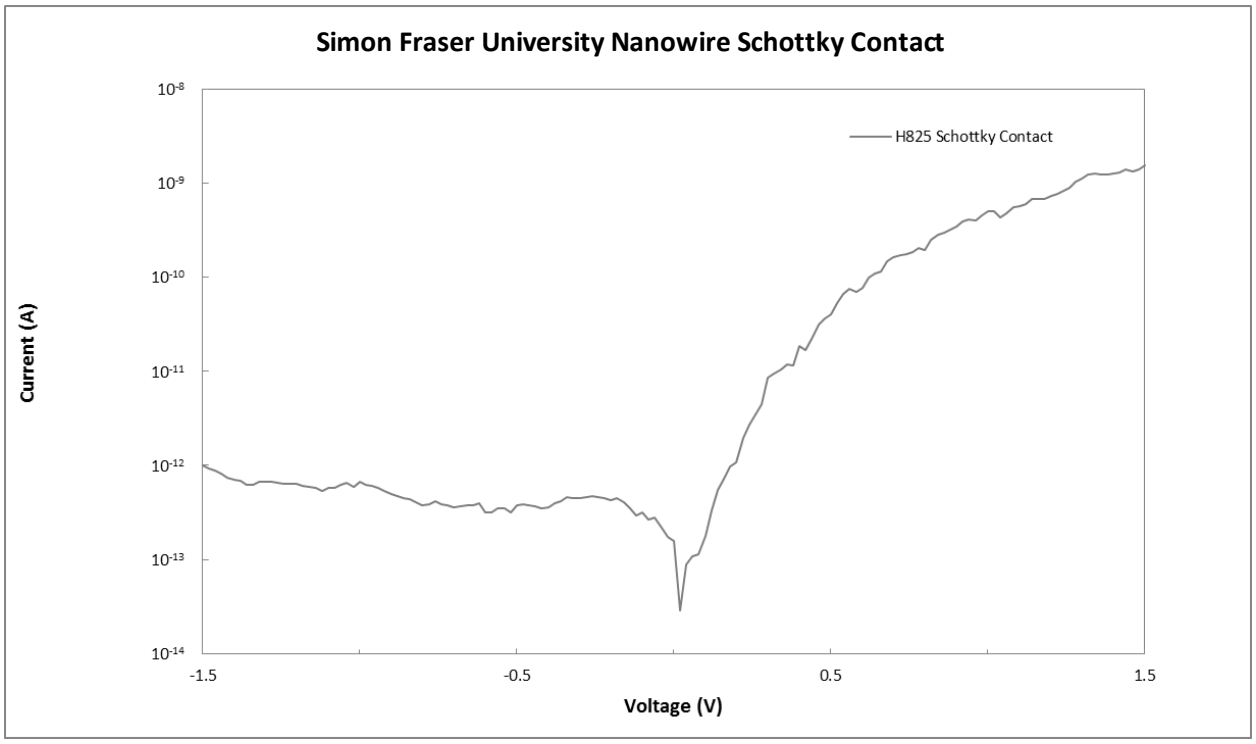

Figure 34: IV curve of Simon Fraser University nanowire H825 contacted with the lower Ti/Au ohmic contact and the right-side AgOx Schottky contact.

Figure 34 shows the IV response of the Schottky contact and the lower Ohmic contact (as in Figure 33) shown in Figure 33 measured in air. The current roll-off in the forward bias direction indicates a high series resistance, but despite this, the Schottky contact shows four orders of magnitude rectification between the forward and reverse bias regions at ±1.5 V. This compares favourably with results published in the literature for Schottky contacts on ZnO nanowires which typically report approximately three orders of magnitude rectification using Schottky contacts such as metallic platinum [36] and gold [37].

Using the IV curve, an ideality factor and barrier height can be calculated to measure the quality of the contact against an ideal diode. The ideality factor is calculated using Equation 1:

$$n = \frac{q}{kT}\left(\frac{dV}{d(\ln(I))}\right) \qquad \textbf{[1]}$$

Where q is the elementary charge (1.602 x 10^{-19} C), k is the Boltzmaan constant (1.38 x 10^{-23} $m^2kgs^{-2}K^{-1}$), T is the temperature (293 K at room temperature). The gradient of the log-linear plot was empirically measured as 19.313, producing an ideality factor, n, of 2.05. An ideal diode has an ideality factor of 1, but real diodes on ZnO range from close to unity to nearly 5 [38] with the majority of studies clustering around 1.6-1.8. ZnO nanowire diodes have been fabricated with an ideality factor close to 3 [37]. The high ideality

factors in ZnO diodes are sometimes attributed to the high intrinsic carrier count of the strongly n-type material which increases the amount of electron tunnelling through the barrier [38].

The barrier height, Φ_B, is the height of the Schottky barrier formed by the metal/semiconductor junction. It can be calculated from the extrapolated intercept of the steepest gradient of the IV curve with the y-axis and the area of the curve using Equation 2:

$$\Phi_B = \frac{kT}{q} \ln\left(\frac{AA^*T^2}{I_o}\right) \quad \textbf{[2]}$$

Where A is the area of the contact, A* is the Richardson constant for ZnO (32 $Acm^{-2}K^{-2}$) and I_o is the extrapolated intercept from Figure 34. Using this fomula, the Schottky barrier height for this diode can be calculated to be 0.656 eV. This is directly comparable to many of the barrier heights recorded for Ag and Au on bulk ZnO, which ranged between 0.5-0.7 eV [38].

These calculations show that the diode fabricated on the nanowire was within the margins of expectation for ZnO Schottky diodes. This is perhaps a little surprising for a nanowire diode, especially since the resistance of the Ohmic contacts in section 5.7 was so high. It is possible that the surface depletion reported by Lord et el. [1] as well as the generally high resistance in air could reduce the number of carriers available near the contact, resulting in less tunnelling through the barrier and a more ideal diode. This effect could potentially offset any ideality reduction caused by the constraints of nanowire device fabrication, bringing the performance back in line with bulk.

5.9 Spontaneous Nanowire Contact Failures

So far, nanowires had been successfully contacted with both ohmic and Schottky contacts with well-behaved ohmic and rectifying I-V characteristics. Further tests were intended, including operating the Schottky gated Simon-Fraser nanowire as a MESFET. However a severe fault began to occur with the testing apparatus which rendered further testing impossible. A spontaneous discharge occurred at random which obliterated both the nanowires and their electrical contacts. Figure 35 shows the destruction of the Schottky contacted nanowire from Figure 33. The nanowire has broken in several places and the metal contacts appear to have melted, mostly along the interface between the nanowire and with the large contact pads. Only two of the contacts were actively tested at any given time on this device (so transistor functionality was never measured), but despite this, all three pads were completely destroyed. Despite attempts to diagnose the cause of the problem, this also occurred to all of the other contacted nanowires. Figure 36 shows a similar failure of Swansea R2C1 from Figure 22.

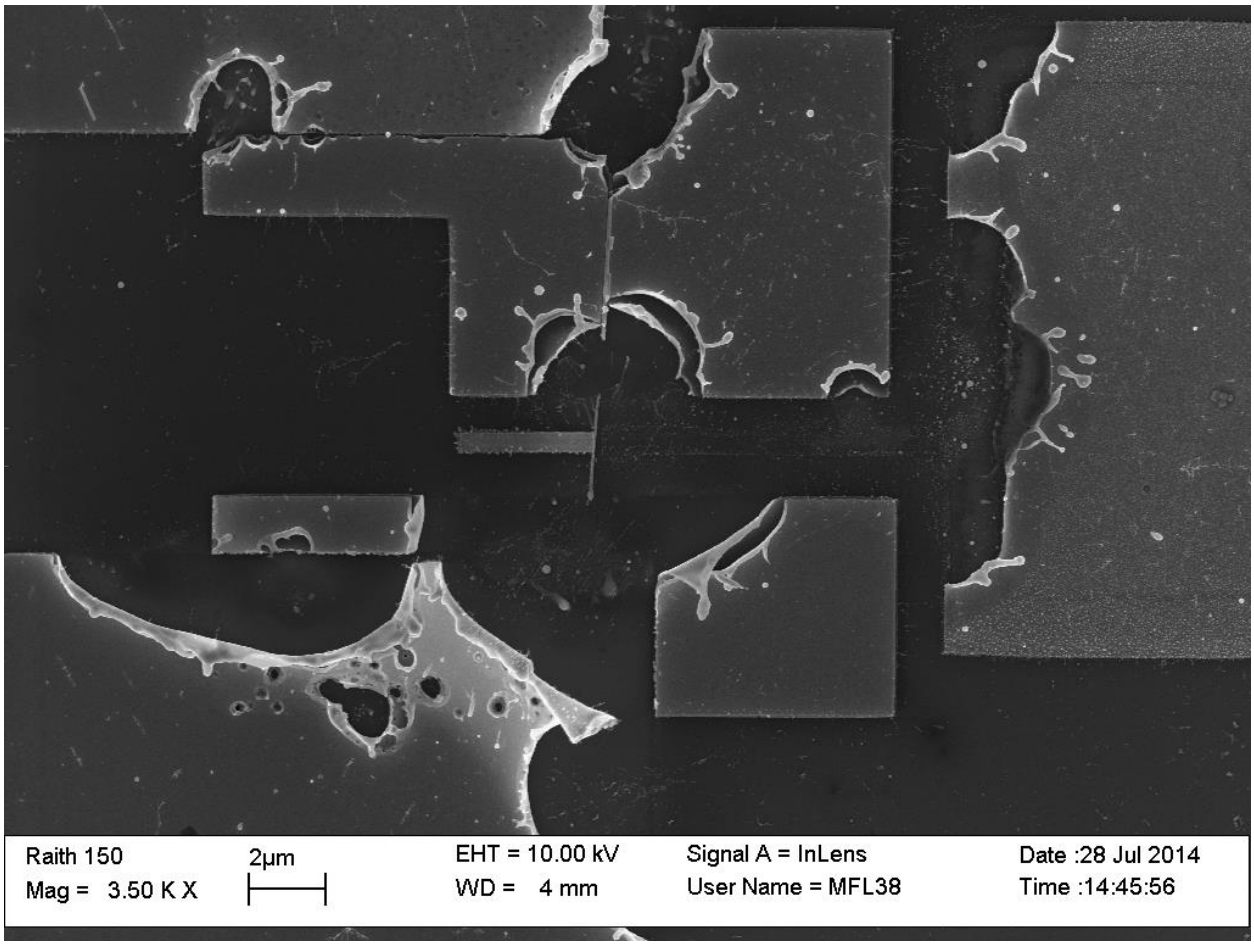

Figure 35: A fascinating SEM image showing the complete destruction of the Schottky gated SFU nanowire shown in Figure 32. The double layers of the Ti/Au are clearly visible and the nanoscopic debris shows evidence of melting.

The damage was not caused by inappropriate use of high voltages or currents. The Swansea R2C1 nanowire was stable up to 10 V in forward and reverse bias and had been held at 1 V for many hours with no damage. When this device failed, it was undergoing a routine 1 V bias UV illumination test. Contacted nanowires suffered similar damage during different stages of testing once the problem began to occur, suggesting an issue with the test apparatus. There appeared to be no relationship between the amount of

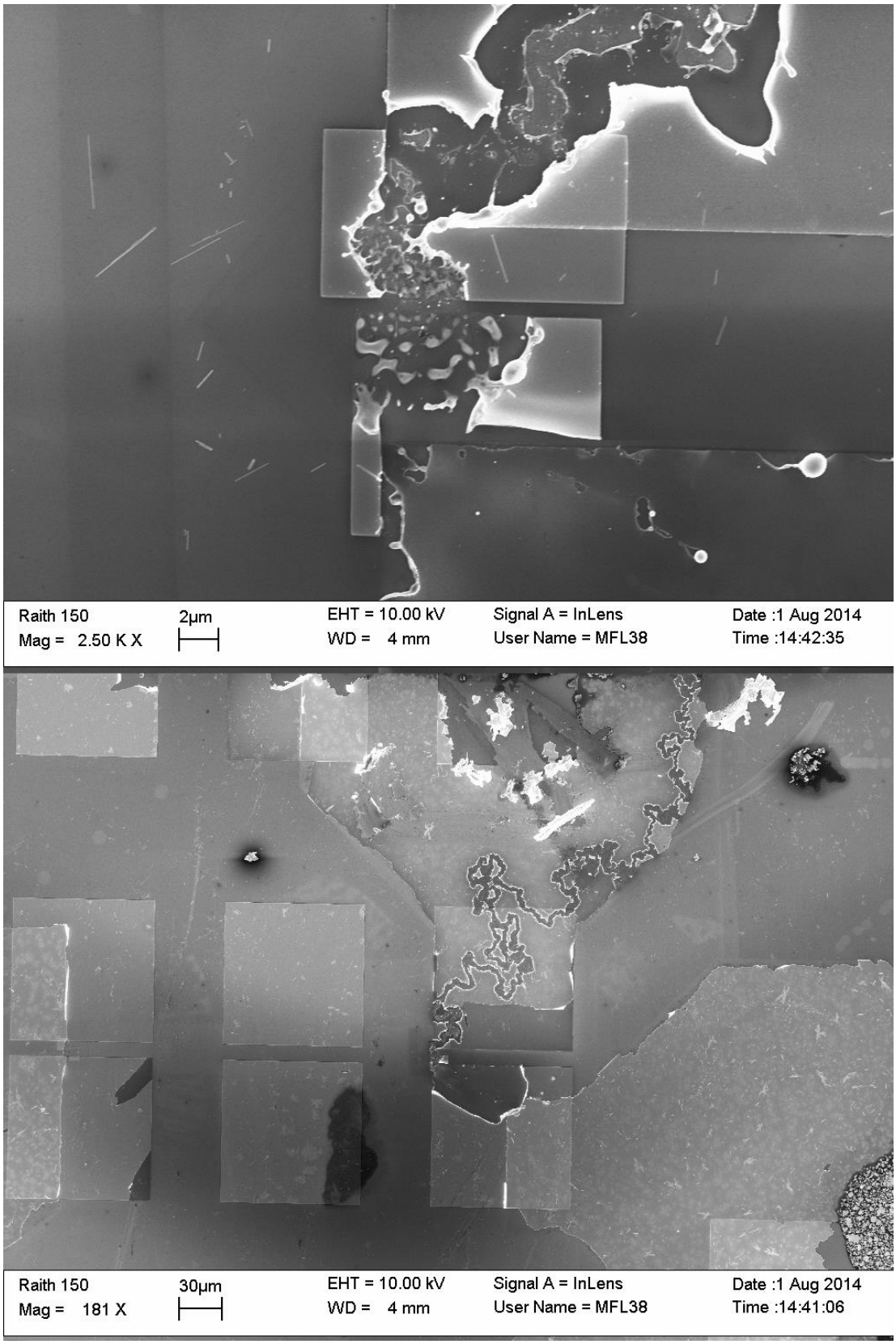

Figure 36: Catastrophic failure of Swansea nanowire contact R2C1 shown at two magnifications. A discharge path has clearly been burned into the upper metal contact, while the lower one seems to have separated entirely.

testing required before a sample would be damaged; Swansea R2C1 and Simon Fraser R9C10 were tested many times on different days before any damage occurred, but other devices did not complete a single IV sweep before being destroyed. Testing apparatus compliance current settings did not seem to assist in preserving the contacted nanowires. Failures were observed when the compliance current was set to both 10 nA and 1 µA.

5.10 Summary

This chapter details the development of electron beam lithography as a technique to pattern permanent contacts onto ZnO nanowires.

- ZnO nanowires were contacted with both Ti/Au ohmic contacts and AgO_x/Au Schottky contacts using electron beam lithography.
- Nanowires from collaborator Alex Lord from Swansea University had a measured resistance of approximately 3 GΩ, which was significantly higher than Lord *et al.*'s own testing.
- I believe that a significant source of this discrepancy is the fact that Lord *et al.* conducted their resistance measurements after their nanowires had been exposed to an SEM's electron beam, which the literature and my own experiments suggest is capable of generating additional carriers in ZnO nanowires.
- Exposure to UV light resulted in a large, immediate increase in nanowire current in excess of 3 orders of magnitude, due to the removal of oxygen adsorbates and photogeneration of carriers in the nanowire.
- A large fraction of the photocurrent was found to persist for hours after exposure in air and almost indefinitely in vacuum confirming the role of the surface absorbates.
- Photogenerated electron-hole pairs not related to oxygen adsorption did decay in vacuum and in atmosphere, demonstrating that there are two mechanisms responsible for the photocurrent.
- Venting to atmosphere immediately quenched a large proportion of the photocurrent and exposure in vacuum followed by venting to atmosphere caused the photocurrent to decay to pre-illumination levels faster than being allowed to decay naturally in either air or vacuum.
- Schottky contacts made from AgO_x were highly rectifying, with four orders of magnitude rectification.
- The ideality factor and barrier height were calculated as 2.05 and 0.656 eV respectively, in agreement with literature values for ZnO Schottky contacts.

- Wire bonding was found to be more efficient than silver paste for making contacts to the nanowire contact pads due to the lower difficulty in fabricating the connections.
- A fault in the test equipment caused catastrophic failure of nanowire devices, making it infeasible to continue experimentation.

5.11 References

[1] A. M. Lord, T. G. Maffeis, A. S. Walton, D. M. Kepaptsoglou, Q. M. Ramasse, M. B. Ward, *et al.*, "Factors that determine and limit the resistivity of high-quality individual ZnO nanowires," *Nanotechnology*, vol. 24, 2013.

[2] T. Nakayama, O. Kubo, Y. Shingaya, S. Higuchi, T. Hasegawa, C. S. Jiang, *et al.*, "Development and application of multiple-probe scanning probe microscopes," *Advanced Materials*, vol. 24, pp. 1675-1692, 2012.

[3] D. Erts, B. Polyakov, B. Daly, M. A. Morris, S. Ellingboe, J. Boland, *et al.*, "High density Germanium nanowire assemblies: Contact challenges and electrical characterization," *Journal of Physical Chemistry B*, vol. 110, pp. 820-826, 2006.

[4] B. D. Yuhas and P. Yang, "Nanowire-Based All-Oxide Solar Cells," *Journal of the American Chemical Society*, vol. 131, pp. 3756-3761, 2009.

[5] B. O. Jung, D. C. Kim, B. H. Kong, J. H. Lee, J. Y. Lee, and H. K. Cho, "Direct formation of transparent ITO top electrodes on high-density ZnO nanowires by magnetron sputtering," *Electrochemical and Solid-State Letters*, vol. 14, pp. H446-H449, 2011.

[6] P. Birjukovs, N. Petkov, J. Xu, J. Svirksts, J. J. Boland, J. D. Holmes, *et al.*, "Electrical characterization of bismuth sulfide nanowire arrays by conductive atomic force microscopy," *Journal of Physical Chemistry C*, vol. 112, pp. 19680-19685, 2008.

[7] H. T. Ng, J. Han, T. Yamada, P. Nguyen, Y. P. Chen, and M. Meyyappan, "Single crystal nanowire vertical surround-gate field-effect transistor," *Nano Letters*, vol. 4, pp. 1247-1252, 2004.

[8] V. Schmidt, H. Riel, S. Senz, S. Karg, W. Riess, and U. Gösele, "Realization of a silicon nanowire vertical surround-gate field-effect transistor," *Small*, vol. 2, pp. 85-88, 2006.

[9] P. Woojin, H. Woong-Ki, J. Gunho, W. Gunuk, C. Minhyeok, M. Jongsun, *et al.*, "Tuning of operation mode of ZnO nanowire field effect transistors by solvent-driven surface treatment," *Nanotechnology*, vol. 20, p. 475702, 2009.

[10] P. C. Chang, Z. Fan, C. J. Chien, D. Stichtenoth, C. Ronning, and J. G. Lu, "High-performance ZnO nanowire field effect transistors," *Applied Physics Letters*, vol. 89, 2006.

[11] M. Chen, X. Xia, Z. Wang, Y. Li, J. Li, and C. Gu, "Rectifying behavior of individual SnO2 nanowire by different metal electrode contacts," *Microelectronic Engineering*, vol. 85, pp. 1379-1381, 2008.

[12] Y. W. Heo, L. C. Tien, Y. Kwon, D. P. Norton, S. J. Pearton, B. S. Kang, *et al.*, "Depletion-mode ZnO nanowire field-effect transistor," *Applied Physics Letters*, vol. 85, pp. 2274-2276, 2004.

[13] M. W. Allen, M. M. Alkaisi, and S. M. Durbin, "Metal Schottky diodes on Zn-polar and O-polar bulk ZnO," *Applied Physics Letters*, vol. 89, 2006.

[14] M. W. Allen and S. M. Durbin, "Influence of oxygen vacancies on Schottky contacts to ZnO," *Applied Physics Letters,* vol. 92, 2008.

[15] M. W. Allen, S. M. Durbin, and J. B. Metson, "Silver oxide Schottky contacts on n-type ZnO," *Applied Physics Letters,* vol. 91, 2007.

[16] M. W. Allen, R. J. Mendelsberg, R. J. Reeves, and S. M. Durbin, "Oxidized noble metal Schottky contacts to n -type ZnO," *Applied Physics Letters,* vol. 94, 2009.

[17] S. Elzwawi, H. S. Kim, R. Heinhold, M. Lynam, G. Turner, J. G. Partridge, *et al.*, "Device quality ZnO grown using a Filtered Cathodic Vacuum Arc," *Physica B: Condensed Matter,* vol. 407, pp. 2903-2906, 2012.

[18] S. Elzwawi, H. S. Kim, M. Lynam, E. L. H. Mayes, D. G. McCulloch, M. W. Allen, *et al.*, "Stable n-channel metal-semiconductor field effect transistors on ZnO films deposited using a filtered cathodic vacuum arc," *Applied Physics Letters,* vol. 101, 2012.

[19] C. E. Kendrick, "Revisiting Nitride Semiconductors: Epilayers, p-Type Doping and Nanowires," Doctor of Philosophy PhD, Electrical and Electronic Engineering, University of Canterbury, Christchurch, New Zealand, 2008.

[20] A. M. Lord, A. S. Walton, T. G. Maffeis, M. B. Ward, P. Davies, and S. P. Wilks, "ZnO nanowires with Au contacts characterised in the as-grown real device configuration using a local multi-probe method," *Nanotechnology,* vol. 25, 2014.

[21] A. M. Lord, M. B. Ward, J. E. Evans, P. R. Davies, N. A. Smith, T. G. Maffeis, *et al.*, "Enhanced long-path electrical conduction in ZnO nanowire array devices grown via defect-driven nucleation," *Journal of Physical Chemistry C,* vol. 118, pp. 21177-21184, 2014.

[22] A. M. Lord, M. B. Ward, A. S. Walton, J. Evans, N. Smith, T. G. Maffeis, *et al.*, "Examining the crystal growth that influences the electronic device output from vertical arrays of ZnO nanowires," in *Materials Research Society Symposium Proceedings*, 2014.

[23] A. M. Lord, T. G. Maffeis, M. W. Allen, D. Morgan, P. R. Davies, D. R. Jones, *et al.*, "Surface state modulation through wet chemical treatment as a route to controlling the electrical properties of ZnO nanowire arrays investigated with XPS," *Applied Surface Science,* vol. 320, pp. 664-669, 2014.

[24] A. M. Lord, T. G. Maffeis, O. Kryvchenkova, R. J. Cobley, K. Kalna, D. M. Kepaptsoglou, *et al.*, "Controlling the Electrical Transport Properties of Nanocontacts to Nanowires," *Nano Letters,* vol. 15, pp. 4248-4254, 2015.

[25] E. S. Kumar, I. P. Anderson, Z. Deng, F. Mohammadbeigi, T. Wintschel, D. Huang, *et al.*, "Effect of group-III donors on high-resolution photoluminescence and morphology of ZnO nanowires grown by metalorganic vapour phase epitaxy," *Semiconductor Science and Technology,* vol. 28, 2013.

[26] F. Mohammadbeigi, E. S. Kumar, S. Alagha, I. Anderson, and S. P. Watkins, "Carbon related donor bound exciton transitions in ZnO nanowires," *Journal of Applied Physics,* vol. 116, 2014.

[27] E. Senthil Kumar, F. Mohammadbeigi, S. Alagha, Z. W. Deng, I. P. Anderson, T. Wintschel, *et al.*, "Optical evidence for donor behavior of Sb in ZnO nanowires," *Applied Physics Letters,* vol. 102, 2013.

[28] J. Bao, I. Shalish, Z. Su, R. Gurwitz, F. Capasso, X. Wang, *et al.*, "Photoinduced oxygen release and persistent photoconductivity in ZnO nanowires," *Nanoscale Research Letters,* vol. 6, pp. 1-7, 2011.

[29] Z. M. Liao, K. J. Liu, J. M. Zhang, J. Xu, and D. P. Yu, "Effect of surface states on electron transport in individual ZnO nanowires," *Physics Letters, Section A: General, Atomic and Solid State Physics,* vol. 367, pp. 207-210, 2007.

[30] D. Cammi and C. Ronning, "Persistent photoconductivity in ZnO nanowires in different atmospheres," *Advances in Condensed Matter Physics,* vol. 2014, 2014.

[31] Q. H. Li, T. Gao, Y. G. Wang, and T. H. Wang, "Adsorption and desorption of oxygen probed from ZnO nanowire films by photocurrent measurements," *Applied Physics Letters,* vol. 86, pp. 1-3, 2005.

[32] Y. Li, F. Della Valle, M. Simonnet, I. Yamada, and J. J. Delaunay, "Competitive surface effects of oxygen and water on UV photoresponse of ZnO nanowires," *Applied Physics Letters,* vol. 94, 2009.

[33] B. Liu, Y. Bando, M. Wang, C. Zhi, X. Fang, C. Tang, *et al.*, "Electron-beam irradiation induced conductivity in ZnS nanowires as revealed by in situ transmission electron microscope," *Journal of Applied Physics,* vol. 106, p. 034302, 2009.

[34] Q. Zhang, J. Qi, Y. Huang, H. Li, X. Li, R. Wang, *et al.*, "Utilization of electron beam to modulate electron injection over Schottky barrier," *Current Applied Physics,* vol. 11, pp. 586-589, 2011.

[35] M. Ichimiya, Y. Sawada, M. Ashida, and T. Itoh, "Free exciton luminescence of ZnO:Zn microcrystals under electron beam excitation," in *Physica Status Solidi C: Conferences,* 2006, pp. 1189-1192.

[36] Y. W. Heo, L. C. Tien, D. P. Norton, S. J. Pearton, B. S. Kang, F. Ren, *et al.*, "Pt/ZnO nanowire Schottky diodes," *Applied Physics Letters,* vol. 85, pp. 3107-3109, 2004.

[37] C. S. Lao, J. Liu, P. Gao, L. Zhang, D. Davidovic, R. Tummala, *et al.*, "ZnO nanobelt/nanowire schottky diodes formed by dielectrophoresis alignment across au electrodes," *Nano Letters,* vol. 6, pp. 263-266, 2006.

[38] Ü. Özgür, Y. I. Alivov, C. Liu, A. Teke, M. A. Reshchikov, S. Doğan, *et al.*, "A comprehensive review of ZnO materials and devices," *Journal of Applied Physics,* vol. 98, pp. 1-103, 2005.

Chapter 6: Optical and Diffraction Analysis of ZnO Nanowire Arrays

6.1 Motivation

Various optical techniques exist for the characterisation of semiconductor films. By studying the diffraction, re-emission and scattering of incident radiation, useful data can be inferred about the composition of the material and how it will perform electrically. A major advantage of optical techniques is that they are generally non-destructive. The sample does not need to be modified in any way in order to be measured and the tests themselves do cause permanent changes to the crystal lattice.

In this chapter, nanowires grown in the previous chapters are characterised using Photoluminescence (PL), X-Ray Diffraction (XRD), and Tunnelling Electron Microscopy (TEM).

6.2 Photoluminescence of ZnO Nanowire Arrays

6.2.1 ZnO Photoluminescence in the literature

Photoluminescence (PL) is a very powerful tool for gathering data on the quality and composition of a semiconductor film and the principles of its operation are described in Chapter 2, Section 9. The spectra of bulk ZnO [1-3] thin films [4-6] and nanowires [7-11] have been extensively reported since the 1960s [12]. However, disagreement exists concerning the exact origin of various peaks and features [3], and new research is constantly being published proposing new explanations [1, 13]. There are two main regions of interest in the PL spectra of ZnO: The excitonic region (approximately 3.26-3.40 eV) and the defect band (approximately 1.8-3.0 eV).

The excitonic region is characterised by a range of sharp, narrow peaks, with each peak corresponding to a different excitonic transition. These transitions can be band to band, the recombination of free excitons, the recombination of excitons bound to either donors or acceptors, the recombination of free excitons or the recombination of donor-acceptor pairs. The recombinations involving donor or acceptor bound excitons are particularly useful, especially where the dopant responsible for producing a certain peak is known, as that peak can then be used as evidence that the dopant is present in the crystal. Comparing the magnitudes of different donor/acceptor bound peaks can also be used to estimate the relative concentration of each dopant. Figure 1 shows an extremely high quality ZnO spectra produced by R. Heinhold [1] with significant peaks labelled and named.

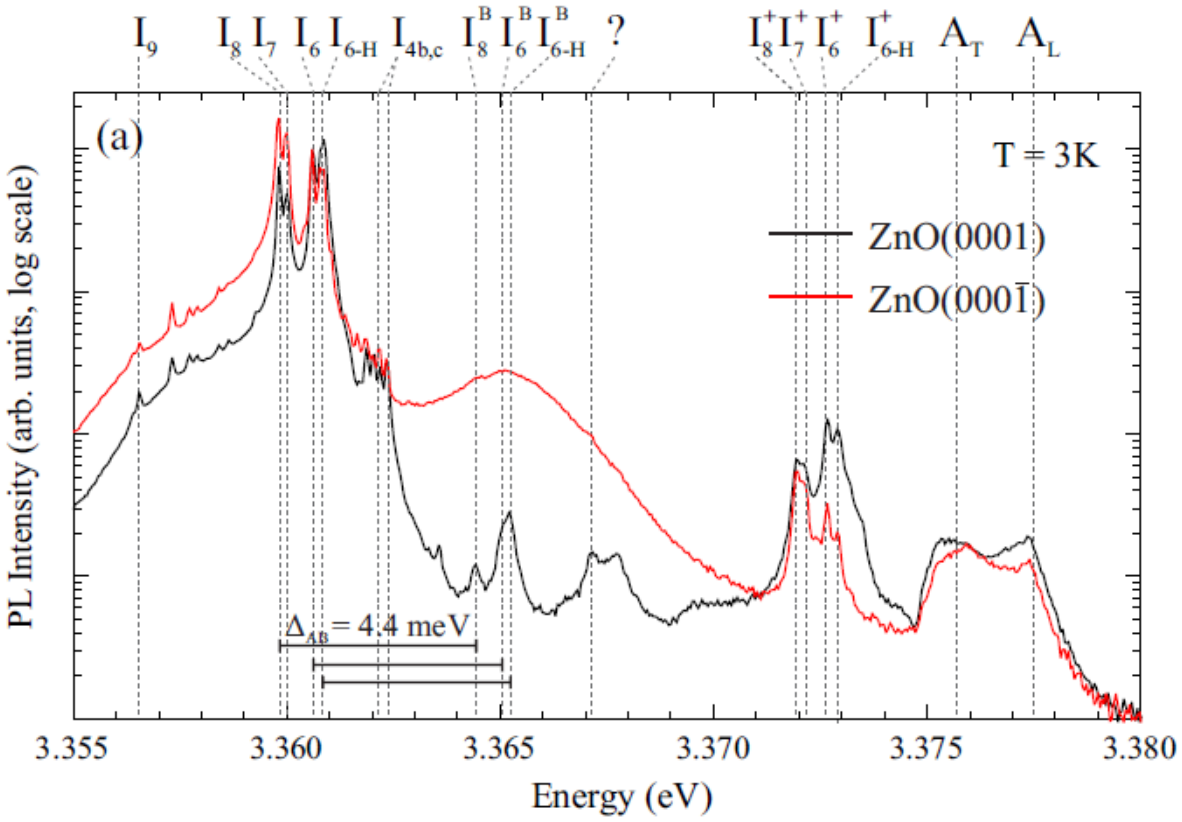

Figure 1: Exceptionally high quality PL spectra showing the positions of notable peaks in bulk ZnO which has been annealed in oxygen. The Zn-polar face (black) has a different spectra to the O-polar face (red), most interestingly a large surface feature in the 3.374 – 3.362 eV region. Data reproduced from the thesis of R. Heinhold [1].

Table 1 Significant excitonic peaks in ZnO

Peak	λ (nm)	Energy (eV)	Identity
I_9	369.37	3.3567	Indium [3]
I_8	369.03	3.3598	Ga [3]
I_7	369.01	3.3600	Unknown [1,3]
I_6	368.92	3.3608	Aluminium [3]
$I_{6\text{-}H}$	368.96	3.3604	Al-Li-H complex [1]
I_4	368.34	3.3628	Hydrogen [1, 3]

Important peaks in the excitonic region are shown in Table 1, following the widely used naming convention introduced by Reynolds *et al.* [14] in 1965. Many of these peaks have replicas in the B-valence band exciton region, denoted I_8^B and I_6^B etc. These are much less prominent than the primary excitonic peaks (which are related to the A-valence band) and are generally only detected with very high quality ZnO crystals. Excitons will readily bind to ionised donors as well as to neutral ones. This causes an additional

set of replica peaks denoted I_8^+, I_6^+ etc. between 3.372 and 3.375 eV. Between the energies of approximately 3.363 and 3.37 eV on ZnO exists a large, wide bulge, especially prominent on the O-polar face. This can be reduced with annealing and while its exact cause is unknown, it has been shown that it is related to surface effects in the crystal [1]. At higher energies than the ionised donor bound excitons, exists the free exciton band denoted by A_T and A_L for transverse and longitudinal excitons respectively.

The defect band is a wide region in the lower energy spectrum extending into the visible wavelengths. Emission from this band in ZnO is related to structural defects and deep impurity states in the bandgap. It forms a very broad peak as it contains contributions from many different types of defect configuration at different energies. ZnO is known to luminesce strongly in the green [4, 15] and yellow [16] regions due to both intrinsic defect states such as oxygen vacancies and zinc interstitials respectively and also extrinsic states introduced by deep donor and acceptor impurities such as copper. Contention exists in the literature over the exact composition of the defects responsible [17].

When comparing photoluminescence between studies, an important consideration is the resolution of the respective scans. The University of Canterbury PL system has a very high resolution of 0.001 nm (although 0.01 nm is more commonly used) and is capable of resolving many more peaks than are often reported in the literature [1]. With this high resolution, features once thought to be single peaks can be seen to split into two or more peaks located very close to one another. This effect is especially pronounced in material of high crystal quality as sharp peaks are a characteristic of good crystallinity.

6.2.2 Photoluminescence of ZnO nanowires

Nanowire arrays are of significant interest to the science of photoluminescence because of their extreme dimensions and generally very high crystal quality. The photoluminescence of ZnO nanowires has been found to vary with the morphology of the wires. Green luminescence from the defect band has been shown to increase with decreasing nanowire diameter [7, 8]. Djurišić *et al.* [18] stressed that while emission at orange, yellow and green wavelengths could all be observed from different types of ZnO nanostructures under

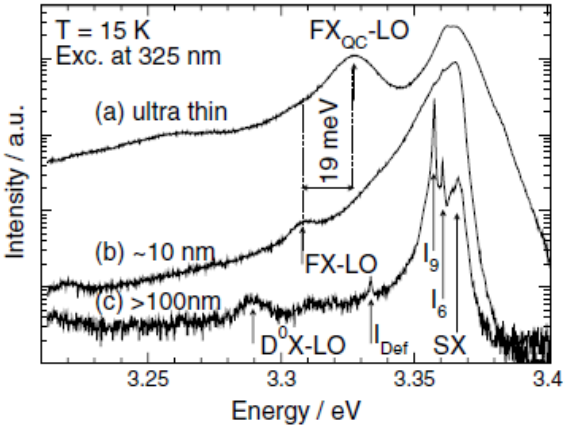

Figure 2 Stichtenoth *et al*. [20] proposed that this shift of the phonon replica of the free exciton band in 4 nm diameter nanowires is indicative of

different excitation (and that therefore the defect emission itself was not caused by morphology), each nanostructure had a dominant defect emission for a given excitation wavelength. Quantum confinement is not often seen in the PL of ZnO, a fact attributed to the small exciton Bohr radius in ZnO of approximately 2 nm [19]. However, Stichtenoth *et al.* [20] observed a shift in the phonon replica of the free exciton emission in nanowires approximately 4 nm in diameter that they suggested was due to exciton confinement. Figure 2 shows this peak shift compared to their nanowires of larger diameter.

6.2.3 Excitonic Region of EPLD Nanowires

Several of the best nanowire arrays grown by EPLD in the previous chapters were characterised by low temperature (3 K) photoluminescence, focusing on the exciton recombination region and the defect band region, with the results compared to the PL from bulk ZnO crystals and nanowires supplied by our collaborators from Swansea University and Simon Fraser University. Figure 3 shows a comparison of the excitonic region of several of the best EPLD grown ZnO nanowire arrays grown in Chapter 4. Table 2 lists the nanowires shown in Figure 3.

Table 2: EPLD nanowires characterised PL in Figure 3.

Sample	Trace
EPLD 20 nm commercial Au colloids	Violet
EPLD 10 nm commercial Au colloids	Red
EPLD 5 nm commercial Au colloids	Dark Green
EPLD Au101 clusters	Lime Green
EPLD Au9 clusters	Cyan

The UV photoluminescence of the nanowire samples from the exciton recombination region was extremely strong, allowing a small photodetector slit size to be used. The dominant excitonic peak in all the samples grown by EPLD is I_9, which is attributed by Meyer [3] to indium and the energy axis is referenced to this peak. Indium is not an unexpected primary dopant, as during the PLD growth, an indium-tin eutectic is used to attach the sapphire substrates to the PLD heater. Although care was taken to prevent the melted indium metal from coming in contact with the surface of the sapphire substrates, indium has been found to become extremely mobile above 520 °C on ZnO and able to migrate from the underside of an indium-adhered bulk single crystal substrate onto the surface [21].

A broad surface feature (Sx) was observed on all the nanowire samples at a localisation energy of approximately 10-12 meV (~3.366 eV). This feature is often seen in the PL of ZnO nanowires and has been shown to be caused by excitons binding to surface states [20, 22, 23]. The position and magnitude of this peak remained fairly constant across all of the EPLD nanowires, indicating that the differences in nanowire size was not causing a significant change in the density of these surface states. Although the tip sizes of the

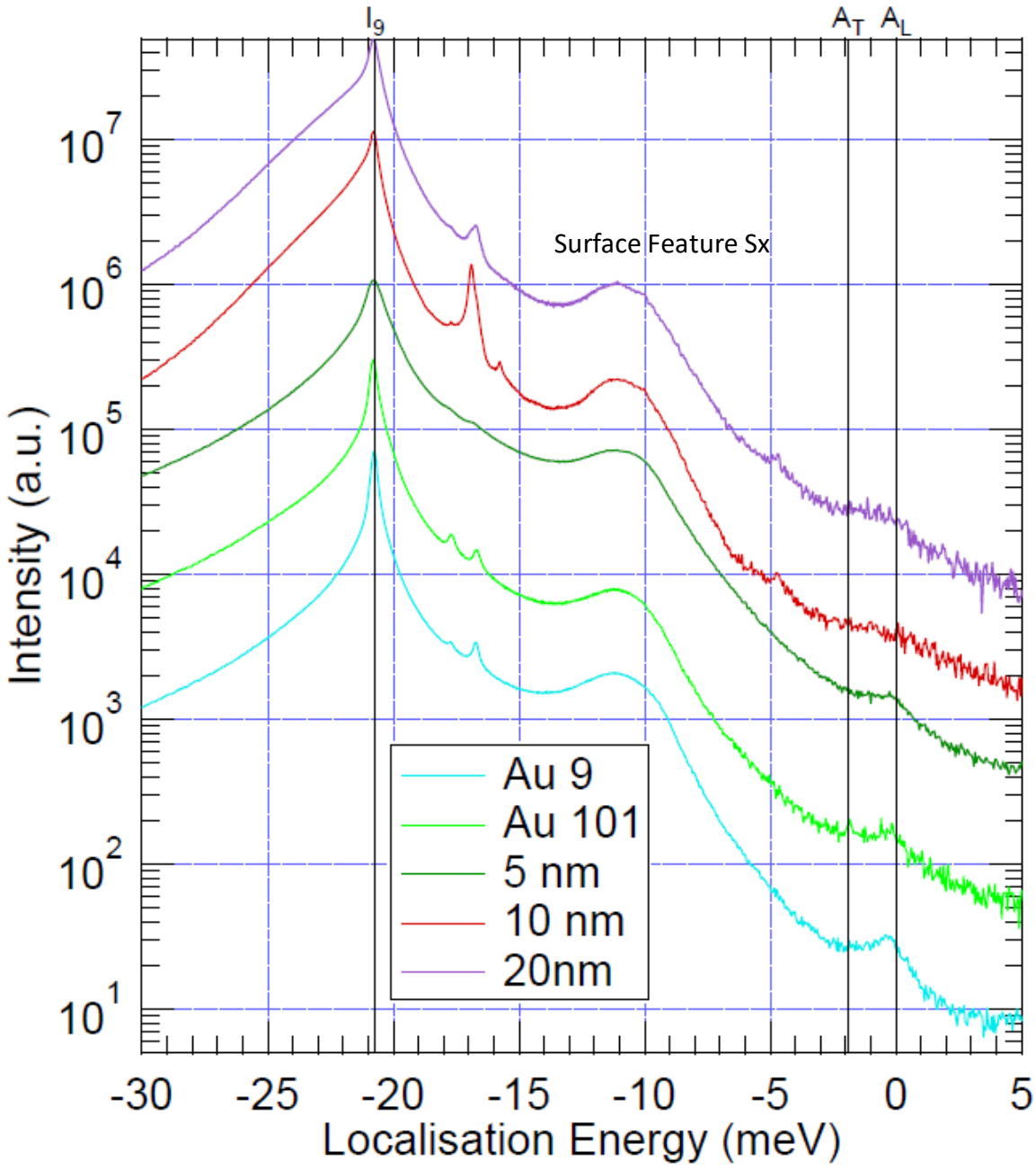

Figure 3: PL of the excitonic region of EPLD nanowires showing a dominant I_9 peak and a strong surface feature.

nanowires decreased proportionally to the size of the catalyst gold nanoparticles, the tapered morphology of the EPLD nanowires probably renders differences in overall surface area fairly small.

The free excitonic peaks, A_T and A_L were visible only as a broad feature the nanowires grown from larger, 10 and 20 nm colloids. As the nanowire tip sizes decreased, A_L began to become more distinct, but A_T remained obscured in the tail of the surface feature. PL measurements on the Zn-polar (0001) face of bulk crystal ZnO often show a more prominent A_L peak compared to the A_T peak but the two are usually of similar magnitude on the O-polar ($000\bar{1}$) face [1]. As nanowires typically grow in the <002> direction (which is shown to be the case for these EPLD nanowires using XRD in Section 3 of this chapter), it is not surprising that the free exciton region more closely resembles the (0001) face of bulk ZnO than the ($000\bar{1}$) face.

6.2.4 Excitonic Region of Collaborators' Nanowires

Low temperature PL was also conducted on the nanowires received from Swansea University and Simon Fraser University and discussed in Chapter 5, in order to compare with the PL from the EPLD nanowires. As these nanowires were grown using different growth conditions, including deliberate doping in the case of some of the Simon Fraser nanowires, the effects of these changes on the PL spectra were of interest. The excitonic region was plotted against PL from a set of EPLD nanowires catalysed using standard 13 nm Au

Table 3: Nanowires supplied by collaborators as displayed in Figure 4.

Sample	Trace
Mitsubishi O-polar ZnO Bulk Crystal (control)	Grey
UC EPLD 13 nm colloid	Red
Swansea University Catalytic	Blue
SFU MOCVD H836 50 sccm Ga-Doped (short)	Cyan
SFU MOCVD H839 100 sccm Ga-Doped	Black
SFU MOCVD H603 Undoped on GaN Substrate	Lime Green
SFU MOCVD H825 Undoped on Sapphire (long)	Dark Green
SFU MOCVD H845 Undoped on Sapphire (short)	Purple
SFU MOCVD H853 50 sccm Ga-Doped (long)	Orange

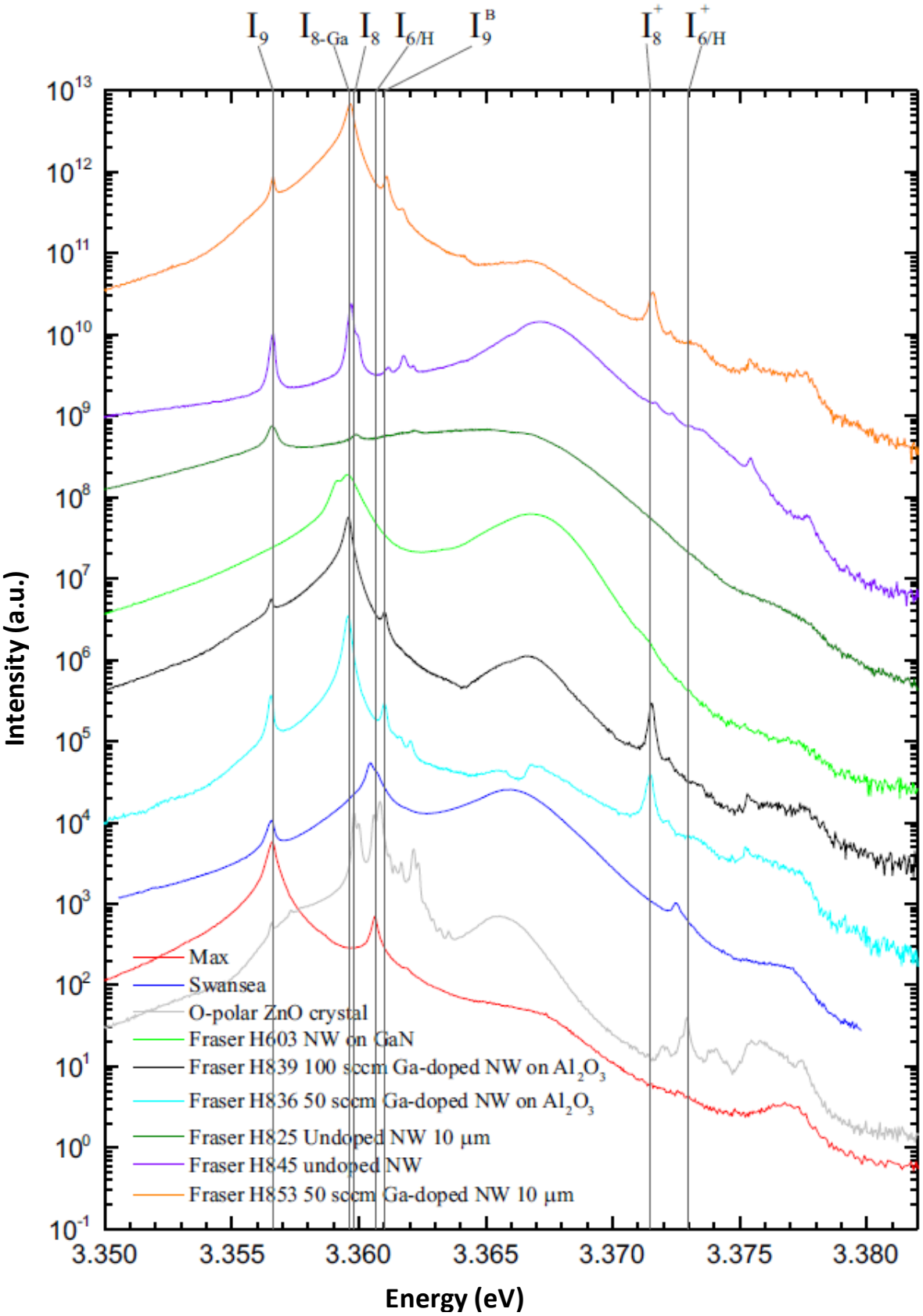

Figure 4: Excitonic region PL of nanowires supplied by collaborators.

colloids (From Growth #61, Appendix 1) and an O-polar bulk crystal supplied by Mitsubishi Chemical Corporation, Tokyo, Japan. Table 3 lists the nanowires shown.

I_8 (gallium) was the dominant peak in all the nanowires from Simon Fraser University. This is due to the fact that many of the nanowires supplied were intentionally gallium doped or grown on GaN substrates. The gallium doped nanowires have such a strong I_8 peak that the ionised I_8^+ replica is also visible. Even their undoped nanowires were grown in a system where residual gallium was likely to be present and as a result, the undoped nanowires show a reduced but still resolvable I_8 emission. These nanowires had a wide variety of morphologies (see Figure 18 in Chapter 5) and as such, the broad surface feature at 3.366 - 3.368 eV also varies in shape and intensity. Neither gallium doping nor nanowire length appeared to reliably predict the size or shape of the surface feature. This combined with the fact that the surface feature was similar in size and shape across all the EPLD nanowires characterised in Figure 3, which had similar morphologies but different sizes, it is reasonable to assume that the shape of the nanowires has a greater influence on the size and shape of this PL surface feature than the size or dopant concentration of the nanowires.

Swansea University's catalytic nanowires had a different dominant peak to either the EPLD nanowires or the SFU nanowires. Located close to 3.360 eV, this was assigned as I_6, which is due to aluminium impurities. These nanowires are not intentionally doped and do not have the large concentration of indium present in the EPLD nanowires, so it is possible that the aluminium was either introduced from the precursor material or that it diffused into the nanowires from the sapphire substrate. Although this leaching might also be expected in other nanowires grown on sapphire substrates, it is possible that the dominance of I_9 and I_8 in the EPLD and SFU nanowires respectively simply obscures the emission of I_6.

6.2.5 Defect Band

The defect band is associated with visible luminescence in ZnO films and nanowires, so it was surprising to find that the EPLD grown nanowires luminesced almost entirely in the UV region with no detectable green, yellow or orange emission. Figure 5 compares the defect band emission of the 10 nm colloid catalysed EPLD nanowires and a high quality Tokyo Denpa hydrothermal ZnO bulk crystal. The defect band emission in the EPLD nanowires is almost completely non-existent, at least 5 orders of magnitude lower in intensity than the emission from the excitonic region, compared to approximately 3.5 orders for the bulk crystal. The complete lack of defect emission band indicates excellent crystallinity with very few intrinsic defect states or states due to deep donors or acceptors. This is unusual for nanowires in the literature [7, 8]. It is especially surprising since PL from the excitonic region of the EPLD nanowires indicates a high

concentration of incorporated indium which could be expected to create strain or defects in the lattice, thereby distorting the crystal structure.

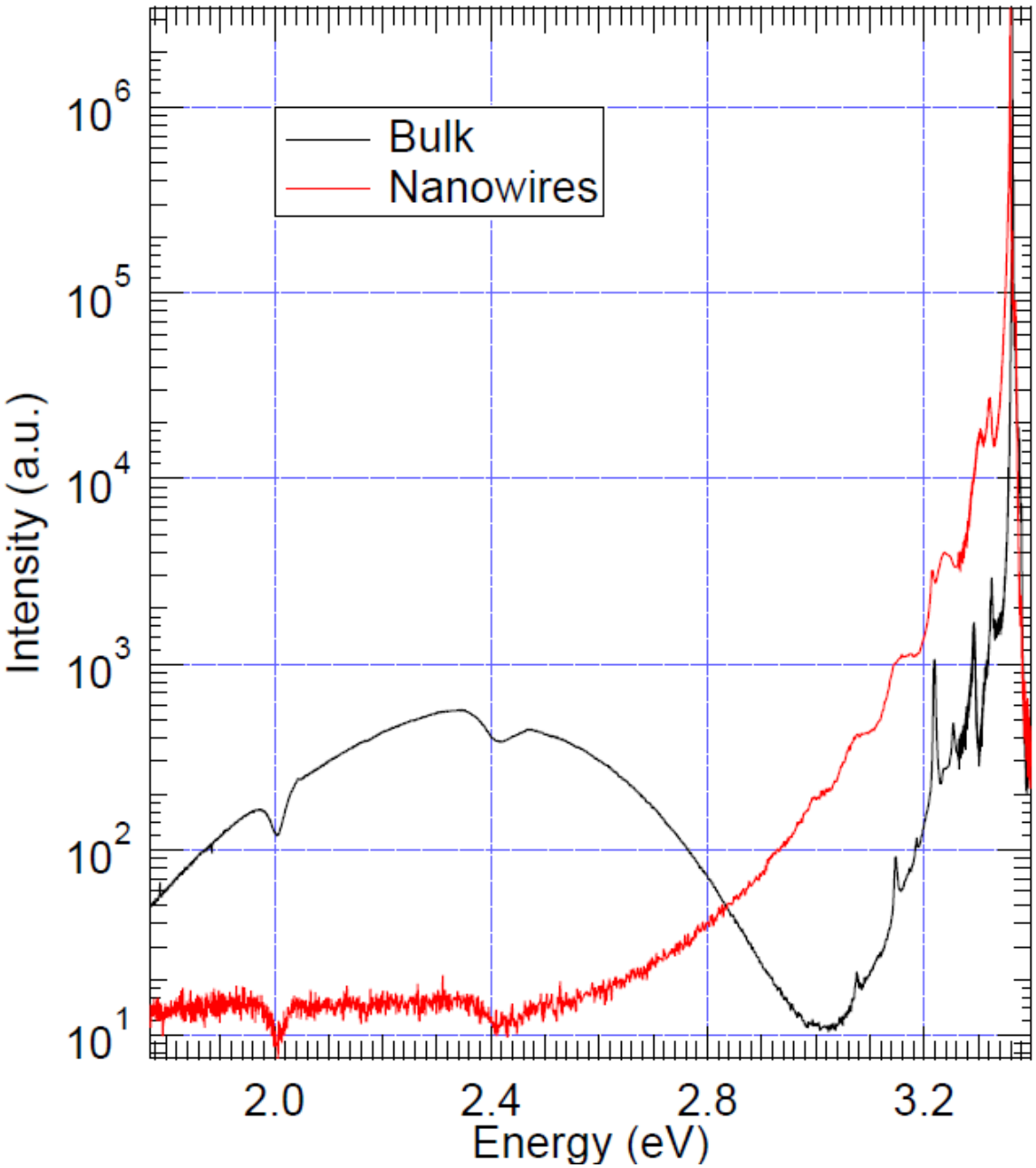

Figure 5: Defect band comparison between EPLD nanowires and bulk crystal ZnO. The magnitudes are normalized to the dominant excitonic peak so it can be seen that the visible region luminescence is almost two orders of magnitude lower in the nanowires.

It must also be noted that while the defect band is much lower than the bulk crystal in Figure 5, the nanowires show greater luminescence in the region between 2.8 and 3.2 eV. This region is known as the phnonic region and contains emission from excitons that bind to lattice vibrations known as phonons.

Phonon-bound excitons replicate peaks in the excitonic region, although the entire range is significantly higher in the nanowires, rather than just peaks. Phonons travel like waves through the crystal, so it is possible that some manner of phonon confinement is occurring due to the small size of the nanowires. Additionally, the tapered morphology of the nanowires means that this confinement could be different depending on how far along the nanowire a laterally moving phonon was, leading to a broad signal, rather than a sharp peak that might be expected if every phonon was subject to the same constraints. Phonon confinement has been documented in nanowires and is typically detected by a change in resistivity [24].

6.2.6 Blueshift in Ultrafine EPLD nanowires

When comparing the excitonic regions of the EPLD nanowires, the spectra were aligned for ease of comparison, with the position of the dominant I_9 indium emission at 3.3565 eV being the reference peak. However, the absolute positions of the I_9 peaks (established using Hg calibration lamps) were blueshifted as shown in Figure 6. Interestingly, the magnitude of this blueshift increases inversely with the tip sizes of

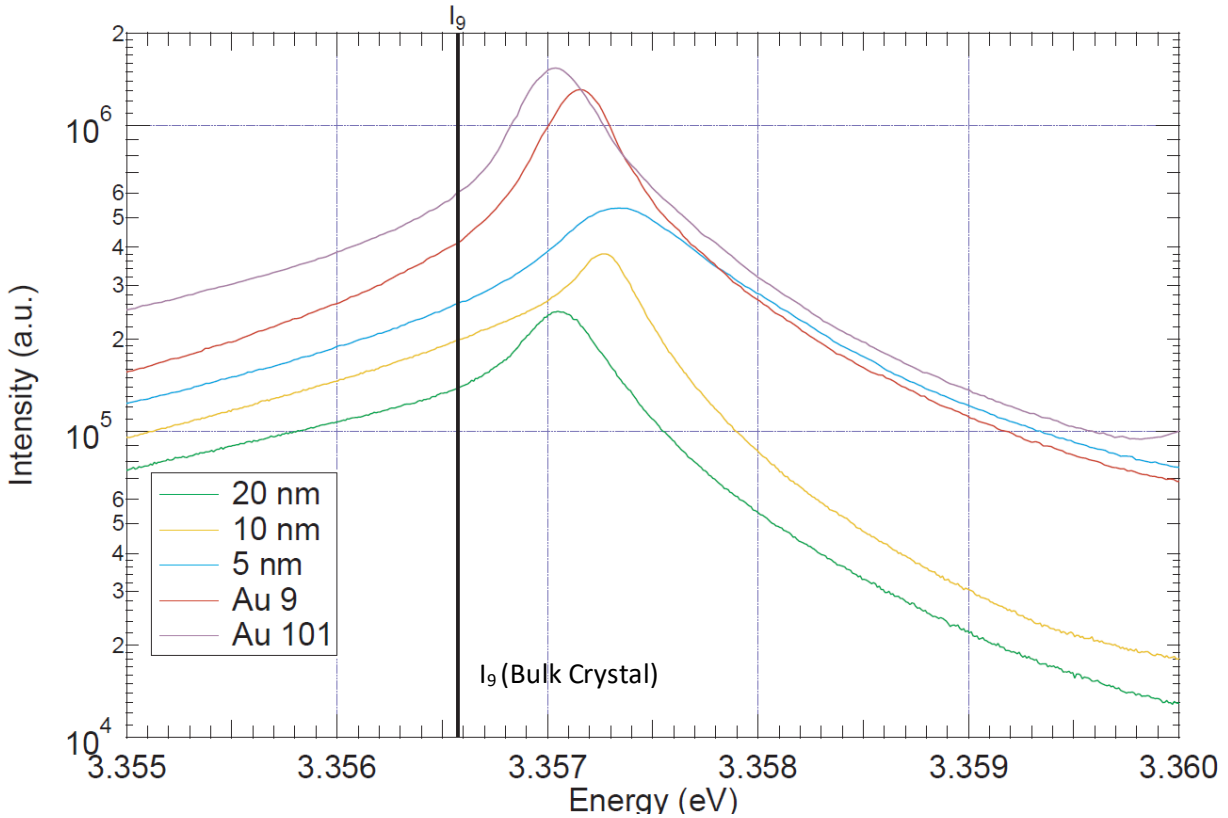

Figure 6 A blueshift was observed in the absolute position of the I_9 peak, increasing inversely to the tip diameter of the nanowires.

the nanowires in both the Au colloid and atomic cluster catalysed series, potentially suggesting that some form of quantum confinement effect is occurring. Senger *et al.* [19] showed that exciton binding energy increases with decreasing diameter of quantum dots, which is consistent with the results shown here.

Surprisingly, the nanowires with the smallest tip diameters (Au101 and Au9 catalysed nanowires) showed a smaller blueshift than the colloid-catalysed nanowires with larger tip diameters. However, the smaller tipped Au9 catalysed nanowires did show a larger blueshift than the Au101 catalysed nanowires.

6.3 X-Ray Diffraction of EPLD ZnO Nanowires

X-Ray Diffraction (XRD) is a diffraction technique used to analyse the crystal planes present in a sample, described in Chapter 2, Section 2. It is typically used for bulk crystals and thin films as it uses a beam of x-rays diffracted off the flat surface of the material to determine which crystal planes are present on the surface and how well ordered the crystal domains are [25]. XRD is usually performed on nanorods to assess the preferential crystal growth direction and crystallinity of the rods [26].

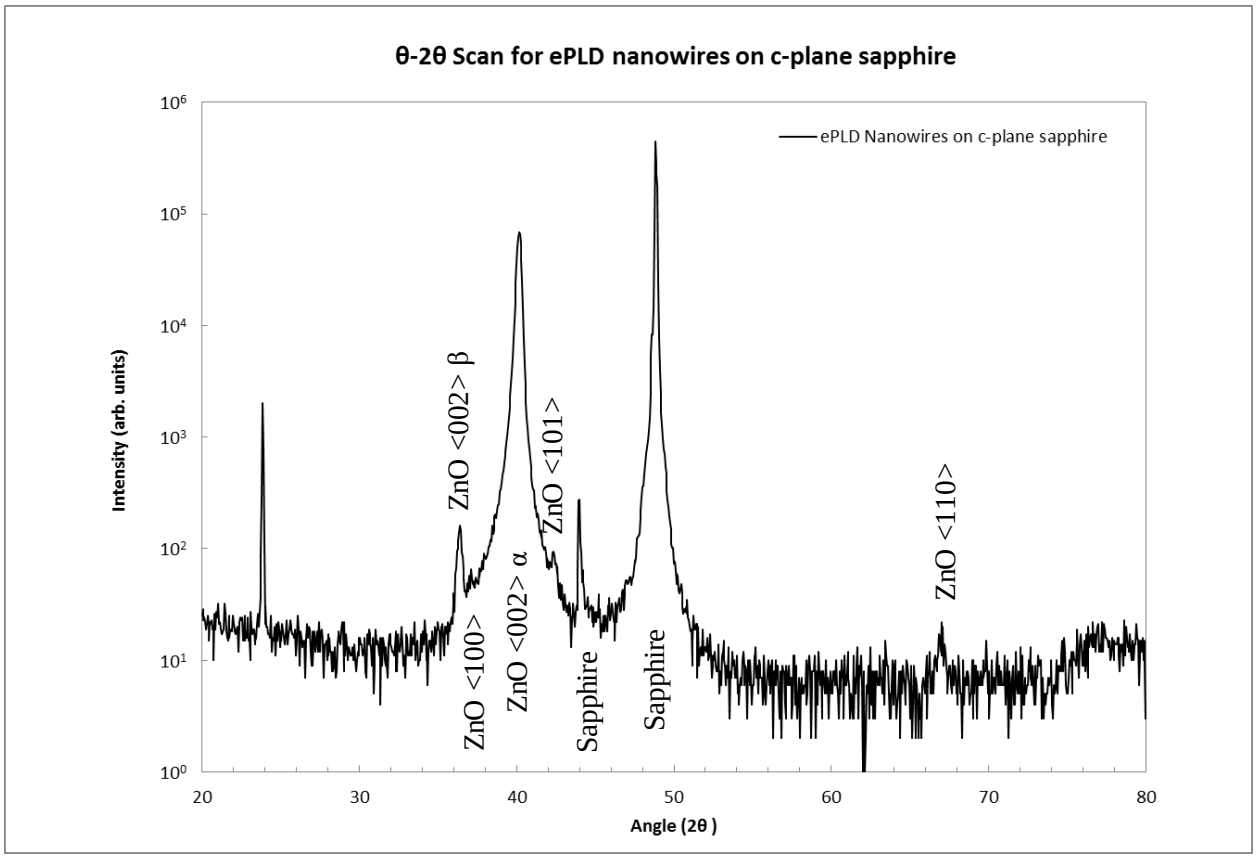

Figure 7: XRD θ-2θ curve of EPLD grown ZnO nanowires showing peaks at 36.4°, 37.1°, 40.2°, 42.4° and 67.0°.

One of the most highly ordered nanowire arrays grown using the 13 nm chemically synthesised colloids after optimisation of the growth method in Chapter 3 (Growth no. 57, Appendix 1) was sent to Callaghan Innovation in Lower Hutt for XRD measurements. Figure 7 shows the θ-2θ curve of this sample. Peaks can be seen at 2θ = 40.2° and 36.4°, which represent the alpha and beta peaks of the ZnO <002> axis. Peaks representing ZnO <100>, <101> and <110> are visible at 2θ = 37.1°, 42.4° and 67.0° respectively, but these are much smaller in magnitude than the <002>, indicating that the <002> direction or c-axis is the overwhelmingly dominant growth direction of the ZnO nanorods in the array. This is the expected result

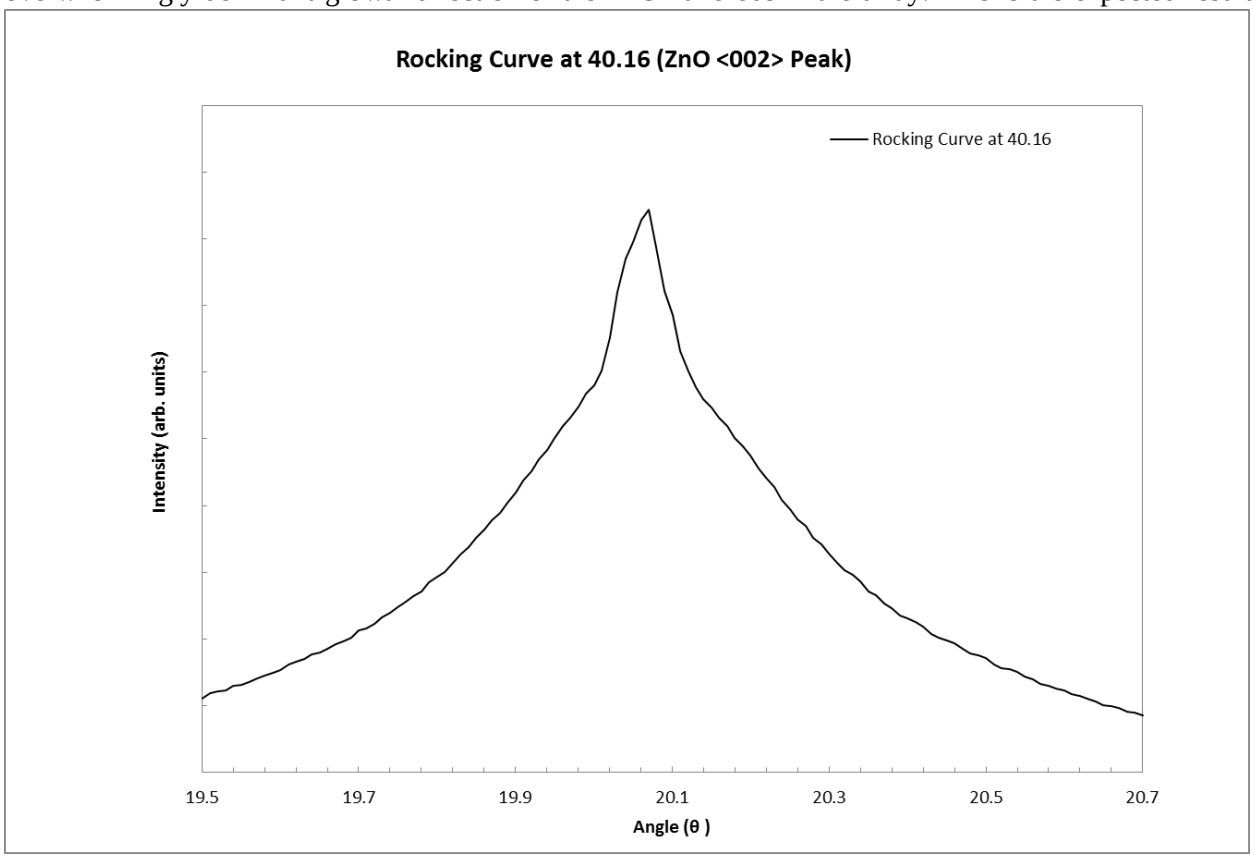

Figure 8: XRD rocking curve taken about the 2θ = 40.16° ZnO <002> plane peak. The peak is relatively broad with a FWHM of 0.33° and appears to be comprised of a narrow peak superimposed upon a broader peak.

for epitaxially grown ZnO nanorods as it is well known that this is the preferential ZnO growth direction as explained in Chapter 1, Section 6. The presence of the other planes in the θ-2θ curve does not necessarily mean that nanorods grew in these directions. There was still a degree of disorder in these nanorods, with some nanorods growing off-angle from the normal and so it is very likely that some of these disordered rods would present other crystal planes as the x-rays diffract off their sidewalls. Additional peaks visible at 2θ = 23.9°, 44.0° and 48.8° in Figure 6 correspond to the c-plane sapphire substrate.

A rocking curve taken about the $2\theta = 40.16°$ ZnO <002> peak was mostly symmetrical, with a FWHM of 0.33. This is broader than often reported in the literature for ZnO [25], even for nanowire arrays [26], but this is likely due to the imperfect alignment of the EPLD nanowires or from their tapered morphology. The rocking curve appears to be a summation of two contributing curves, a sharp peak on top of a broad, Gaussian background. These are likely due to contributions from strongly c-axis oriented vertical nanowires and off-angled nanowires, respectively. It is also possible that this underlying Gaussian shape indicates a base layer of ZnO film between the nanowires. Such a layer would likely be strained due to mismatch with the sapphire substrate lattice and distortion around the bases of the nanowires, causing a broad peak on the rocking curve.

6.4 Summary

This chapter detailed optical measurements carried out on ZnO nanowires grown by EPLD as well as ZnO nanowires supplied by collaborators. Photoluminescence and x-ray diffraction were used to investigate the composition and crystallinity of the nanowires.

- Photoluminescence (PL) spectra in the excitonic recombination region were measured at 3 K from nanowires grown via EPLD using different sized Au catalyst particles and with correspondingly different sized nanowire tip diameters. Nanowires catalysed by 20 nm, 10 nm and 5 nm diameter commercially produced Au colloids as well as by atomically precise clusters of Au101 and Au9 were measured.
- Indium (I_9) was the dominant impurity in the EPLD nanowires. Indium incorporation is thought to originate from the liquid indium-tin eutectic used to adhere the sapphire substrates to the PLD heater. Indium mobility is enhanced at high temperatures and it can possibly migrate from the underside of the substrate and thinly coat the ZnO surface during growth.
- The longitudinal free exciton (A_L) was observed clearly in the ZnO nanowires with the smallest tip diameters (5 nm, Au101 and Au9) but the transverse free electron was not seen. Decreasing nanowire tip diameter made the longitudinal free exciton appear more prominently.
- Nanowires grown by MOCVD provided by collaborators at Simon Fraser University (SFU) and by a vapour-phase method at Swansea University were also examined using 3 K PL. The SFU nanowires in particular included different doping levels and morphologies.
- I_8 (gallium) was the dominant peak in the PL spectra of the SFU nanowires as many of them had been intentionally doped with gallium. Even nanowires which were nominally undoped contained gallium as the dominant impurity, probably due to residual gallium in the growth system.

- I_6 (aluminium) was the dominant peak in the PL spectra of the Swansea nanowires. As these were undoped, it is possible that the impurity was present in the growth system, precursor material or that it had come from the sapphire substrates.
- The surface feature between 3.366 - 3.368 eV was very similar on all of the EPLD nanowires, but varied significantly in both magnitude and shape between the SFU nanowires. Nanowire length or dopant concentration did not seem to directly influence the surface feature, indicating the surface feature is likely related to the shape of the nanowires rather than the size.
- Nanowires grown by EPLD had no detectable defect band and associated visible-wavelength luminescence, with at least five orders of magnitude difference in intensity between the dominant peak in the excitonic region and the defect band, indicating very high crystal quality.
- XRD θ-2θ scans were conducted on ZnO nanowires grown using 13 nm chemically synthesised, APTMS-tethered colloids as catalysts. XRD peak locations showed <002> to be the dominant growth direction for the ZnO nanowires, in line with expectations.
- A rocking curve of the ZnO <002> peak gave a full-width half-maximum value of 0.33° which is higher than expected. This would likely indicate poor crystallinity in a film or bulk crystal, but is probably caused by off-angled nanowires in the EPLD sample.

6.5 References

[1] R. Heinhold, "Hydrogen-related effects in the optical and surface electronic properties of ZnO," Doctor of Philosophy PhD, Department of Electrical and Computer Engineering, University of Canterbury, 2014.

[2] R. Mendelsberg, "Photoluminescence of ZnO Grown by Eclipse Pulsed Laser Deposition," Doctor of Philosophy PhD, Department of Physics, University of Canterbury, 2009.

[3] B. K. Meyer, H. Alves, D. M. Hofmann, W. Kriegseis, D. Forster, F. Bertram, *et al.*, "Bound exciton and donor-acceptor pair recombinations in ZnO," *Physica Status Solidi (B) Basic Research,* vol. 241, pp. 231-260, 2004.

[4] B. Lin, Z. Fu, and Y. Jia, "Green luminescent center in undoped zinc oxide films deposited on silicon substrates," *Applied Physics Letters,* vol. 79, pp. 943-945, 2001.

[5] X. L. Wu, G. G. Siu, C. L. Fu, and H. C. Ong, "Photouminescence and cathodoluminescence studies of stoichiometric and oxygen-deficient ZnO films," *Applied Physics Letters,* vol. 78, pp. 2285-2287, 2001.

[6] X. W. Sun and H. S. Kwok, "Optical properties of epitaxially grown zinc oxide films on sapphire by pulsed laser deposition," *Journal of Applied Physics,* vol. 86, pp. 408-411, 1999.

[7] M. H. Huang, Y. Wu, H. Feick, N. Tran, E. Weber, and P. Yang, "Catalytic growth of zinc oxide nanowires by vapor transport," *Advanced Materials,* vol. 13, pp. 113-116, 2001.

[8] P. Yang, H. Yan, S. Mao, R. Russo, J. Johnson, R. Saykally, *et al.*, "Controlled growth of ZnO nanowires and their optical properties," *Advanced Functional Materials*, vol. 12, pp. 323-331, // 2002.

[9] H. T. Ng, B. Chen, J. Li, J. Han, M. Meyyappan, J. Wu, *et al.*, "Optical properties of single-crystalline ZnO nanowires on m-sapphire," *Applied Physics Letters*, vol. 82, pp. 2023-2025, 2003.

[10] J. Wang and L. Gao, "Hydrothermal synthesis and photoluminescence properties of zno nanowires," *Solid State Communications*, vol. 132, pp. 269-271, 2004.

[11] Y. W. Wang, L. D. Zhang, G. Z. Wang, X. S. Peng, Z. Q. Chu, and C. H. Liang, "Catalytic growth of semiconducting zinc oxide nanowires and their photoluminescence properties," *Journal of Crystal Growth*, vol. 234, pp. 171-175, 2002.

[12] R. Dingle, "Luminescent transitions associated with divalent copper impurities and the green emission from semiconducting zinc oxide," *Physical Review Letters*, vol. 23, pp. 579-581, 1969.

[13] K. Vanheusden, W. L. Warren, C. H. Seager, D. R. Tallant, J. A. Voigt, and B. E. Gnade, "Mechanisms behind green photoluminescence in ZnO phosphor powders," *Journal of Applied Physics*, vol. 79, pp. 7983-7990, 1996.

[14] D. C. Reynolds, C. W. Litton, and T. C. Collins, "Zeeman effects in the edge emission and absorption of ZnO," *Physical Review*, vol. 140, 1965.

[15] Y. W. Heo, D. P. Norton, and S. J. Pearton, "Origin of green luminescence in ZnO thin film grown by molecular-beam epitaxy," *Journal of Applied Physics*, vol. 98, 2005.

[16] M. A. Reshchikov, J. Q. Xie, B. Hertog, and A. Osinsky, "Yellow luminescence in ZnO layers grown on sapphire," *Journal of Applied Physics*, vol. 103, 2008.

[17] Ü. Özgür, Y. I. Alivov, C. Liu, A. Teke, M. A. Reshchikov, S. Doğan, *et al.*, "A comprehensive review of ZnO materials and devices," *Journal of Applied Physics*, vol. 98, pp. 1-103, 2005.

[18] A. B. Djurišić, Y. H. Leung, K. H. Tam, L. Ding, W. K. Ge, H. Y. Chen, *et al.*, "Green, yellow, and orange defect emission from ZnO nanostructures: Influence of excitation wavelength," *Applied Physics Letters*, vol. 88, 2006.

[19] R. T. Senger and K. K. Bajaj, "Optical properties of confined polaronic excitons in spherical ionic quantum dots," *Physical Review B - Condensed Matter and Materials Physics*, vol. 68, pp. 453131-453138, 2003.

[20] D. Stichtenoth, C. Ronning, T. Niermann, L. Wischmeier, T. Voss, C. J. Chien, *et al.*, "Optical size effects in ultrathin ZnO nanowires," *Nanotechnology*, vol. 18, 2007.

[21] R. Heinhold, R. J. Reeves, G. T. Williams, D. A. Evans, and M. W. Allen, "Mobility of indium on the ZnO(0001) surface," *Applied Physics Letters*, vol. 106, 2015.

[22] J. Grabowska, A. Meaney, K. K. Nanda, J. P. Mosnier, M. O. Henry, J. R. Duclère, *et al.*, "Surface excitonic emission and quenching effects in ZnO nanowire/nanowall systems: Limiting effects on device potential," *Physical Review B - Condensed Matter and Materials Physics*, vol. 71, 2005.

[23] L. Wischmeier, T. Voss, I. Rückmann, J. Gutowski, A. C. Mofor, A. Bakin, *et al.*, "Dynamics of surface-excitonic emission in ZnO nanowires," *Physical Review B - Condensed Matter and Materials Physics*, vol. 74, 2006.

[24] I. C. Robin, P. Marotel, A. H. Ei-Shaer, V. Petukhov, A. Bakin, A. Waag, *et al.*, "Compared optical properties of ZnO heteroepitaxial, homoepitaxial 2D layers and nanowires," *Journal of Crystal Growth*, vol. 311, pp. 2172-2175, Mar 2009.

[25] Y. Chen, D. M. Bagnall, H. J. Koh, K. T. Park, K. Hiraga, Z. Zhu, *et al.*, "Plasma assisted molecular beam epitaxy of ZnO on c-plane sapphire: Growth and characterization," *Journal of Applied Physics*, vol. 84, pp. 3912-3918, 1998.

[26] Y. K. Tseng, C. J. Huang, H. M. Cheng, I. N. Lin, K. S. Liu, and I. C. Chen, "Characterization and Field-Emission Properties of Needle-like Zinc Oxide Nanowires Grown Vertically on Conductive Zinc Oxide Films," *Advanced Functional Materials*, vol. 13, pp. 811-814, 2003.

Chapter 7: Growth and Optical Characterisation of ZnMgO Nanowires

7.1 Motivation

An advantage of compound semiconductor alloys over silicon is the ability to modify the electrical properties of the material by altering the ratios of the component elements. Zinc atoms in zinc oxide can be replaced by gallium [1], indium[2], magnesium [3], tin [2], cadmium [4], aluminium [5] or combinations thereof, resulting in new compounds with a wide range of electrical and optical properties. Recently, the amorphous zinc oxide derived semiconductor IGZO (indium gallium zinc oxide) has enjoyed commercial success as a replacement for amorphous silicon in LCD displays due to a combination of high mobility and transparency and it low-temperature growth on flexible plastic substrates [6, 7].

Magnesium oxide has a very wide band gap of 7.8 eV and a rock salt crystal structure. Despite a high lattice mismatch between itself and ZnO (ZnO: 3.25 Å, MgO: 4.22 Å), single-phase wurtzite $Zn_{1-x}Mg_xO$ films have been fabricated with up to 55% MgO on a 20% MgO buffer layer [8] and with as much as 45% MgO on ordinary <111> silicon [9]. It had previously been thought that the percentage MgO limit in wurtzite ZnMgO was approximately 30%, although Koike *et al.* [9] determined that this was limited by the solid solubility of MgO in ZnO. At lower temperatures (below 600 °C), this limit was higher, allowing the Mg concentration to be increased.

The primary objective of adding MgO to ZnO is to tune the band gap. With a band gap of 3.36 eV at room temperature, ZnO emits and absorbs in the UVA spectrum but by adding Mg, the bandgap can be increased up to 4.55 eV in the UVC band [3, 8-10] or to an intermediate value in the UVB range. The ability to fabricate broad spectrum UV detectors from cheap, abundant materials such as ZnO and MgO is of great interest to medical research as UVB radiation is responsible for cancer-causing sunburn [11]. Existing tunable photodiode sensors in the UVB range of the electromagnetic spectrum are presently made from the more expensive AlGaN ternary alloy system. ZnMgO nanowires have been reported in the literature grown by RF co-sputtering [12], by a hydrothermal method [13] and by MOPVE [14] and PLD [15].

7.2 ZnMgO Nanowire Growth

7.2.1 Growth of $Zn_{0.95}Mg_{0.05}O$ Nanowires

A growth was conducted using the standard EPLD method described in Chapter 2, 3 and 4, using a Testbourne Ltd. 99.99% purity $Zn_{0.95}Mg_{0.05}O$ PLD target. The substrate used was a 10 mm x 10 mm x 0.5 mm sample of c-plane sapphire treated with APTMS and the commercial, 10 nm Au colloids produced by Sigma Aldrich, as described in Chapter 4. Tapering nanowires were grown on the sapphire substrate wherever the gold colloids were present, as shown in Figure 1. Figure 2 shows that the tips of some of the wires tapered down to approximately 10 nm, the diameter of the catalyst Au colloids. There was also evidence of the presence of gold capping particle on the nanowires, consistent with the VLS growth mechanism. The morphology of the ZnMgO nanowires was indistinguishable from that of ZnO nanowires grown under the same conditions (as shown in Figure 3, overleaf) with a similar degree of vertical alignment, similar nanowire density and similar tapering. Knife shaped nanosheets and other irregular nanostructures occurred at a similar low rate among both the ZnO and ZnMgO nanowires.

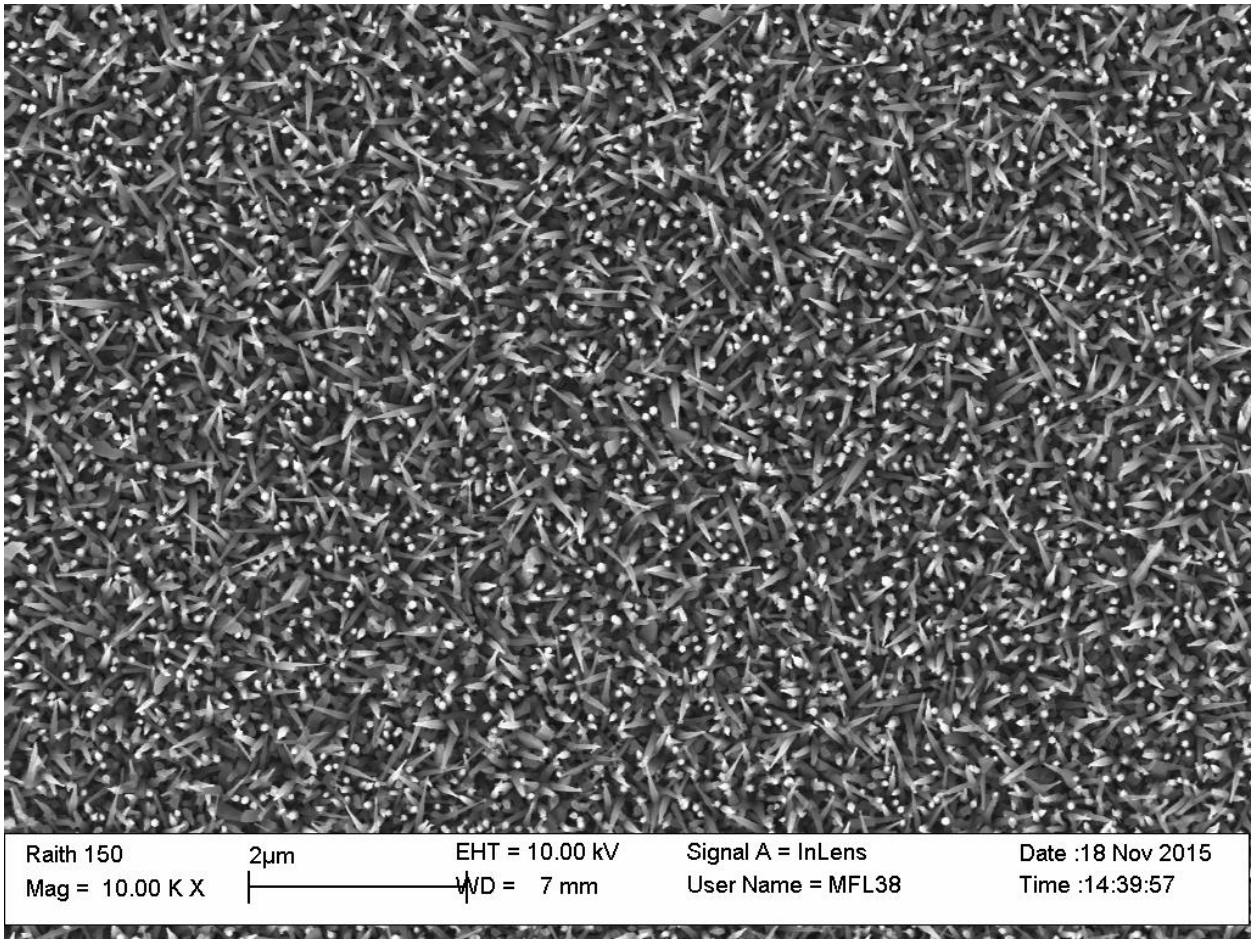

Figure 1: ZnMgO nanowires grown on c-plane sapphire using 10 nm commercially produced Au colloids as catalyst. (Growth 98)

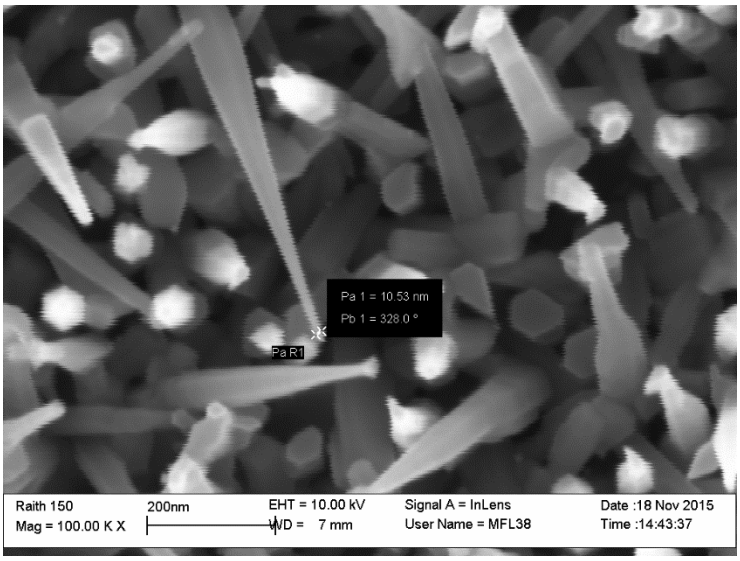

Figure 2: High resolution SEM image showing the approximately 10 nm tip diameter and gold capping particle.

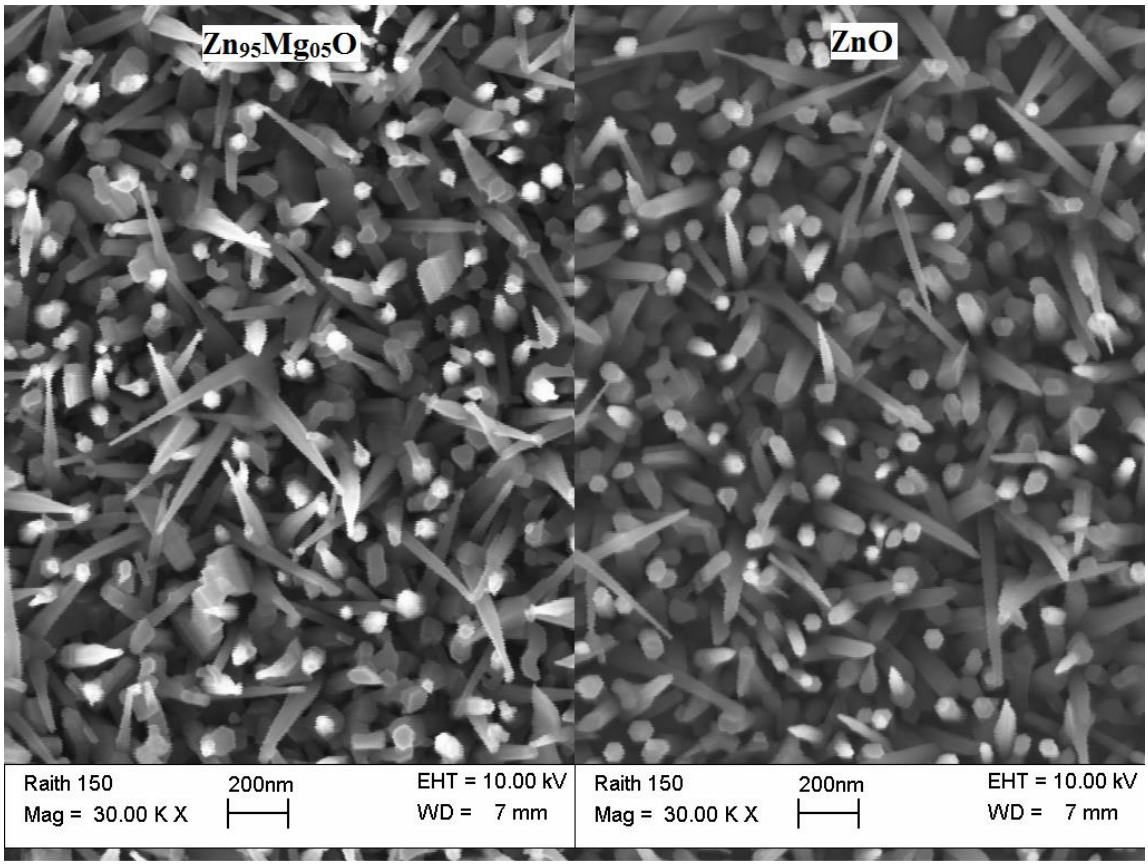

Figure 3: Comparison between nanowires grown under identical conditions with $Zn_{95}Mg_{05}O$ target (left) and pure ZnO target (right). The morphology of the nanowires is indistinguishably similar.

7.2.2 Growth of $Zn_{0.90}Mg_{0.10}O$ Nanowires

An eclipse PLD growth was conducted using a $Zn_{0.90}Mg_{0.10}O$ PLD target with all other parameters held the same as in the 5% Mg growth. Nanowires grew on the c-plane sapphire substrate and are shown in Figure 4. The nanowires produced by this higher, 10% Mg composition target had tip diameters similar to the 10

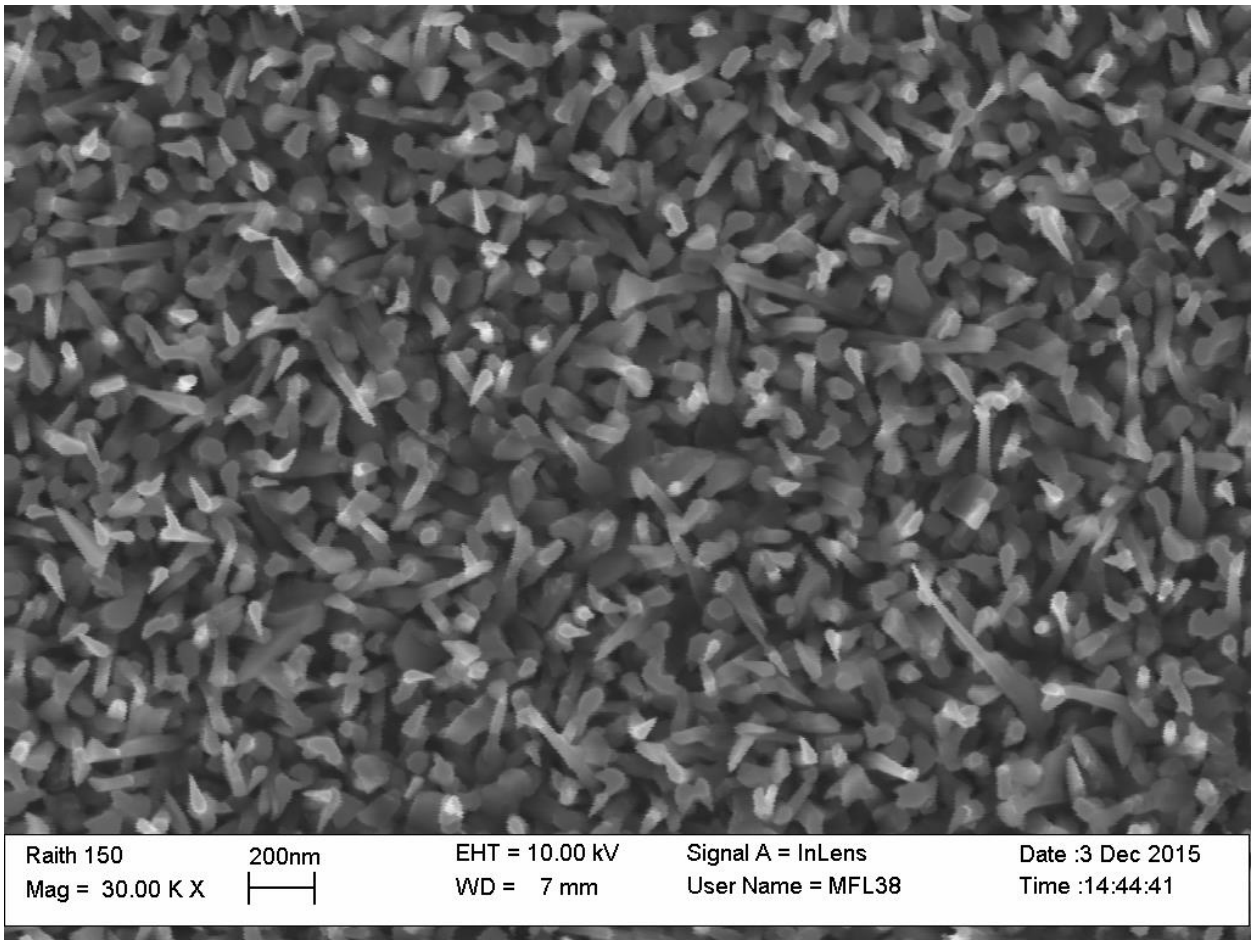

Figure 4: ZnMgO Nanowires grown from a $Zn_{90}Mg_{10}O$ PLD target and 10 nm commercially produced Au colloids. The nanowires exhibit more disorder and are shorter and more tapered than the nanowires grown with the $Zn_{95}Mg_{05}O$ target. (Growth 100)

nm catalyst colloid sizes but were of significantly lower overall quality and were more disordered than the nanowires grown from the 5% Mg target. This is consistent with other results reported in the literature where nanowires grown with increasing magnesium content have become larger and often more disordered [13, 15]. This is not unexpected because of the large lattice mismatch and different crystal structure of ZnO and MgO. Nanowires depend on achieving very high crystal quality and the strain introduced by mixing two differently structured crystals may compromise the formation of good quality nanowires [10].

7.2.3 Growth of $Zn_{0.85}Mg_{0.15}O$ Nanowires

An eclipse PLD growth (No. 105, Appendix 1) was also conducted to investigate whether nanowires could be grown from a $Zn_{0.85}Mg_{0.15}O$ PLD target, with all other parameters kept the same as the previous ZnMgO nanowire growths. An a-plane and a c-plane sapphire sample were coated with APTMS-tethered 10 nm colloids and placed alongside each other on the substrate heater during growth. Figure 5 shows typical images from each of these substrates.

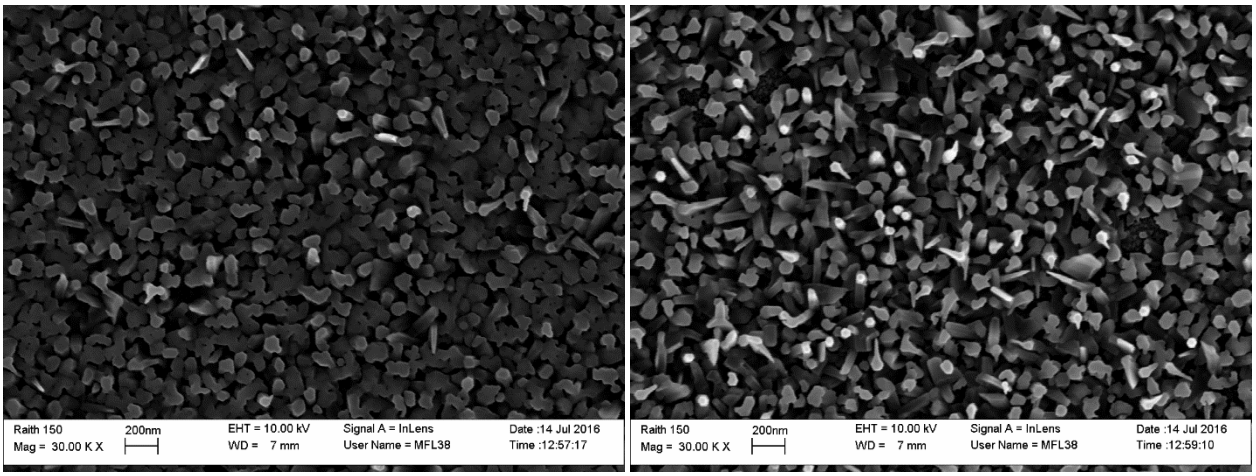

Figure 5: ZnMgO nanorods grown from a 15% Mg PLD target on a-plane (left) and c-plane (right). In this growth, the c-plane sapphire substrate appeared to produce more of the needle-shaped rod structures. (Growth 105)

Nanorods grew on each substrate, albeit with a relatively high degree of disorder. The c-plane sapphire substrate appeared to contain more of the tapered nanorods characteristic of pure ZnO growths than the a-plane sapphire. This is interesting as in the case of the ZnO nanowire growths, relatively little difference was observed between the morphologies of nanowires grown on a- and c-plane sapphire substrates. Both samples had fewer pointed, upright nanorods than either the 5% or 10% Mg growths, indicating a shift away from this structure as a preferred crystal shape. The solid solubility limit of MgO in wurtzite ZnO, described earlier, is known to be approximately 30% for conventional ZnMgO growths. Although PLD is generally assumed to stoichiometrically transfer the chemical composition of a multi-element target to the substrate, PLD deposited ZnMgO thin films often show a more than 50% enhancement in Mg concentration [15, 16]. Therefore, it is possible that the nanowires produced using the 15% Mg target could have a Mg concentration higher than 22.5%, approaching the 30% limit. A growth using a 20% Mg target would be likely to produce Mg concentrations in excess of 30% Mg, resulting in mosaicking of the growth structure.

7.3 Photoluminescence of ZnMgO Nanowires and Films

7.3.1 $Zn_{0.95}Mg_{0.05}O$ Film Growth

Two ZnMgO thin films were grown by eclipse PLD using the same conditions and parameters as the $Zn_{95}Mg_{05}O$ nanowires to produce a control sample for photoluminescence. This was achieved by simply omitting the deposition of the catalyst gold colloids on the substrates. Both films appeared similar under the SEM. Figure 6 shows the surface of the film on c-plane sapphire is not perfectly smooth, however there are no nanowires present without the gold to catalyse the VLS process.

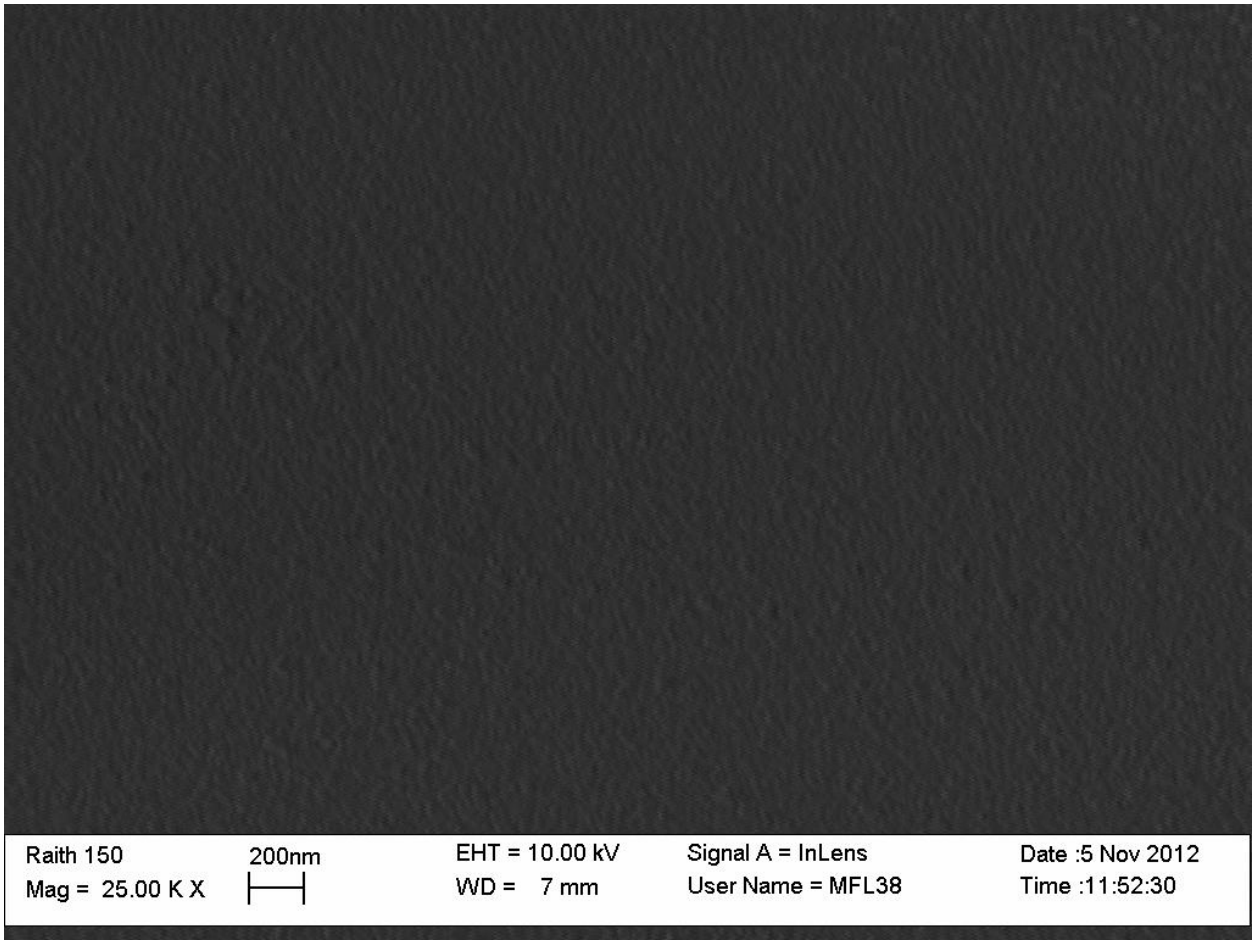

Figure 6: ZnMgO thin film grown on c-plane sapphire. Target composition was $Zn_{95}Mg_{05}O$. (Growth 98)

7.3.2 Low Temperature ZnMgO Photoluminescence

Low temperature (3 K) photoluminescence spectra were taken in the excitonic recombination regions of the $Zn_{0.95}Mg_{0.05}O$ films grown on both a-plane and c-plane sapphire as well as the $Zn_{0.95}Mg_{0.05}O$ nanowires. Figure 7 shows these spectra compared to the PL spectra of the Au9 ultra-fine nanowires grown in Chapter 4. The large blueshift caused by adding Mg to the ZnO crystal is immediately apparent, but surprisingly, each of the three $Zn_{0.95}Mg_{0.05}O$ samples with nominally the same Mg concentration appeared to be shifted by a different amount. . The peaks for films grown on a-plane and c-plane sapphire were located at 3.470 and 3.445 eV respectively. Gruber *et al.* [17] conducted a study on the optical properties of ZnMgO at various Mg concentrations and reported that the dominant PL peak was at at 3.481 eV for $Zn_{0.94}Mg_{0.06}O$, at a slightly higher energy than either of the two films characterised here. This is consistent with the expectation that a 6% Mg film would have a wider bandgap and therefore a larger blueshift than 5% Mg films. The shift between the film grown on the c-plane sapphire substrate and the film grown on the a-plane substrate is surprising. It is possible that this shift is due to different levels of strain induced in the crystal by different amounts of lattice mismatch with the substrates.

Although the 5% Mg nanowires appeared to have good morphology as indicated by the SEM, the ZnMgO nanowires and films measured in Figure 7 all had very broad peaks, which typically indicates poor crystallinity. This is especially apparent when the spectra of the ZnMgO samples are compared to that of the Au9 catalysed ZnO nanowires. Three peaks appeared in the ZnMgO nanowires spectra, but only two peaks appeared in each of the two ZnMgO films. All three samples were grown in the same system, so it is likely that any dopants or impurities found in large concentrations in one would be found in all three. It is therefore reasonable to conclude that the nanowire morphology is responsible for the appearance of the third peak at approximately 3.50 eV in the PL spectra of the ZnMgO nanowires.

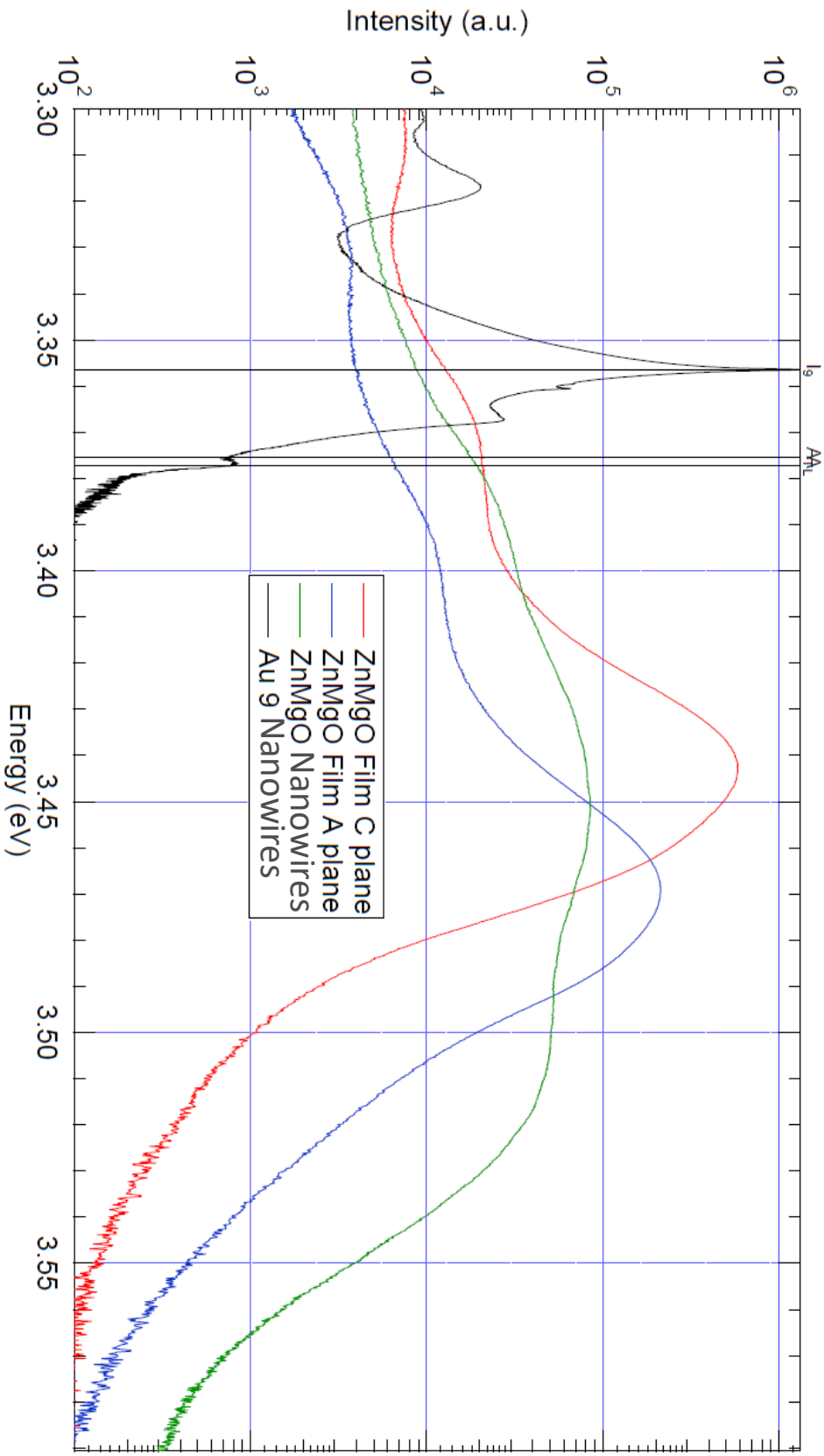

Figure 7: Near band edge photoluminescence of ZnMgO films (Growth 99) and nanowires, (Growth 98) compared against ZnO nanowires catalysed by Au9 clusters (Growth 102).

7.4 Summary

This chapter detailed a series of experiments to grow and optically characterise ZnMgO nanowires using EPLD on substrates treated with APTMS-tethered Au colloids across a range of Mg concentrations.

- $Zn_{1-x}Mg_xO$ nanowires were grown by eclipse pulsed laser deposition on sapphire substrates for x = 0.05, 0.1 and 0.15, using APTMS-tethered, 10 nm commercially produced gold colloids as catalysts for VLS growth.
- Gold capping particles were observed at the tips of some of the nanowires. Nanowire tip diameter corresponded to the 10 nm diameter of the Au colloid catalysts as previously observed with pure ZnO in Chapters 3 and 4, indicating that VLS growth was occurring.
- Increasing Mg content resulted in progressively more disordered nanowire morphologies, which was attributed to increased lattice strain due to the incorporation of MgO (which prefers to adopt a rock-salt crystal structure) into wurtzite ZnO.
- Low temperature (3 K) photoluminescence of nanowires grown using the $Zn_{0.95}Mg_{0.05}O$ PLD target was compared to spectra of $Zn_{0.95}Mg_{0.05}O$ thin films and ZnO nanowires grown using Au9 clusters as catalysts. A significant blueshift of the PL from the ZnMgO nanowires and film was observed, confirming that the addition of Mg had significantly increased the bandgap of the material.
- The PL spectra of $Zn_{0.95}Mg_{0.05}O$ nanowires was broad, indicating poor quality crystallinity, even though their morphology was similar to that of the pure ZnO nanowires.
- A third peak at approximately 3.50 eV was visible on the PL spectra of the $Zn_{95}Mg_{05}O$ nanowires that was not observed in the corresponding films. This could be related to surface effects similar to those seen in pure ZnO nanowires.

7.5 References

[1] V. Bhosle, J. T. Prater, F. Yang, D. Burk, S. R. Forrest, and J. Narayan, "Gallium-doped zinc oxide films as transparent electrodes for organic solar cell applications," *Journal of Applied Physics*, vol. 102, 2007.

[2] T. Minami, "Transparent and conductive multicomponent oxide films prepared by magnetron sputtering," *Journal of Vacuum Science and Technology A: Vacuum, Surfaces and Films*, vol. 17, pp. 1765-1772, 1999.

[3] I. V. Maznichenko, A. Ernst, M. Bouhassoune, J. Henk, M. Däne, M. Lüders, *et al.*, "Structural phase transitions and fundamental band gaps of Mg xZn1-x O alloys from first principles," *Physical Review B - Condensed Matter and Materials Physics*, vol. 80, 2009.

[4] T. Gruber, C. Kirchner, R. Kling, F. Reuss, A. Waag, F. Bertram, *et al.*, "Optical and structural analysis of ZnCdO layers grown by metalorganic vapor-phase epitaxy," *Applied Physics Letters*, vol. 83, pp. 3290-3292, 2003.

[5] J. Loureiro, N. Neves, R. Barros, T. Mateus, R. Santos, S. Filonovich, *et al.*, "Transparent aluminium zinc oxide thin films with enhanced thermoelectric properties," *Journal of Materials Chemistry A*, vol. 2, pp. 6649-6655, 2014.

[6] K. Nomura, H. Ohta, A. Takagi, T. Kamiya, M. Hirano, and H. Hosono, "Room-temperature fabrication of transparent flexible thin-film transistors using amorphous oxide semiconductors," *Nature*, vol. 432, pp. 488-492, 2004.

[7] H. Yabuta, M. Sano, K. Abe, T. Aiba, T. Den, H. Kumomi, *et al.*, "High-mobility thin-film transistor with amorphous InGaZnO4 channel fabricated by room temperature rf-magnetron sputtering," *Applied Physics Letters*, vol. 89, 2006.

[8] X. Du, Z. Mei, Z. Liu, Y. Guo, T. Zhang, Y. Hou, *et al.*, "Controlled growth of high-quality ZnO-based films and fabrication of visible-blind and solar-blind ultra-violet detectors," *Advanced Materials*, vol. 21, pp. 4625-4630, 2009.

[9] K. Koike, K. Hama, I. Nakashima, G. Y. Takada, K. I. Ogata, S. Sasa, *et al.*, "Molecular beam epitaxial growth of wide bandgap ZnMgO alloy films on (1 1 1)-oriented Si substrate toward UV-detector applications," *Journal of Crystal Growth*, vol. 278, pp. 288-292, 2005.

[10] K. Liu, M. Sakurai, and M. Aono, "ZnO-based ultraviolet photodetectors," *Sensors*, vol. 10, pp. 8604-8634, 2010.

[11] M. Allen and R. McKenzie, "Enhanced UV exposure on a ski-field compared with exposures at sea level," *Photochemical and Photobiological Sciences*, vol. 4, pp. 429-437, 2005.

[12] J. P. Kar, M. C. Jeong, W. K. Lee, and J. M. Myoung, "Fabrication and characterization of vertically aligned ZnMgO/ZnO nanowire arrays," *Materials Science and Engineering: B*, vol. 147, pp. 74-78, 1/25/ 2008.

[13] C. Y. Lee, T. Y. Tseng, S. Y. Li, and P. Lin, "Single-crystalline MgxZn1-xO ($0 \leq x \leq 0.25$) nanowires on glass substrates obtained by a hydrothermal method: Growth, structure and electrical characteristics," *Nanotechnology*, vol. 16, pp. 1105-1111, 2005.

[14] M. Zhi, L. Zhu, Z. Ye, F. Wang, and B. Zhao, "Preparation and properties of ternary ZnMgO nanowires," *Journal of Physical Chemistry B*, vol. 109, pp. 23930-23934, 2005.

[15] M. Lorenz, E. M. Kaidashev, A. Rahm, T. Nobis, J. Lenzner, G. Wagner, *et al.*, "Mgx Zn1-x O ($0 \leq x < 0.2$) nanowire arrays on sapphire grown by high-pressure pulsed-laser deposition," *Applied Physics Letters*, vol. 86, pp. 1-3, 2005.

[16] A. Ohtomo, M. Kawasaki, I. Ohkubo, H. Koinuma, T. Yasuda, and Y. Segawa, "Structure and optical properties of ZnO/$Mg_{0.2}Zn_{0.8}O$ superlattices," *Applied Physics Letters*, vol. 75, pp. 980-982, 1999.

[17] T. Gruber, C. Kirchner, R. Kling, F. Reuss, and A. Waag, "ZnMgO epilayers and ZnO-ZnMgO quantum wells for optoelectronic applications in the blue and UV spectral region," *Applied Physics Letters*, vol. 84, pp. 5359-5361, 2004.

Chapter 8: Miscellaneous Nanowire Growths

8.1 ZnO Nanowires Catalysed by Platinum Group Metals

8.1.1 Motivation

During the literature review for this thesis, it was found that many metals can be used as catalysts for VLS ZnO nanowire growth. While gold is the most common catalyst [1-4], various groups have succeeded in growing ZnO nanowires via catalytic VLS using tin [5, 6], germanium [7], silver [8], platinum [8], copper [9] and selenium [10]. The selection criteria for these metal catalysts is that they must be able to form a liquid alloy with zinc at the growth temperature used and that they must also not form a solid solution with ZnO under the same conditions [6]. If these two conditions are satisfied, then the liquid droplet can catalyse the VLS growth without the catalyst itself becoming incorporated into the nanowire.

It was surprising that Zhang *et al.* [8] reported that platinum was able to satisfy these conditions as bulk platinum has a melting point of 1768 °C, far higher than the 800 °C growth temperature that they used to grow nanowires in their report. Their explanation cited Park *et al.* [11], who proposed a size-dependent reduction in the melting point of very thin metal films and nanoparticles. Zhang *et al.* also observed that their Pt thin film retracted into droplets even before zinc was introduced, indicating that it had transitioned to a liquid phase.

Moser [12] reported that the Zn-Pt system is not a eutectic, but that there are several eutectoids, peritectoids and peritectic states that exist at temperatures lower than 800 °C. In particular, a peritectic alloy with 94.9% atomic zinc occurs that is completely liquid above 729 °C. Vapour solid (VS) nanowire growth is usually considered to be a non-catalytic process where the nanowire crystal condenses on itself without the assistance of a catalyst. However, it is possible that a eutectoid or peritectic relationship between catalyst and the nanowire material could result in directional, catalytic VS growth that resembles catalytic VLS growth but remains entirely in the solid phase.

The successful growth of ZnO nanowires from a Pt catalyst suggests that other noble metals might also be capable of catalysing ZnO nanowire growth, even though their bulk melting points are very much higher than the 750 °C growth temperature. Consequently, a series of ZnO nanowire growth experiments was conducted to evaluate the catalytic performance of sputtered thin films of palladium and ruthenium.

8.1.2 Sputtered Palladium Catalysed ZnO Nanowire Growth

With a bulk melting point lower than platinum of 1554.9 °C, palladium was the most likely candidate of the platinum group metals to be able to fulfil the criteria for the catalysis of ZnO nanowires. Cleaned a-plane and c-plane sapphire substrates were sputter coated with palladium for one minute using a 50W DC argon sputtering plasma. This resulted in a film of approximately 1.5 nm thickness as measured by the calibrated crystal growth monitor of the sputterer. ZnO was then deposited on both substrates by eclipse PLD using the standard growth conditions described earlier in Chapter 3.

ZnO nanowires grew on both substrates wherever catalyst material was present as shown in Figure 4 (opposite). Areas with no palladium produced only a rough film. The nanowires were not well ordered but showed a clear preferential growth towards the vertical direction on both substrates. The tips of the wires varied in size expected when using a sputtered catalyst film. Figure 1 shows the measurement of a 5 nm tipped nanowire. The presence of such a fine nanowire is not unexpected as the film was only 1.5 nm thick meaning it would likely have dewetted into droplets of just a few nm in diameter. Structures resembling the tetrapods observed in Chapter 4, Section 4.2 were again observed in seemingly random locations on both substrates as shown in Figure 2, although at a much lower density than previously observed (5-10% in the regions where they were present). Their morphology was also significantly less regular.

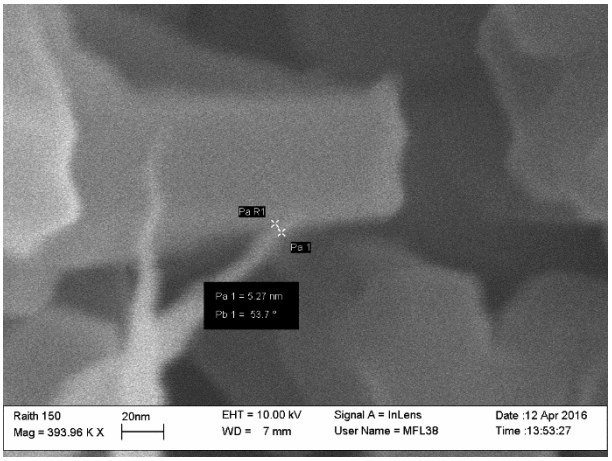

Figure 1: Measurement of an ultra-fine ZnO nanowire tip.

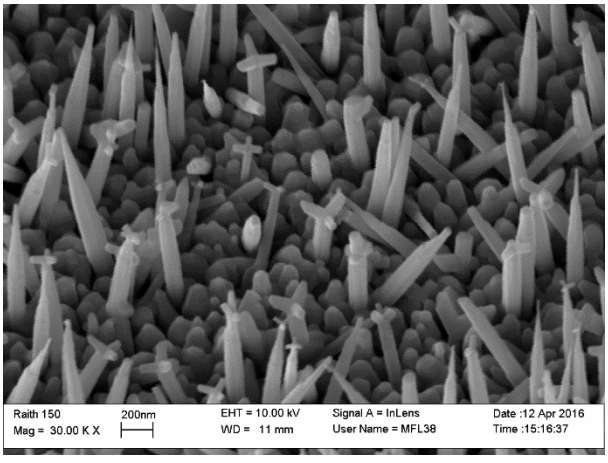

Figure 2: Tetrapod nanostructures were observed in some areas of both a-plane and c-plane substrates.

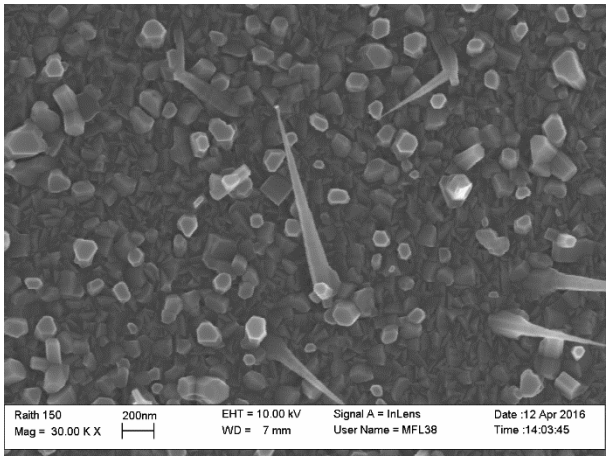

Figure 3: ZnO nanowire capped with a metallic cap, indicative of VLS growth.

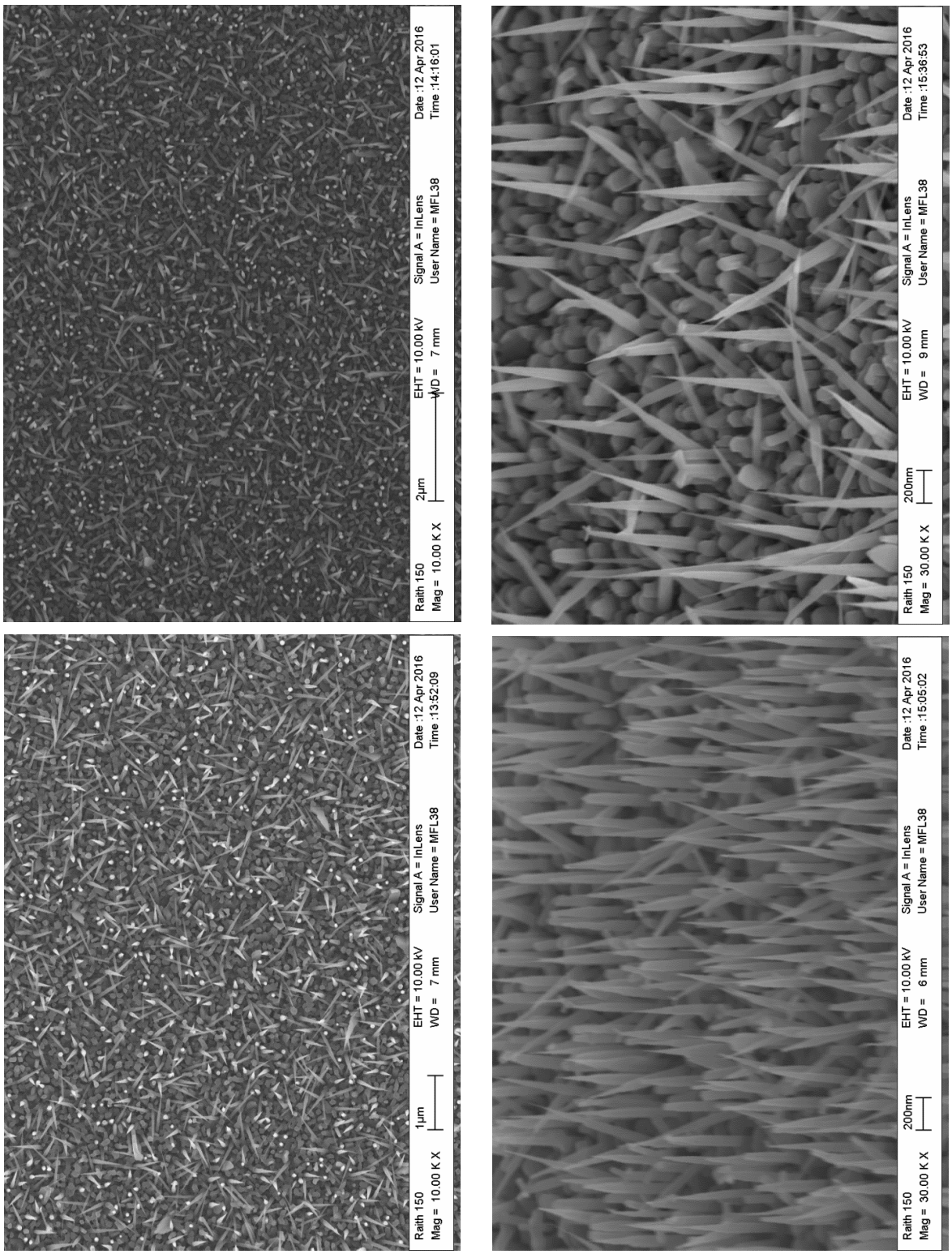

Figure 4: ZnO nanowires grown from sputtered palladium catalyst on a-plane (left) and c-plane (right) sapphire viewed from overhead (top) and 45° side view (bottom).

Several nanowires were also discovered to have metallic caps at their ends, characteristic of VLS growth. As shown in Figure 3, this confirms that the palladium was having a catalytic action on the growth of the ZnO nanowires. The overall quality and consistency of the morphology of these nanowires was comparable to the nanowires grown using sputtered Au in Chapter 3, Section 10.

8.1.3 Ruthenium Film Catalysed ZnO Nanowire Growth

Ruthenium has a bulk melting point of 2334 ℃, significantly higher than either platinum or palladium. A film of Ruthenium was DC sputtered onto cleaned a-plane and c-plane sapphire substrates for one minute, to produce a film of an approximate thickness of 2-3 nm. ZnO was grown on these substrates by eclipse PLD under identical conditions to the palladium catalysed growth.

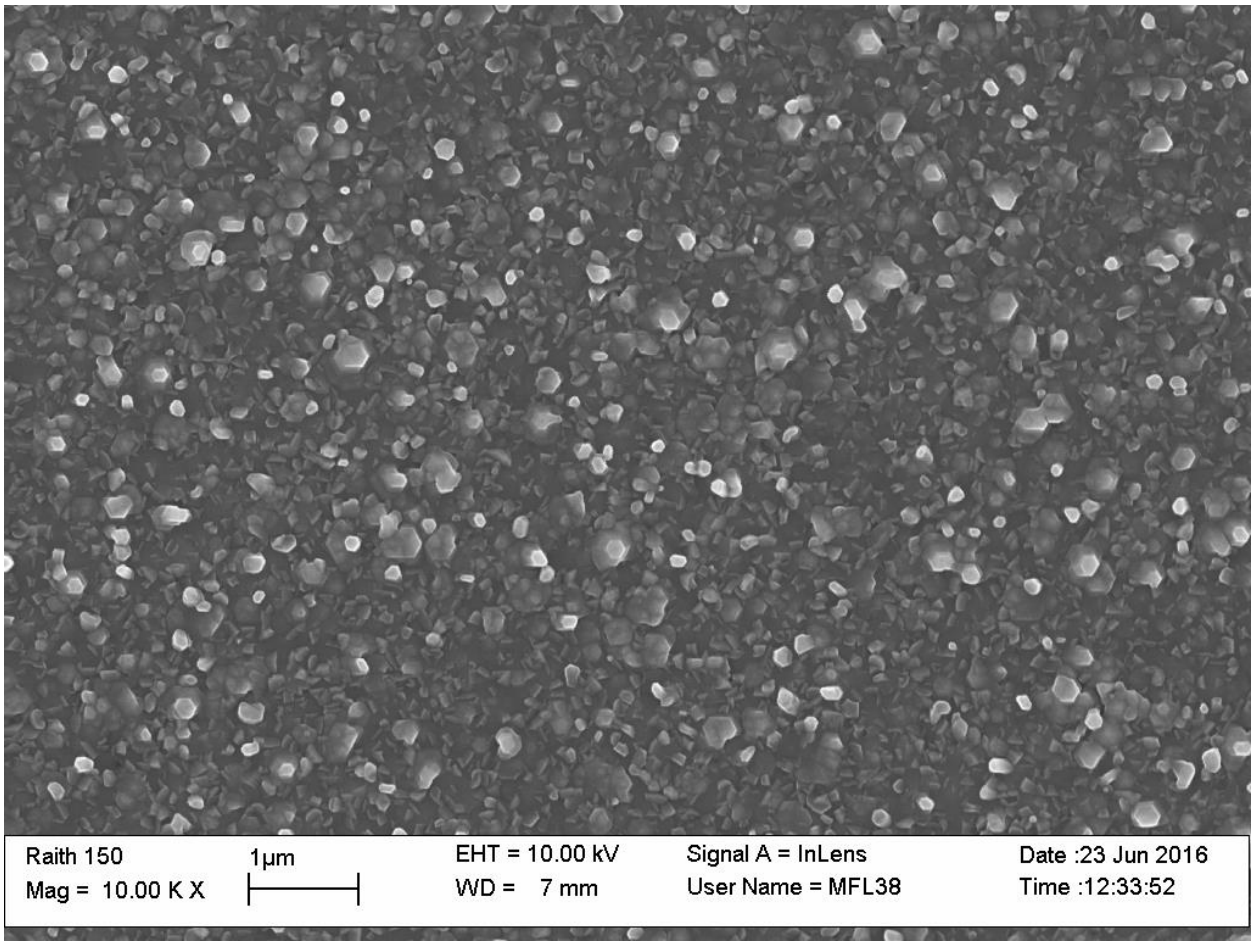

Figure 5: Attempted ZnO nanowire growth using a ruthenium film as catalyst. No nanowires were observed.

A rough film with some nano-scale texturing was found to cover both samples as shown in Figure 5, but no well-formed nanorods or wires were observed on either sample. Considering that a thickness-dependent melting point reduction was observed with other platinum group metals, it is likely that the same occurs with ruthenium. Despite this, the growth temperature of 750 °C was obviously insufficient to melt the thin, sputtered ruthenium film to the extent where it could initiate catalytic ZnO nanowire growth. The texturing and roughness of the resulting ZnO film indicates that local growth nuclei were present, but the ZnO material appears to be simply agglomerating around these and not catalytically interacting with them.

8.2 ZnO Nanowire Growth by Molecular Beam Epitaxy

8.2.1 Motivation

Molecular Beam Epitaxy (MBE) is a deposition method used in the production of very high purity thin films [13-15] and is described in Chapter 2, Section 11. Under optimised conditions, MBE is capable of depositing a single atomic layer of material at a time with very few impurities. Although ZnO nanowires have been grown by MBE in the literature [16], the number of groupss reporting successful ZnO nanowire growth by MBE is surprisingly low. The effectiveness of the APTMS-tethered gold colloids for the growth of ZnO nanowires using PLD has been well established in this thesis and MBE offered an opportunity to investigate whether this substrate preparation method could be used with a different growth technique.

8.2.2 Initial MBE Nanorod Growth

Initial MBE growths used the 10 nm commercially produced colloids, tethered to a-plane and c-plane sapphire substrates by the standard APTMS surface modification using the hybrid drop coating method developed in Chapter 4. The MBE growth was carried out in collaboration with Adam Hyndman at the University of Canterbury, Physics Department. The initial growth conditions are shown in Table 1:

Table 1: System parameters for the initial ZnO MBE growth.

Temperature	750 °C
Growth Time	120 minutes
Oxygen Partial Pressure	5×10^{-5} Torr
Zn Cell Temperature	320 °C
Plasma Power	200 W

Typically an oxygen plasma power of 250 W is used for ZnO film growth [15], but this was reduced to 200 W to minimise damage to the colloids on the surface of the substrates. Before any growths were conducted, a test was performed to determine if the colloids would be damaged by the substrate heating and the oxygen plasma. Conductive silicon substrates were coated with APTMS and 10 Au nm colloids using the same method as for the sapphire growth substrates. These samples were imaged via SEM before and after heating in the MBE chamber at the intended growth temperature in the presence of the 200 W oxygen plasma to simulate growth conditions. Figure 6 shows the results of this test. The density of Au colloids is essentially the same before and after the test, indicating that the colloids were not being damaged or removed by the highly oxidising plasma.

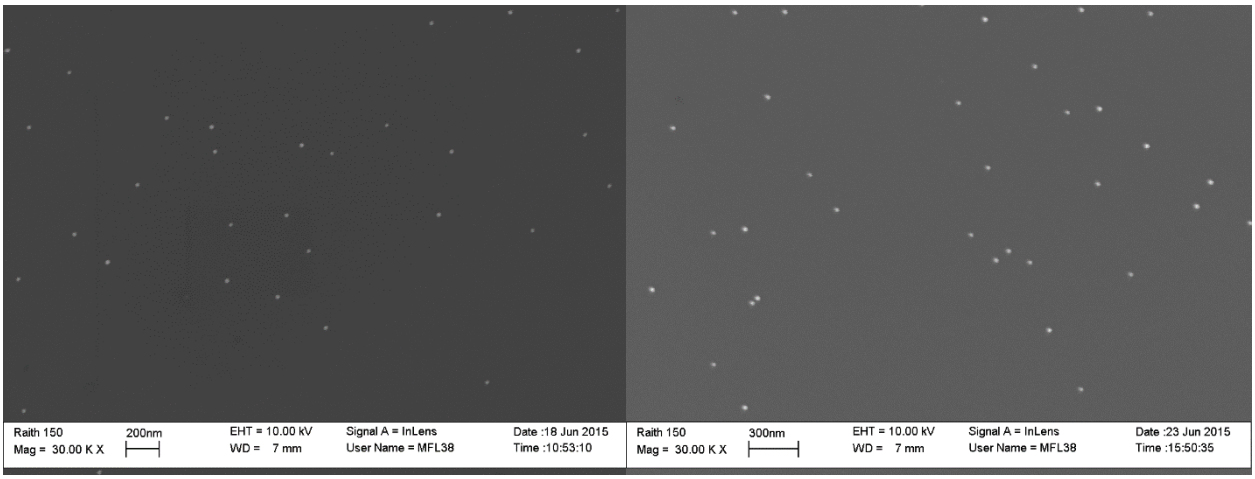

Figure 6: Silicon substrates coated with APTMS-tethered 10 nm Au colloids before (left) and after (right) heating at 750 °C with 250 W oxygen plasma. The density of colloids is essentially unchanged.

Figure 7 shows a typical area of the c-plane sapphire substrate after the ZnO MBE growth. Nanorods were present over the entire substrate but were highly disordered and showed no consistent morphology or preferential growth direction. Figure 8 shows an enhanced magnification SEM image showing large, multi-faceted block-like structures, indicating crystal growth in all directions. Some nanosheet-like structures are also visible. A nanosheet is circled in Figure 8 which appears to be capped with a Zn/Au nanoparticle, which may indicate that some VLS growth had occurred.

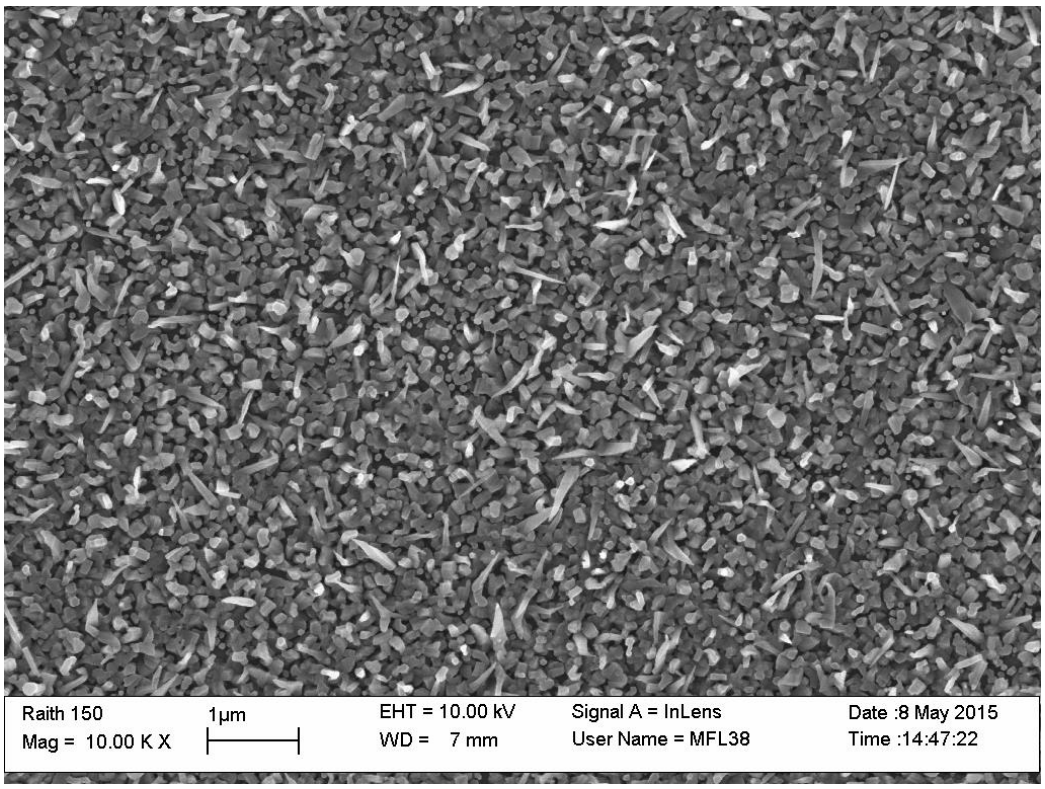

Figure 7: ZnO nanorods grown via MBE showing a high level of disorder.

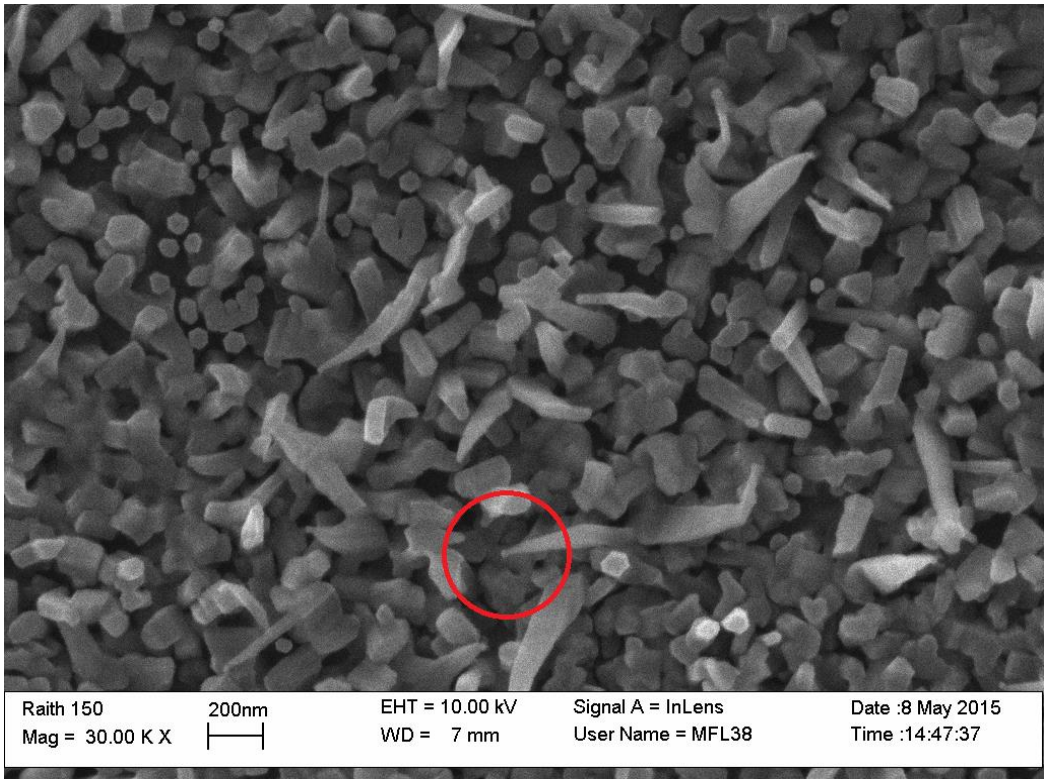

Figure 8: Enhanced magnification of MBE ZnO nanorods. Circled is a nanosheet tipped with a Zn/Au nanoparticle.

The lack of any discernible order or preferential growth direction in this initial growth was disappointing. MBE growth is slow and typically produces films of very high crystal quality, however in the PLD growth experiments conducted in Chapter 3, Sections 5 and 12, it was found that growths with lower deposition rates often resulted in poor quality nanorods similar to what was observed here in the MBE growth.

8.2.3 Reflective High Energy Electron Diffraction

Reflective High Energy Electron Diffraction (RHEED) measurements were taken in situ as the MBE nanorods were being grown. RHEED is a qualitative method used to estimate the quality of films during growth by producing a projected image of the surface crystal structure itself. Typically, streaked lines indicate high crystal quality but spots and asymmetry represents scattering and disorder. Figure 9 shows the RHEED patterns of the bare sapphire and after 10, 40 and 120 minutes of MBE growth. The bare sapphire is a very high quality bulk crystal so its RHEED pattern is streaky with visible, diagonal Kikuchi lines, a marker of quality only seen in the highest quality crystals. After the first 10 minutes of growth, the first few layers of ZnO also showed high quality crystallinity, with the new material producing a different

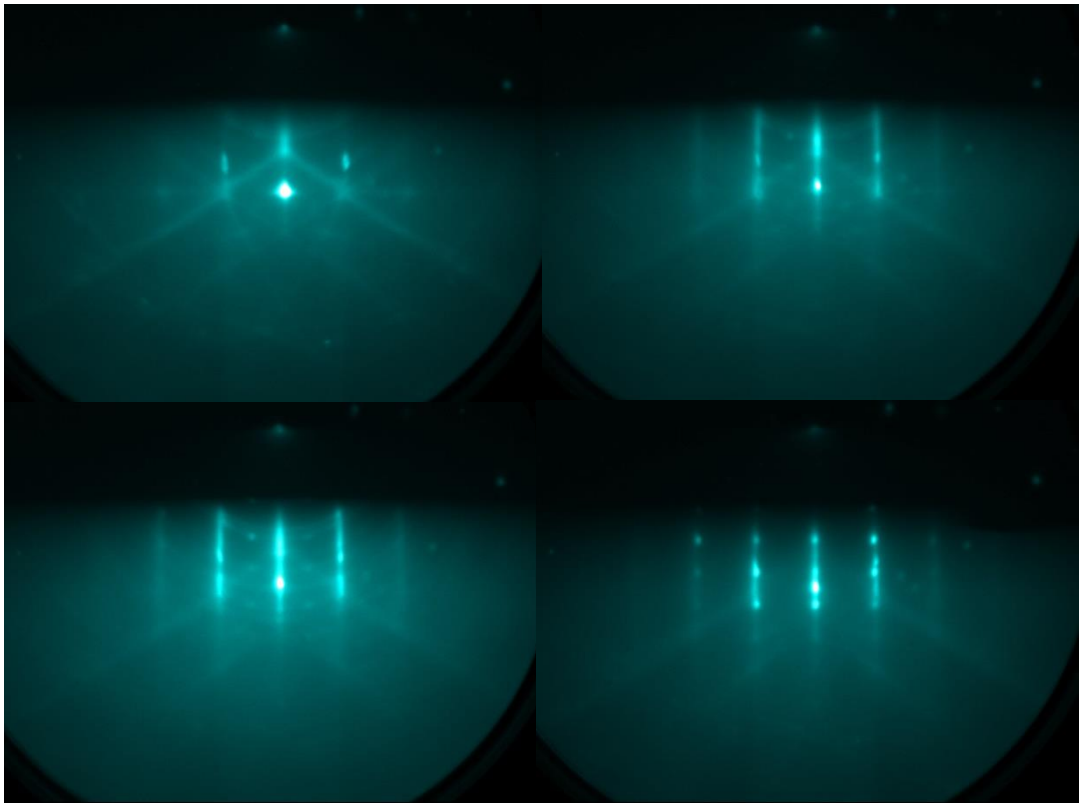

Figure 9: RHEED patterns captured before deposition start (top left), after 10 mins (top right), after 40 mins (bottom left) and after 120 mins (bottom right). As the nanorods grow, the streaks separate into distinct spots indicating greater scattering.

pattern. As the growth continued to 40 and 120 minutes, it can be seen that the streaks separate into discrete spots. In a film this would indicate poor crystallinity, but here it is more likely due to scattering between the disordered nanostructures as RHEED is a grazing-angle technique.

8.2.4 Thermal Cleaning of Substrates

The MBE process is very sensitive to contamination as described in Chapter 2. It was decided to repeat the growth, using both APTMS-tethered 10 nm colloid treated a-plane and c-plane sapphire and to perform a thermal clean at 800 °C prior to the growth in order to remove any surface contaminants. Bare sapphire substrates of each plane were also loaded as controls. Figure 10 shows the typical morphology of the a-plane and c-plane sapphire substrates after ZnO MBE deposition.

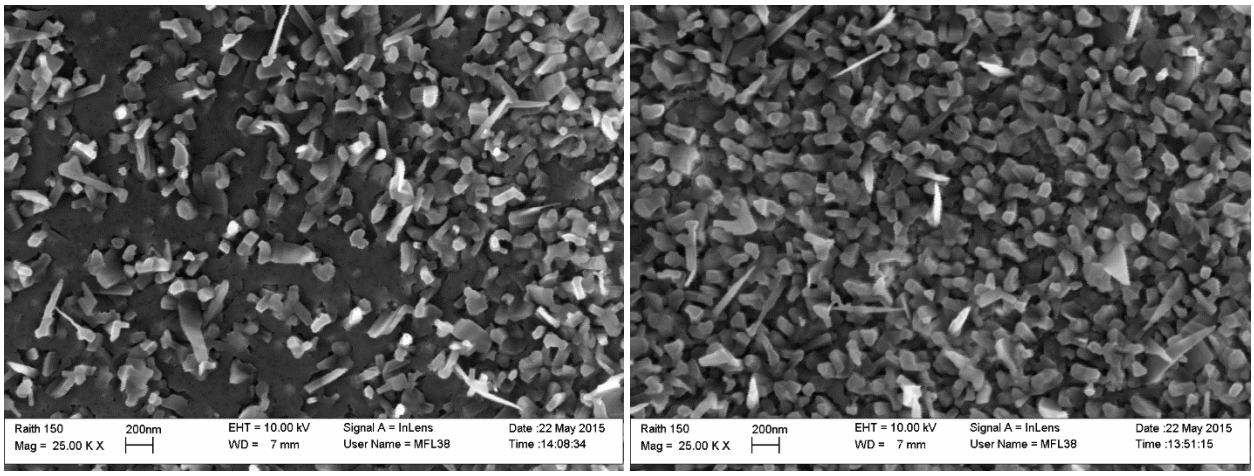

Figure 10: MBE growth of ZnO nanowires after 800 °C thermal clean on a-plane (left) and c-plane (right) sapphire. The morphology and disorder of the nanowires is very similar.

There was very little difference in the morphologies of nanorods grown on a-plane and c-plane sapphire which is consistent with experiments involving PLD nanowire growth. The addition of the thermal cleaning step did not appear to improve the order or morphological consistency of the nanorods and both samples were still dominated by block-like crystal structures with no apparent preferential growth direction. Various nanosheets and needle-like rods were visible scattered amongst the block-like structures on both substrates. The ZnO films on the control substrates without Au colloids were both similar in appearance, with a typical region of the film grown on bare a-plane sapphire shown in Figure 10. These films were relatively smooth with various scattered imperfections but nothing to indicate any systematic problem with the ZnO MBE growth.

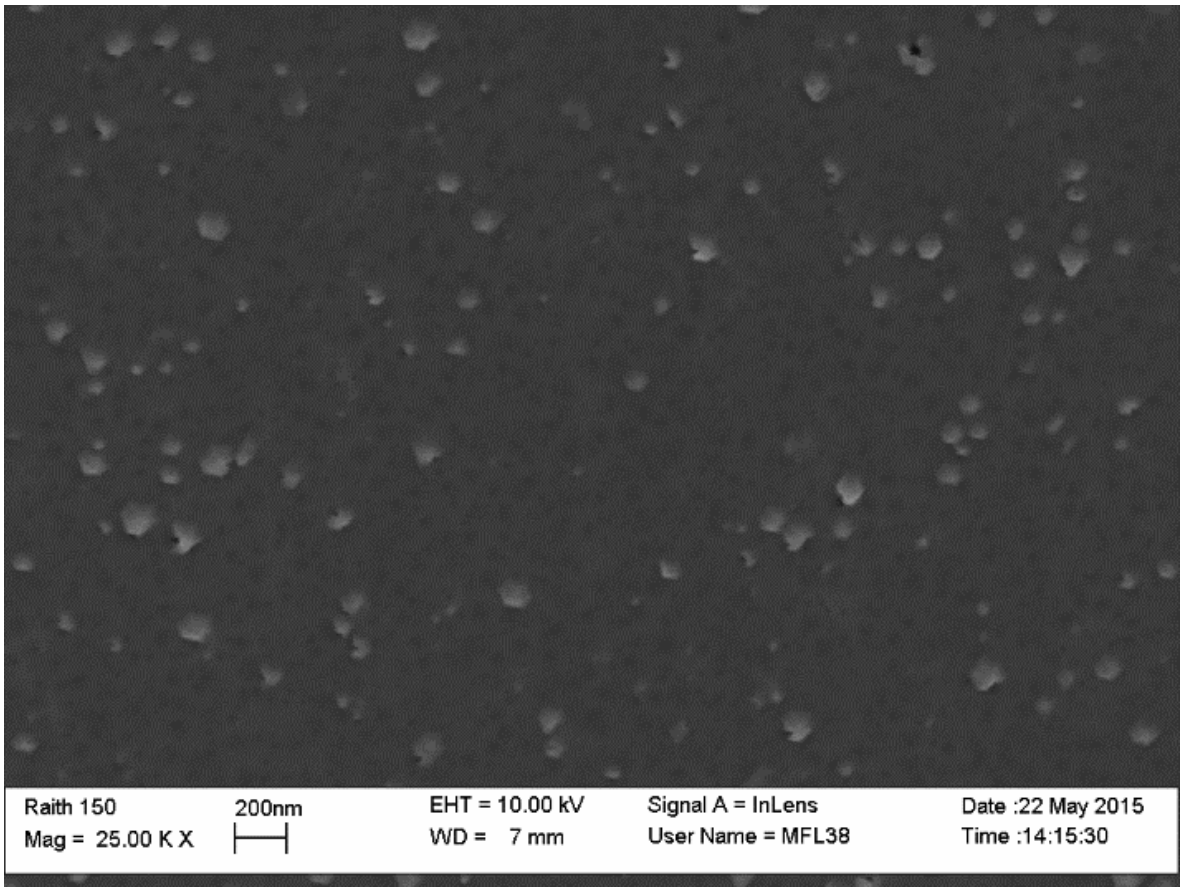

Figure 11: ZnO MBE film grown on a blank a-plane control substrate.

8.2.5 Zn-Rich Growth

Further repetitions of these MBE growths did not yield any improvements to the ordering of the nanorods produced. After considering the results of other film growth experiments using the MBE system, it was thought that the MBE grown nanorods could be Zn deficient. A growth was conducted using the same conditions as previously, including c-plane sapphire substrates coated with APTMS-tethered, 10 nm Au colloids, but increasing the temperature of the Zn cell, T_{Zn}, by 50 °C to 370 °C. Increasing the temperature of an effusion cells increases the intensity of the resulting particle beam and with the oxygen plasma conditions unchanged, this was expected to produce a more Zn-rich ZnO deposition.

Figure 12 shows the results of this Zn-rich deposition on c-plane sapphire. The Zn-rich deposition produced only a film of material with block-like imperfections, perhaps caused by gold colloids underneath a layer of ZnO material. In some regions the imperfections in the film were more numerous, as shown in Figure 13, but no nanorod-like structures were observed anywhere on the substrates. These findings were

a setback for future MBE nanorod growths as they indicated that increasing the deposition rate by increasing the Zn-flux would not improve the morphology of the ZnO nanorods grown. It was somewhat surprising that MBE was less effective than PLD for the growth of ZnO nanorods as MBE is widely regarded as one of the best techniques for growing high quality ZnO material. Considering the effects of growth rate on PLD ZnO nanowire growth described in Chapter 3, Section 12, it is probable that the problems encountered in growing ZnO nanorods using MBE stem from the intrinsically low deposition rate of the process.

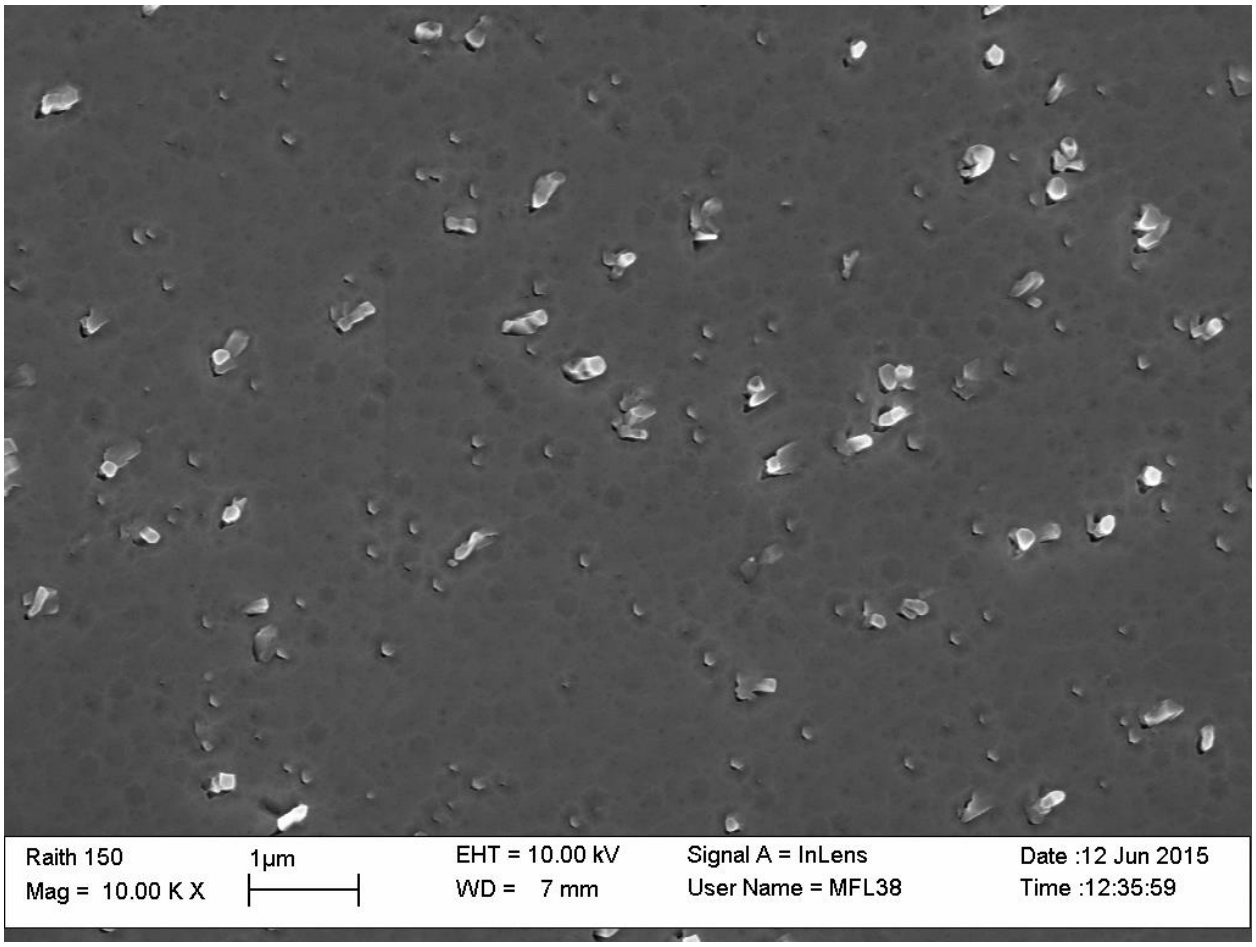

Figure 12: Zn-rich MBE growth on 10 nm Au colloid coated c-plane sapphire. The resulting growth appears to be a film, broken by scattered and irregular nanostructures.

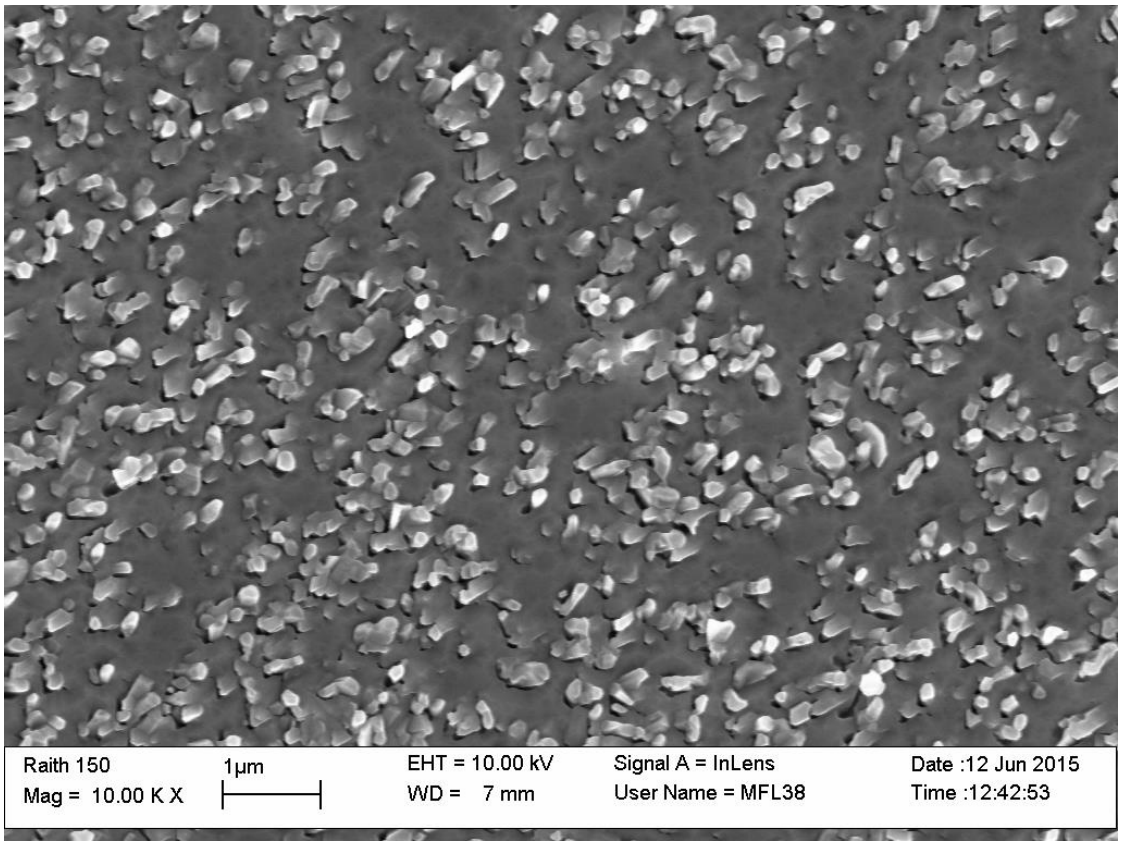

Figure 13: A different region of the substrate with ZnO deposited under Zn-rich conditions. This area shows a higher density of disruptions to the film, possibly due to a local increase in colloid density, but the morphology remains similar to Figure 12.

8.3 Summary

ZnO nanowires were successfully grown using sputtered palladium as a catalyst, while the attempted catalytic growth of ZnO nanowires using sputtered ruthenium films was unsuccessful. The quality of nanorods grown using molecular beam epitaxy with APTMS-tethered Au colloid coated substrates was surprisingly poor.

- Palladium was found to be effective at catalysing ZnO nanowires when sputter coated at a thickness of approximately 1.5 nm onto both a-plane and c-plane sapphire samples. This represents the first successful use of palladium as a catalyst in ZnO nanowire growth.
- The fact that this is possible despite the growth temperature of 750 °C being significantly lower than the 1554.9 °C melting point of palladium is attributed to a size dependent reduction in melting point as suggested by Park *et al.* [11].

- Ruthenium was found to be an ineffective catalyst for ZnO nanowires at a growth temperature of 750 °C and an attempted ZnO nanowire growth using a sputtered film of ruthenium approximately 2-3 nm thick produced only a coarsely textured film.
- ZnO nanorods grown by MBE using APTMS-tethered, commercial, 10 nm Au colloids as catalysts were of poor morphological consistency and displayed no ordering or preferential growth direction. Nanostructures of different shapes were formed, with a minority of these structures developing into nanorods and nanosheets.
- Increasing the Zn-flux did not improve the morphology or length of the nanorods and instead resulted in a relatively smooth film with scattered nanostructured imperfections.
- The highly disordered nanorods produced by the MBE were similar to those produced by the low deposition rate PLD growth conducted in Chapter 1, Section 12, suggesting that the low growth rates characteristic of MBE may be counter-productive in producing high quality ZnO nanowires.

8.4 References

[1] A. Marcu, L. Trupina, R. Zamani, J. Arbiol, C. Grigoriu, and J. R. Morante, "Catalyst size limitation in vapor-liquid-solid ZnO nanowire growth using pulsed laser deposition," *Thin Solid Films,* vol. 520, pp. 4626-4631, 2012.

[2] M. H. Huang, Y. Wu, H. Feick, N. Tran, E. Weber, and P. Yang, "Catalytic growth of zinc oxide nanowires by vapor transport," *Advanced Materials,* vol. 13, pp. 113-116, 2001.

[3] A. M. Lord, T. G. Maffeis, A. S. Walton, D. M. Kepaptsoglou, Q. M. Ramasse, M. B. Ward, *et al.*, "Factors that determine and limit the resistivity of high-quality individual ZnO nanowires," *Nanotechnology,* vol. 24, 2013.

[4] F. Falyouni, L. Benmamas, C. Thiandoume, J. Barjon, A. Lusson, P. Galtier, *et al.*, "Metal organic chemical vapor deposition growth and luminescence of ZnO micro- and nanowires," *Journal of Vacuum Science and Technology B:Nanotechnology and Microelectronics,* vol. 27, pp. 1662-1666, 2009.

[5] P. X. Gao, Y. Ding, and Z. L. Wang, "Crystallographic orientation-aligned ZnO nanorods grown by a tin catalyst," *Nano Letters,* vol. 3, pp. 1315-1320, 2003.

[6] Y. Ding, P. X. Gao, and Z. L. Wang, "Catalyst-Nanostructure Interfacial Lattice Mismatch in Determining the Shape of VLS Grown Nanowires and Nanobelts: A Case of Sn/ZnO," *Journal of the American Chemical Society,* vol. 126, pp. 2066-2072, 2004.

[7] Z. W. Pan, S. Dai, C. M. Rouleau, and D. H. Lowndes, "Germanium-catalyzed growth of zinc oxide nanowires: A semiconductor catalyst for nanowire synthesis," *Angewandte Chemie - International Edition,* vol. 44, pp. 274-278, 2005.

[8] Z. Zhang, S. J. Wang, T. Yu, and T. Wu, "Controlling the growth mechanism of ZnO nanowires by selecting catalysts," *Journal of Physical Chemistry C,* vol. 111, pp. 17500-17505, 2007.

[9] S. Y. Li, C. Y. Lee, and T. Y. Tseng, "Copper-catalyzed ZnO nanowires on silicon (1 0 0) grown by vapor-liquid-solid process," *Journal of Crystal Growth,* vol. 247, pp. 357-362, 2003.

[10] Y. C. Kong, D. P. Yu, B. Zhang, W. Fang, and S. Q. Feng, "Ultraviolet-emitting ZnO nanowires synthesized by a physical vapor deposition approach," *Applied Physics Letters,* vol. 78, pp. 407-409, 2001.

[11] H. D. Park, A. C. Gaillot, S. M. Prokes, and R. C. Cammarata, "Observation of size dependent liquidus depression in the growth of InAs nanowires," *Journal of Crystal Growth,* vol. 296, pp. 159-164, 2006.

[12] Z. Moser, "The Pt-Zn (Platinum-Zinc) system," *Journal of Phase Equilibria,* vol. 12, pp. 439-443, 1991// 1991.

[13] Y. Chen, D. M. Bagnall, Z. Zhu, T. Sekiuchi, K. T. Park, K. Hiraga, *et al.*, "Growth of ZnO single crystal thin films on c-plane (0 0 0 1) sapphire by plasma enhanced molecular beam epitaxy," *Journal of Crystal Growth,* vol. 181, pp. 165-169, 1997.

[14] S. F. Chichibu, A. Tsukazaki, M. Kawasaki, K. Tamura, Y. Segawa, T. Sota, *et al.*, "Photoreflectance spectra of a ZnO heteroepitaxial film on the nearly lattice-matched ScAlMgO4 (0001) substrate grown by laser molecular-beam epitaxy," *Applied Physics Letters,* vol. 80, pp. 2860-2862, 2002.

[15] A. R. Hyndman, M. W. Allen, and R. J. Reeves, "Growth of epitaxial ZnO films on sapphire substrates by plasma assisted molecular beam epitaxy," in *Proceedings of SPIE - The International Society for Optical Engineering*, 2015.

[16] Y. W. Heo, B. S. Kang, L. C. Tien, D. P. Norton, F. Ren, J. R. L. A. Roche, *et al.*, "UV photoresponse of single ZnO nanowires," *Applied Physics A: Materials Science and Processing,* vol. 80, pp. 497-499, 2005.

Chapter 9: Conclusions and Outlook

ZnO and ZnMgO nanowires were grown using the eclipse pulsed laser deposition (EPLD) technique. A new method of controlling the tip diameters of these nanowires was developed using chemically synthesised Au colloids and atomic cluster catalysts attached to sapphire substrates using the silanising ligand 3-aminopropyl trimethoxysilane (APTMS). Electrical and optical characterisation of the resulting nanowires confirmed their high crystal quality, in particular, narrow line widths of the excitonic UV photoluminescence spectra and the complete lack of defect-related emission.

9.1 Development of Au Colloid Catalysed ZnO Nanowire Growth by Eclipse Pulsed Laser Deposition

Chemically synthesised Au colloids were found to effectively catalyse the vapour-liquid-solid (VLS) growth of ZnO nanowires on sapphire substrates using EPLD. Silanisation of the surface of the sapphire substrates using APTMS prior to the application of the Au colloids significantly improved colloid adhesion, resulting in more even colloid coverage and significantly improved alignment and morphology in the resulting nanowires. Heating the substrates to the growth temperature of 750 °C in the presence of oxygen served to remove residual APTMS and other contaminants. This prevented unwanted contamination from interfering with the epitaxial relationship between the ZnO nanowires and the sapphire substrates.

Using this technique, ZnO nanowires were grown in well-aligned arrays. The nanowires showed a tapered morphology but the diameter of the nanowire tips was found to match the diameter of the colloid catalysts. Consequently, ZnO nanowires with tip diameters ranging from 5-40 nm were able to be reproducibly grown by selecting the diameters of the Au colloid catalysts. The preferred growth direction of the nanowires was confirmed by x-ray diffraction to be in line with the ZnO <002> plane.

9.2 ZnO Nanowires Grown by EPLD Using Non-Metallic Au Clusters as Catalysts

ZnO nanowires were grown by EPLD using atomically precise, non-metallic clusters of 101 and 9 Au atoms as catalysts. The diameters of these atomic Au clusters were smaller than the 2 nm threshold necessary for gold to form metallic bonds and they instead adopt the structure of covalently bonded molecules with a fixed number of Au atoms. The ZnO nanowires resulting from these atomic cluster catalysts had tip

diameters of less than 1.5 nm, narrower than any ZnO nanowires previously reported in the literature. These results showed that it is not necessary for Au nanoparticles to have a metallic structure in order to effectively catalyse the growth of ZnO nanowires via VLS. Indeed, clusters of only 9 Au atoms were able to effectively catalyse the VLS growth of ZnO nanowires. If a lower limit on the size of Au clusters able to catalyse the ZnO VLS growth process does exist, then it is beyond the measurement limits of the SEM equipment that was available in this thesis.

Ultra-fine ZnO nanowires with tip diameters of 5 nm or less were found to spontaneously bend towards their neighbours and fuse together when exposed to the electron beam of an SEM. The electron beam injects negative charge into an ultra-fine nanowire, which in turn induces a positive charge in neighbouring nanowires. The extremely narrow tips of the nanowires intensify the electric fields and the resulting electrostatic attraction increases between the nanowires until one nanowire bends into contact with another to neutralise the respective charges, with the energy released fusing them together.

9.3 Electrical Properties of ZnO Nanowires

Ti/Au ohmic and silver-oxide (AgO_x) Schottky contacts were successfully fabricated onto individual ZnO nanowires using electron beam lithography (EBL). The nanowires were found to have very high resistances of several giga-ohms, but this was consistent with the resistances of other ZnO nanowires reported in the literature. Exposure to 365 nm UV illumination for 30 s at a constant bias voltage of 1 V caused an increase in nanowire current of more than three orders of magnitude. This photocurrent was highly persistent and took approximately 5000 s to decay to pre-illumination levels in atmosphere. Exposure to the same UV illumination in vacuum also caused an increase in current of three orders of magnitude, but the photocurrent did not completely decay and still remained two orders of magnitude higher than the pre-illumination level after 5000 s. This showed that the photocurrent in ZnO nanowires is generated by two mechanisms acting in parallel, one which is linked to atmospheric oxygen. The photogeneration of electron-hole pairs is independent of the presence of oxygen and this photocurrent component decays in both vacuum and atmosphere, however UV exposure also causes the desorption of oxygen from the surface of the ZnO nanowires. This surface oxygen is an electron acceptor that depletes the near-surface region of the nanowire and so the UV-induced desorption of surface oxygen significantly increases the conductivity of the nanowire. As a result, this increase in nanowire conductivity will persist indefinitely while the nanowire remains in vacuum. Subsequent exposure to atmosphere causes the re-adsorption of oxygen onto the surface of the nanowire, decreasing its conductivity to pre-illumination levels.

AgO_x Schottky contacts fabricated onto ZnO nanowires were highly rectifying with four orders of magnitude rectification between forward and reverse bias currents at biases of ±1.5 V. A nanowire MESFET was fabricated, but an unidentifiable fault in the testing equipment caused an electrical discharge which destroyed the nanowire devices being tested.

9.4 Low Temperature Photoluminescence of ZnO Nanowires

Low temperature (3 K) photoluminescence (PL) was used to characterise the Au colloid catalysed ZnO nanowires grown by EPLD. PL spectra from the UV excitonic recombination region showed very narrow line widths, indicating high crystal quality. The dominant excitonic PL peak was found to be I_9, indicating that indium was the most significant impurity present. The indium-tin eutectic used to adhere substrates to the PLD heater is the most likely source of this impurity, as it has been found that indium becomes mobile above 520 °C and can migrate onto the surface of the ZnO during growth.

No detectable PL emission in the visible wavelength defect band region was observed, with at least five orders of magnitude difference in intensity between the UV excitonic emission and any defect band emission. Green and yellow PL emission is commonly reported in ZnO nanostructures but was not observed. This is a further indication of very high crystal quality of the EPLD grown nanowires, as even commercially produced ZnO single crystals typically show only three orders of magnitude intensity difference between the excitonic and the defect band emission.

9.5 ZnMgO Nanowire Growth

ZnMgO targets with Mg concentrations of 5%, 10% and 15% were used to grow nanowires by EPLD on APTMS-tethered Au colloid coated substrates. The tip diameter of the ZnMgO nanowires was found to match the diameters of the catalyst colloids, however both nanowire morphology and ordering degraded with increased Mg content due to the lattice mismatch between the ZnO and MgO crystal structures. Low temperature (3 K) PL characterisation of the ZnMgO nanowires showed very broad line widths indicating reduced crystal quality compared to the pure ZnO nanowires. The introduction of Mg into the ZnO nanowires caused the dominant excitonic emission peak to shift by approximately 90 meV, consistent with a widening of the bandgap.

9.6 ZnO Nanowires Catalysed by Sputtered Palladium Film

A 1.5 nm thin film of palladium was used for the first time to catalyse the growth of ZnO nanowires. Palladium has a bulk melting point of 1554.9 °C, significantly higher than the 750 °C growth temperature of EPLD ZnO nanowires, however a size dependent melting point reduction effect may have enabled the palladium to become liquid at this growth temperature. Metallic capping particles were found on the tips of some of the ZnO nanowires catalysed by the palladium film indicating that VLS growth had occurred. An attempt to grow ZnO nanowires using a similarly thin film of sputtered ruthenium as a catalyst was unsuccessful. Ruthenium's bulk melting point of 2334 °C was found to be too high to catalyse VLS nanowire growth, even when only very thin layers of ruthenium were used.

9.7 ZnO Nanorods Grown by Molecular Beam Epitaxy

Molecular beam epitaxy (MBE) was also used to grow ZnO nanorods on APTMS-tethered Au colloid coated substrates. ZnO nanorods grown by this method were highly disordered and did not show a preferential growth direction. MBE has the capacity to grow very high quality single crystal films, but it has a very low deposition rate. ZnO nanorod growth experiments conducted using EPLD showed that a low deposition rate typically resulted in disordered nanorods, so it is likely that the deposition rates involved in MBE are simply too slow to produce high quality ZnO nanowires.

9.8 Outlook and Future Research

A new method of catalysing metal oxide nanowires that allows for the direct control of the nanowire tip diameter was demonstrated in this thesis. Nanowires grown by EPLD using chemically synthesised, APTMS-tethered Au colloids and atomic clusters were found to have exceptionally low defect levels and the tip diameters could be controlled to within a few nanometres. However the tapered morphology of the EPLD nanowires (whether catalysed by APTMS-tethered colloids or by sputtered metal films) limits the usefulness of controlling this dimension. The growth of non-tapered, catalytic, VLS grown ZnO nanowires by other methods such as chemical vapour deposition (CVD) has been reported on in the literature. If the APTMS-tethering method of catalyst application could be combined with a growth method capable of reliably producing non-tapered ZnO nanowires, it is very likely that the entire diameters of these nanowires could be tuned by selecting the colloid sizes. If the blueshift in the PL spectra of the tapered nanowires characterised in this thesis was indeed due to quantum confinement effects, these effects would certainly be intensified if the entire nanowire had a uniform width as narrow as the tips.

The ZnO nanowires were very sensitive to UV illumination, showing three orders of magnitude increase in current after exposure to 365 nm UV light. Additionally, the emission of the nanowires during PL was almost entirely in the UV wavelengths with five orders of magnitude higher emission intensity in the excitonic UV region than in the visible defect region. This is a good indication that these nanowires have sufficiently high crystal quality to function as visible-blind UV detectors. Schottky diodes fabricated using AgO_x demonstrated four orders of magnitude rectification without any real attempts being made to optimise the contact efficiency. Further research into single-nanowire, AgO_x Schottky diodes using EPLD grown ZnO nanowires could have significant applications in visible-blind UV detection.

Appendix 1: List of PLD Growths

The following is a list of PLD growths carried out during the course of the research described in this thesis. The most important parameters are listed. O_2 Partial pressure remained constant at 5×10^{-2} Torr throughout. Although every growth was imaged by SEM, many of these growths were repeats of other growths conducted for assessing reproducibility or growths which failed to produce significant results. As such, not every growth listed here is discussed in the main text.

Table 1: Complete list of PLD growths.

No.	Date	E_L (mJ)	Subs	t_{Grow}	f_{Laser}	Temp (ºC)	E-PLD	Section	Motivation
1	21/03/12	100	A	1h	10	750	No	3.4	First growth.
2	3/04/12	100	A	1h	10	600	No	3.5	Lower temp
3	26/04/12	100	A	1h	10	750	No		Replicate 01. Si, Quartz.
4	2/05/12	100	A	1h	10	750	No		Replicate 01.
5	7/05/12	68	A	1h	10	750	No		Lower laser fluence
6	10/05/12	70	A	1h	10	750	No	3.5	Repeat 05
7	17/05/12	100	A	1h	10	750	No		Test chamber
8	17/05/12	100	A	1h	10	750	No		Test sputtered Au
9	18/05/12	100	A	2h	10	750	Yes	3.6	Try eclipse plate
10	30/05/12	100	A	1h	10	750	Yes	3.6	Repeat 09
11	24/05/12	100	A	30m	10	750	Yes		Lower growth time
12	26/06/12	100	C	1h	10	750	Yes	3.7	C-Axis Sapphire
13	28/06/12	100	C	1h	10	750	Yes		Repeat 12 new target
14	3/07/12	100	C	1h	10	750	Yes		Repeat 12 with new target
15	10/07/12	100	M	1h	10	750	Yes	3.7	M Plane Substrate
16	10/07/12	100	R	1h	10	750	Yes	3.7	R Plane Substrate
17	28/07/12	100	C	10m	10	750	Yes		Observe formative stages
18	3/08/12	100	Al	1h	10	750	Yes		Dimpled Al target
19	10/08/12	100	C	1h	10	750	Yes		Dip coated 3.2 nm
20	10/08/12	100	C	1h	10	750	Yes	3.8	Dip coated 13 nm
21	10/08/12	100	C	1h	10	750	Yes		Control for 19 and 20
22	2/09/12	100	C	1h	10	750	Yes	3.9	Polystyrene Spheres
23	9/09/12	100	C	1h	10	750	Yes		Conc. increase dip coating
24	9/09/12	100	C	1h	10	750	Yes		Conc. increase dip coating
25	9/09/12	100	C	1h	10	750	Yes		Conc. increase dip coating
26	13/09/12	100	R	1h	10	750	Yes		Repeat 16
27	13/09/12	100	M	1h	10	750	Yes		Repeat 15

28	13/09/12	100	C	1h	10	750	Yes		Control
29	19/09/12	100	C	1h	10	750	Yes		Polystyrene Spheres
30	28/09/12	100	C	1h	10	750	Yes		O2 Plasma treated dip coat
31	28/09/12	100	C	1h	10	750	Yes		Normal dip coat
32	28/09/12	100	C	1h	10	750	Yes		Control
33	5/10/12	100	C	1h	10	750	Yes		13nm, 3nm and dip 3nm
34	5/10/12	100	C	1h	10	750	Yes		13nm, 3nm and dip 3nm
35	5/10/12	100	C	1h	10	750	Yes		13nm, 3nm and dip 3nm
36	20/10/12	100	C	1h	10	750	Yes		Repeat 33
37	20/10/12	100	C	1h	10	750	Yes		Repeat 34
38	20/10/12	100	C	1h	10	750	Yes		Repeat 35
39	1/11/12	100	A	1h	10	750	Yes		ZnMgO
40	9/11/12	100	C	1h	10	750	Yes	3.10	Sputtered AuNPs
41	19/12/12	100	C	1h	10	750	Yes		30 min deposition
42	20/12/12	100	C	1h	10	750	Yes		15 min deposition
43	11/01/13	100	C	1h	10	750	Yes	3.11	"Adjusted Citrate Ligands"
44	11/01/13	100	C	1h	10	750	Yes		"Adjusted Citrate Ligands"
45	11/01/13	100	C	1h	10	750	Yes		"Adjusted Citrate Ligands"
46	16/01/13	100	C	1h	10	750	Yes		Use newer APTMS
47	16/01/13	100	C	1h	10	750	Yes		Use newer APTMS
48	16/01/13	100	C	1h	10	750	Yes		Use newer APTMS
49	25/01/13	100	C	1h	10	750	Yes		Repeat 44-46
50	25/01/13	100	C	1h	10	750	Yes		Repeat 44-46
51	25/01/13	100	C	1h	10	750	Yes		Repeat 44-46
52	23/02/13	100	C	1h	10	750	Yes		25% Au conc
53	23/02/13	100	C	1h	10	750	Yes		50% Au conc
54	23/02/13	100	C	1h	10	750	Yes		100% Au conc (control)
55	19/03/13	100	C	1h	10	750	Yes	3.11	Heating under oxygen
56	20/03/13	100	C	1h	10	750	Yes		Heating under oxygen
57	28/03/13	100	C	1h	10	750	Yes		Heating under oxygen
58	10/04/13	100	C	1h	10	750	Yes		Repeat 54
59	16/04/13	100	C	2.5h	4	750	Yes	3.12	Low frequency, high time
60	25/04/13	100	C	1h	10	750	Yes		Reproduce 49 and 50
61	2/05/13	100	C	1h	10	750	Yes	3.13	Position dependence
62	8/05/13	100	C	1h	10	750	Yes		Repeat 58 with low conc.
63	9/05/13	100	C	24m	25	750	Yes	3.12	High Freq, inverse of 56
64	20/05/13	100	C	1h	10	750	Yes		Ag Paste
65	27/05/13	100	C	1h	10	750	Yes		Repeat 61 with 8.5mM
66	11/07/13	100	C	1h	10	750	Yes		4.25mM soln.
67	12/07/13	100	C	1h	10	750	Spiral		Spiral eclipse plate
68	17/07/13	100	C	48m	25	750	Yes		High freq, double time

69	6/08/13	100	C	1h	10	750	Yes		Check heater
70	22/08/13	100	A	1h	10	750	Yes		A-Plane test with APTMS
71	28/01/14	100	A+C	1h	10	750	Yes	4.2	Vladimir Colloids test
72	25/02/14	100	C	1h	10	750	Yes		Elec Colloids test
73	1/04/14	100	C	1h	10	750	Yes		Repeat 69
74	19/02/15	100	C	1h	10	750	Yes		Colloid 1hr/3hr
75	9/03/15	100	C	1h	10	750	Yes		No APTMS test
76	13/03/15	100	C	1h	10	750	Yes		Repeat 69
77	20/03/15	100	C	1h	10	750	Yes		Different APTMS time
78	19/06/15	100	C	1h	10	750	Yes		Commercial 20 nm
79	24/06/15	100	C	1h	10	750	Yes		Repeat 75
80	26/06/15	100	C	1h	10	750	Yes	4.3	10 nm, 20 nm, 40 nm
81	2/07/14	100	C	1h	10	750	Yes		Repeat 77, blank control
82	8/07/15	100	C	30m	20	750	Yes		Repeat 77, higher freq
83	14/07/15	100	C	1h	10	750	No		Repeat 77, no e-plate
84	16/07/15	100	C	1h	10	750	Yes		Sputtered AuNPs
85	22/07/15	100	C	1h	10	750	Yes		10/30 mins 10 nm AuNP
86	24/07/15	100	C	1h	10	750	Yes		Overnight 10 nm AuNP
87	30/07/15	100	C	1h	10	750	Yes		Hybrid drop coating
88	16/08/15	100	C	1h	10	750	Yes		Hybrid 1hr/3hr
89	8/09/15	100	C	1h	10	750	Yes		Repeat 85, Si control
90	11/09/15	100	C	1h	10	750	Yes	4.3	Position dependent 10 nm
91	24/09/15	100	C	1h	10	750	Yes		Position dependent 40 nm
92	1/10/15	100	C	1h	10	750	Yes	4.3	Position dependent 5 nm
93	6/10/15	100	C	1h	10	750	Yes		Repeat 89
94	13/10/15	100	C	1h	10	750	Yes		Repeat 89
95	16/10/15	100	C	1h	10	750	Yes		Commercial 30 nm
96	21/10/15	100	C	1h	10	750	Yes		Repeat 92
97	4/11/15	100	C	30m	20	750	Yes		Commercial hi-freq
98	17/11/15	100	C+A	1h	10	750	Yes	7.2	ZnMgO 5% NW
99	23/02/16	100	C+A	1h	10	750	Yes	7.3	ZnMgO 5% film
100	25/03/16	100	C+A	1h	10	750	Yes	7.2	ZnMgO 10% NW
101	16/03/16	100	C+A	1h	10	750	Yes	4.4	Au101
102	20/04/16	100	C+A	1h	10	750	Yes	4.4	Au9
103	22/06/16	100	C+A	1h	10	750	Yes	8.1	Palladium
104	1/07/16	100	C+A	1h	10	750	Yes	8.1	Ruthenium
105	13/07/16	100	C+A	1h	10	750	Yes	7.2	ZnMgO 15% NW